[153] Walker, G. (1987). *Astronomical Observations*, (Cambridge : Cambridge University Press)

[154] Webbink, R. (1985). in *Dynamics of Star Clusters*, editied by J. Goodman, & P. Hut, (Dordrecht : Reidel), IAU Symp. **113**, p 541

[155] West, M. J., Côté, P., Jones, C., Forman, W., & Marzke, R. O. (1995). *Astrophysical Journal Letters*, **453**, L77

[156] Zinn, R. & West, M. (1984). *Astrophysical Journal Supplement*, **55**, 4

[141] Stetson, P. B. (1987). *Publications of the Astronomical Society of the Pacific*, **99**, 191

[142] Stetson, P. B., & Harris, W. E. (1988). *Astronomical Journal*, **96**, 909

[143] Stetson, P. B., Davis, L. E., & Crabtree, D. R. (1990). in *CCDs in Astronomy*, edited by G. H. Jacoby, (San Francisco : ASP), ASP Conf. Ser. **8**, p. 289

[144] Taylor, B. J. (1986) *Astrophysical Journal Supplement*, **60**, 577

[145] Trager, S. C., Djorgovski, & King, I. R. (1993). in *Structure and Dynamics of Globular Clusters*, editied by S. Djorgovski, & G. Meylan, (San Francisco : ASP), ASP Conf. Ser. **50**, p. 347

[146] Tripicco, M. J. (1989). *Astronomical Journal*, **97**, 735

[147] van den Bergh, S. (1993). *Astrophysical Journal*, **411**, 17

[148] van den Bergh, S. (1991). *Publications of the Astronomical Society of the Pacific*, **103**, 1053

[149] van den Bergh, S. (1969). *Astrophysical Journal Supplement*, **19**, 145

[150] Vetešník, M. (1962). *Bulletin of the Astronomical Institute of Czechoslovakia*, **13**, 180

[151] Vio, R., Fasano, G., Lazzarin, M., & Lessi, O. (1994). *Astronomy & Astrophysics*, **289**, 640

[152] Walker, A. R. (1990). in *CCDs in Astronomy*, edited by G. H. Jacoby, (San Francisco : ASP), ASP Conf. Ser. **8**, p 319

[129] Schweizer, F. (1979). *Astrophysical Journal*, **233**, 23

[130] Scheiner, J. (1898). *Astronomische Nachrichten*, **148**, 325

[131] Silverman, B. W. (1982). *Applied Statistics*, **31**, 93

[132] Simoda, M. & Kimura, H. (1968). *Astrophysical Journal*, **151**, 133

[133] Slipher, V. M. (1913). *Lowell Bulletin # 58*, **2**, 56

[134] Smail, I., Hogg, D. W., Yan, L., & Cohen, J. G. (1995). *Astrophysical Journal Letters*, **449**, L10

[135] Spassova, N. M., Staneva, A. V., & Golev, V. K. (1988). in *Globular Clusters in Galaxies*, edited by J. E. Grindley, & A. G. Davis Philip, (Kluwer : Dordrecht), p. 569

[136] Spitzer, L. (1987). in *Dynamical Evolution of Globular Clusters*, (Princeton : Princeton University Press)

[137] Stetson, P. B. (1996). private communication

[138] Stetson, P. B. (1994). *Publications of the Astronomical Society of the Pacific*, **106**, 250

[139] Stetson, P. B. (1992). in *Astronomical Data Analysis Software and Systems I*, edited by D. M. Worrall, C. Biemesderfer, & J. Barnes, (San Fransisco : ASP), ASP Conf. Ser. **25**, p. 297

[140] Stetson, P. B. (1991). in *The Third ESO/ST-ECF Data Analysis Workshop*, edited by P. J. Grosbol, & H. R. Warmels, (Garching : ESO), p. 187

[116] Ratnatunga, K. U., & Bahcall, J. N. (1985). *Astrophysical Journal Supplement*, **59**, 63

[117] Renzini, A, & Fusi Pecci, F. (1988). *Annual Reviews of Astronomy & Astrophysics*, **26**, 199

[118] Rich, R. M., Sosin, C., Djorgovski, S. G., Piotto, G. King, I. R., Renzini, A., Phinney, E. S., Dorman, B., Liebert, J., & Meylan, G. (1997). *Astrophysical Journal Letters*, **484**, L25

[119] Rich, R. M., Mighell, K. J., Freedman, W. L., & Neill, J. D. (1996). *Astronomical Journal*, **111**, 768

[120] Rich, R. M., & Mighell, K. J. (1995). *Astrophysical Journal*, **439**, 145

[121] Richardson, W. H. (1972). *Journal of the Optical Society of America*, **62**, 55

[122] Richer, H. B., Harris, W. E., Fahlman, G. G., Bell, R. A., Bond, H. E., Hesser, J. E., Holland, S., Pryor, C., Stetson, P. B., VandenBerg, D. A., & van den Bergh, S. (1996). *Astrophysical Journal*, **463**, 602

[123] Roberts, M. (1966). *Astrophysical Journal*, **144**, 639

[124] Rubin, V. C., & Ford, W. K. (1970). *Astrophysical Journal*, **159**, 379

[125] Sarajedini, A., & Layden, A. C. (1995). *Astronomical Journal*, **109**, 108

[126] Sarajedini, A., Lee, Y.-W., & Lee, D. H. (1995). *Astrophysical Journal*, **450**, 712

[127] Sargent, W. L. W., Kowal, C. T., Hartwick, F. D. A., & van den Bergh, S. (1977). *Astronomical Journal*, **82**, 947

[128] Schade, D. J., & Elson, R. A. W. (1993). *Astronomical Journal*, **105**, 1581

[102] Murali, C., & Weinberg, M. D. (1996). in *Formation of the Galactic Halo*, ASP Conf. Ser. **92**, edited by H. Morrison, & A. Sarajedini, (San Fransisco : ASP), p. 491

[103] Oh, K. S., & Lin, D. N. C. (1992). *Astrophysical Journal*, **386**, 519

[104] Ortolani, S., Barbuy, B., & Bica, E. (1990). *Astronomy & Astrophysics*, **236**, 362

[105] Okazaki, T., & Tosa, M. (1995). *Monthly Notices of the Royal Astronomical Society*, **274**, 48

[106] Peacock, J. A. (1983). *Monthly Notices of the Royal Astronomical Society*, **202**, 61

[107] Pease, F. G. (1918). *Proceedings of the Natural Academy of Sciences*, **4**, 21

[108] Peterson, C. (1993). in *Structure and Dynamics of Globular Clusters*, edited by S. Djorgovski, & G. Meylan, (San Francisco : ASP), ASP Conf. Ser. **50**, p. 337

[109] Peterson, C. J., & Reed, B. C. (1987). *Publications of the Astronomical Society of the Pacific*, **99**, 20

[110] Peterson, C. J., & King, I. R. (1975). *Astronomical Journal*, **80**, 427

[111] Primini, F. A., Forman, W., & Jones, C. (1993). *Astrophysical Journal*, **410**, 615

[112] Pritchet, C. J. & van den Bergh, S. (1994). *Astronomical Journal*, bf 107, 173

[113] Pritchet, C. J., & van den Bergh, S. (1988). *Astrophysical Journal*, **331**, 135

[114] Pritchet, C. J., & van den Bergh, S. (1987). *Astrophysical Journal*, **316**, 517

[115] Pritchet, C., & van den Bergh, S. (1984). *Publications of the Astronomical Society of the Pacific*, **96**, 804

[87] Lee, S.-W. (1977). *Astronomy & Astrophysics Supplement*, **27**, 381

[88] Lee, Y.-K., Demarque, P., & Zinn, R. (1994). *Astrophysical Journal*, **423**, 248

[89] Lucy, L. B. (1974). *Astronomical Journal*, **79**, 745

[90] Lupton, R. H. (1989). *Astronomical Journal*, **97**, 1350

[91] Lupton, R. H., & Gunn, J. E. (1987). *Astronomical Journal*, **93**, 1106

[92] Lyngå, G., & Wramdemark, S. (1984). *Astronomy & Astrophysics*, **132**, 58

[93] Madore, B. F., & Freedman, W. L. (1997). preprint

[94] Madore, B. (1980). in *Globular Clusters*, edited by D. Hanes, & B. Madore, (Cambridge : CUP), p 21

[95] McClure, R. D., Grundmann, W. A., Rambold, W. N., Fletcher, M., Richardson, E. H., Stilburn, J. R., Racine, R., Christian, C. A., & Waddell, P. (1989). *Publications of the Astronomical Society of the Pacific*, **101**, 1156

[96] Merritt, D., & Tremblay, B. (1994). *Astronomical Journal*, **108**, 514

[97] Michie, R. W. (1963). *Monthly Notices of the Royal Astronomical Society*, **125**, 127

[98] Mighell, K. J. (1990). *Astronomy & Astrophysics Supplement*, **82**, 207

[99] Miyamoto, M., & Nagai, R. (1975). *Publications of the Astronomical Society of Japan*, **27**, 533

[100] Moffat, A. F. J. (1969). *Astronomy & Astrophysics*, **3**, 455

[101] Mould, J., & Kristian, J. (1986). *Astrophysical Journal*, **305**, 591

[73] Holtzman, J. A., Burrows, C. J., Casertano, S., Hester, J. J, Trauger, J. T., Waterson, A. M., & Worthey, G. S. (1995b). *Publications of the Astronomical Society of the Pacific*, **107**, 1065

[74] Hoskin, M. A. (1970). *Journal for the History of Astronomy*, **1**, 44

[75] Hubble, E. P. (1925). *Obs.*, **48**, 139

[76] Huchra, J. P. Brodie, J. P., & Kent, S. M. (1991). *Astrophysical Journal*, **370**, 495 (HBK)

[77] Ibata, R. A., Cilmore, G. G., & Irwin, M. J. (1994). *Nature*, **370**, 19

[78] Innanen, K. A., Harris, E. W., & Webbink, R. F. (1983). *Astronomical Journal*, **88**, 338

[79] Jablonka, P., Bridges, T., Sarajedini, A., Meylan, G., Meynet, G., & Maeder, A. (1997). *Bulletin of the American Astronomical Society*, **28**, 1364

[80] Jedrzejewski, R. I. (1987). *Monthly Notices of the Royal Astronomical Society*, **226**, 747

[81] Jones, K. G., (1971). *Journal for the History of Astronomy*, **2**, 29

[82] King, I. R. (1966). *Astronomical Journal*, **71**, 64

[83] King, I. R. (1962). *Astronomical Journal*, **67**, 471

[84] Kormendy, K., & McClure, R. D. (1993). *Astronomical Journal*, **105**, 1793

[85] Landolt, A. U. (1983). *Astronomical Journal*, **88**, 439

[86] Lin, D. H., & Richer, H. B. (1992). *Astrophysical Journal Letters*, **388**, L5

[61] Gunn, J. E., & Griffin, R. F. (1979). *Astronomical Journal*, **84**, 752

[62] Harris, W. E. (1991). *Annual Reviews of Astronomy & Astrophysics*, **29**, 543

[63] Harris, W. E., & Racine, R. (1979). *Annual Reviews of Astronomy & Astrophysics*, **17**, 241

[64] Heald, M. A. (1984). *American Journal of Physics*, **52**, 25

[65] Heasley, J. N., Christian, C. A., Friel, E. D., & Janes, K. A. (1988). *Astronomical Journal*, **96**, 1312

[66] Heggie, D. C., R̂amamani, N. (1995). *Monthly Notices of the Royal Astronomical Society*, **272**, 317

[67] Hernquist, L. (1990). *Astrophysical Journal*, **356**, 359

[68] Hesser, J. E., Harris, W. E., VandenBerg, D.A., Allwright, J. W. B., Shott, P., & Stetson, P. B. (1987). *Publications of the Astronomical Society of the Pacific*, **99**, 73

[69] Hesser, J. E., & Hartwick, F. D. A., (1977). *Astrophysical Journal Supplement*, **33**, 361

[70] Hodder, P. J. C. (1995). Ph.D. Thesis, UBC.

[71] Hodge, P. (1992). *The Andromeda Galaxy*, (Dordrecht : Kluwer)

[72] Holtzman, J. A., et al.(1995a). *Publications of the Astronomical Society of the Pacific*, **107**, 156

[51] Fahlman, G. G. (1993). in *The Globular Cluster–Galaxy Connection*, ASP Conf. Ser. **48**, edited by G. H. Smith, & J. P. Brodie, (San Francisco : ASP), p. 117

[52] Fahlman, G. G., Richer, H. B., Searle, L., & Thompson, I. B. (1989). *Astrophysical Journal Letters*, **343**, L49

[53] Feast, M. W., & Catchpole, R. M. (1997). *Monthly Notices of the Royal Astronomical Society*, **286**, L1

[54] Freedman, W. L., & Madore, B. F. (1990). *Astrophysical Journal*, **365**, 18

[55] Frogel, J. A., Persson, S. E., & Cohen, J. G. (1980). *Astrophysical Journal*, **240**, 785

[56] Fusi Pecci, F., Buonanno, R., Cacciari, C., Corsi, C. E., Djorgovski, S. G., Federici, L., Ferraro, F. R., Parmeggiani, G., & Rich, R., M. (1996). *Astronomical Journal*, **112**, 1461

[57] Fusi Pecci, F., Battistini, P., Bendinelli, O. Bònoli, F., Cacciari, C., Djorgovski, S., Federici, L., Ferraro, F. R., Parmeggiani, G., Weir, N., & Zavatti, F. (1994). *Astronomy & Astrophysics*, **284**, 349

[58] Grillmair, C. J., Ajhar, E. A., Faber, S. M., Baum, W. A., Holtzman, J. A., Lauer, T. R., Lynds, C. R., & O'Neil, Jr., E. J. (1996). *Astronomical Journal*, **111**, 2293 (GAF)

[59] Grillmair, C. J., Freeman, K. C., Irwin, M., & Quinn, P. J. (1995). *Astronomical Journal*, **109**, 255

[60] Guarnieri, M. D., Montegriffo, P., Ortolani, S., Moneti, A., Barbuy, B., & Bica, E. (1995) *ESO Messenger*, **79**, 2

[36] Da Costa, G. S., & Armandroff, T. E. (1990). *Astronomical Journal*, **100**, 162 (DCA)

[37] Davidge, T. J. (1993). *Astrophysical Journal*, **409**, 190

[38] Davoust, E., & Prugniel, P. (1990). *Astronomy & Astrophysics*, **230**, 67

[39] de Freitas Pacheco, J. A. (1997), *Astronomy & Astrophysics*, **319**, 394

[40] de Vaucouleurs, G. (1987). *Sky & Telescope*, **74**, 595

[41] de Vaucouleurs, G., & Corwin, H. (1985). *Astrophysical Journal*, **295**, 287

[42] de Vaucouleurs, G. (1958). *Astrophysical Journal*, **128**, 46

[43] Djorgovski, S. (1993). in *Structure and Dynamics of Globular Clusters*, ASP Conf. Ser. **50**, edited by S. Djorgovski & G. Meylan (San Fransisco : ASP), p. 347

[44] Djorgovski, S., & King, I. R. (1986). *Astrophysical Journal Letters*, **305**, L61

[45] Djorgovski, S., & King, I. R. (1984). *Astrophysical Journal Letters*, **277**, L49

[46] Drukier, G. A., Fahlman, G. G., Richer, H. B., & VandenBerg, D. A. (1988). *Astronomical Journal*, **95**, 1415

[47] Dubath, P., & Grillmair, C. J. (1997). *Astronomy & Astrophysics*, **321**, 379

[48] Durrell, P. R., Harris, W. E., & Pritchet, C. J. (1994). *Astronomical Journal*, **108**, 211

[49] Emerson, D. T. (1974). *Monthly Notices of the Royal Astronomical Society*, **169**, 607

[50] Faber, S. (1995) in *Stellar Populations*, IAU Symp. **169**, edited by L. G. Gilmore, & P. van der Kruit, (Dordrecht : Kluwer), (in press)

[23] Burstein, D., & Heiles, C. (1982). *Astronomical Journal*, **87**, 1165

[24] Carney, B. W., Storm, J., & Jones, R. V. (1992). *Astrophysical Journal*, **386**, 663

[25] Carney, B. W., Fullton, L. K., & Trammell, S. R. (1991). *Astronomical Journal*, **101**, 1699

[26] CFHT Observers' Manual (1990).

[27] Chaboyer, B., Demarque, P., Kernan, P. J., Krauss, L. M. (1997). submitted to *Astrophysical Journal*

[28] Chaboyer, B., Demarque, P., & Sarajedini, A. (1996). *Astrophysical Journal*, **459**, 558

[29] Christian, C. A., & Heasley, J. N. (1991). *Astronomical Journal*, **101**, 84

[30] Cohen, J. G., & Freeman, K. C. (1991). *Astronomical Journal*, *101*, 483

[31] Couture, J., Racine, R., Harris, W. E., & Holland, S. (1995). *Astronomical Journal*, **109**, 205

[32] Covino, S., Pasinetti Fracassini, L. E., Malagnini, M. L., & Buzzoni, A. (1994). *Astronomy & Astrophysics*, **289**, 775

[33] Crampton, D., Cowley, A. P., Schade, D., & Chayer, P. (1985). *Astrophysical Journal*, **288**, 494

[34] Crotts, A. P. S. (1986). *Astronomical Journal*, **92**, 292

[35] Cuillandre, J.-C., Lequeux, J., Mellier, Y., & Allen, R. J. (1997). submitted to *Astronomy & Astrophysics*

[11] Bergbusch, P. A., & VandenBerg, D. A. (1992). *Astrophysical Journal Supplement*, **81**, 163

[12] Bertelli, G., Bressan, A., Chiosi, C., Fagotto, F, & Nasi, E. (1994). *Astronomy & Astrophysics Supplement*, **106**, 275

[13] Bessell, M. S., & Brett, J. M. (1988). *Publications of the Astronomical Society of the Pacific*, **100**, 1134

[14] Bhatia, R. K., & Hatzidimitriou, D. (1988). *Monthly Notices of the Royal Astronomical Society*, **230**, 21

[15] Bi, H., & Börner, G. (1994). *Astronomy & Astrophysics Supplement*, **108**, 409

[16] Bico, E., & Alloin, D. (1986). *Astronomy & Astrophysics*, **162**, 21

[17] Binney, J., & Tremaine, S. (1987). *Galaxtic Dynamics*, (Princeton : Princeton University Press)

[18] Bohlin, R. C., Deutsch, E. W., McQuade, K. A., Hill, J. K., Landsman, W. B., O'Connell, R. W., Roberts, M. S., Smith, A. M. Stecher, T. P. (1993). *Astrophysical Journal*, **417**, 127

[19] Brewer, J. P., Richer, H. B., Crabtree, D. R. (1995). *Astronomical Journal*, **109**, 2480

[20] Brinks, E., & Bajaja, E. (1986). *Astronomy & Astrophysics*, **169**, 14

[21] Burstein, D., Faber, S. M., Gaskell, C. M., & Krumm, N. (1984) *Astrophysical Journal*, **287**, 586

[22] Burstein, D., & Heiles, C. (1984). *Astrophysical Journal Supplement*, **54**, 33

References

[1] Ajhar, E. A., Grillmair, C. J., Lauer, T. R., Baum, W. A., Faber, S. M., Holtzman, J. A., Lynds, C. R., & O'Neil, Jr., E. J. (1996). *Astronomical Journal*, **111**, 1110

[2] Alcaino, G. (1977). *Publications of the Astronomical Society of the Pacific*, **89**, 491

[3] Ashman, K. M., Conti, A, & Zepf, S. E. (1995). *Astronomical Journal*, **110**, 1164

[4] Ashman, K. M., & Bird, C. M. (1993). *Astronomical Journal*, **106**, 2281

[5] Baev, P. V., Spassova, N., & Staneva, A. (1997). *Astronomy & Astrophysics*, **319**, 45

[6] Bahcall, J. N., & Soneira, R. M. (1984). *Astrophysical Journal Supplement*, **55**, 67

[7] Battistini, P., Bònoli, F, Buonanno, R., Corsi, C. E., & Fusi Pecci, F. (1982). *Astronomy & Astrophysics*, **113**, 39

[8] Bendinelli, O. Cacciari, C., Djorgovski, S., Federici, L. Ferraro, F. R., Fusi Pecci, F., Parmeggiani, G., Weir, N., & Zavatti, F. (1993). *Astrophysical Journal*, **409** L17

[9] Bendinelli, O., Parmeggiani, G., Zavatti, F., & Djorgovski, S. (1990). *Astronomical Journal*, **99**, 774

[10] Bendinelli, O., Parmaggiani, G., Piccioni, A., & Zavatti, F. (1987). *Astronomical Journal*, **94**, 1095

consensus as to what the values of α and β are (e.g. Carney et al. (1992) [24], Chaboyer et al. (1996) [28], Chaboyer et al. (1997) [27]). Published disagreement in the values of these parameters can give results that differ by $\pm \sim 0.2$ mag. A second problem is that the photometric uncertainties at the level of the RR Lyrae gap ($V \sim 25$) are $\sigma_V \sim 0.1$. Over the next two years twenty additional globular clusters will be imaged with the *HST*. This should provide a large enough database to obtain a mean distance to the M31 globular cluster system to an accuracy of $\pm \sim 0.02$ mag, not counting uncertainties in the [Fe/H]–M_V(RR) relation.

CMD and the distance modulus can be adjusted until the red-giant branch is at its best agreement with the spectroscopically-determined iron abundance. This technique would require that the reddening towards the globular cluster be well-known. However, since M31 lies at a high Galactic latitude, and most of the M31 globular clusters that have published CMDs lie well beyond the edge of the disc of M31 the uncertainties in the reddening towards these clusters are small.

3. Hodder (1995) [70] found a field in the northeast quadrant of the halo of M31 that contains two to three times more stars than would be expected using a version of the Bahcal & Soneira (1984) [6] Galaxy model that he adapted for use in M31. Most of the studies of the stellar populations in the halo of M31 have been done in the northeast quadrant of M31 to avoid contamination from M32 and NGC 205. Further, because of the small sizes ($\sim$ a few arcminutes square) of CCDs in the past all published CCD studies of the halo of M31 have sampled the halo of M31 and not mapped it in its entirety. I have obtained UHCam images of two $0\fdg5 \times 0\fdg5$ fields in the halo of M31. The first field is centred on the field containing Hodder's (1995) [70] overdensity while the second is located on the opposite side of the major axis of M31. A comparison of the star counts and the CMDs in these two fields will tell us if the overdensity is due to the structure of M31 (e.g. a flattened halo, or a thick disc), or a clump in the northeast quadrant of the halo.

4. At present there are nine globular clusters in M31 which have CMDs that reach to the horizontal branch. The mean V-band magnitudes of the stars in the RR Lyrae gaps of these clusters have been measured by Fusi Pecci et al. (1996) [56] and in Chapter 5.1. Combining these $V_{\rm RR}$ values with spectroscopic iron abundances and the [Fe/H]–M_V(RR) relation for RR Lyraes gives the distance modulus to the globular cluster in question, $\mu_0 = V_{\rm RR} - \alpha[{\rm Fe/H}] - \beta$. Unfortunately there is no

8.3 Unanswered Questions

There are still many unanswered questions about the nature of M31. In this section I will list a few projects that will add to our knowledge of that galaxy.

1. The metallicity distribution in the halo of M31 is still not well known. All of the attempts to determine the metallicity distribution to date have involved comparing CMDs of the upper red-giant branch of M31's halo to fiducial red-giant branches of known metallicity. This approach will work provided that the photometric uncertainties are small *and* that the distance to M31 is well known. However, the recent *Hipparcos* parallaxes have led to an uncertainty of $\pm \sim 0.25$ mag in M31's distance modulus, which calls into question the existing distance-dependent metallicity estimates for the halo of M31. The results presented in Chapter 6.1.2 assumed a distance modulus of $\mu_0 = 24.3 \pm 0.1$, which was the accepted distance modulus when this work was started. If M31 is actually more distant then the mean metallicity of the halo will decrease.

   A better way of determining the metallicity of the halo of M31 would be to obtain deep narrow-band photometry of a large number of upper red-giant branch stars. The Strömgren v, b, and y filters can be used to obtain a metallicity index, $m_1 = (v - b) - (b - y)$, that is independent of the distance to M31. Such observations would be possible with the approximately two nights of observing with UHCam at the CFHT.

2. Spectroscopic iron abundances exist for most of the M31 globular clusters. These can be used to estimate the distances to the M31 globular clusters if good-quality $(V, (V-I))$ photometry of the upper red-giant branch is available. A series of fiducial red-giant branches of known iron abundances can be overlaid on the cluster's

8.2 The Halo of M31

This thesis presents the results of a photometric study of the stellar populations in two fields in the halo of M31. This study used *HST* WFPC2 V- and I-band photometry to show that the stellar halo of M31 has a mean metallicity of $[\mathrm{m/H}] \simeq -0.6$ with a spread of $-2 \lesssim [\mathrm{m/H}] \lesssim -0.2$, comparable to the metallicity determinations made using ground-based observations. $[\mathrm{m/H}] \simeq -0.6$ is ~ 15 times more metal-rich than the halo of the Galaxy ($[\mathrm{m/H}] \simeq -1.8$). This result is primarily based on a comparison of the morphology of the halo red-giant branch to fiducial sequences of Galactic globular clusters and theoretical red-giant branch isochrones. As such the metallicity estimate is distance dependent. If M31 lies at a greater distance the mean metallicity will decrease. Therefore, it is important that distance-independent estimates of the metallicities of stars in the halo of M31 be made.

The halo horizontal branch consists primarily of red-clump stars, similar to what is seen in 47 Tuc, and a small number of blue stars. The horizontal branch morphology ratio is $(N_B - N_R)/(N_B + N_R) \simeq -0.9$, suggesting that there is a metal-poor population present in the halo of M31 that could give rise to the RR Lyrae variables seen by Pritchet & van den Bergh (1987) [114]. The derived helium abundance is $Y \simeq 0.20$ to 0.27, similar to that in Galactic globular clusters.

There is no conclusive evidence for a difference in stellar population between the G302 field and the G312 field. The metallicity distribution of the red giants indicates that there is no significant difference in the ratio of metal-rich to metal-poor stars in the two fields. Deep photometry will be needed in a large number of fields in the M31 halo to determine how (or if) metallicity varies with position in the halo of M31.

per Gyr which corresponds to a projected escape rate of $\dot{r} = (2.3 \pm 0.9) \times 10^{-3}$ per half-mass relaxation time. The projected escape rate from G312 is $\dot{r} = (0.38 \pm 2.95) \times 10^{-3}$ per half-mass relaxation time. These are consistent with the escape rates predicted by Oh & Lin (1992) [103]. The large photometric uncertainties near the tidal radius of G312 makes the escape rate for this globular cluster much less reliable than that for G302.

A comparison of published structural parameters obtained using *HST* and ground-based data shows that ground-based observations (with sub-arcsecond seeing) are sufficient to obtain reliable King tidal radii for M31 globular clusters. Ground-based observations can reliably determine the core radii *if* the core radii are at least 0.25 times the FWHM of the seeing disc. This requires seeing of FWHM $\lesssim 0\farcs1$ in order to reliably measure a core radius of $\lesssim 0\farcs03$ ($\simeq 0.1$ pc) in an M31 globular cluster. Therefore, ground-based determinations of core radii are not, in general, reliable, except to establish broad concentration classes.

At present reliable tidal radii have been obtained for ~ 50 globular clusters in M31, but reliable core radii have only been obtained for ~ 20 of these. The *HST* is scheduled to obtain V- and I-band WFPC2 images of twenty M31 globular clusters during Cycles 6 and 7. Since the globular clusters in the two galaxies appear to have identical distributions of structural parameters there it is not critical to obtain more images to study the core structures of these clusters. On the other hand, M31's globular clusters offer ideal laboratories to study the structure of globular clusters near their King tidal radii. This thesis presents evidence for an extended halo of unbound stars around G302. Ten to twenty orbits with the *HST* would be needed to resolve stars down to $V_{\rm lim} \sim 28$, which would increase the number of stars that could be photometered in an extended halo by approximately a factor of two. This would greatly improve the statistical significance of stellar density measurements beyond the formal King tidal radius and allow the shape of an extended halo to be determined to greater accuracy than was possible in this study.

similar tidal fields and similar amounts of bulge- and disc-shocking. In light of this it is not surprising that the globular clusters appear to be structurally identical in a mean sense.

The *HST* WFPC2 photometry was used to construct deep ($V \simeq 27$) CMDs for two globular clusters in the halo of M31. Both globular clusters appear to have a single old population of stars similar to what is found in Galactic globular clusters. The shape of the red-giant branch for G302 gives an iron abundance of $[\mathrm{Fe/H}] = -1.85 \pm 0.12$, in agreement with the published values obtained using spectroscopy. G312 has an iron abundance of $[\mathrm{Fe/H}] = -0.56 \pm 0.03$, which is somewhat more metal-rich than the spectroscopically determined value. Neither globular cluster shows any indication that there is a second parameter acting upon their horizontal branch morphologies.

Both globular clusters have Michie–King tidal radii of $r_t \simeq 10''$, core radii of $r_c \simeq 0\farcs2$, central concentrations of $c \simeq 1.7$, and half-mass radii of $r_h \simeq 0\farcs5$. There is no evidence for velocity anisotropy in either G302 or G312. G302 has a colour of $(V-I)_0 = 0.83$ while the colour of G312 is $(V-I)_0 = 1.07$. Both of these colours are consistent with the integrated colours of Galactic globular clusters with similar metallicities.

G302 has a projected ellipticity of $\epsilon = 0.195$ with the major axis oriented approximately towards the centre of M31. This globular cluster has an excess of light beyond its formal tidal radius that is not consistent with either an isotropic or an anisotropic Michie–King model. The two-dimensional distribution of stars around G302 is consistent with the presence of an extended halo of unbound stars extending to two to three times the formal tidal radius from the cluster. G312, on the other hand, has an ellipticity of $\epsilon \simeq 0$ and neither the integrated light nor star counts show any evidence for an extended stellar halo. It is possible that such a halo does exist for G312 but is oriented along the line of sight.

I have estimated the projected mass-loss rate from G302 to be $\dot{\mathcal{M}} = 4500 \pm 1800\,\mathcal{M}_\odot$

Chapter 8

Conclusions

8.1 The Globular Star Clusters of M31

This thesis presents the results of two studies of the globular clusters in the M31 system. The first study was done using V- and I-band images obtained with the HRCam at the CFHT. The second study made use of V- and I-band *HST* WFPC2 images of two globular clusters in M31.

Two-dimensional, seeing-convolved Michie–King models were fit to seventeen globular clusters in M31. The fitted tidal radii are the same as those of Galactic globular clusters. This confirms the work of Cohen & Freeman (1991) [30], who compared the tidal radii of thirty M31 globular clusters with the tidal radii of the Galactic globular clusters. I also find that the projected ellipticities of the M31 globular clusters are consistent with the ellipticities of the Galactic globular clusters, confirming the work of Lupton (1989) [90]. The core radii and half-mass radii of globular clusters in the two galaxies appear to be similar, but seeing effects make it impossible to obtain accurate values for these quantities using the CFHT HRCam data.

This similarity in structural parameters suggests that the two globular cluster systems formed in a similar way and have had similar dynamical histories. M31 is structurally very similar to the Milky Way Galaxy so globular clusters in both galaxies will experience

7.7 Conclusions

G185 and G185B appear to be two separate globular star clusters in M31. There is no direct evidence that the two clusters are interacting. There is no evidence of tidal disruption in either clusters although the I-band ellipticity of G185 is greater than can be accounted for due to seeing effects and G185 is approximately oriented towards G185B.

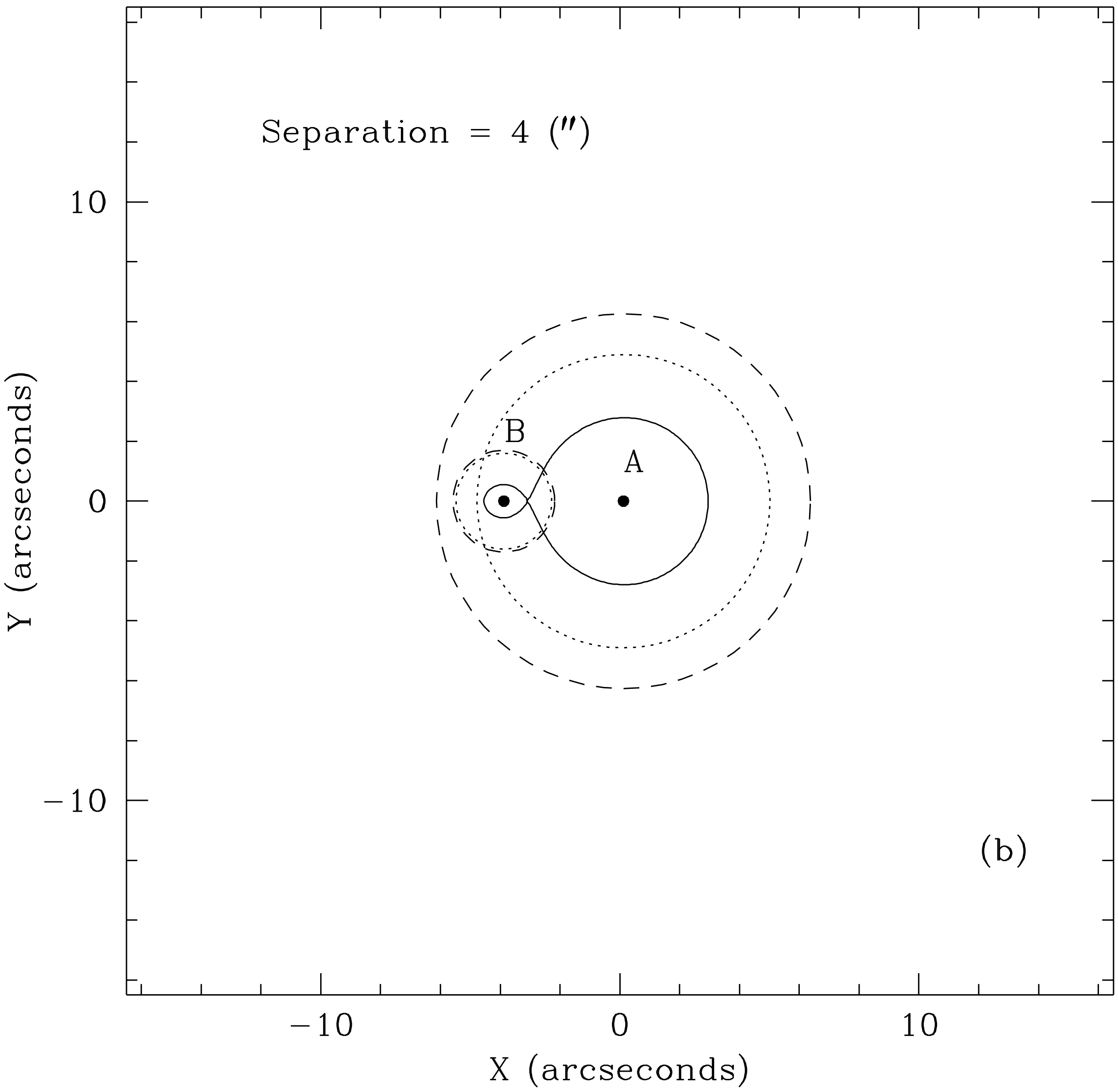

Figure 7.14: This figure is the same as Figure 7.13 except the two clusters are assumed to have a true separation of 14 pc ($\sim 4''$), the same as the observed projected separation between G185 and G185B.

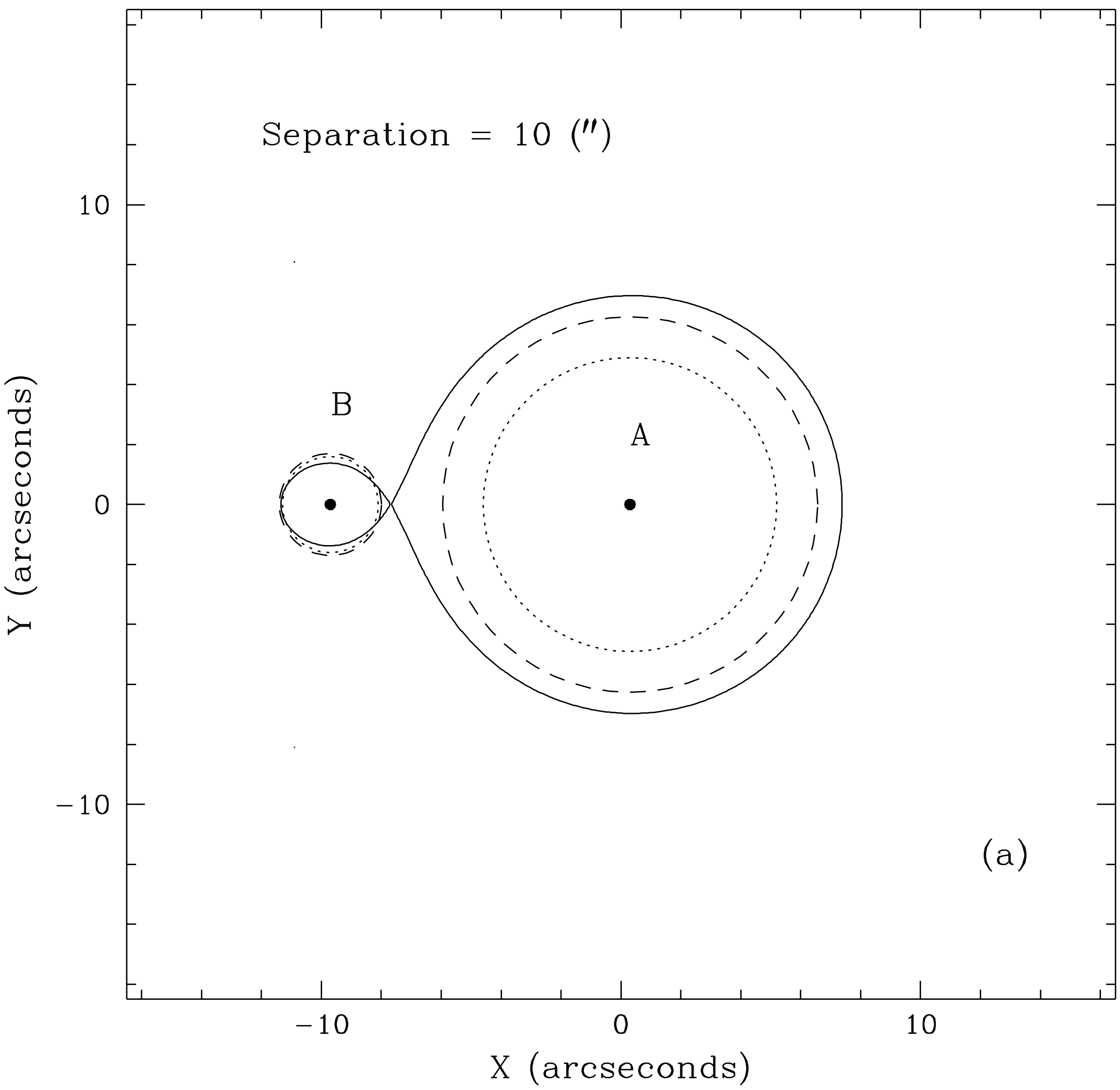

Figure 7.13: This figure shows the Roche lobes for the two clusters computed assuming the clusters are interacting and can be approximated by point masses (see Chapter 7.6.3 for a justification of the latter assumption). The solid lines show the Roche lobes while the dashed lines are the fitted I-band Michie–King tidal radii from Table 7.3. The dotted lines show the outermost point of the observed surface brightness profile for each cluster. The two clusters are assumed to have a true separation of 35 pc ($\sim 10''$).

7.6.3 The Roche Limit of the System

The mean radial velocity of a globular cluster in the M31 system relative to M31 is $v = 125\ \mathrm{km{\cdot}s^{-1}}$ (Huchra et al. 1991 [76]) which implies an encounter time-scale of at least 10^5 to 10^6 years, assuming a nearly head-on encounter (i.e. the geometry that produces the fastest possible encounter). This minimum encounter time is similar to the crossing time for a star in a globular cluster so interacting clusters will have sufficient time to be spatially distorted by each others' tidal fields. I have calculated the shapes of the Roche lobes for G185 and G185B assuming that the two clusters are interacting and that they can be modeled by point masses. In reality the two clusters are not true point sources, but since the half-mass radii of the Michie–King models fitted to them are comparable to their fitted core radii, this assumption is reasonable. The fitted half-mass radii for G185 and G185B respectively are $1\farcs05 \pm 0\farcs07$ and $0\farcs49 \pm 0\farcs16$.

Figure 7.13 shows that the cut-offs imposed by the tidal field of M31 are approximately the same as the cut-offs imposed by the mutual tidal fields of the two clusters if G185 and G185B have a true separation of ~ 35 pc ($\simeq 10''$). If the true separation is greater than this then the shapes of the clusters will be determined by the tidal field of M31. If, however, the true separation is smaller then inter-cluster tidal forces will have a significant effect on the internal dynamics of each cluster. Figure 7.14 shows that if the true separation is equal to the observed projected separation (14 pc $\simeq 4''$) then the cut-offs imposed by their mutual tidal fields are closer to the clusters' centres than the tidal cut-offs imposed by M31. Since light is observed beyond these Roche limits the clusters are either not interacting or have not had time to dynamically respond to each others' tidal fields.

The radial velocity difference between the two background fields should be zero. However, the two spectra were taken 45 minutes apart. Since the detailed absorption spectrum of the Earth's atmosphere can change on time scales of only a few minutes it is likely that the difference in Δv_{bkgd} in the three spectral regions are due to temporal variations in the atmospheric lines. If this is the case then some portion of the variations in the Δv_{GC} values obtained from the three spectral regions will also be due to the temporal variations in the atmospheric absorption lines. Therefore, it is not possible to draw any conclusion about the radial velocity difference between G185 and G185B with this data.

7.6.2 The Radial Velocities

The radial velocity of G185B relative to G185 was determined by cross-correlating the spectrum of G185B with the spectrum of G185 using the NOAO.RV.FXCOR task in IRAF. Cross-correlating the entire G185 and G185B spectra yields a relative radial velocity of $\Delta v = +41.5 \pm 98.6$ km$\cdot$s^{-1}. This velocity difference is define as $\Delta v \equiv v_{\mathrm{G185}} - v_{\mathrm{G185B}}$. The uncertainty in the velocity difference is the standard deviation of the best-fitting Gaussian to the cross-correlation peak. Cross-correlating the two background spectra gives $\Delta v = -11.4 \pm 79.4$ km$\cdot$s^{-1}.

Unfortunately the spectra of the globular clusters contain significant contamination from the nucleus of M31 and absorption lines in Earth's atmosphere. The most obvious of these are the Telluric A and B blends at $\lambda \sim 7600$ Å and $\lambda \sim 6900$ Å respectively. Unfortunately the low signal-to-noise ratio of these spectra, and the strengths of the atmospheric features makes it difficult to separate features from globular cluster from features from the background and atmosphere. In order to prevent the cross-correlation algorithm from locking onto the atmospheric features the spectra were split into three regions: (1) 6400 Å to 6875 Å, (2) 7100 Å to 7500 Å, and (3) 7850 Å to 8200 Å. These regions were chosen to exclude the Telluric A and B bands. The relative radial velocities returned by cross correlating the G185 and G185B spectra in these three wavelength regions are given in Table 7.5.

Region	$\lambda\lambda$ (Å)	Δv_{GC} (km$\cdot$s^{-1})	Δv_{bkgd} (km$\cdot$s^{-1})
1	6400 – 6875	$+4.6 \pm 53.1$	-58.0 ± 154.7
2	7100 – 7500	$+28.9 \pm 164.1$	$+23.1 \pm 31.3$
3	7850 – 8200	$+11.4 \pm 15.6$	$+20.0 \pm 104.7$

Table 7.5: Relative radial velocities for G185, G185B, and the background.

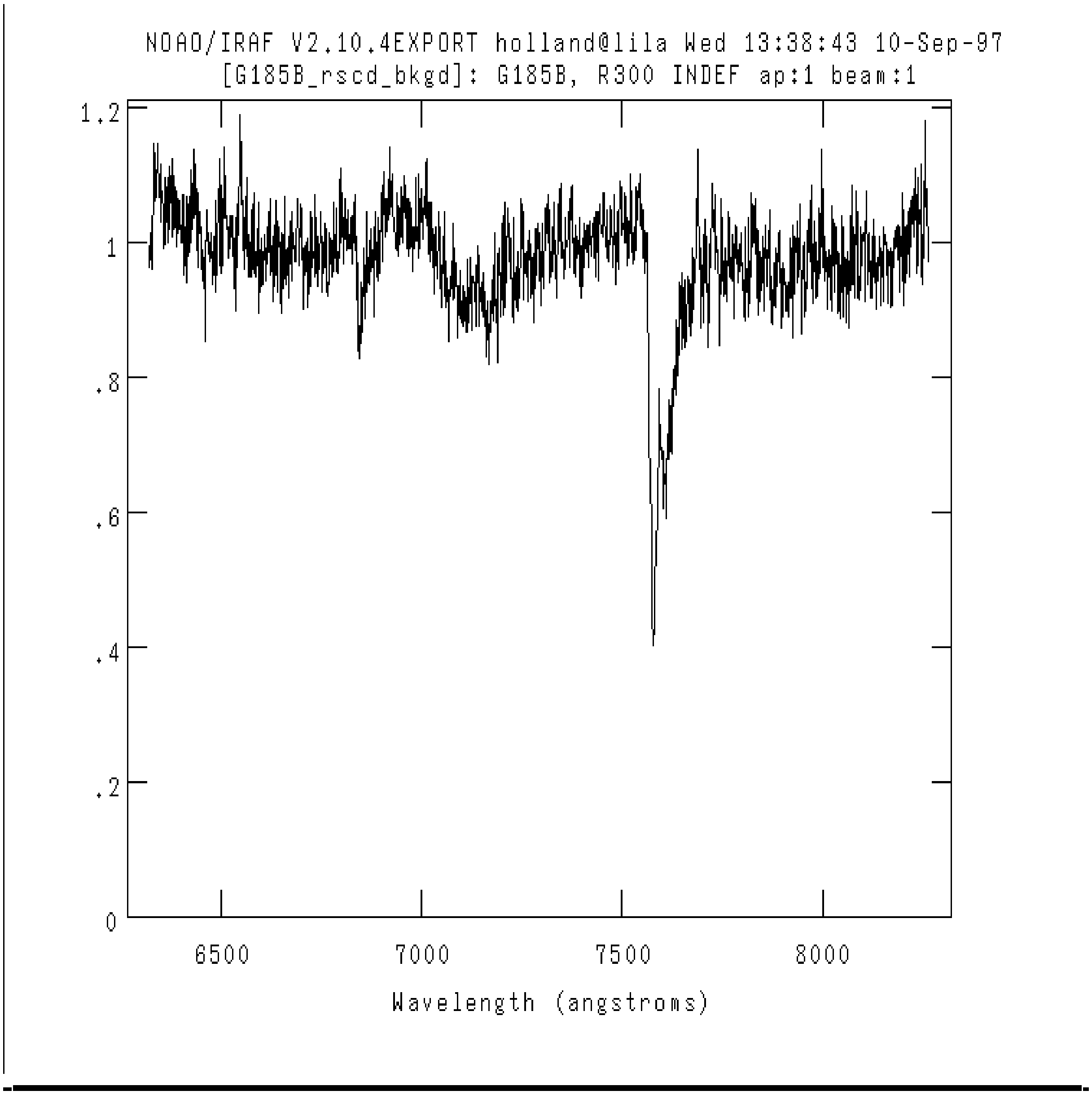

Figure 7.12: This figure shows the spectrum of the background. This spectrum is the sum of the five rows on each edge of the original G185B spectrum.

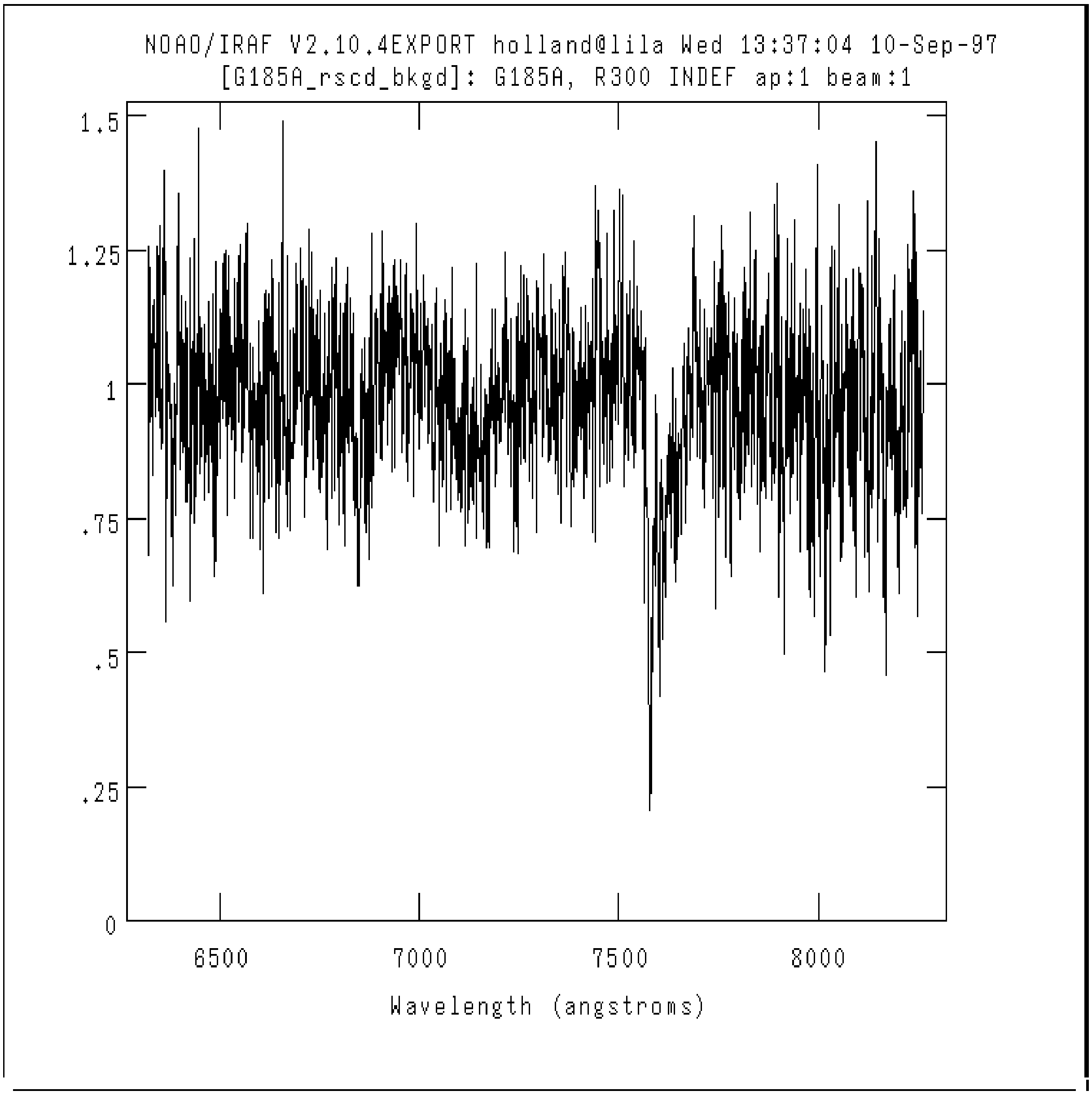

Figure 7.11: This figure shows the spectrum of the background. This spectrum is the sum of the five rows on each edge of the original G185 spectrum.

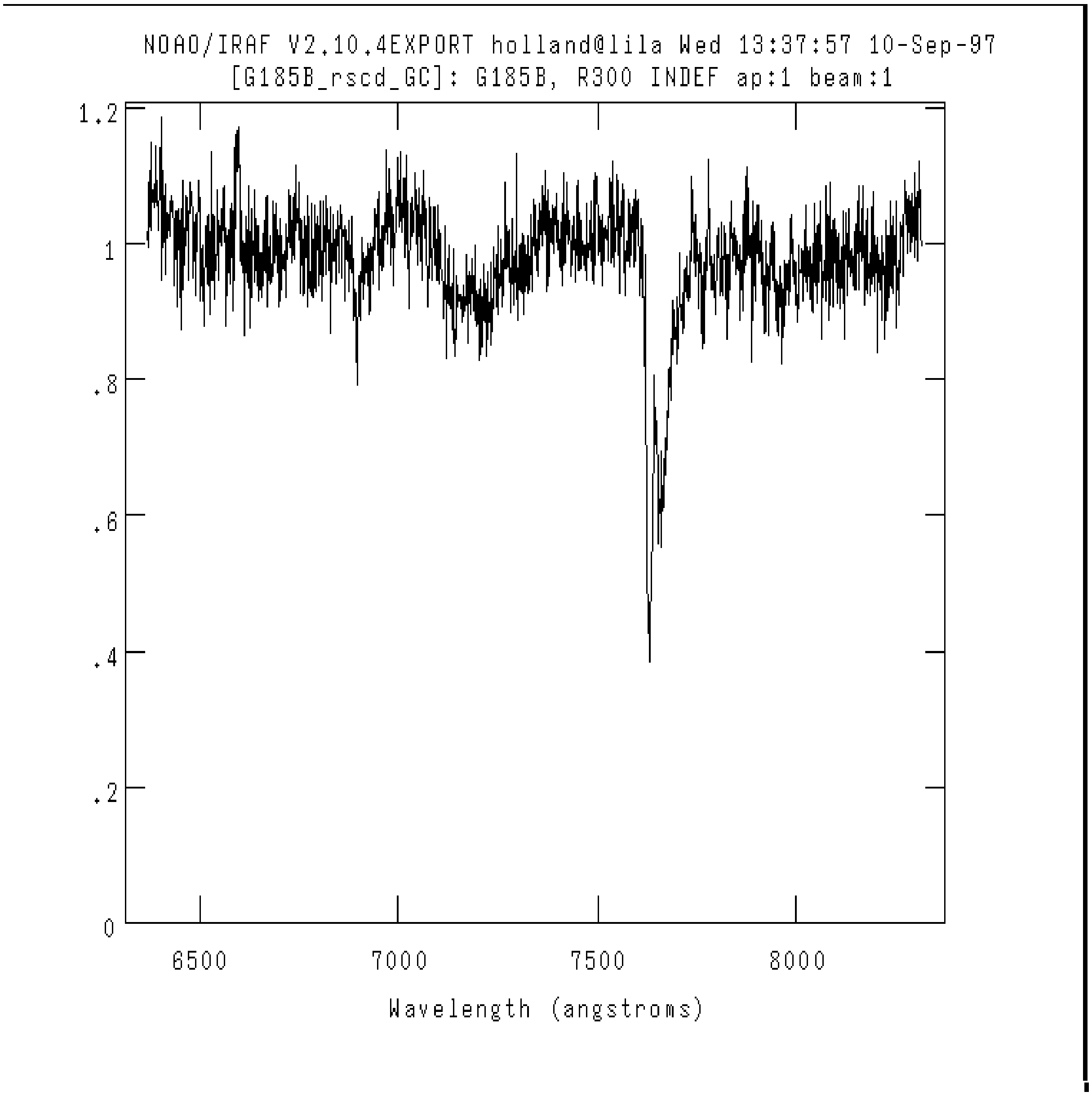

Figure 7.10: This figure shows the spectrum for G185B. This spectrum is the sum of the five rows centred on the centre of G185B.

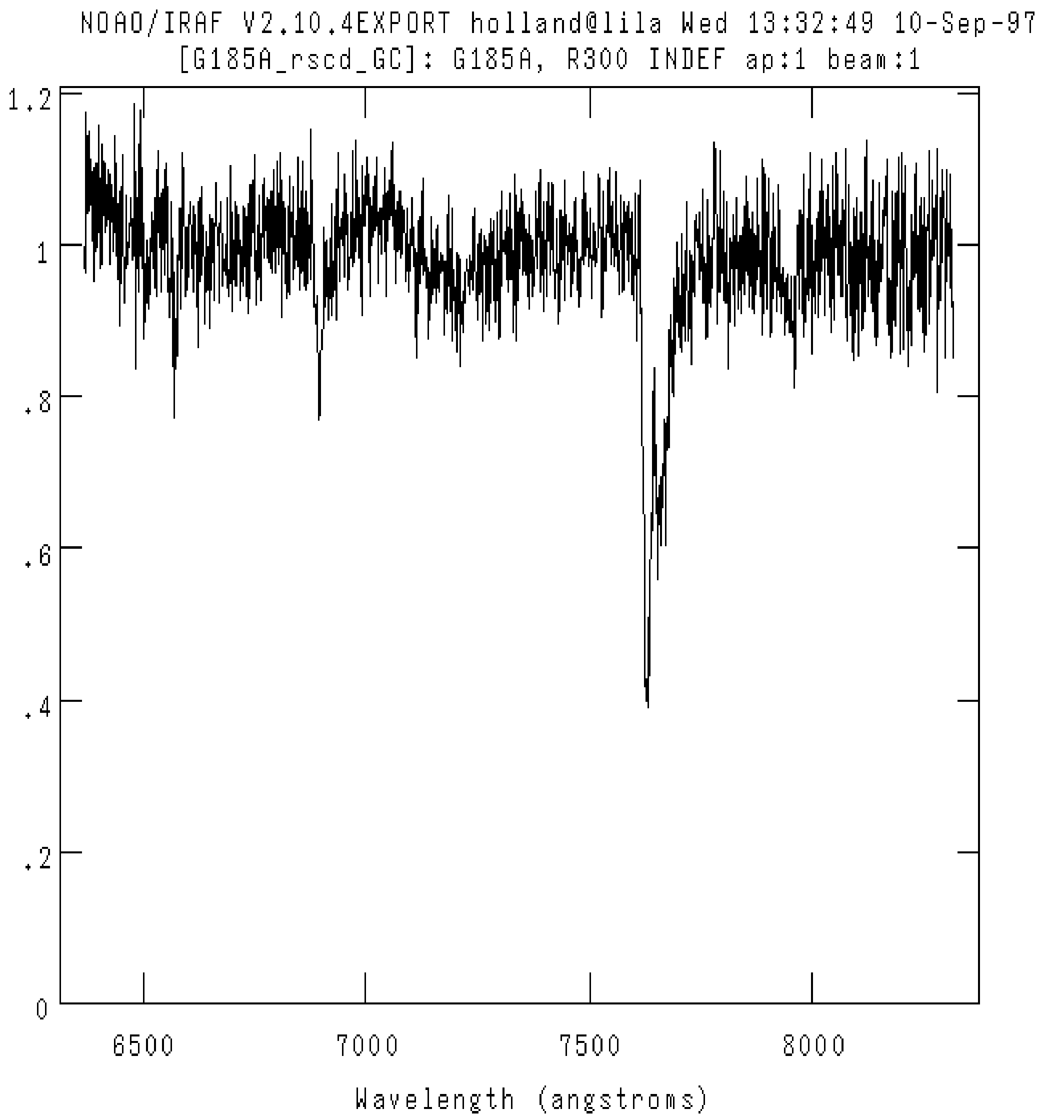

Figure 7.9: This figure shows the spectrum for G185. This spectrum is the sum of the five rows centred on the centre of G185.

and G185B. Figures 7.11 and 7.12 show the spectra of the M31 nucleus near each globular cluster. The spectral features near $\lambda \sim 7600$ Å and $\lambda \sim 6900$ Å are the Telluric oxygen bands.

7.6 Dynamical Considerations

7.6.1 The SIS Spectra

In order to further check if G185 and G185B were associated with each other, long-slit spectra were obtained for each object. The spectra were taken by Christian Vanderriest on the night of August 31, 1995 using the SIS at the CFHT. The spectra were taken using the R300 grism and a slit width of $1\farcs2$. The R300 grism is centred on a wavelength of $\lambda = 7307$ Å and has a dispersion of 1.0 Å/15 μm pixel. The Loral 3 CCD was used since it has a gain of 1.45 e^{-1}/ADU. The spectra consisted of one 120 second exposure of G185 and one 600 second exposure of G185B. Both spectral have signal-to-noise ratios of ~ 5 per pixel. Bias subtraction and flat fielding were done in the same manner as for the CFHT image data (see Chapter 2.1). The spectra were extracted using the NOAO.ONEDSPEC tasks in IRAF. Since the SIS was used in long-slit mode the central rows of the spectrum will be dominated by light from the core of the globular cluster while the outer rows will contain a higher fraction of background light from the nucleus of M31. To compensate for this the central five rows of each spectrum were extracted and used to produce summed spectra of G185 and G185B. The outer five rows of each spectrum were extracted and summed to produce background spectra for G185 and G185B. The SIS slit was aligned perpendicular to the line formed by connecting the centres of the two globular clusters. This was done to minimize the amount of contamination from the other globular cluster.

The spectra were calibrated by taking a 6.0 second exposure of the CFHT neon and argon calibration arcs. This spectrum was pre-processed and summed in exactly the same way as the program spectra. The arc lines were identified using the IRAF task NOAO.ONEDSPEC.IDENTIFY. Figures 7.9 and 7.10 show the calibrated spectra for G185

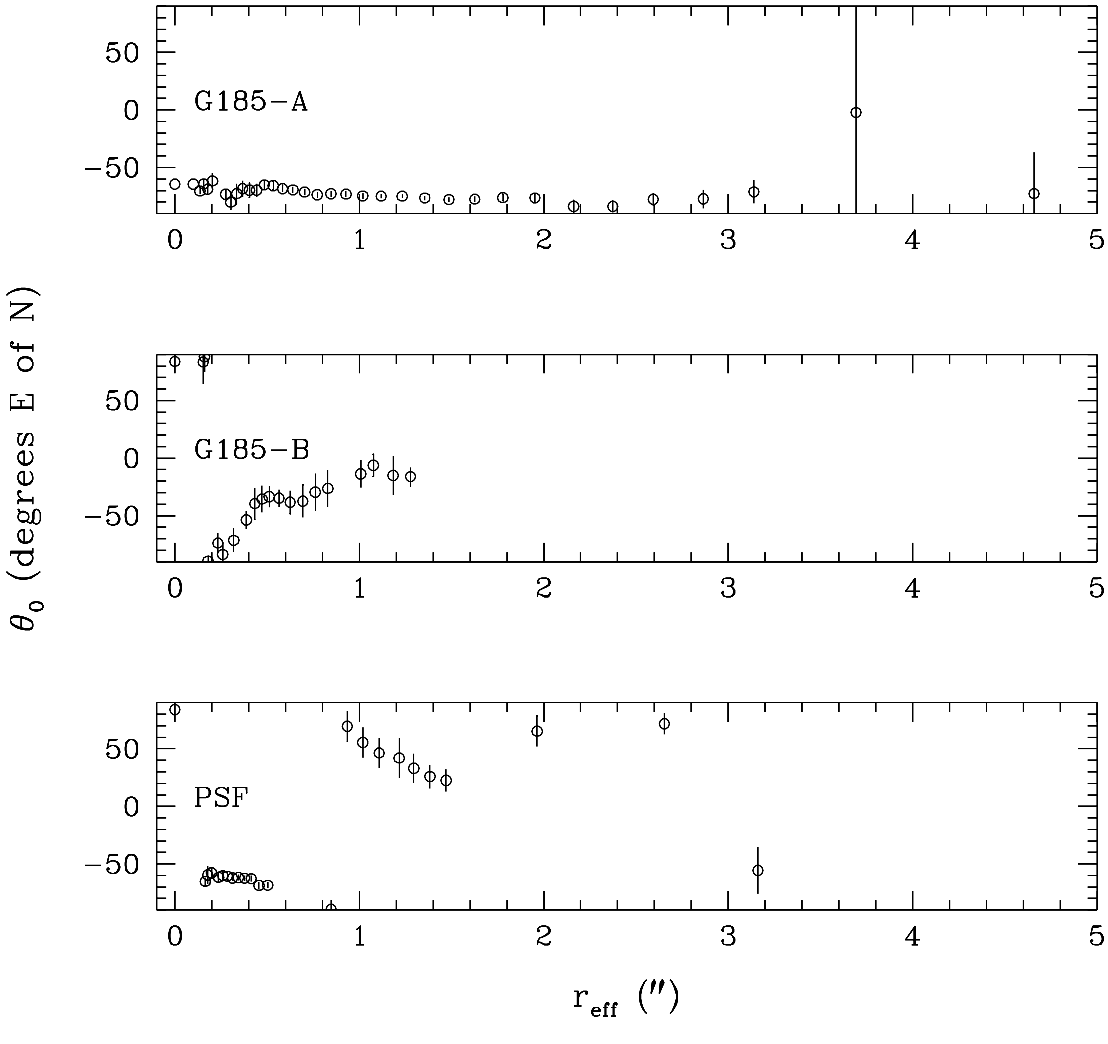

Figure 7.8: *I*-band position angle profiles of G185, G185B, and the PSF. The same caveats apply as did for Figure 7.7. The position angles are measured in degrees east on the sky from north. Since these profiles are all measured within the inner regions of the clusters (where seeing dominates the observed shape, see Chapter 7.5.2) the large variations in θ_0 for G185B are probably due to the seeing and not intrinsic to the cluster.

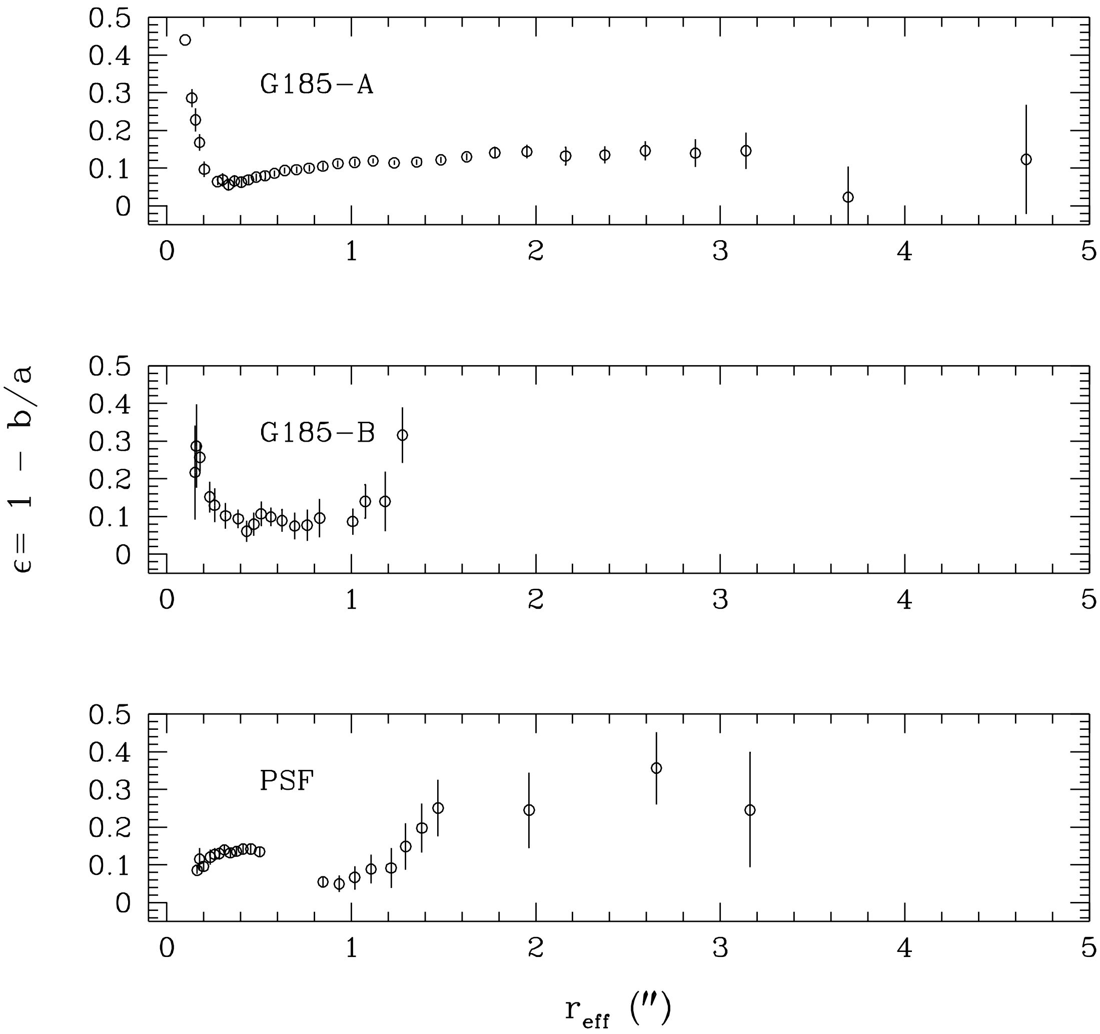

Figure 7.7: *I*-band ellipticity profiles of G185, G185B, and the PSF. Only points where ELLIPSE (see Chapter 7.2) was able to successfully fit an elliptical isophote are shown. The increase in ellipticity in the inner 0″.5 is probably an artifact of the fitting algorithm and seeing effects. I was unable to reliably measure ellipticities or position angles in the outer regions of the clusters since Poisson noise and surface brightness fluctuations dominate the signal there.

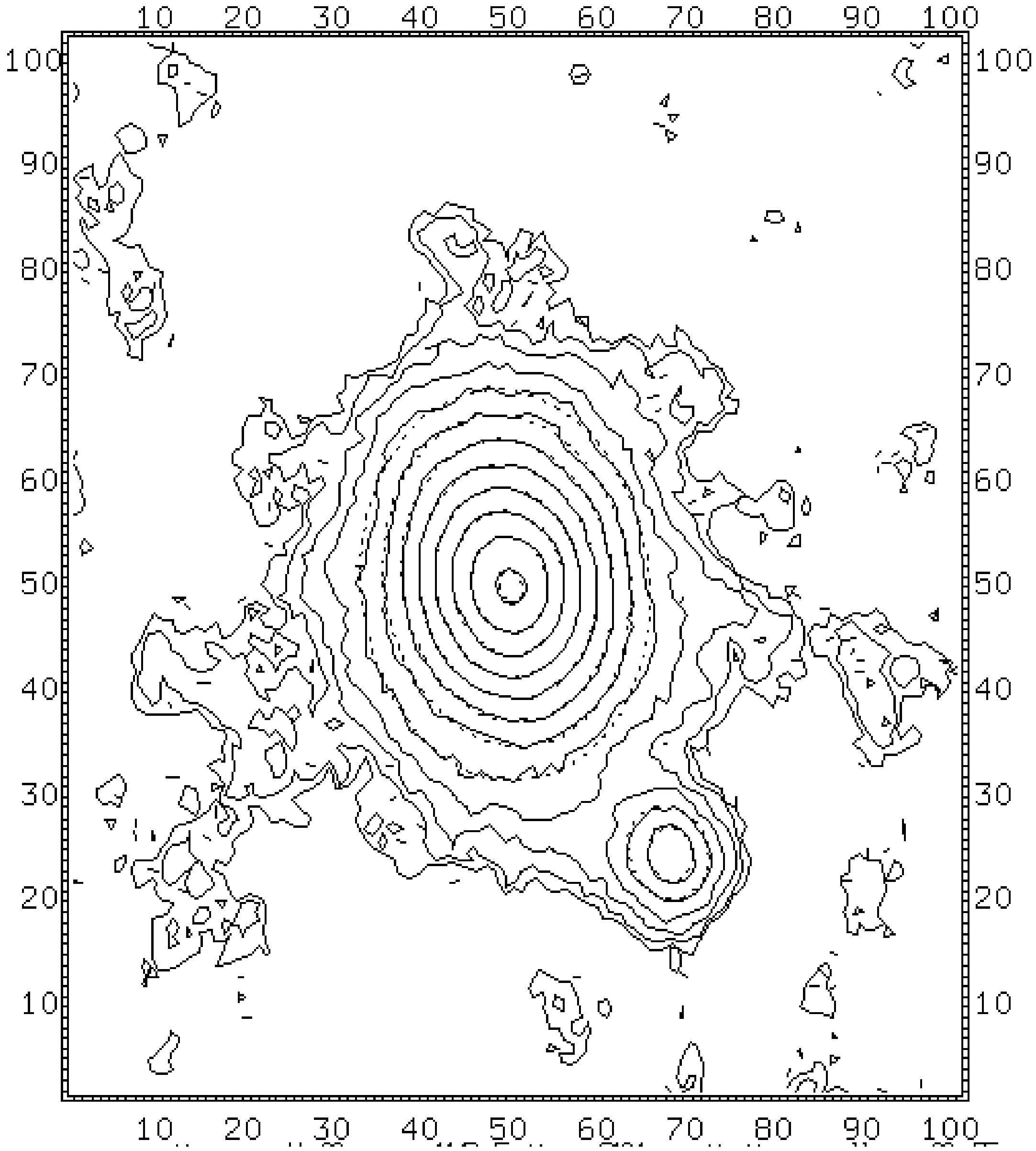

Figure 7.6: This figure shows a contour plot of the I-band image of G185 and G185B. The solid contours show surface brightnesses spaced between $\mu_I = 14.5$ and $\mu_I = 20.0$ while the dashed contours show fitted isophotal ellipses. G185B is located $4''$ northwest of G185. The centre of M31 is $\sim 6°$ west of north (the top of the plot is points towards $84°$ east of north).

I-band ellipticities of G185B are similar but the orientations are different suggests that G185B is not simply a multiple-star system[1].

The apparent elongation of G185 has the cluster pointing $13\overset{\circ}{.}1$ west of G185B and $\sim 75\overset{\circ}{.}$ west of the centre of M31. However, G185 is elongated in approximately the same direction that the PSF is oriented, and G185B is not distorted in the direction of G185. The observed V-band shape of G185 were reproducible with artificial clusters of zero ellipticity but the observed ellipticity in the I-band was not. It is, therefore, uncertain if G185 is actually oriented towards G185B or the observed elongation is merely due to the seeing and background fluctuations. As noted in Chapter 7.2 the surface brightness fluctuations in the I-band are greater than those in the V-band so they would be expected to cause a greater distortion in the observed shape of G185 in the I-band image.

[1]It can be argued that a globular cluster is nothing more than a large multiple star system, but in this thesis I will use the traditional definition of the term multiple-star system.

out to $\sim 5''$ for the best defined cluster. This, and the similarities between the ellipticities of the clusters and the PSFs, suggests that the observed projected ellipticities of G185 and G185B are due to seeing effects.

To test this conclusion a series of artificial globular clusters were built based on G185 but with ellipticities between 0.00 and 0.21. These were placed on the I-band data frame and elliptical isophotes fitted to them as was done for the real globular cluster data. The recovered I-band ellipticities at a given location on the image showed no trend with input ellipticity and had a mean of $\overline{\epsilon} = 0.036 \pm 0.004$ (standard deviation). Artificial clusters were added to three locations on the original data frame and found that the recovered mean ellipticities and position angles varied significantly with position. Recovered ellipticities were between 0.029 and 0.041 while recovered position angles varied by up to 60°. Positional dependence is due to the presence of large pixel-to-pixel surface brightness fluctuations in the unresolved light from the bulge of M31. These fluctuations are blurred by the seeing so that they have the same shape and orientation as the PSF. The luminosity of a fluctuation depends on the number of stars in the line of sight and thus its location on the frame relative the centre of M31. Further, the PSF on an HRCam image is known to vary with position on the frame so the size and shape of the surface brightness fluctuations will also vary with position. This would account for the variation in recovered ellipticity and position angle with location on the frame and partially explain why the three clusters are observed to have different ellipticities and position angles. A further reason for cluster-to-cluster ellipticity variations is that the light from each cluster is dominated by a small number of stars near the tip of the red giant branch which will result in small-number statistics dominating the observed shapes of the clusters. This effect should be more noticeable in small clusters and may explain the large observed ellipticity of G185B. This conclusion is supported by the fact that the orientation of G185B is significantly different in each colour. The fact that the V- and

7.5.2 Ellipticities

Figure 7.6 shows observed isophotes and some fitted isophotal ellipses for G185 and G185B. Observed weighted mean ellipticities, $\overline{\epsilon}$, and position angles, $\overline{\theta}_0$, were calculated for each cluster based on the fitted isophotes. These are presented in Table 7.4 along with the number, N, of fitted ellipses used to compute these values. Figures 7.7 and 7.8 show the radial variations of these quantities for G185, G185B and the PSF. Position angles are measured from north to east on the sky. The quoted uncertainties are due to the variation in the fitted position angle from the centre to the outer edge of each cluster, and to the estimated uncertainties in orienting the CCD images with respect to north. Large uncertainties are indicative of a large radial variation in position angle. Figures 7.7 and 7.8 show that radial changes in the ellipticity and orientation of the PSF are echoed in the shape of G185B suggesting that seeing is the dominant effect in determining the shape of G185B.

Cluster	Filter	$\overline{\epsilon}$	$\overline{\theta}_0$	N
G185	V	0.034 ± 0.004	$-87.^\circ1 \pm 38.^\circ7$	29
	I	0.105 ± 0.005	$-73.^\circ8 \pm 4.^\circ3$	34
G185B	V	0.115 ± 0.016	$-14.^\circ4 \pm 14.^\circ5$	16
	I	0.108 ± 0.012	$-52.^\circ8 \pm 23.^\circ8$	19
vdB2	V	0.027 ± 0.002	$-8.^\circ0 \pm 15.^\circ8$	26
	I	0.036 ± 0.001	$-78.^\circ9 \pm 5.^\circ2$	29
PSF	V	0.029 ± 0.002	$-7.^\circ8 \pm 33.^\circ4$	24
	I	0.199 ± 0.006	$-64.^\circ1 \pm 31.^\circ5$	23

Table 7.4: Ellipticities and position angles for G185, G185B, and vdB2.

The observed ellipticity of a semi-resolved globular cluster is dominated by the shape of the PSF out to ~ 8 times the seeing FWHM. This corresponds to $5.''7$ in the I-band and $6.''9$ in the V-band. However Figures 7.7 and 7.8 show that ellipses could only be fit

has an apparent tidal radius approximately three-and-a-half times smaller than that of G185. For this difference in size to be a purely geometric effect G185B would have to be located at ~3.5 times the distance of G185 meaning that either G185 or G185B is not a member of the M31 globular cluster system. Huchra et al. (1991) [76] give a radial velocity for G185 of $v = -185 \pm 25$ km·s^{-1} relative to M31, consistent with G185 being a member of the M31 globular cluster system. Since G185 contributes $\sim$ 97% of the total light this radial velocity will be a reasonable estimate of the radial velocity of G185. The colour of G185B is not unduly red for an old globular cluster so it is unlikely that G185B is being viewed through the bulge of M31. This suggests that G185B is a member of the M31 globular cluster system and is intrinsically smaller than G185.

The fitted core radius for G185 is somewhat smaller than that found by Cohen & Freeman (1991) [30]. I found a core radius of $0.''46 \pm 0.''04$ (= 1.6 ± 0.1 pc) and a tidal radius of $6.''13 \pm 0.''69$ (= 21.5 ± 2.4 pc) for G185. Cohen & Freeman (1991) [30] found $r_c = 2.9$ pc and $r_t = 20$ pc. The difference in core radius is probably due to the improved seeing conditions of the observations. It may also be due to the identification of G185B as a separate object.

7.5 Structural Parameters

7.5.1 Cluster Concentrations

The procedure described in Chapter 3.2.6 was used to estimate the central potentials, core and tidal radii, and ellipticities of G185, G185B, and vdB2. Table 7.3 lists Michie–King parameters for each cluster and bandpass derived using this two-dimensional modeling. The quoted uncertainties were estimated as follows. A series of artificial globular clusters with $W_0 = 5$, $r_c = 0\farcs5$, $r_t = 5\farcs35$, and $\epsilon = 0.0$ were constructed. Two-dimensional models were then fit to these clusters. The scatter in the recovered parameters was taken to be indicative of the uncertainties in the best-fitting models. This, however, does not include uncertainties due to the model PSF. I was unable to constrain the Michie–King parameters of G185B as well as was done for the other two clusters. This is reflected in the larger uncertainties quoted for G185B in Table 7.3.

Cluster	Filter	W_0	r_c	r_t	c
G185	V	5.2 ± 0.4	$0\farcs50 \pm 0\farcs08$	$6\farcs09 \pm 0\farcs58$	1.07 ± 0.09
	I	5.5 ± 0.3	$0\farcs46 \pm 0\farcs03$	$6\farcs26 \pm 1\farcs09$	1.14 ± 0.07
G185B	V	3.0 ± 1.0	$0\farcs40 \pm 0\farcs13$	$1\farcs77 \pm 0\farcs30$	0.67 ± 0.17
	I	3.0 ± 1.0	$0\farcs39 \pm 0\farcs13$	$1\farcs70 \pm 0\farcs25$	0.67 ± 0.17
vdB2	V	6.5 ± 0.3	$0\farcs13 \pm 0\farcs02$	$5\farcs90 \pm 0\farcs67$	1.39 ± 0.09
	I	7.0 ± 0.3	$0\farcs17 \pm 0\farcs02$	$5\farcs90 \pm 0\farcs67$	1.53 ± 0.09

Table 7.3: Two-dimensional Michie–King model fits to G185, G185B, and vdB2.

G185B appears to be a very loose cluster with a concentration of 0.67 ± 0.17. This is less than that of the majority of the Galactic globular clusters. In fact, only a handful of outer halo Galactic clusters have similar concentrations (Trager et al. 1993 [145]). This, and the fact that G185B does not appear to be unusually reddened, argues that G185B is not situated near the centre of M31 and may be located well in front of M31. G185B

have dereddened colours that are consistent with the $V-I_0$ colours of the Galactic globular clusters (e.g. Peterson 1993 [108]). The $V-I$ colours of G185 and G185B suggest that they are old objects similar in age to the rest of the M31 globular cluster system. Therefore it is unlikely that G185 and G185B are a pair of young clusters that formed together and are currently separating. The field around G185 shows a large number of dust clouds which obscure the bulge of M31. The fact that none of the three clusters exhibits an unusual degree of reddening suggests that they all lie on the near side of the centre of M31 and may be situated in front of the majority of the material in M31.

7.4 Colours

The total integrated magnitudes for G185, G185B, and vdB2 were determined using aperture photometry with uncertainties estimated from fluctuations in the flat portion of the curve of growth for each cluster. To test this method of determining the uncertainties in the integrated magnitudes, a series of artificial globular clusters were constructed by adding artificial stars to the HRCam images using realistic luminosity and radial density profiles. The luminosity function used was that of 47 Tuc (Hesser et al. 1987 [68]) with the horizontal branch stars distributed uniformly over the horizontal part of the horizontal branch. In practice the exact form of the luminosity function did not affect the results. The radial stellar density profiles used were generated from the Michie–King models that were fit to the clusters (see Chapter 7.5.1). From these artificial globular clusters the uncertainties in the aperture magnitudes were estimated to be less than 0.1 magnitudes. The total magnitudes for each cluster were computed by integrating under the observed surface brightness profiles. The two methods of measuring magnitudes agreed to within 1σ for all three clusters. The total calibrated aperture magnitudes are listed in Table 7.2. No corrections for reddening have been applied to these values.

Cluster	I	$(V-I)$
G185	13.05 ± 0.03	1.19 ± 0.03
G185B	16.87 ± 0.10	1.09 ± 0.14
vdB2	13.35 ± 0.03	1.17 ± 0.03

Table 7.2: Integrated magnitudes for G185, G185B and vdB2.

Burstein & Heiles (1984) [22] quote an external reddening of $E_{B-V} = 0.080 \pm 0.003$ for M31. Using $E_{V-I} = 1.25 E_{B-V}$ (Taylor 1986 [144], Fahlman et al. 1989 [52]), and ignoring internal reddening within M31, gives $E_{V-I} = 0.10 \pm 0.01$ so all three globular clusters

7.3 Probability that G185 and G185B are Line-of-Sight Objects

The probability that two globular clusters $1'.7$ from the core of M31 will have an observed separation of $4''$ by chance is estimated as follows. Crampton et al. (1988) [33] find that the projected density of the M31 globular cluster system drops as $R^{1/4}$ with projected distance from the centre of M31. This density relation gives a probability of such a chance alignment on a $2' \times 2'$ field as 0.002. There are, however, ~ 5.34 such fields within an annulus of width $2'$ centred $1'.7$ from the centre of M31. Therefore, the probability that a randomly selected field $1'.7$ from the centre of M31 will contain such a pair of globular clusters is $\sim 0.002 \times 5.34 = 0.01$. This calculation assumes that there is no angular dependence in the distribution of globular clusters in M31. In reality the small number density of globular clusters in this annulus will result in Poisson fluctuations in the number of clusters observed in different fields located at the same distance from the centre of M31. To account for this the method of Bhatia & Hatzidimitriou (1988) [14] was used to estimate the probability that a $2' \times 2'$ field containing three globular clusters will contain two globular clusters separated by $4''$ or less. This method gives a probability of 0.016 for a single field. The probability of finding such a pair within the annulus, then, is 0.09 ± 0.03. A chi-square test indicates that this is significant at the 99% (2.5σ) confidence level, however the small sample size (three clusters) suggests that this result not be given too much weight.

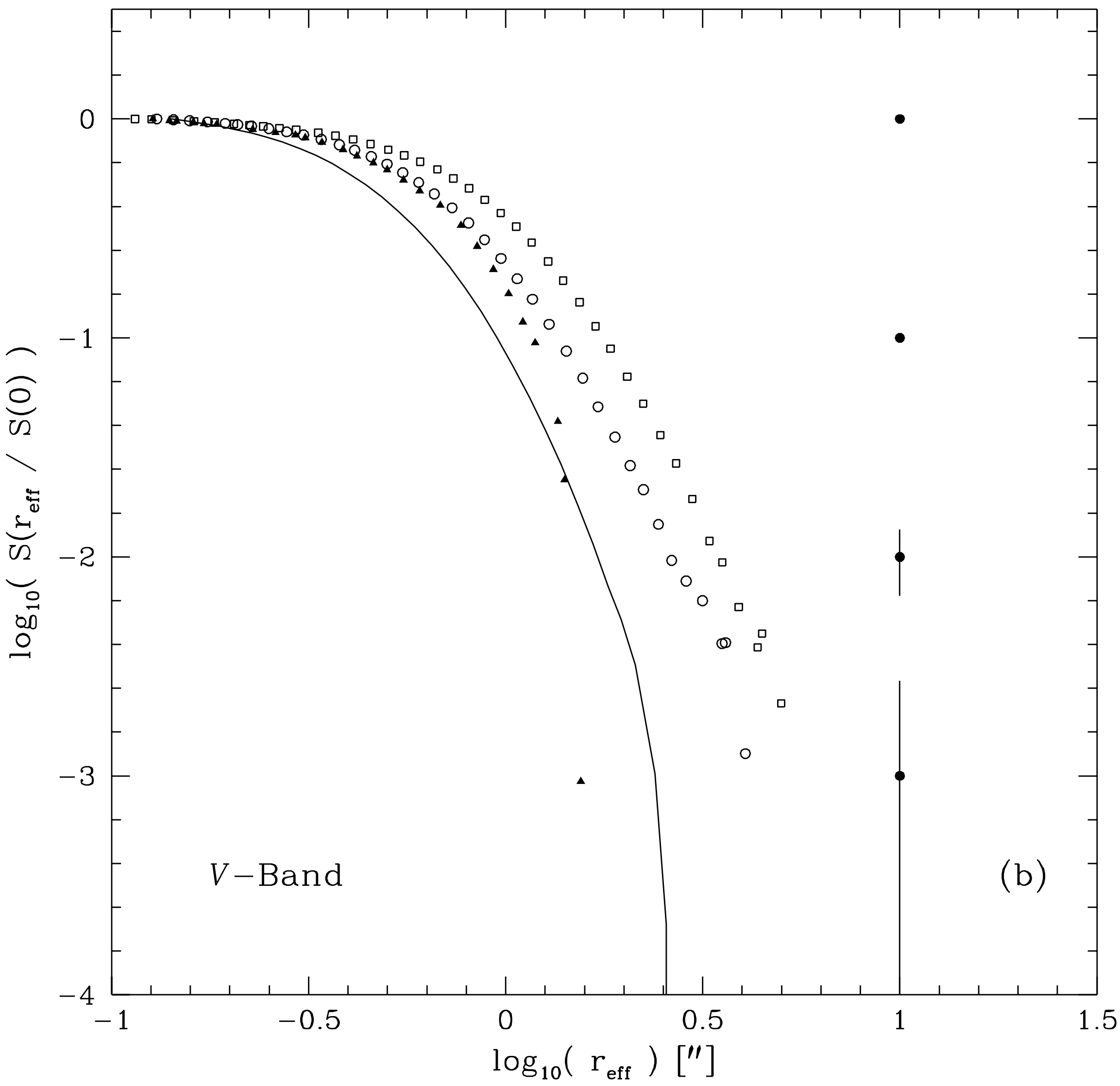

Figure 7.5: This figure is the same as Figure 7.4 except is shows V-band surface brightness profiles. G185B is nearly four magnitudes fainter than the other two clusters so its uncertainties will be greater than indicated by the error bars. To estimate the uncertainties in the G185B profiles shift the given error bars up by approximately 1.5 units in $\log_{10}(S)$.

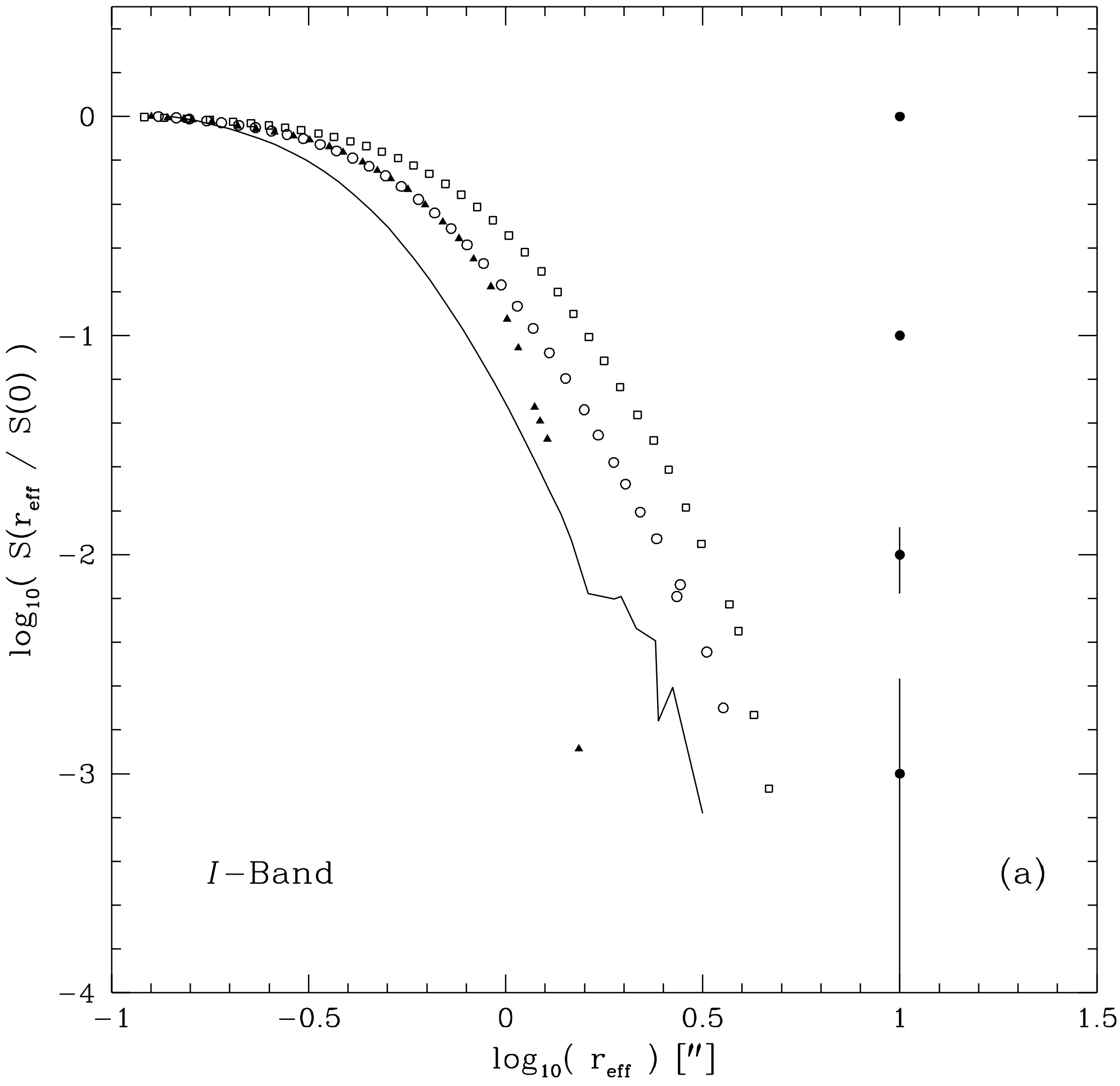

Figure 7.4: The normalized observed surface brightness profiles of each cluster and the PSF in the *I*-band. G185 is denoted by open squares, G185B by filled triangles, vdB2 by open circles and the PSF by the solid line. The noise in the wings of the *I*-band PSF is due the higher signal-to-noise ratio of the *I*-band image causing larger surface brightness fluctuations in the background. The error bars show the approximate uncertainties in the surface brightness profiles of G185 and vdB2 at the given intensity levels. G185B is nearly four magnitudes fainter than the other two clusters so its uncertainties will be greater than indicated by the error bars To estimate the uncertainties in the G185B profiles shift the given error bars up by approximately 1.5 units in $\log_{10}(S)$.

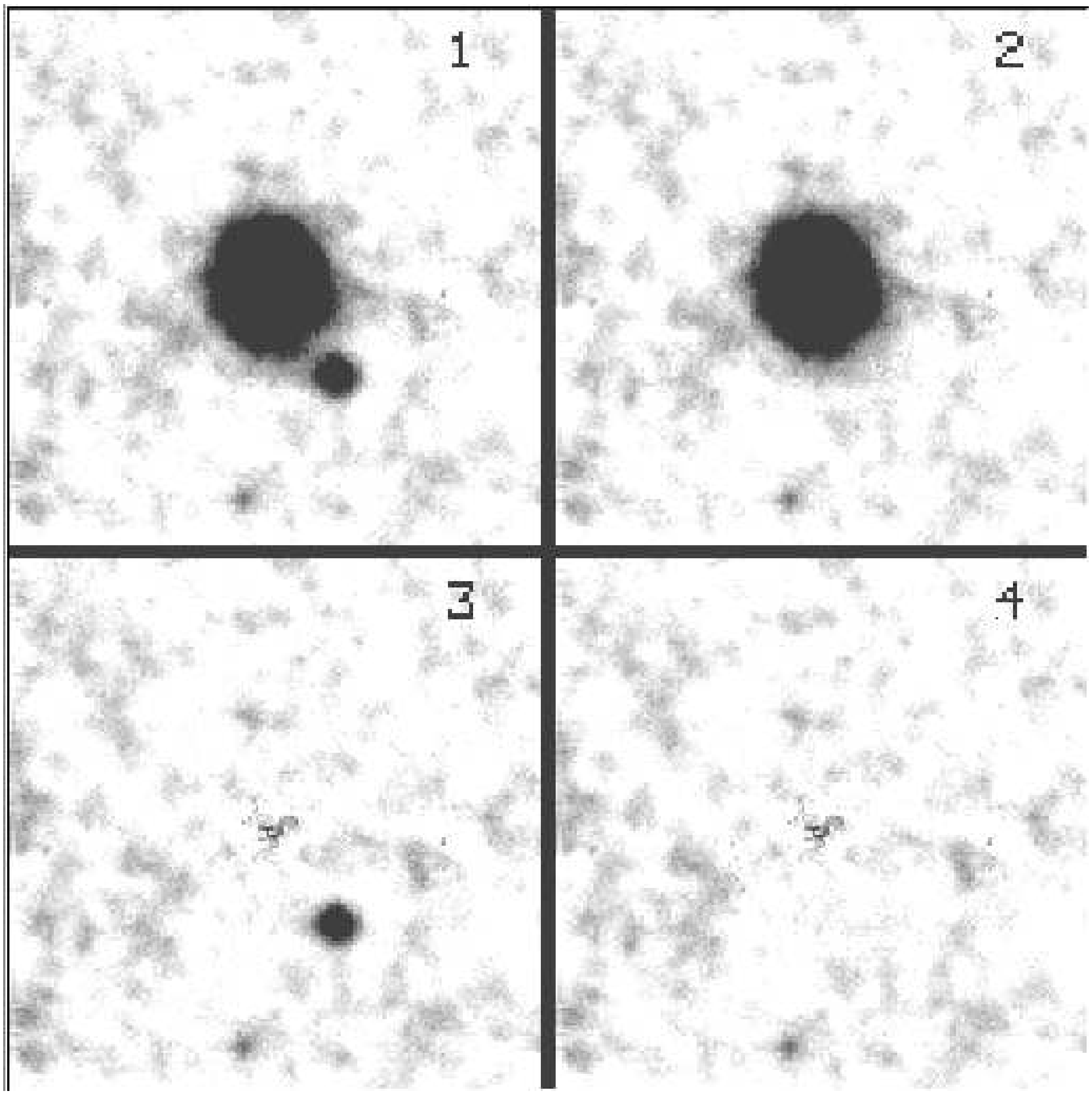

Figure 7.3: This figure shows G185 and G185B at various stages of the iterative fit-and-subtract procedure described in Chapter 7.2. (1) shows the two clusters G185 and G185B. (2) shows the same field with G185B subtracted while (3) shows the field with only G185 subtracted. (4) shows both clusters removed from the field.

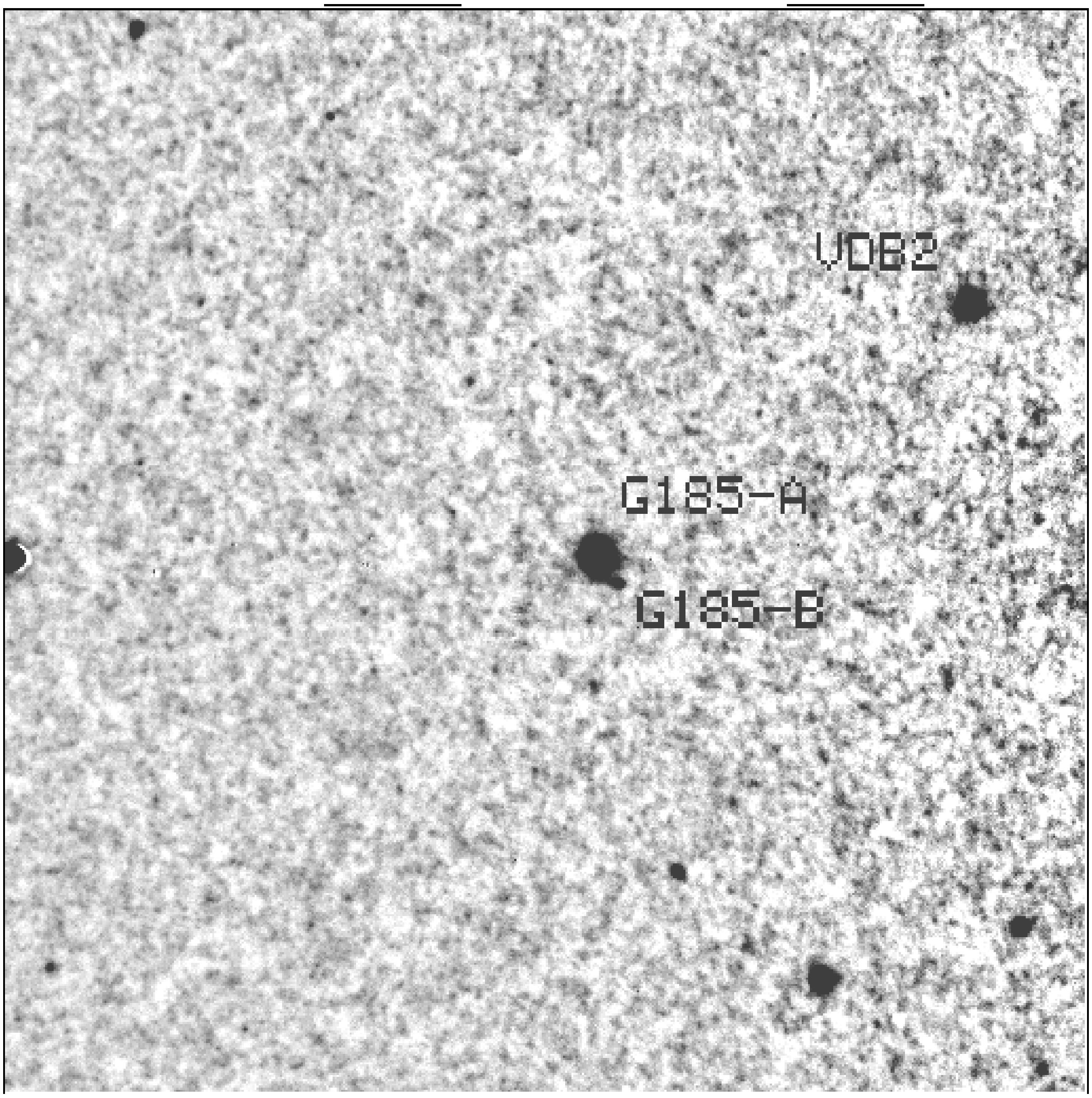

Figure 7.2: This figure is the same as Figure 7.1 except the unresolved light from the bulge of M31 has been subtracted leaving dust lanes and surface brightness fluctuations visible. Notice the surface brightness fluctuations are greater on the right-hand side of the image (towards the centre of M31).

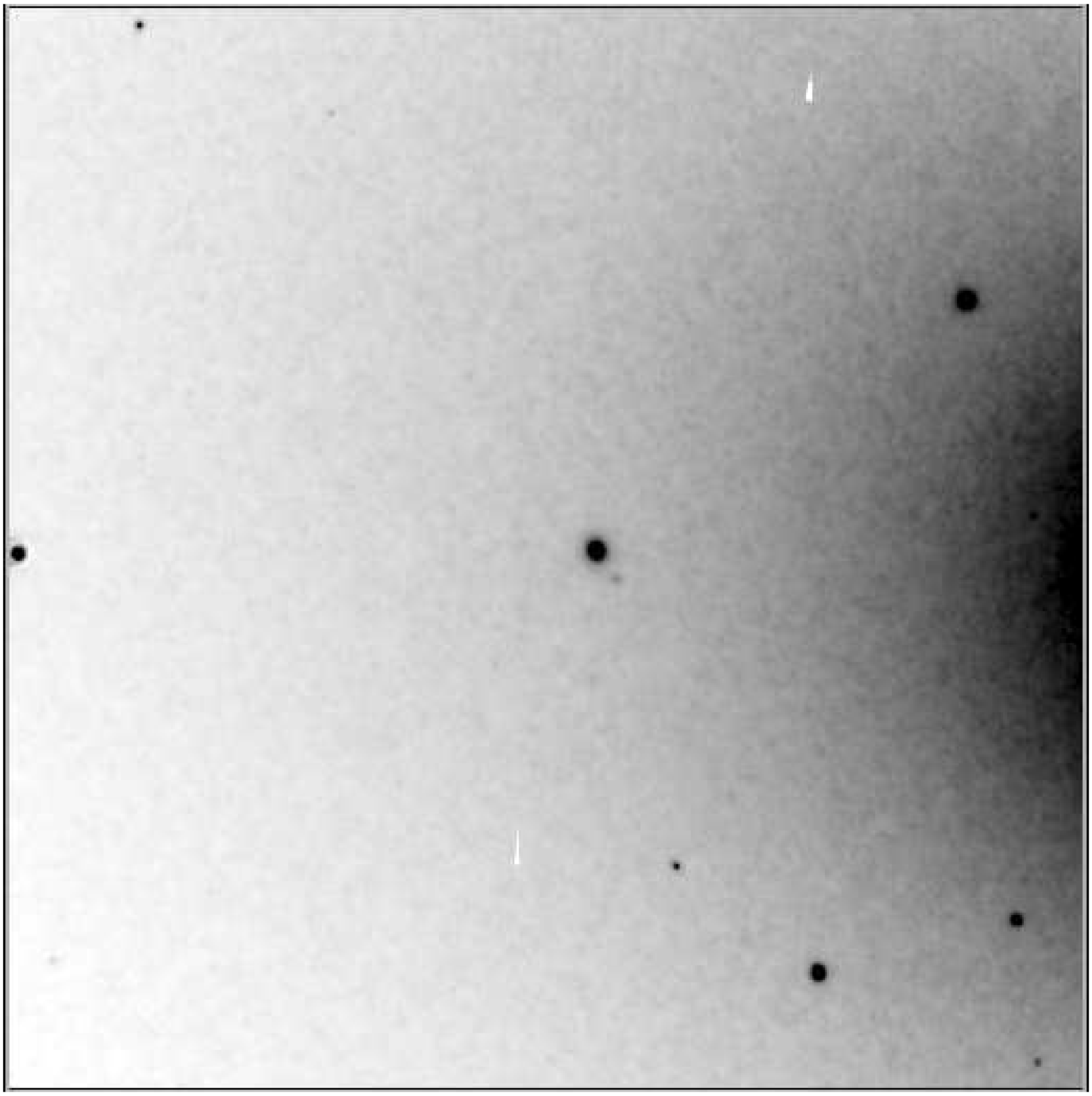

Figure 7.1: This figure shows the I-band image of G185 (centre), G185B (just below and to the right of G185), and vdB2 (upper right). The centre of M31 is located to the right of the frame. The top of the image is oriented 84° east of north.

of the PSF, however in the wings of the PSF surface brightness fluctuations in the field can significantly influence the shape of the PSF. The large signal-to-noise ratio of the I-band data results in larger surface brightness fluctuations in the I-band than in the V-band making the wings of the PSF harder to measure in I than in V. This can be seen in the wings of the PSF profiles in Figures 7.4 and 7.5.

The observed surface brightness profiles for each cluster and the PSFs are shown in Figures 7.4 and 7.5. G185B is clearly more extended than the PSF suggesting that it is not merely a foreground star. However, the outermost points of the surface brightness profile of G185B actually crosses the profile of the PSF. This, and the extreme truncation of the cluster profile, is likely an artifact of the uncertainties in measuring the surface brightness profiles of G185B and the PSF. G185B has only $\sim 3\%$ of the luminosity of G185 or vdB2. This results in the uncertainties in the surface brightness profile of G185B being correspondingly larger than the uncertainties in the profiles of G185 and vdB2 at similar fractions of the central surface brightness. Further, fitting and subtracting the unresolved background light from M31, and removing G185 from the images, results in additional uncertainties in the surface brightness measurements.

the G185 V- or I-band images within the error ellipses of the X-ray sources.

The IRAF implementation of the STSDAS task ELLIPSE was used to fit elliptical isophotes to each cluster. Surface brightness profiles were then extracted along the effective radius axes of each cluster.

The two objects were fitted iteratively as follows. First, the fainter component (G185B) was fitted and and subtracted from the original image. Next, the brighter (G185) component was fitted using the image with the G185B component subtracted. The G185 component was then subtracted from the original image and a new fit made to the G185B component. This cycle was repeated until the fitted ellipses for the two components were stable from one iteration to the next. Two or three iterations were sufficient for both the V- and I-band images. Figure 7.3 shows the subtractions of each component of G185 from the original image.

Describing the stellar PSF for each image was somewhat difficult since there were very few bright, non-saturated stars in the field. I attempted to fit both one-dimensional Moffatians and one-dimensional multi-Gaussians (Bendinelli et al. 1987 [10]) to the stars on each frame but found that the wings of the PSFs (beyond $\sim 1\farcs25$) were not well fit by either functional form. Therefore, DAOPHOT II was used to define a PSF in each band. I created a set of noiseless bright artificial stars and fit elliptical isophotes to these in the same manner as was done for the globular clusters. This worked well out to $\sim 1\farcs25$ but beyond this the uncertainties in the intensities of the fitted ellipses became larger than the PSF intensities. The difficulty in describing the PSFs beyond $\sim 1\farcs25$ is due to small-scale (a few pixels) fluctuations in the image background. Since the program field is located only ~ 360 pc from the centre of M31 there are large numbers of unresolved bulge and halo stars in the line of sight to each pixel. The PSF stars are sitting atop these large surface brightness fluctuations which in turn contribute to the shape of the PSF. In the core of the PSF the stellar luminosity is large enough to dominate the shape

7.2 The HRCam Images

The CFHT data (see Chapter 2) contained several Johnson V- and Cousins I-band images of a $2' \times 2'$ field near the core of M31 that includes G185 ($\alpha_{2000.0} = 00^{\rm h}42^{\rm m}44\overset{\rm s}{.}2$, $\delta_{2000.0} = +41°14'28''$) and vdB2 (van den Bergh 1969 [149]) ($\alpha_{2000.0} = 00^{\rm h}42^{\rm m}41\overset{\rm s}{.}1$, $\delta_{2000.0} = +41°15'26''$). These images were all taken on the night of August 16/17, 1990 and were pre-processed in the manner described in Chapter 2.2. A summary of the observations of the G185 field is given in Table 7.1.

Frame	Filter	UT	Exposure (s)	Airmass	FWHM
83922	V	12:15:21.7	200	1.109	$0\overset{''}{.}69$
83924	I	12:24:54.1	100	1.099	$0\overset{''}{.}68$
83925	I	12:31:03.4	100	1.094	$0\overset{''}{.}83$
83926	I	12:34:32.7	100	1.091	$0\overset{''}{.}72$
83927	I	12:38:06.0	100	1.089	$0\overset{''}{.}68$
83928	I	12:41:37.4	100	1.086	$0\overset{''}{.}69$
83929	I	12:45:09.7	100	1.084	$0\overset{''}{.}70$

Table 7.1: Log of the HRCam observations of G185.

The unresolved background light was removed by fitting and subtracting a two-dimensional cubic spline as described in Chapter 2.2.3. The residual variations in the background were approximately 1%, not including small-scale variations due to dust lanes and surface brightness fluctuations arising from unresolved stars in the bulge and halo of M31. Figure 7.1 shows the I-band image of the field containing the three globular clusters. Figure 7.2 shows the same field with the unresolved light from M31 removed. Dust lanes and surface brightness fluctuations are clearly visible. Primini et al. (1993) [111] report two *ROSAT* X-ray sources located within $0\overset{'}{.}5$ of G185 (their sources 39 and 46) but find no evidence for an X-ray source in G185. There are no unusual features on either

multiple clusters are young compared to the ages of Galactic globular clusters. Because of their young age the LMC multiple clusters may not be true dynamically bound multiple cluster systems but rather clusters sharing common origins that are currently parting company.

move away from each other. Galactic globular clusters are among the oldest objects in the Galaxy so a primordial binary globular cluster will have undergone many Galactic orbits and thus could not survive, as a binary cluster, to the present day. The mass of M31 is approximately twice that of the Galaxy so it is even less likely that a binary globular cluster could survive in M31. A transient binary globular cluster, however, may be observed if two clusters passed near enough to interact with each other, although such an encounter would likely destroy the two clusters since a typical encounter time-scale is longer than the time required for stars in one cluster to respond to the other cluster's gravitational field.

There is evidence that star clusters form in groups where the individual clusters are not gravitationally bound to each other. Lyngå & Wramdemark (1984) [92] cite similarities in metallicities, stellar content, and stellar ages to argue that several multiple open clusters in the direction of the Gould Belt have a common origin. Such systems, however, are probably not dynamically bound binary clusters but simply clusters that have a common origin and are in the process of either separating or merging. The Galactic open clusters h & χ Persei are one possible such pair. This scenario is unlikely among the M31 globular clusters since that system appears to have an age comparable with that of the Galactic globular cluster system (Frogel et al. 1980 [55], Bohlin et al. 1993 [18]).

The Large Magellanic Cloud (LMC), however, presents a more promising environment for binary clusters. The tidal field of the LMC is weak enough that a binary globular cluster could survive indefinitely (Innanen et al. 1972 [78]) without experiencing fatal disruption. Bhatia & Hatzidimitriou (1988) [14] have catalogued 69 pairs of stellar clusters in the LMC with inter-cluster separations of less than $13''$ ($\simeq 3.16$ pc) and use statistical arguments to show that only about half of these pairs are due to chance. Radial velocity studies have shown that the individual components of some of these multiple objects are interacting with each other while colour–magnitude studies show that several of these

Chapter 7

G185: A Potential Double Globular Cluster

7.1 Multiple Globular Clusters

When the HRCam images of G185 were being examined it became apparent that an object $\sim 4''$ northwest of G185 had an extended surface brightness profile resembling that of a globular cluster. No multiple globular clusters have been observed in the Galaxy or in any large extra-Galactic system, although some multiple globular clusters have been found in the Magellanic Clouds.

Binary globular star clusters are dynamically very fragile objects so it is not surprising that none have been observed in the Galaxy. Innanen et al. (1972) [78] have used numerical simulations to show that a binary globular cluster with a separation of less than ~ 50 pc, and a periGalacticon of less than ~ 1 kpc, would not survive a single Galactic orbit. Two globular clusters that are near enough to each other to avoid being separated by the Galactic tidal field will be too close to avoid being disrupted by the mutual tidal field of the clusters. Alternately, if the inter-cluster separation is large enough that mutual gravitation is insufficient to cause the two clusters to merge into a single object then the effects of the Galactic tidal field would be great enough to cause the two clusters to

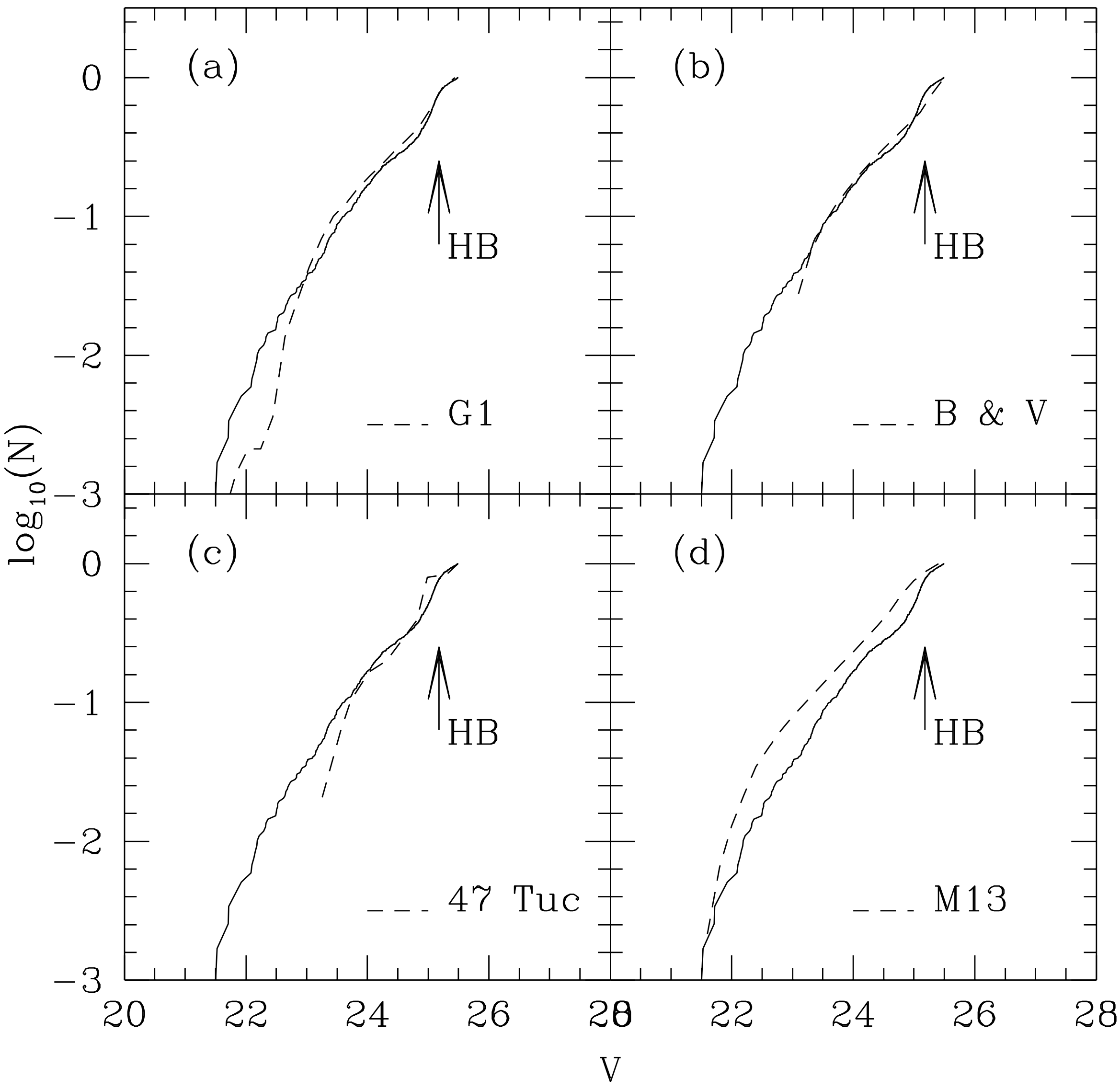

Figure 6.7: This figure compares the cumulative luminosity function for the M31 halo field near G312 with the four comparison luminosity functions used in Figure 6.6.

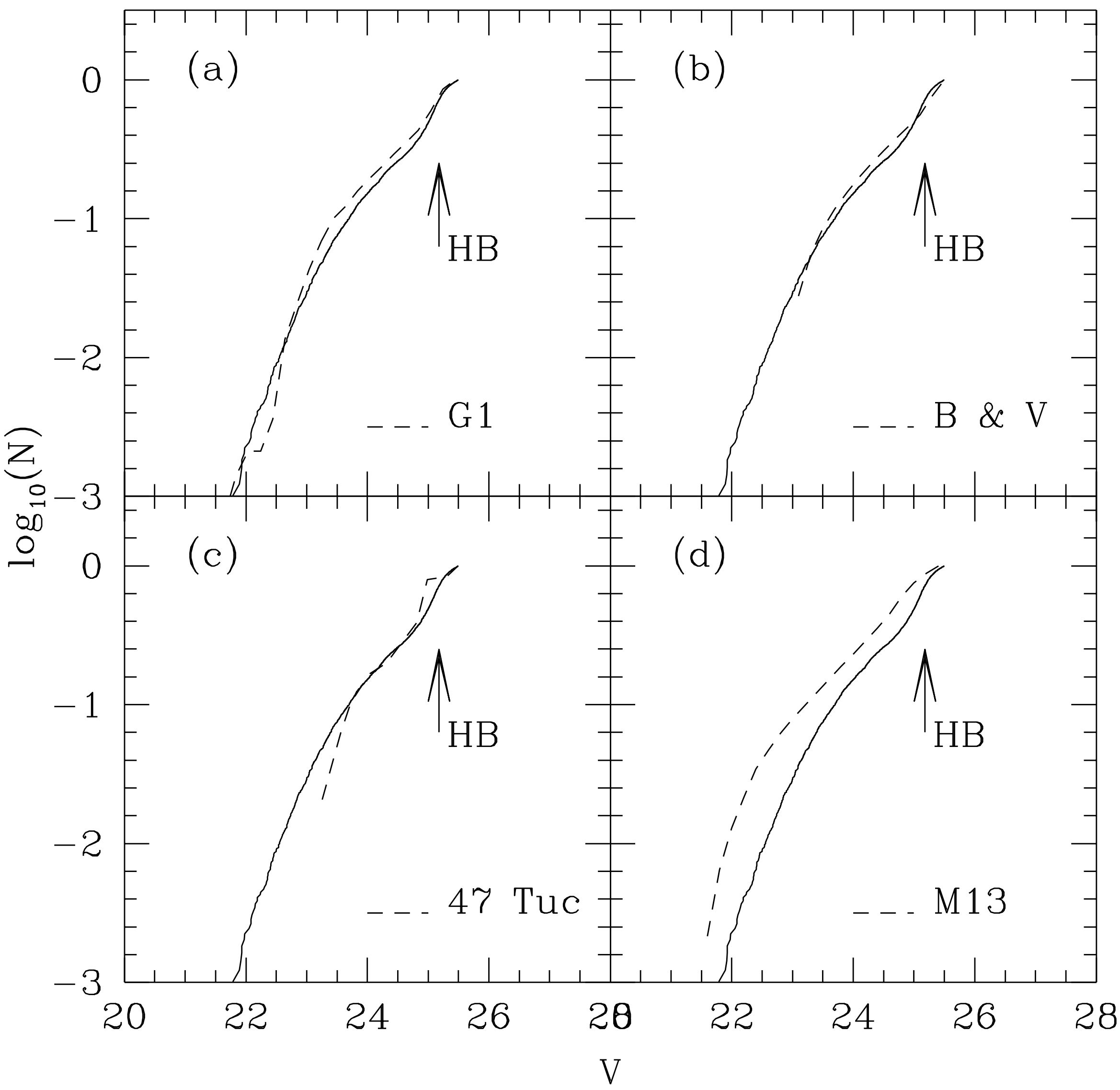

Figure 6.6: This figure compares the cumulative luminosity function for the M31 halo field near G302 (solid lines) with four comparison luminosity functions (dashed lines): (a) the G1 luminosity function, (b) a theoretical luminosity function (B & V) with [Fe/H] = −0.47, [O/Fe] = +0.23 and t_0 = 14 Gyr, (c) the 47 Tuc luminosity function, and (d) the M13 luminosity function. The faint cut-off magnitude was set to $V = 25.5$ because the photometry is reasonably complete down to approximately this point (see Chapter 6.2).

V	$n(V)$ G302F	$n(V)$ G312F	I	$n(I)$ G302F	$n(I)$ G312F
26.00	419	126	26.00	254	90
26.20	398	129	26.20	185	78
26.40	355	98	26.40	81	43
26.60	300	101	26.60	43	23
26.80	257	86	26.80	13	5
27.00	150	77	27.00	5	4
27.20	97	40	27.20	0	1
27.40	40	31	27.40	1	0
27.60	14	11	27.60	0	0
27.80	6	2	27.80	0	0
28.00	1	1	28.00	0	0

6.1 (continued)

V	$n(V)$ G302F	$n(V)$ G312F	I	$n(I)$ G302F	$n(I)$ G312F
20.00	0	0	20.00	2	0
20.20	2	0	20.20	4	2
20.40	1	1	20.40	8	4
20.60	1	0	20.60	17	9
20.80	0	0	20.80	35	5
21.00	1	1	21.00	42	9
21.20	0	0	21.20	53	12
21.40	0	1	21.40	49	9
21.60	2	1	21.60	46	9
21.80	4	3	21.80	49	11
22.00	9	3	22.00	71	25
22.20	8	6	22.20	69	18
22.40	20	5	22.40	113	28
22.60	29	10	22.60	89	28
22.80	45	8	22.80	121	30
23.00	65	10	23.00	154	42
23.20	78	20	23.20	194	52
23.40	106	36	23.40	174	45
23.60	123	25	23.60	225	44
23.80	180	46	23.80	304	68
24.00	168	52	24.00	555	138
24.20	222	52	24.20	1204	275
24.40	217	52	24.40	987	237
24.60	263	58	24.60	586	145
24.80	478	115	24.80	418	106
25.00	953	259	25.00	388	110
25.20	1260	275	25.20	357	115
25.40	674	144	25.40	346	110
25.60	476	122	25.60	319	96
25.80	436	125	25.80	290	102

Table 6.1: The observed V- and I-band halo luminosity functions.

clusters that do not appear to correspond to clumps in the red-giant branches of these clusters.

The large spread in metallicity in the halo of M31 makes it very difficult to distinguish between asymptotic-giant branch stars and stars on the upper red-giant branch. Since most of the observed width is due to the real spread in metallicity further improvement in photometric accuracy will not help in identifying helium shell-burning stars in the halo of M31.

small number statistics, and confusion between red giants, asymptotic giants, and horizontal branch stars. The artificial star tests described in Chapter 4.4 suggest that incompleteness is not a problem for $V \gtrsim 25$. To see if the shape of the M31 halo luminosity function changes significantly if the size of the magnitude bins are altered the stars were rebinned in 0.1, 0.25, and 0.5 magnitude bins. The comparison luminosity functions were compared to the rebinned M31 data using a KS test. In all cases the KS tests showed that the M31 halo luminosity function and the comparison luminosity function were the same at less than the 50% confidence level, suggesting that the M31 halo luminosity function is different from the comparison luminosity functions. In light of this, it is unlikely that the differences between the M31 halo data and the comparison data are merely due to statistical uncertainties in the data or the binning process.

Lee et al. (1977) [87] found that $\sim 15\%$ of the stars in 47 Tuc that are more than ~ 1 mag brighter than the horizontal branch are shell-helium burning stars on the asymptotic-giant branch. Since 47 Tuc has a similar metallicity and age as the stars in the halo of M31 near G302 and G312, it is reasonable to assume that a similar fraction of the stars brighter than the horizontal branch are asymptotic-giant branch stars and not part of the red-giant branch. Hesser & Hartwick (1977) [69] obtained separate luminosity functions for the red giants and the asymptotic giants of 47 Tuc. There is no significant difference in the slopes of these two luminosity functions, but stars on the asymptotic-giant branch had more of a tendency to be grouped in magnitude than stars on the red-giant branch did. If the ratio of red giants to asymptotic giants is the same at all magnitudes above the horizontal branch then including asymptotic giants in the halo luminosity function should not affect its shape. However, if the luminosity function of the asymptotic-giant branch is clumpy then confusion between the two giant branches can alter the observed shape of the luminosity function. Evidence for this can be found in Rich et al. (1997) [118]. They observe clumps in the asymptotic-giant branches for four metal-rich Galactic globular

6.2 The Halo Luminosity Function

Artificial star tests (see Chapter 4.4) indicate that the photometry is complete to approximately the level of the horizontal branch ($V \simeq 25$) in both the G302 and G312 fields. This is consistent with the results of Rich et al. (1996) [119] who found that star-counts in the halo of M31 obtained using WFPC2 data were complete to at least $V \sim 26$. The raw V- and I-band luminosity functions in each field are tabulated in Table 6.1. The $n(V)$ values are the number of stars in each field per 0.2 magnitude bin. The total area of each field is $\sim 3.2\ \Box'$ after masking and bad pixels are taken into account. Figure 6.6 shows the luminosity function for the G302 field compared with luminosity functions for the metal-rich M31 globular cluster G1 (Rich et al. 1996 [119]), a theoretical luminosity function for an old ($t_0 = 14$ Gyr) metal-rich ([Fe/H] $= -0.47$, [O/Fe] $= +0.23$) population (Bergbusch & VandenBerg 1992 [11]), the metal-rich Galactic globular cluster 47 Tuc (Hesser et al. 1987 [68]), and the metal-poor Galactic globular cluster M13 (Simoda & Kimura 1968 [132]). Figure 6.7 show the luminosity function for the G312 field and the same comparison luminosity functions.

Bergbusch & VandenBerg (1992) [11] calculated a series of oxygen-enhanced stellar models for old stars and used these models to investigate the relationships between the shape of the luminosity function of the red-giant branch and various astrophysical parameters. They found that neither iron abundance, nor age, has any detectable affect on the slope of the upper portion of the red-giant branch. Similarly, in a review of the literature, Renzini & Fusi Pecci (1988) [117] found that luminosity functions of red giants are much more sensitive to details of stellar structure than they are to the stellar ages.

The discrepancies between the luminosity function of the halo of M31 and the various comparison luminosity functions is probably due to a combination of incompleteness,

finite depth of the halo of M31 also introduces a small broadening in the V-band (see Chapter 6.1.2) of the horizontal branch. However, this broadening is negligible ($\sim 3\%$) compared with the broadening introduced by photometric uncertainties so it was ignored. The resulting distribution of V-band magnitudes was converted to iron abundances using the relation of Chaboyer et al. (1996) [28], see below. The derived mean iron abundance is $[\mathrm{Fe/H}] = -0.5 \pm 0.6$ (standard deviation) in the G302 field and $[\mathrm{Fe/H}] = -0.5 \pm 0.4$ in the G312 field. This is consistent with the iron-abundance distribution seen in the red giants.

The relationship between iron abundance and horizontal branch magnitude is very sensitive the adopted value of the distance modulus. An error of only 0.02 magnitudes in the distance modulus will result in an uncertainty of ~ 0.1 dex in metallicity. Therefore, the metallicity distribution estimated from the red-giant branch is a better indicator of the mean metallicity of the M31 halo than the metallicity distribution obtained from the horizontal branch. However, it should be noted that the metal-poor edge of the horizontal branch metallicity distribution $\left(\overline{[\mathrm{Fe/H}]} - 3\sigma_{[\mathrm{Fe/H}]}\right)$ occurs at $[\mathrm{Fe/H}] \simeq -2$, in rough agreement with the metallicity distribution of red-giant branch stars. The lack of horizontal branch stars with $[\mathrm{Fe/H}] \lesssim -2$ supports the conclusion that the metal-poor tail of the red-giant branch metallicity distribution is due to calibration uncertainties and contamination of the blue side of the red-giant branch by asymptotic-giant branch stars.

The metal-rich edge of the horizontal branch metallicity distribution $\left(\overline{[\mathrm{Fe/H}]} + 3\sigma_{[\mathrm{Fe/H}]}\right)$ occurs at $[\mathrm{Fe/H}] \simeq +1$. The red-giant branches show no evidence for stars with $[\mathrm{Fe/H}] \gtrsim -0.2$ so the metal-rich tail in the horizontal branch metallicity distribution is most likely an artifact of fitting a Gaussian to a non-Gaussian distribution. In general, red horizontal branches have a well defined faint edge but photometric uncertainties and contamination from red giants make it impossible to identify this faint edge in the data. Therefore the metal-rich tail of the horizontal branch metallicity distribution is spurious.

blue horizontal branch extends to below the $\sigma_{(V-I)} = 0.2$ photometric limit suggesting that incompleteness may be causing a seriously underestimate of N_B. The theoretical horizontal branches of Lee et al. (1994) [88] were used to estimate the expected values of the horizontal branch type given the metallicity ratios determined in Chapter 6.2. The predicted horizontal-branch-ratios were -0.6 ± 0.3 in the G302 field and -0.1 ± 0.1 in the G312 field, somewhat more positive than the values measured from the CMDs. This suggests that either the blue horizontal branch suffers from a high degree of incompleteness, or that there is a second parameter contributing to the morphology of the horizontal branch in the halo of M31. Detailed incompleteness tests suggest that the results are due to incompleteness in the blue end of the horizontal branch (see Figure 4.4). The morphology of the horizontal branch in the halo of M31 is broad agreement with the metallicity distribution determined from the red-giant branch morphology but further work is needed to determine if the lack of blue horizontal branch stars (relative to the metallicity spread observed in the red-giant branch stars) is due to photometric limits in the data or a second parameter effect[1].

The $(V, (V-I)_0)$ CMDs (Figures 6.3 and 6.4) show that the horizontal branch is not horizontal in the V-band. To estimate the spread in the magnitudes of the horizontal branch stars the horizontal branch was split into bins with widths of $\Delta(V-I) = 0.1$ and fit a sloping Gaussian to the distribution of stars in the V-band in each bin. The mean width of these Gaussians was $\sigma_V = 0.14 \pm 0.01$ (standard error) in the G302 field and $\sigma_V = 0.12 \pm 0.03$ in the G312 field. The mean photometric uncertainty at the level of the red horizontal branch is $\sigma_V = 0.086$. Subtracting this quadratically from the observed spread in the V-band magnitude of the horizontal branch gives intrinsic spreads of $\sigma_V = 0.11 \pm 0.01$ in the G302 field and $\sigma_V = 0.08 \pm 0.03$ in the G312 field. The

[1] Ideally V- and I-band photometry reaching to the main-sequence turn-off in the M31 halo ($V \sim 29$) would be needed to do a high-precision photometric study of the horizontal branch morphology. Such a study would require at least forty orbits of *HST* time per field using the WFPC2.

6.1.3 The Horizontal Branch

The horizontal branch stars in both fields are concentrated in a red clump between $0.5 \leq (V-I)_0 \leq 1.0$ with a handful of blue stars between $0.0 \lesssim (V-I)_0 \leq 0.5$. The red clump is consistent with what is seen in metal-rich Galactic globular clusters such as 47 Tuc while the small number of blue horizontal branch stars is indicative of a metal-poor population. However, an age spread of $\sim$ 5 Gyr in the halo population could produce a horizontal branch morphology similar to what a metallicity spread of $\sim$ 1 dex would produce. This is the classic "second parameter" problem (see van den Bergh 1993 [147], Lee et al. 1994 [88], and Chaboyer et al. 1996 [28] for recent reviews) affecting the colours of horizontal branch stars. The lack of any extended asymptotic-giant branch candidates in the data, or in any other published M31 halo fields, suggests that a young population ($\lesssim$ 5 Gyr) is not present. However, it does not rule out the possibility that the M31 halo may contain stars as young as $\sim$ 10 Gyr.

The morphology of the horizontal branch in each field can be parameterized by counting the number of red and blue horizontal branch stars, and computing the horizontal-branch-ratio $= (N_B - N_R)/(N_B + N_V + N_R)$ where N_B is the number of horizontal branch stars bluer than the instability strip, N_V is the number of stars in the instability strip, and N_R is the number of horizontal branch stars redder than the instability strip. Since photometric scatter is quite large ($\sigma_{(V-I)} \simeq 0.16$) at the level of the instability strip, and the instability strip has a width of only $\sim$ 0.25 mag, I did not attempt to identify RR Lyrae candidates. Instead the horizontal branch was split at $(V-I)_0 = 0.5$ so the ratio $(N_B - N_R)/(N_B + N_R)$ could be calculated. The G302 field has a horizontal-branch-ratio of -0.91 ± 0.12 (Poisson uncertainty) while the G312 field has a horizontal-branch-ratio of -0.92 ± 0.26 suggesting that both fields have the same horizontal branch morphology. These ratios are lower limits on the actual horizontal-branch-ratios since the

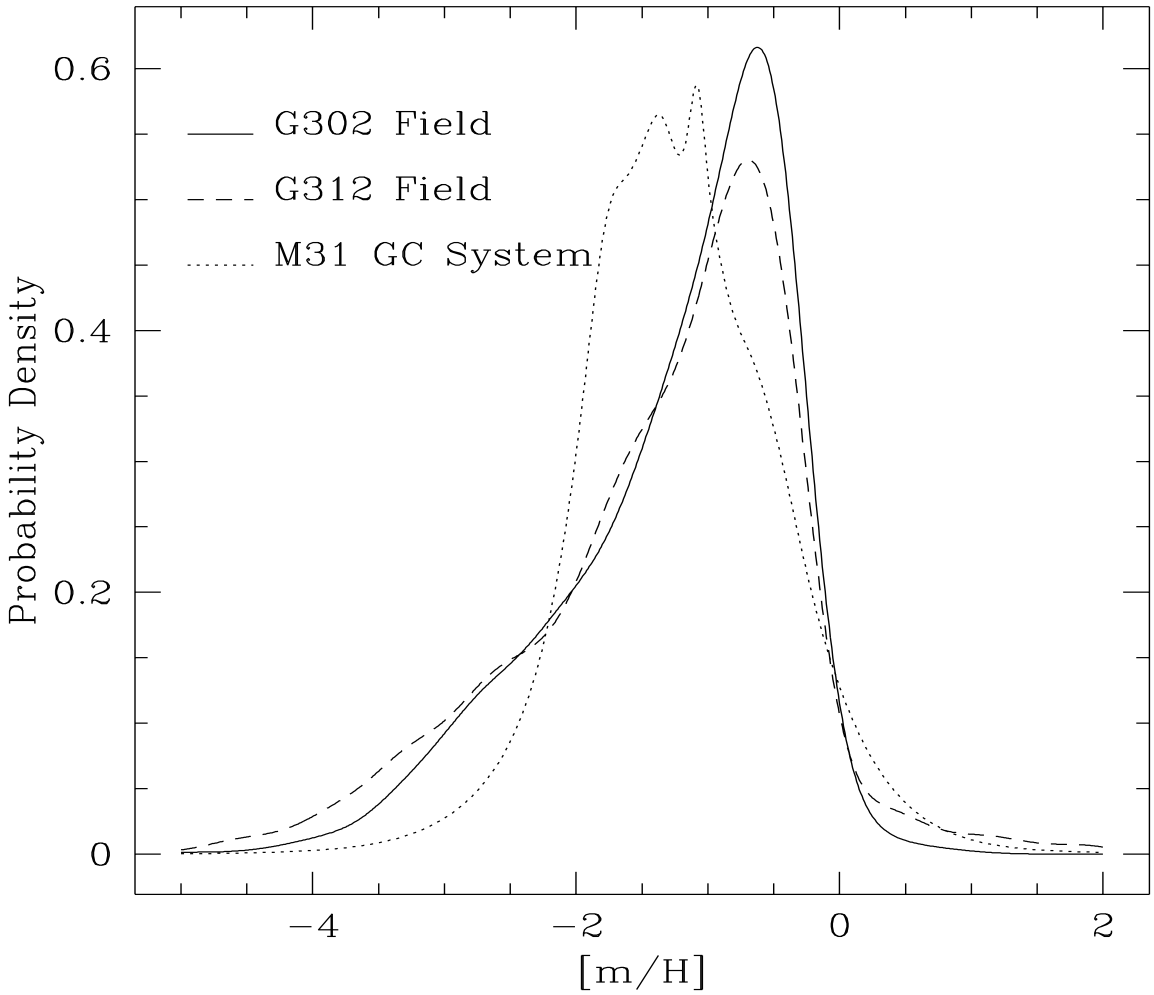

Figure 6.5: The probability density distribution for the metallicity of the red giants in the field around G302 (solid line), the field around G312 (dashed line), and the M31 globular cluster system (dotted line). For each star a unit Gaussian with a standard deviation of $\sigma = 0.25$ dex, the estimated uncertainty in the metallicity determination for an individual star, was generated. For the globular clusters the $\sigma_{\mathrm{[Fe/H]}}$ values from HBK were used. The normalized sum of these Gaussians is a non-parametric histogram of the probability density, $P(\mathrm{[m/H]})$, distribution. The sharp edge at the metal-rich end the distribution ($\mathrm{[m/H]} \sim 0$) suggests that there is a well-defined upper limit to the metallicity of stars in these fields. The slow decline on the metal-poor edge suggests that the metal-poor stars cover a range of metallicities. A portion of the metal-poor tail arises from the confusion of asymptotic-giant branch stars with metal-poor red-giant branch stars.

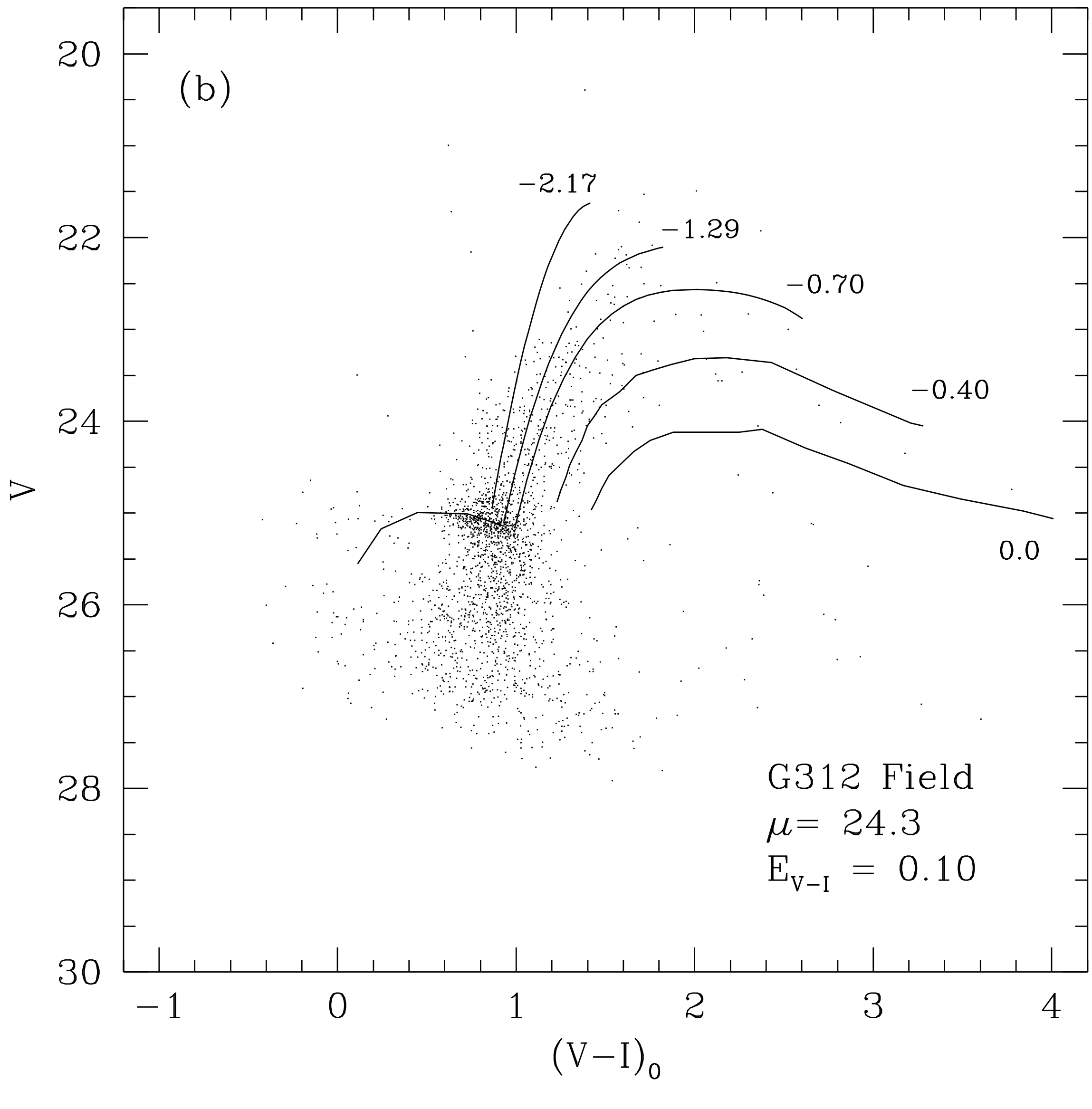

Figure 6.4: This figure shows the CMD for stars images on the WF2 and the WF4 CCDs in the G312 field. The fiducial sequences are described in Chapter 6.1.2.

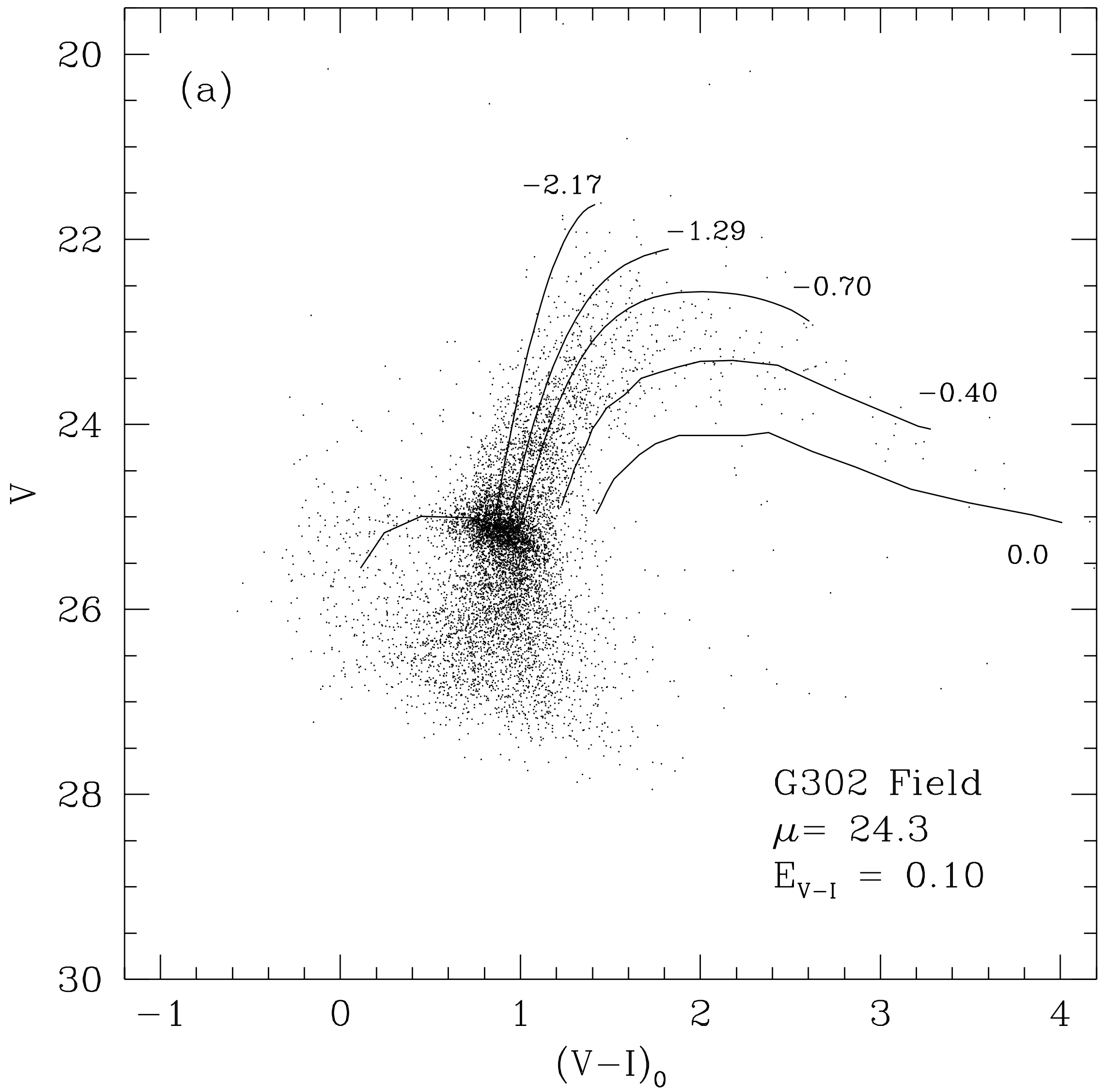

Figure 6.3: This figure shows the CMD for stars images on the WF2 and the WF4 CCDs in the G302 field. The fiducial sequences are described in Chapter 6.1.2.

and 1.5 dex for the G312 field. The halo stars are clearly more metal-rich than, and have a slightly greater spread in metallicity than, the M31 globular cluster system.

The halo metallicity distribution is clearly asymmetric with an extended metal-poor tail. This is partly due to the presence of asymptotic-giant branch stars on the blue edge of the red-giant branch and partly due to the metallicities less than $[m/H] = -2.19$ being extrapolated from the higher-metallicity fiducial sequences. Therefore the shape of the metallicity distribution beyond $[m/H] \sim -2$ should be regarded with caution. There is a sharp cut-off in the halo metallicity distribution at approximately Solar metallicity. The metal-rich tail of the metallicity distribution drops to zero quite rapidly between $[m/H] \simeq -0.2$ and $[m/H] \simeq +0.2$. A visual examination of the locations of the $[m/H] = -0.4$ and $[m/H] = 0.0$ isochrones in Figures 6.3 and 6.4 shows the most metal-rich red-giant branch stars having $[m/H] \simeq -0.2$ suggesting that the extra-Solar metallicity tail in Figure 6.5 is an artifact of the uncertainties in the metallicity determination.

the molecular opacity in the star's atmosphere can become high enough to reduce the luminosity of the star enough that these stars become fainter as they ascend the red-giant branch. However, Figures 6.3 and 6.4 shows that this flattening will not explain all of the structure in the red-giant branch. Therefore a portion of the width of the red-giant branch is due to an intrinsic spread in the metallicity of the M31 halo stars.

In order to estimate the metallicity distribution of red-giant branch stars metallicity values for each star were interpolated based on the fiducial sequences in Figures 6.3 and 6.4 and the theoretical isochrone of Bertelli et al. (1994) [15] with [m/H] = +0.4 (not plotted). It was assumed that the age of the M31 halo is $t_0 \simeq 14$ Gyr, comparable with the age of the Galactic halo globular cluster system (e.g. Richer et al. 1996 [122]). The morphology of the red-giant branch is not sensitive to changes in age of a few Gyr so the exact age adopted for the red-giant branch isochrones is not critical. Figure 6.5 shows the probability density distributions of metallicity ([m/H]) for red-giant branch stars with $I < 23$ in the G302 and G312 fields. Based on the photometric uncertainties in the data at the level of the red-giant branch, and the uncertainties inherent in matching theoretical isochrones to observational data, the metallicity estimates for the red-giant branch stars have uncertainties of $\sigma_{[\mathrm{m/H}]} \sim 0.25$. A KS test shows that the two metallicity distributions differ at less than the $5.0 \times 10^{-6}\%$ confidence level, strongly suggesting that the stellar populations are the same in both fields. The G302 field distribution has a peak at $[\mathrm{m/H}] = -0.6$ and a FWHM of 1.3 dex while the G312 field distribution has a peak at $[\mathrm{m/H}] = -0.7$ and a FWHM of 1.6 dex. These FWHMs are overestimates of the true metallicity distribution since the probability density distribution function shown in Figure 6.5 is essentially a convolution of the data with a unit Gaussian that has a dispersion equal to the uncertainty in a typical measurement ($\sigma_{[\mathrm{m/H}]} = 0.25$). The intrinsic spread in the metallicity can be estimated by deconvolving this Gaussian from the probability density distribution function. This gives an intrinsic FWHM of 1.2 dex for the G302 field

$$\log_{10}\Big(\Sigma(R)/\Sigma(R_e/\alpha_s)\Big) = -3.3307\left[\left(\frac{R}{R_e/\alpha_s}\right)^{1/4} - 1\right] \tag{6.1}$$

with an effective radius of $R_e = 1.3$ kpc and an axial ratio of $\alpha_s = 0.55$, in accordance with Pritchet & van den Bergh (1994) [112]. The volume density, $\rho(r)$, can be obtained from $\Sigma(R)$, through Abel's integral, as follows:

$$\rho(r) = -\frac{1}{\pi}\int_{R=r}^{+\infty} \frac{d\Sigma(R)}{dR}\frac{dR}{\sqrt{R^2 - r^2}} \tag{6.2}$$

where R is the projected distance of the field from the centre of M31 and r is the true galactocentric distance of the volume element $\rho(r)$ from the centre of M31.

The density distributions along the lines-of-sight at projected distances of $32'$ and $50'$ from the centre of M31 were computed. The spread due to the depth of the halo has a half-power width in the V-band of ~ 0.02 mag at $R_{\rm M31} = 32'$ (the G302 field) and ~ 0.03 mag at $R_{\rm M31} = 50'$ (the G312 field). Changing the effective radius and axial ratio over the ranges found by Hodder (1995) [70] in his study of the structure of M31 does not significantly alter these results. A change of a few hundredths of a magnitude along any of the DCA fiducial red-giant branches corresponds to a negligible change in colour which suggests that the depth of the M31 halo does not contribute significantly to the observed width of the red-giant branch.

The mean photometric uncertainties in the data are $\sigma_{V-I} \simeq 0.05$ near the tip of the red-giant branch ($I \simeq 20$) and increase to $\sigma_{V-I} \simeq 0.10$ at the level of the horizontal branch, yet the observed spread in colour along the red-giant branch is ~ 0.5 mag at the level of the horizontal branch and ~ 2 mag near $I \simeq 20$. These spreads are too large to be due to photometric uncertainties or the depth of the M31 halo. The turn-over in the red-giant branch near $V = 23$ is due to the increased opacity from molecular bands as giants expand and become cooler. For shell-hydrogen burning stars with [m/H] $\gtrsim -1$

halo stars, background galaxies, and the disc of M31 (see Chapter 6.1.1) makes a direct comparison between the distribution of stars within the red-giant branches of the two halo fields difficult. Therefore, the weak evidence for a difference in stellar populations in the two locations should be treated with some caution.

Figures 6.3 and 6.4 show the $(V, (V-I)_0)$ CMDs for the M31 halo fields around G302 and G312 with a series of red-giant branch fiducial sequences for Galactic globular clusters of different iron abundances added. The three metal-poor fiducial sequences are the red-giant branch ridge lines for the Galactic globular clusters M15 ([Fe/H] $= -2.19$), NGC 1851 ([Fe/H] $= -1.29$), and 47 Tuc ([Fe/H] $= -0.71$) taken from DCA. The two metal rich fiducials are the $t_0 = 13.8$ Gyr isochrones of Bertelli et al. (1994) [15] with [m/H] $= -0.4$ and [m/H] $= 0.0$. The horizontal branch fiducial sequence is that of M54 ([m/H] $= -1.42$) from Sarajedini & Layden (1995) [125].

The spread in metallicity in the red giants is clearly visible from the locations of the fiducial sequences. The observed distribution of stars along the red end of the red-giant branch is consistent with a metal-rich population while the blue side of the red-giant branch is consistent with a metal-poor population. However, photometry of 47 Tuc (Lee 1977 [87]) shows that $\sim 15\%$ of the stars ~ 1 mag brighter than the horizontal branch are evolved asymptotic giant branch stars. If this ratio holds for the halo of M31 then many of the stars blueward of the [Fe/H] $= -1.29$ fiducial sequence will be asymptotic-giant branch stars. The majority of the stars, however, have [Fe/H] > -0.7, consistent with recent studies (see references in Chapter 1.2) which have found metallicities of [m/H] ~ -0.6 for the halo of M31.

To estimate the contribution to the width of the red-giant branch from the finite depth of the halo it was assumed that the projected surface density distribution of stars in the M31 halo follows a de Vaucouleurs $R^{1/4}$ law:

6.1.2 The Red-Giant Branch

The red-giant branches in the G302 and G312 fields are morphologically similar except for a clump of stars at $I \sim 23$ in the red-giant branch of the G302 field (see Figure 6.1). There is no apparent corresponding clump visible in the G312 field (see Figure 6.2). This clump is similar to the clumps of stars seen approximately one magnitude above the horizontal branch in several metal-rich Galactic globular clusters (Rich et al. (1997) [118]). In order to check if this clump is a real feature of the red-giant branch I determined the differential luminosity function for each red-giant branch for $22 \leq V \leq 24.5$ using a non-parametric histogram. A second luminosity function was constructed where the clump was removed by interpolating the differential luminosity function across the region containing the clump. The resulting "clumpless" luminosity function was compared to the observed luminosity function using a KS test. The results of this test implied that the density enhancement at $V \sim 24.25$ is significant at less than the $5.0 \times 10^{-6}\%$ confidence level. This suggests that the null hypothesis (that the clump in the red-giant branch is not real) can not be rejected.

Peacock's (1983) [106] two-dimensional KS test was applied to the entire red-giant branch above $V = 24.5$ to determine if the distribution of stars within the red-giant branch is the same in G302 and G312. The KS test results said that the red-giant branch stars in the G302 and G312 fields were drawn from the same distributions at the 91% confidence level. The same tests found that the distributions of stars on the blue sides of the upper red-giant branches ($V \leq 24$, $(V-I)_0 \leq 1.6$) were the same at the 85% confidence level and that the red sides of the upper red-giant branches ($V \leq 24$, $(V-I)_0 \geq 1.6$) were the same at the 93% confidence level. This is weakly suggestive that the two fields have different stellar populations. However, the small number of stars in the red-giant branch of G312 (335 stars with $V \leq 24.5$) and the contamination from Galactic

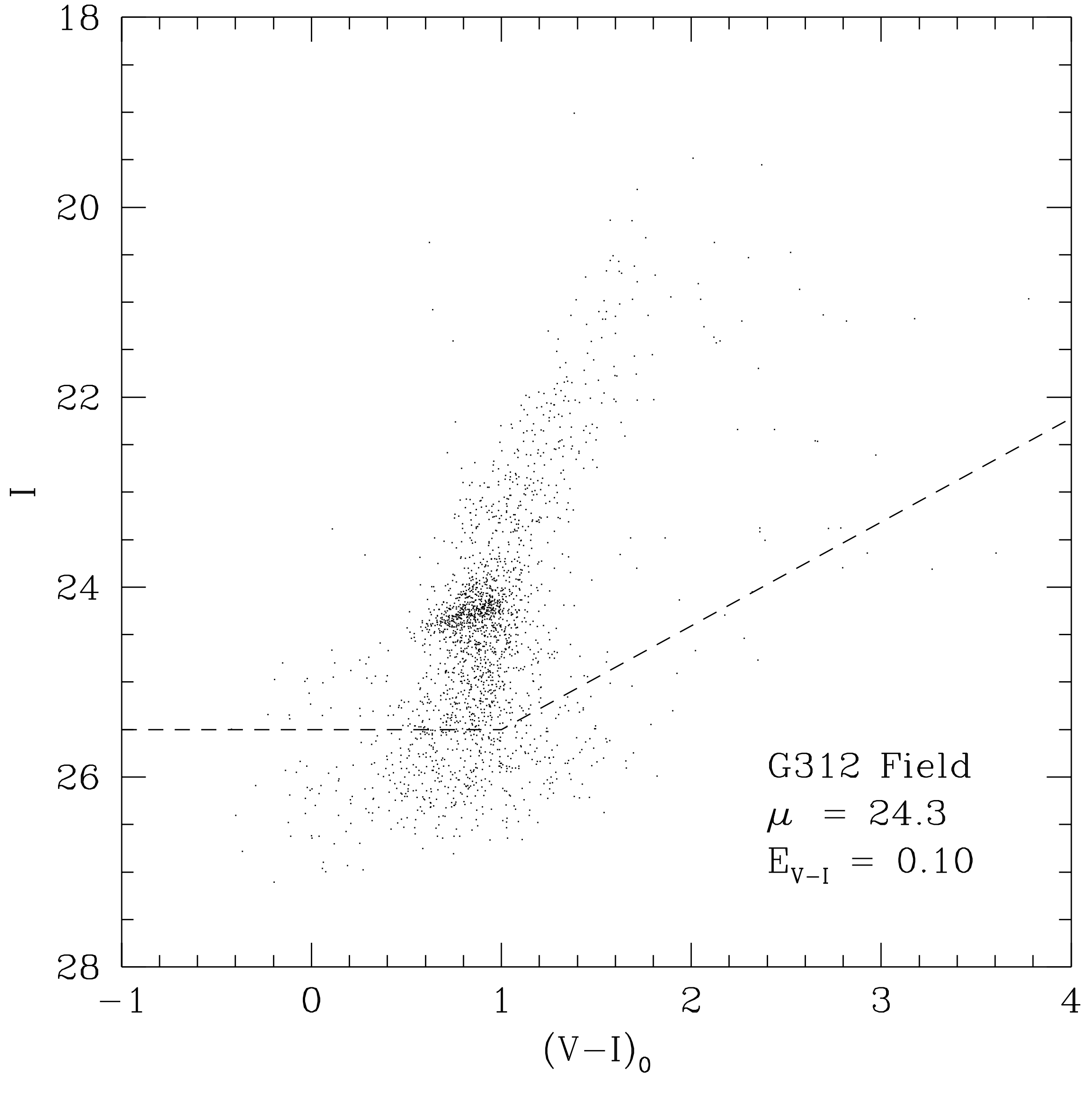

Figure 6.2: This figure is the same as Figure 6.1 but shows the CMD for the M31 halo field around the globular cluster G312.

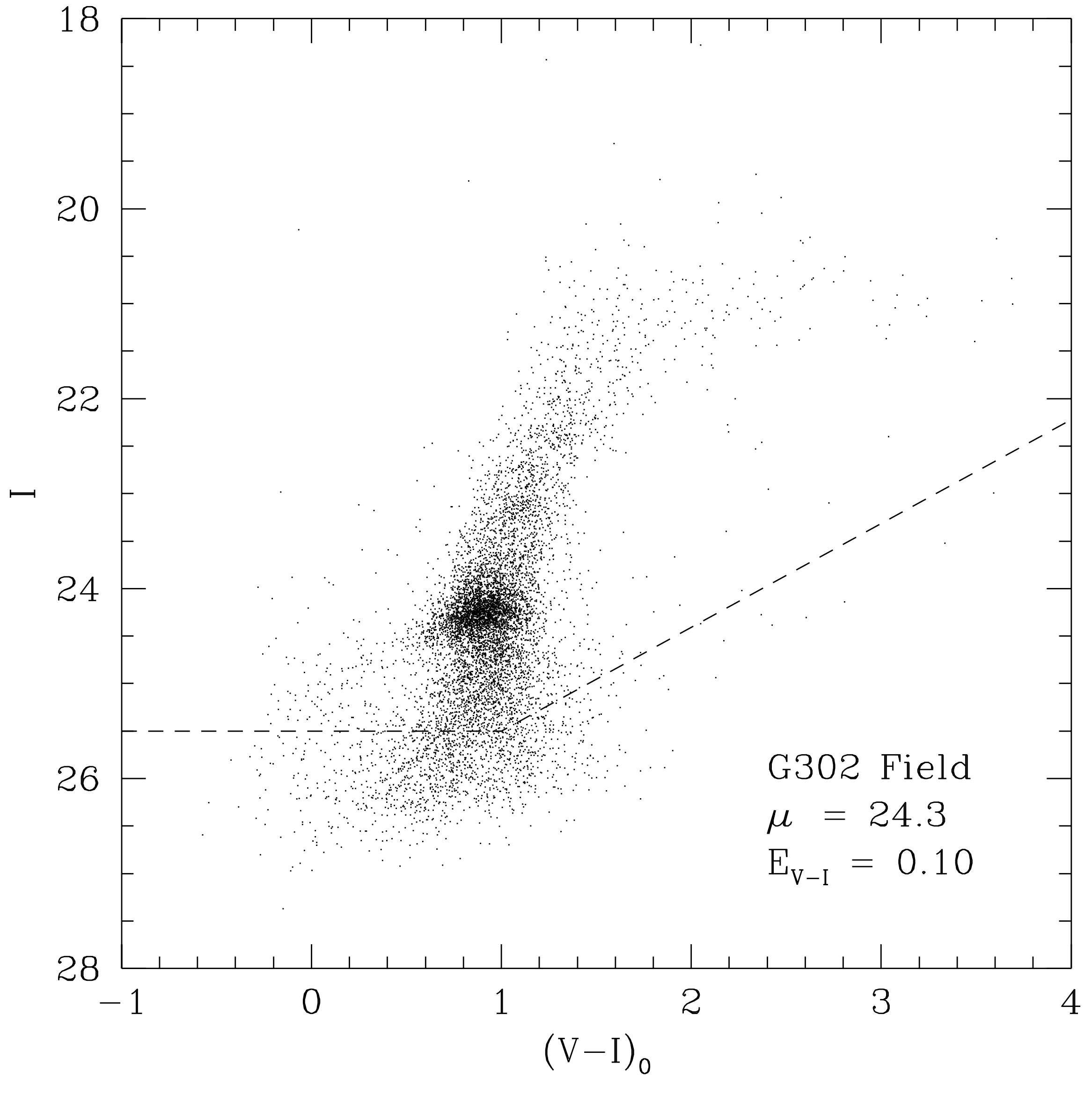

Figure 6.1: This figure shows the CMD for the M31 halo field around the globular cluster G302. All the stellar sources in the WF2 and WF4 images are shown. No attempt has been made to remove foreground or background contamination. The dashed line shows the location where the photometric uncertainties are $\sigma_{(V-I)} \simeq 0.2$. This also corresponds to the approximate location where the data becomes incomplete. The extinction quoted is the value that was used to calibrate the photometry (see Holtzman et al. 1995b [73]).

a field $40'$ from the centre of M31 along the southeast minor axis with various models and found that even with a thick disk component the disk-to-halo ratio would be $\lesssim 0.04$. Hodder (1995) [70] adapted the Bahcall & Soneira (1984) [6] Galaxy model to provide star counts and colour distributions for an external spiral galaxy. He used this model to estimate a disk-to-halo number-density ratio of ~ 0.1 in a field around G302 and ~ 0.03 in a field around G312, although these ratios are somewhat dependent on the details of the disk and halo models. Taking the worst-case scenario for disk contamination (that of Hodder 1995 [70]) leads to the conclusion that less than 10% of the stars in the G302 field, and less than 3% in the G312 field, are due to contamination from the disk of M31.

On the basis of these calculations *at most* $\sim$ 13% of the objects in each field are background galaxies or stars that are not members of the M31 halo. Therefore, the overall morphologies in the CMDs represent real features in the halo population of M31. The exception is the group of blue objects visible $\sim$ 1 mag above the horizontal branch in the G302 field (see Figure 6.1). A visual examination of the individual CCD frames of the G302 field showed that approximately half of these objects fall on or near background galaxies, saturated stars, or pixels that have been flagged as bad for whatever reasons. The remaining $\sim$ 10 bright blue objects may be nucleated dwarf galaxies, blends of stars, or stars with a large photometric uncertainties.

therefore, contributes only $\sim 0.2\%$ to the total number of stars observed in the G302 halo field and $\sim 0.7\%$ to the G312 halo field. The blue end of the horizontal branch is sparsely populated, but only 1 ± 1 foreground stars are expected on the blue side of the red-giant branch, so uncertainties due to photometric scatter will dominate over the effects of contamination. The small number of Galactic stars expected in the WFC fields means that foreground contamination is not a problem.

Some faint background galaxies may have been mis-identified as stars in the DAOPHOT/ALLFRAME reductions. The deep galaxy counts of Smail et al. (1995) [134] suggest that 19 ± 2 background galaxies with $20 \leq I \leq 24$ and 168 ± 20 galaxies with $24 \leq I \leq 27$ should be located in each of the two fields. Typical galaxies have colours of $(V-I) \simeq 1.0$ so background galaxies are indistinguishable, by colour, from stars in a CMD. The small expected number of galaxies with $I \leq 24$ suggests that background galaxies are not making a significant contribution to the morphology of the red-giant branch. The blue end of the horizontal branch is ~ 1 mag bluer than typical background galaxies so the blue horizontal branch is not significantly contaminated by galaxies. The galaxy counts also suggest that for $I > 24$ background galaxies make up at most $2.9\% \pm 0.3\%$ of the objects on the G302 field CMD. In the G312 field background galaxies can account for up to $10.4\% \pm 1.2\%$ of the objects on the CMD. DAOPHOT/ALLFRAME will discard objects that are not morphologically similar to the stellar PSF for the frame in question so many of the faint background galaxies will already have been discarded. Therefore mis-identified background galaxies are not significantly biasing the distribution of stars on the CMDs.

A third potential source of contamination is the disk of M31 itself. Mould & Kristian (1986) [101] used the surface photometry of de Vaucouleurs (1958) [42] to estimate that the disk-to-halo ratio in a field $\sim 35'$ from the centre of M31 along the southeast minor axis was $\lesssim 0.014$. Pritchet & van den Bergh (1988) [113] compared star counts in

Chapter 6

HST Observations of the Halo of M31

6.1 Colour–Magnitude Diagrams

6.1.1 Contamination in the Field

Figures 6.1 and 6.2 show the $(I,(V-I)_0)$ CMDs for the halo fields around the M31 globular clusters G302 and G312 respectively. No culling has been applied to these CMDs beyond that done to identify real stellar images, as described in Chapter 4.3. The CMDs have been dereddened and corrected for interstellar absorption as described in Chapter 4.3.

The CMDs of the M31 halo contain contamination from Galactic halo stars. Galactic M-dwarfs have colours of $(V-I) \sim +1.5$ to $+3$ so they will appear to the red of the red-giant branch while main-sequence stars and horizontal branch stars in the Galaxy will appear to the blue of M31's red-giant branch. Star count models of the Galaxy in the direction of M31, from Ratnatunga & Bahcall (1985) [116], suggest that there will be $\sim 14 \pm 4$ stars redder than the red giants and $\sim 1 \pm 1$ stars bluer than the red giants between $21 \leq V \leq 27$ in each of the WFC fields. Galactic field star contamination,

Name	Ground-Based		PC2	WFC
	r_t^{d}	r_t^{e}	r_t^{g}	r_t^{h}
G58	...	...	9.″64	...
G105	...	...	9.″64	...
G108	18.″27	...	12.″32	...
G219	...	...	13.″93	...
G302	...	11.″89	...	10.″21
G312	9.″86	10.″30	...	9.″58

d – Cohen & Freeman (1991) [30]
e – this work
g – Grillmair et al.(1996) [58]
h – this work

Table 5.6: A comparison of tidal radii derived from ground-based and *HST* observations.

Name	Ground-Based					FOC	PC2	WFC
	r_c^{a}	r_c^{b}	r_c^{c}	r_c^{d}	r_c^{e}	HWHM^{f}	r_c^{g}	r_c^{h}
G2	...	...	...	...	0.″11	0.″03	...	...
G11	...	...	...	...	...	0.″07	...	...
G58	0.″19	0.″23	...	...	...	0.″14	0.″17	...
G64	0.″35	0.″26	1.″11	...	...	0.″04	...	...
G78	0.″51	0.″62	0.″91	...	...	0.″08	...	...
G105	...	...	...	...	...	0.″05	0.″09	...
G108	0.″25	0.″33	...	1.″02	...	...	0.″25	...
G219	...	...	...	...	...	...	0.″87	...
G244	0.″22	0.″36	...	...	...	0.″03	...	...
G272	0.″38	0.″68	...	...	...	0.″04	...	...
G302	0.″29	0.″29	...	...	0.″18	...	...	0.″20
G305	...	0.″20	...	...	...	0.″04	...	...
G312	...	...	...	0.″84	0.″14	...	...	0.″20
G319	...	...	...	...	...	0.″05	...	...
G322	...	0.″23	...	...	...	0.″04	...	...
G352	...	...	...	...	...	0.″07	...	...
Bo289	...	...	...	...	...	0.″03	...	...

a – Battistini et al.(1982) [7]
b – Crampton et al.(1985) [33]
c – Davoust & Prugniel (1990) [38]
d – Cohen & Freeman (1991) [30]
e – this work
f – Fusi Pecci et al.(1994) [57]
g – Grillmair et al.(1996) [58]
h – this work

Table 5.5: A comparison of core radii derived from ground-based and *HST* observations.

globular clusters in the M31 system unless some sort of adaptive optics system is used to reduce the seeing to $\lesssim 0\farcs1$.

An examination of Table 5.6 shows that the tidal radii measured from images taken with ground-based telescopes are similar to those measured from images taken with the *HST*. The tidal radii that were derived for G302 and G312 using the CFHT data presented in Chapter 3 are within ~10% of the tidal radii that were derived using *HST* data. Assuming a distance of 725 kpc for the M31 globular clusters gives tidal radii of ~ 35 to ~ 50 pc, comparable to the tidal radii of typical Galactic globular clusters. This suggests that ground-based telescopes, operating under conditions of sub-arcsecond seeing, can obtain reliable tidal radii for M31 globular clusters

is probably due to differences in the methods of determining the core radius and accounting for seeing. Battistini et al. (1982) [7] and Crampton et al. (1985) [33] derived their core radii indirectly from the observed half-width of the cluster at one-quarter of its maximum intensity and compared these values to seeing-convolved King models. Cohen & Freeman (1991) [30] fit seeing-convolved King (1962) [83] models directly to the portion of the one-dimensional surface brightness profile between $1''.3$ and $2''.7$ from the centre of the cluster. This means that the Cohen & Freeman (1991) [30] fits do not include the cores of the clusters, where the effects of seeing are strongest. Therefore these results are given less weight in this thesis than the Battistini et al. (1982) [7] and Crampton et al. (1985) [33] results are.

The core radii for G64 and G78 obtained by Davoust & Prugniel (1990) [38] are two to four times larger than those obtained by Battistini et al. (1982) [7] and Crampton et al. (1985) [33]. They used a similar technique to what Battistini et al. (1982) [7] and Crampton et al. (1985) [33] used to determine core radii but their study suffered from a large pixel size ($0''.324$) and poor seeing (particularly for G64). Therefore the Davoust & Prugniel (1990) [38] results will be given less weight in the following discussion.

If the Cohen & Freeman (1991) [30] data and the Davoust & Prugniel (1990) [38] data is discarded then the published ground-based measurements of core radii for M31 globular clusters have overestimated the core radii of most M31 globular clusters by factors of approximately two to ten. This is due to the core radius being smaller than the radius of the seeing disc for the ground-based observations. However, the core radii presented in Chapter 3 of this thesis agree with core radii obtained from *HST* observations. Table 5.5 shows that ground-based observations can give reasonable estimates of the core radius *only if* seeing is compensated for in a physically realistic manner *and* if the core radius is at least ~ 0.25 times the FWHM of the seeing disc (G58, G108, G302, and G312). This suggests that ground-based observations can not obtain reliable core radii for the

the distance of M31 and used these to derive a relation between $W_{1/4}$ and r_c. Crampton et al. (1985) [33] used a similar technique to derive core radii for 509 globular cluster candidates in the M31 system. Davoust & Prugniel (1990) [38] derived a relation between the observed HWHM and the King core radius by convolving King models with their seeing profiles. They used this relation to estimate core radii for several clusters in the M31 system. Cohen & Freeman (1991) [30] fit seeing-convolved two-dimensional King (1962) [83] profiles to 30 globular clusters to determine their core and tidal radii.

Table 5.5 lists the published core radii for all the M31 globular clusters that have been observed with the *HST*. The core radii have been converted to arcseconds. Similarly Table 5.6 lists the published tidal radii for M31 globular clusters that have been observed with the *HST*.

The core radii derived for G302 and G312 using the CFHT data are within 30% of the core radii for these globular clusters that were measured using the *HST* data. The CFHT data for G2 gives a core radius that is 2.7 times larger than the value derived by Fusi Pecci et al. (1994) [57] by deconvolving pre-refurbishment FOC images. It is tempting to argue that the complexity of the pre-refurbishment FOC PSF, and the uncertainties inherent in non-linear deconvolution, make the Fusi Pecci et al. (1994) [57] core radius unreliable. However, the CFHT images of G2 have exposures of only 100 seconds, and there are two bright stars located near G2, so it is more likely that the core radius that was derived for G2 in Chapter 3 is in error. Further support for the Fusi Pecci et al. (1994) [57] value comes from noticing that the pre-refurbishment and post-refurbishment core radius for G58 are in reasonable agreement with each other. The discrepancy between the pre- and post-refurbishment core radii for G105 is probably due to the presence of a collapsed core in that globular cluster (Bendinelli et al. 1993 [8]).

The core radii obtained for G108 and G312 by Cohen & Freeman (1991) [30] are four to six times larger than those obtained for the same clusters by other groups. This

5.6 A Comparison of the CFHT and *HST* Results

There have been several attempts made to determine core and tidal radii of globular clusters in M31 using data from ground-based telescopes. To investigate how successful these attempts have been I have compared the structural parameters obtained from the ground-based results presented in Chapter 3 to those derived from the *HST* data presented in this chapter. At present there are seventeen globular clusters in M31 that have had their structural parameters derived from *HST* data; six of these have used the post-refurbishment WFPC2 while the rest used FOC data taken before the installation of the Corrective Optics Space Telescope Axial Replacement (COSTAR) package.

The FOC results are from Fusi Pecci et al. (1994) [57]. They used three image restoration techniques to correct for the pre-refurbished FOC's PSF and measured the HWHM of the deconvolved cluster surface brightness profiles. The HWHM is approximately equal to the King core radius. Table 5.5 contains a list the HWHM for each globular cluster obtained by averaging the HWHMs obtained from each of their three deconvolution methods. The typical standard deviation between the HWHM estimates for each globular cluster is $\sigma \sim 0.03$. The PC results for four of the globular clusters (G58, G105, G108, and G219) are from GAF while the data for G302 and G312 were obtained with the WFC and are presented in this thesis.

The structural parameters obtained using ground-based data are taken from Battistini et al. (1982) [7], Crampton et al.(1985) [33], Cohen & Freeman (1991) [30], and this thesis. Battistini et al. (1982) [7] fit a Moffatian with $\beta = 2$ and $\gamma = 2$ to each M31 globular cluster then defined a quantity $W_{1/4}$ (= the half-width of the Moffatian profile at one-quarter of the central intensity = the Moffatian parameter α when $\beta = \gamma = 2$). They then scaled the surface brightness profiles of several Galactic globular clusters to

Using this model, and the observed radial velocity and perigalactic distance of G302 I found that the orbit of G302 has an eccentricity of $e \equiv (d_a - d_p)/(d_a + d_p) = 0.65$ where d_a is the apogalactic distance (in kpc) for G302. This value assumes that all of the space velocity of G302 is along the line-of-sight and gives G302 an apogalactic distance of $\theta_a = 2\overset{\circ}{.}5$ or $d_a = 31.5$ kpc If 40% of G302's space velocity is assumed to be in the plane of the sky then the orbital parameters become $e = 0.71$ and $d_a = 37.0$. Since G302's radial velocity is faster than 95% of the radial velocities of other M31 globular clusters it is unlikely that more than $\sim 5\%$ of G302's space velocity is tangential to the line-of-sight. If this is the case then the orbital eccentricity for G302 is $0.65 \lesssim e \lesssim 0.66$ and the apogalactic distance is $d_a = 31.5$ kpc. The period of G302's orbit was defined to be twice the time required for the globular cluster to move from its perigalacticon to its apogalacticon. If all of the globular cluster's space velocity is along the line-of-sight then the orbital period is $P = 0.42$ Gyr. If 40% of the space velocity is tangential to the line-of-sight then $P = 0.52$ Gyr.

5.5.3 The Orbit of G302

HBK measured a heliocentric radial velocity of -8 ± 32 km·s^{-1} for G302. Correcting for Rubin & Ford's (1970) [124] 21 cm velocity for M31 ($v_{\mathrm{M31}} = -297$ km·s^{-1}) gives G302 a radial velocity of $v = +289 \pm 32$ km·s^{-1} relative to the centre of M31. This is one of the fastest radial velocities observed for a globular cluster in M31 which suggests that almost all of G302's space velocity is along the line-of-sight. This can only occur when G302 is near its perigalactic passage. Since very little of G302's space velocity is in the plane of the sky, and G302 is near its perigalacticon, G302 must be at approximately the same distance from the Earth as the centre of M31. This means that the distance measured on the sky between G302 and the centre of M31 is approximately the true separation; so the perigalactic distance for G302 is $\theta_p \simeq 32\overset{\prime}{.}1$ corresponding to $d_p \simeq 6.77$ kpc assuming a distance modulus of $\mu_0 = 24.3$ for M31.

In order to constrain the orbit of G302 a three-component model for the M31 potential was used. The disc was modeled by a Miyamoto & Nagai (1975) [99] potential, the bulge by a Hernquist (1990) [67] potential, and the halo by a spherical logarithmic potential:

$$\Phi_{\mathrm{disc}} = \frac{-G\mathcal{M}_{\mathrm{disc}}}{\sqrt{R^2 + \left(a + \sqrt{z^2 + b^2}\right)^2}}, \tag{5.6}$$

$$\Phi_{\mathrm{bulge}} = \frac{-G\mathcal{M}_{\mathrm{bulge}}}{r + c}, \tag{5.7}$$

$$\Phi_{\mathrm{halo}} = V_{\mathrm{halo}}^2 \ln(r^2 + d^2) + \ln(C). \tag{5.8}$$

I adopted $\mathcal{M}_{\mathrm{disc}} = 2.0 \times 10^{11} \mathcal{M}_{\odot}$, $\mathcal{M}_{\mathrm{bulge}} = 6.8 \times 10^{10} \mathcal{M}_{\odot}$, $a = 7.8$ kpc, $b = 0.31$ kpc, $c = 0.84$ kpc, $d = 14.4$ kpc, and $V_{\mathrm{halo}} = 128$ km·s^{-1}. These parameters were chosen by scaling the Galactic values to the observed mass and diameter of M31. The constant, C, in Equation 5.8 contains the units required to make the equation dimensionally correct.

5.5.2 Mass Loss from G312

Using the methods described above I find that G312 has a mass of $\mathcal{M} = (0.60 \pm 4.70) \times 10^4 \mathcal{M}_{\odot}$ beyond its fitted isotropic Michie–King tidal radius ($r_t = 9\farcs55$). The large uncertainty in the amount of mass beyond the tidal radius is due to the large uncertainties in the surface brightness profile at large radii. Figure 5.15 does not show any evidence for an extended halo of stars around G312 so it is likely that the light seen beyond the fitted tidal radius in Figure 5.13 is due to low-level variations in the unresolved background light. Alternately, it is possible that the use of multi-mass Michie–King models would result in a larger tidal radius. If I assume that the observed excess of light in Figure 5.13 is due to an extended halo of stars then the mass-loss rate required is $\dot{\mathcal{M}} = 430 \pm 3360\, \mathcal{M}_{\odot}/\mathrm{Gyr}$, approximately 10% of the mass-loss rate from G302. G312 has a half-mass relaxation time of $t_{r,h} = 0.29 \pm 0.02$ Gyr so the escape rate per relaxation time is $\dot{r} = (0.38 \pm 2.95) \times 10^{-3}$. While this is consistent with Oh & Lin's (1992) [103] theoretical values the large uncertainties in the photometry near the tidal radius of G312, and thus the large uncertainty in the computed escape rate, suggests that the observed escape rate is consistent with there being no observable mass-loss from G312.

globular cluster. Following Djorgovski (1993) [43] I adopted $\langle \mathcal{M}_{\star} \rangle = 1/3\mathcal{M}_{\odot}$. The half-mass radius obtained by fitting isotropic Michie–King models to G302 is $r_h = 1.9 \pm 0.1$ pc which gives a half-mass relaxation time of $t_{r,h} = 0.49 \pm 0.04$ Gyr. This yields a projected escape rate of $\dot{r} = (2.3 \pm 0.9) \times 10^{-3}$ per half-mass relaxation time.

Converting observed surface brightnesses to a deprojected mass profile involves solving an Abel integral which contains the radial derivative of the surface brightness distribution. Since the surface brightness data for G302 contains noise this inversion is inherently unstable. Therefore, I chose to project the theoretical escape rates of Oh & Lin (1992) [103] into the plane of the sky before comparing them to the observed escape rate. The Oh & Lin (1992) [103] evaporation rates for isotropic globular clusters with ages of $t_0 \sim 30 t_{r,h}$ in the Galactic potential then become $\sim 10^{-3}$ to 10^{-2} per relaxation time. This is comparable to the escape rate inferred from the data. This result further strengthens my claim to have detected an extended halo of unbound stars around G302.

5.5 Mass Loss and the Orbit of G302

5.5.1 Mass Loss from G302

Figures 5.12 and 5.14 show that there is an excess of both light and stars beyond the tidal radius of the best-fitting Michie–King model for G302. By computing the amount of mass beyond the tidal radius the mass-loss rate for G302 can be estimated. The V-band surface brightness profile for G302 was converted to a projected mass profile using a mean mass-to-light ratio of $\Upsilon_V = 1.9$ Solar units (from Dubath & Grillmair 1997 [47]). The total mass inside the Michie–King tidal radius ($r_t = 10''$) was $\mathcal{M} = (8.89 \pm 0.06) \times 10^5\,\mathcal{M}_\odot$. The total mass of G302 was estimated by applying the mass-to-light ratio to the total integrated V-band magnitude of G302 ($V = 14.90$, from HBK). This gave a mass of $\mathcal{M}_{\rm tot} = (9.52 \pm 0.24) \times 10^5\,\mathcal{M}_\odot$ which gives a total mass of $\mathcal{M} = (0.63 \pm 0.25) \times 10^5\,\mathcal{M}_\odot$ beyond the formal tidal radius of G302. Mass-segregation within a globular cluster can result in Υ_V increasing with radius so the total mass beyond the tidal radius that is derived here will be a lower limit on the true mass in the extended halo around G302.

If G302 has an age of $t_0 = 14$ Gyr, and a constant rate of mass loss is assumed, then the mass-loss rate required for the observed amount of mass to escape beyond the Michie–King tidal radius is $\dot{\mathcal{M}} = 4500 \pm 1800\,\mathcal{M}_\odot/\mathrm{Gyr}$. The relaxation time at the half-mass radius for a globular cluster is given by (Spitzer 1987 [136]):

$$t_{r,h} = 8.933 \times 10^5 (\mathrm{yr}) \frac{\mathcal{M}_{\rm cl}^{1/2}\, r_h^{3/2}}{\langle \mathcal{M}_\star \rangle \ln(0.4 N_\star)}, \tag{5.5}$$

where $\mathcal{M}_{\rm cl}$ is the total mass of the globular cluster in Solar masses, r_h is the half-mass radius of the globular cluster in pc, $\langle \mathcal{M}_\star \rangle$ is the mean mass of the stars in the globular cluster in Solar masses, and $N_\star \equiv \mathcal{M}_{\rm cl}/\langle \mathcal{M}_\star \rangle$ is the estimated number of stars in the

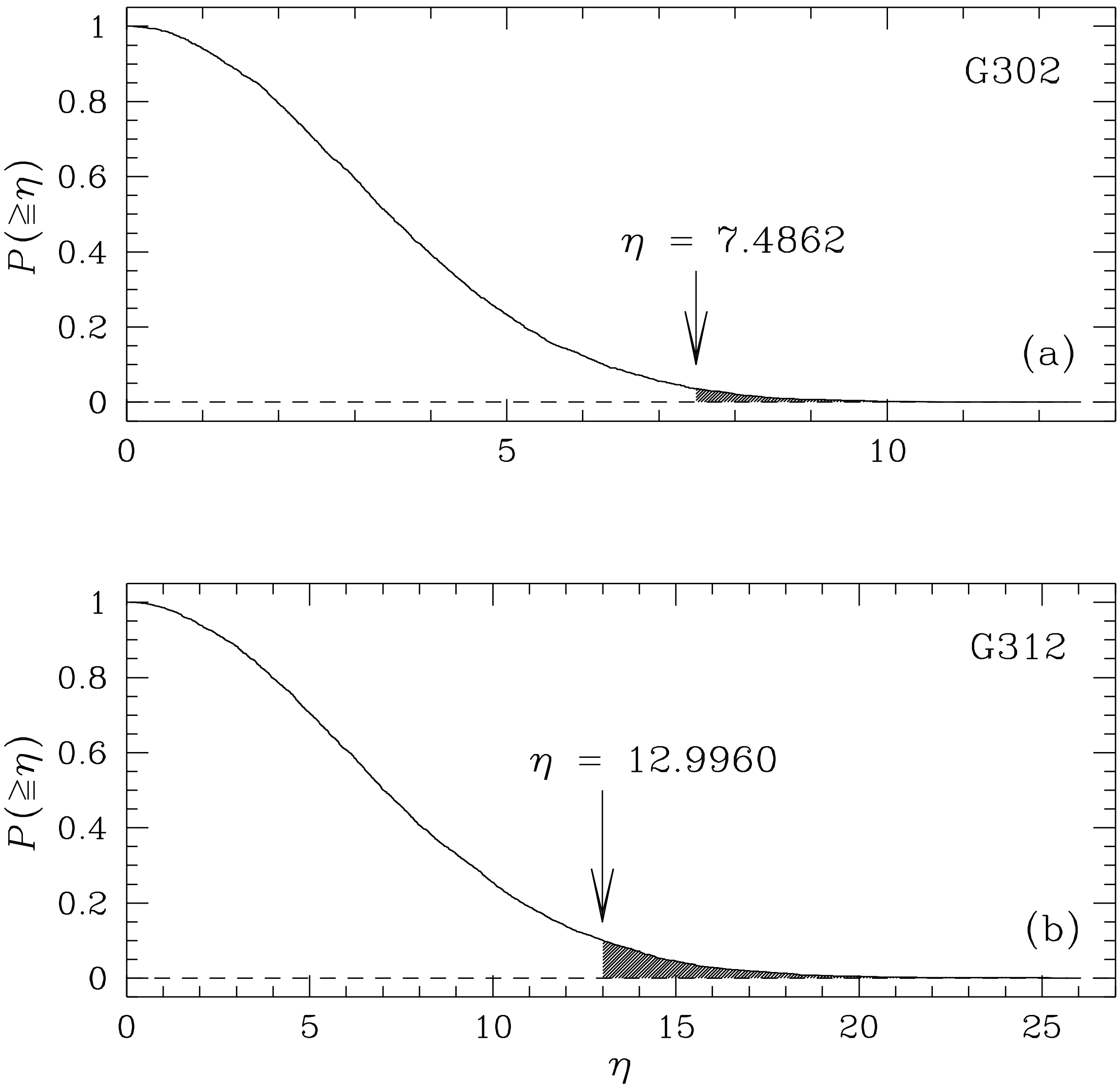

Figure 5.18: This figure shows the cumulative probability distributions for observing a particular value of η by chance if the observed distribution of stars was drawn from a circularly symmetric distribution of stars. The two distributions are different because the fields around G302 and G312 contain different numbers of stars.

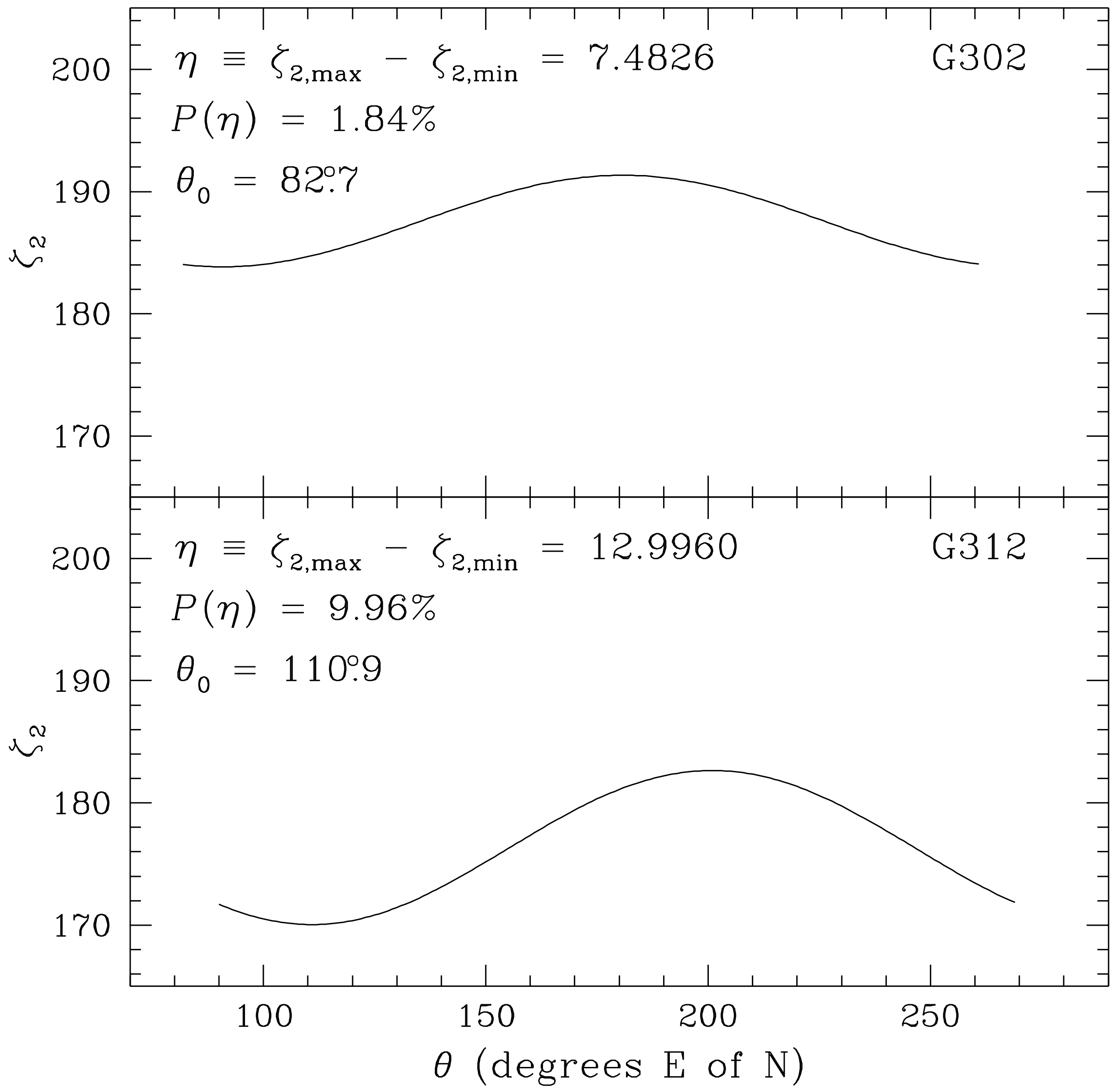

Figure 5.17: The upper panel shows the value of ζ_2 as a function of position angle for G302 while the lower panel shows ζ_2 as a function of position angle for G312.

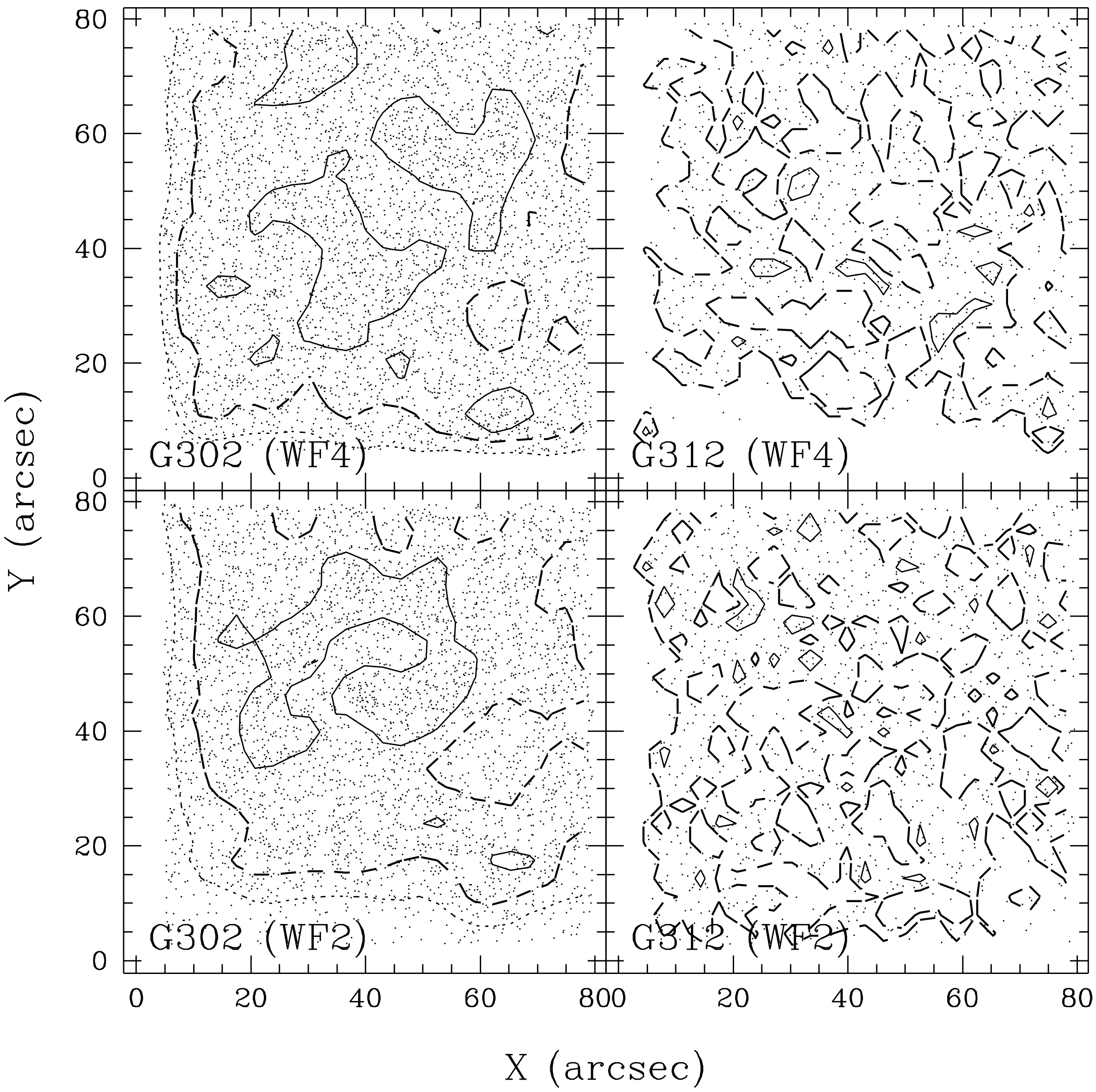

Figure 5.16: This figure shows isodensity contours for the WF2 and WF4 fields for G302 and G312. The contour intervals are the same as for Figures 5.14 and 5.15.

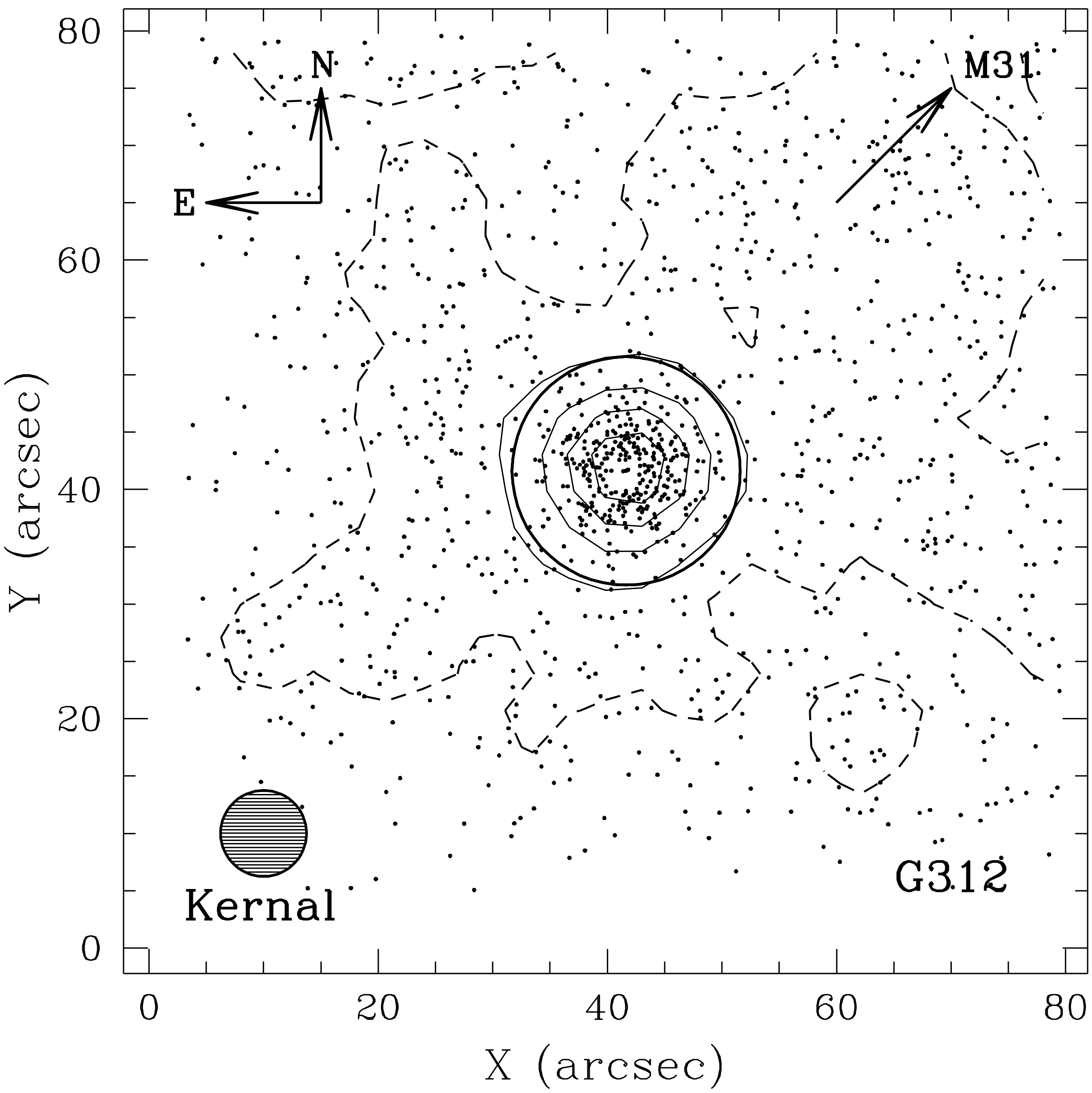

Figure 5.15: The solid circle represents the fitted Michie–King tidal radii of G312. The dashed contour represents the surface density of stars in the M31 halo at the location of G312 ($= \Sigma_{\rm bkgd} = 0.1688$ stars/$\Box'$). The solid contours are $\Sigma = 0.4, 0.8, 1.2, 1.6$ stars/$\Box'$. The innermost contours have not been plotted for clarity.

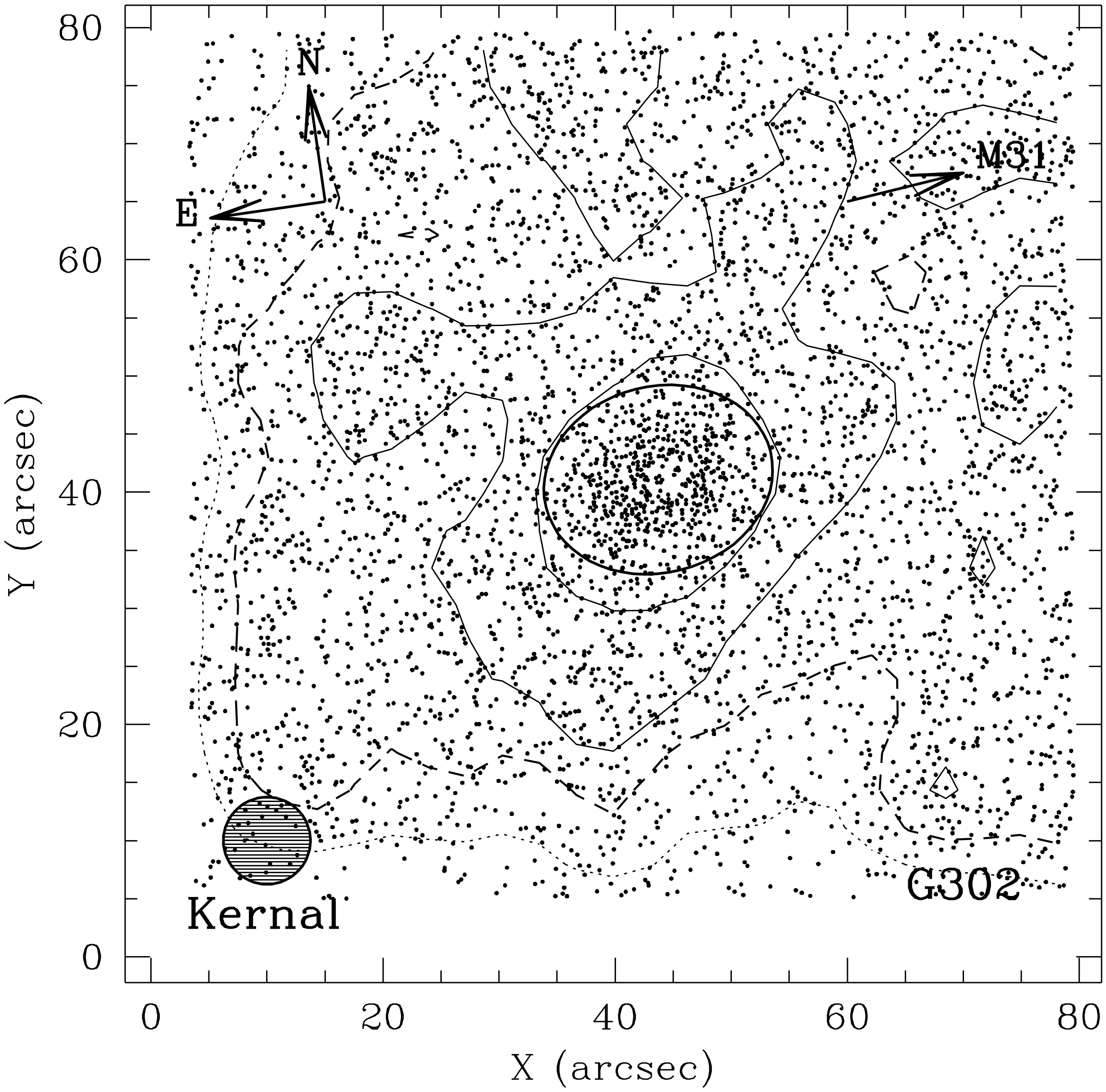

Figure 5.14: The solid ellipse is the fitted Michie–King tidal radius for G302. The dashed contour represents the surface density of stars in the M31 halo at the location of G302 ($= \Sigma_{\rm bkgd} = 0.6196$ stars/$\Box'$). The solid contours are $\Sigma = 0.8, 1.2$ stars/$\Box'$ and the dotted contour is $\Sigma = 0.4$ stars/$\Box''$. The outermost contours are strongly influenced by the size of the WF3 CCD. The contours inside the fitted tidal radii have not been plotted for clarity. The arrow points towards the centre of M31.

field around G302. This data formed the cumulative probability distributions shown in Figure 5.18.

For G302 this analysis yields $\eta = 7.4826$, which occurs at a position angle for the major axis of the extended halo of $83°(= -97°)$ east of north. The Monte-Carlo tests indicate that there is only a 1.84% chance of obtaining this value of η in a random star field. This corresponds to the extended halo being real at the 2.5σ level. In contrast, the WF2 and WF4 fields near G302 yielded η values of 3.5530 and 4.6618 corresponding to 38.47% and 20.62% chances respectively of occurring by chance. The orientation of the extended halo around G302 is 10° to the west of the projected major axis of G302 as observed in the V-band and 26° west of the projected major axis for the globular cluster as observed in the I-band. In light of the lack of coherent overdensities in any of the background images or simulated images, the results of the moment analysis, and the observed overdensity of stars beyond the tidal radius of the best-fitting Michie–King model, I believe that the extended asymmetric halo around G302 that is seen in Figure 5.14 is a real feature of G302.

Since the probability of observing a given value of η by chance depends on the number density of stars on the image, I performed a separate series of 10,000 Monte-Carlo simulations for the G312 data. The resulting probability distribution indicated that the observed value of $\eta = 12.9960$ for the stars beyond the tidal radius G312 in the WF3 field had a 9.96% chance of occurring in a randomly distributed set of stars. The WF2 and WF4 fields around G312 have η values of 9.6342 and 9.1801 respectively, corresponding to 27.65% and 30.73% probabilities of occurring at random. From this, and the lack of a significant excess of stars beyond the tidal radius of the best-fitting Michie–King models, suggests that G312 does not exhibit any evidence for having an extended halo of stars. However, it is possible that such a halo does exist and is aligned along the line-of-sight.

random distribution of stars could give rise to coherent structures that could be mistaken for an extended halo I constructed a series of random star fields with number densities comparable to those found in the G302 and G312 background fields. None of these artificial star fields showed evidence for coherent sub-structure. In addition I used Michie–King surface density profiles to place artificial stars onto randomly generated star fields to see if the presence of a globular cluster would bias the binning/smoothing/contouring process in favour of finding structure beyond the tidal radius when none was really present. None of the Monte-Carlo images showed any evidence for extended halos.

In order to quantify the orientation of the halo around G302 I computed the second moment of the distribution of stars beyond the tidal radius ($r_t \simeq 10''$) determined from fitting Michie–King models to G302 (see Chapter 5.3.3). Only stars between $10''$ and $35''$ from the centre of the globular cluster were used to ensure that neither the globular cluster, nor the edges of the CCD, biased the sample. I computed the statistic $\zeta_2 = \sqrt{\frac{1}{N}\sum_{i=1}^{N} y_i^2}$ where N is the number of stars beyond the tidal radius and y_i is the distance from the i^{th} star to an arbitrary axis of symmetry for the globular cluster. This statistic corresponds to the root-mean-square distance between the stars and the axis of symmetry so the value of ζ_2 will be at its minimum when the assumed axis of symmetry coincides with the true major axis of the distribution. I computed ζ_2 for angles of symmetry between 0° and 180°. This data is shown in Figure 5.17. A second statistic, $\eta \equiv \zeta_{2,\max} - \zeta_{2,\min}$, gives a measure of the degree of symmetry in the distribution of stars about the centre of the globular cluster. The greater the value of η, the greater the deviation from a circular distribution of stars. For a perfectly circular distribution ζ_2 would be the same for all angles, resulting in $\eta = 0$. In order to determine the probability of getting the observed value of η by chance from a random distribution of stars I generated 10,000 sets of stellar coördinates and determined η for each set. The stellar coördinates were randomly drawn from a circular distribution of stars with the same size and number density as the

a balance between the need to keep the bin sizes small compared to the width of the Gaussian and the need to have a large number of data-points in each bin to reduce Poisson noise in the bin. Since I am searching for overdensities of stars beyond the Michie–King tidal radii of the globular clusters the assumption that globular cluster can be approximated by a Gaussian will lead to an underestimate of the bin size needed to maximize the signal-to-noise. After some experimentation I found that bin sizes of 32 pixels ($\simeq 3\farcs2$), approximately two to three times the computed optimal size for Gaussians, provided the best signal-to-noise ratio for the data. I then smoothed the resulting binned data by convolving it with a unit Gaussian with a dispersion equal to the bin size ($\sigma = 3\farcs2$). The resulting stellar number density distribution for G302 is shown in Figure 5.14 and the stellar number density distribution for G312 is shown in Figure 5.15.

Figure 5.14 shows an asymmetric overdensity of stars around G302 extending to at least twice the Michie–King tidal radius. The coherence of the isodensity contours that lie beyond the tidal radius, but inside the background contour, suggest that observed overdensities are not an artifact of the binning, smoothing, or contouring processes. The surface brightness profile of G302 (see Figure 5.12) light beyond the tidal radius ($r_t \sim 10''$) of the globular cluster is in agreement with the asymmetric halo of stars seen in Figure 5.14. The surface brightness profile of G312, however, is consistent with there being no light beyond the tidal radius ($r_t \sim 10''$). This is reflected in the lack of an extended halo of stars in Figure 5.15. The fact that an overdensity of stars is seen beyond the tidal radius of G302, but not beyond the tidal radius of G312, suggests that the overdensity is real and not an artifact of the analysis.

In order to check the reality of the observed halo surrounding G302 I carried out the contouring procedure on the star counts from the WF2 and WF4 images in the G302 and G312 fields. Figure 5.16 shows that no structures of comparable size to the halo around G302 are seen in any of the four background fields. To further test whether or not a

5.4 Extended Stellar Halos

GAF have observed an excess of resolved and unresolved stars beyond the formal Michie–King tidal radii of several globular clusters in M31, as would be expected if stars that have been stripped, or evaporated, from these globular clusters have remained in extended halos around those globular clusters. Another test for extended stellar halos is to identify an asymmetrical overdensity of stars in two dimensions beyond the formal tidal radius. This has been done for some Galactic globular clusters (see Grillmair et al.1995 GF95) using multiple Schmidt photographic plates for each globular cluster. However, it has not been attempted for any of the M31 globular clusters. In M31 the globular cluster, and the background, can be imaged on a single CCD. This eliminates possible systematic effects arising from comparing star counts across multiple fields. I have attempted to find such enhancements beyond the formal isotropic *and* anisotropic tidal radii of G302 and G312.

To search for extended halos around G302 and G312 I examined the two-dimensional distribution of stars beyond the tidal radii of each globular cluster. The total background stellar surface densities around each globular cluster were small ($\Sigma_{\rm bkgd} = 0.6191 \pm 0.0099$ stars/$\square''$ for G302 and $\Sigma_{\rm bkgd} = 0.1688 \pm 0.0052$ stars/$\square''$ for G312). The stellar positions were rebinned into "super-pixels" in order to ensure that there were enough stars in each bin that the Poisson fluctuations in a bin would be small compared to the total number of stars in that bin. In order to compute the optimum binning size I assumed that all the stars on the WF3 CCD were part of the globular cluster and that the globular cluster could be approximated by a Gaussian distribution of stars. It can be shown (Heald 1984 [64]) that for any Gaussian distribution the bin size, δx, which maximizes the signal-to-noise ratio in each bin is given by $\delta x \sim (20/N)^{1/5}\sigma$ where σ is the standard deviation of the Gaussian and N is the size of the sample. This technique provides

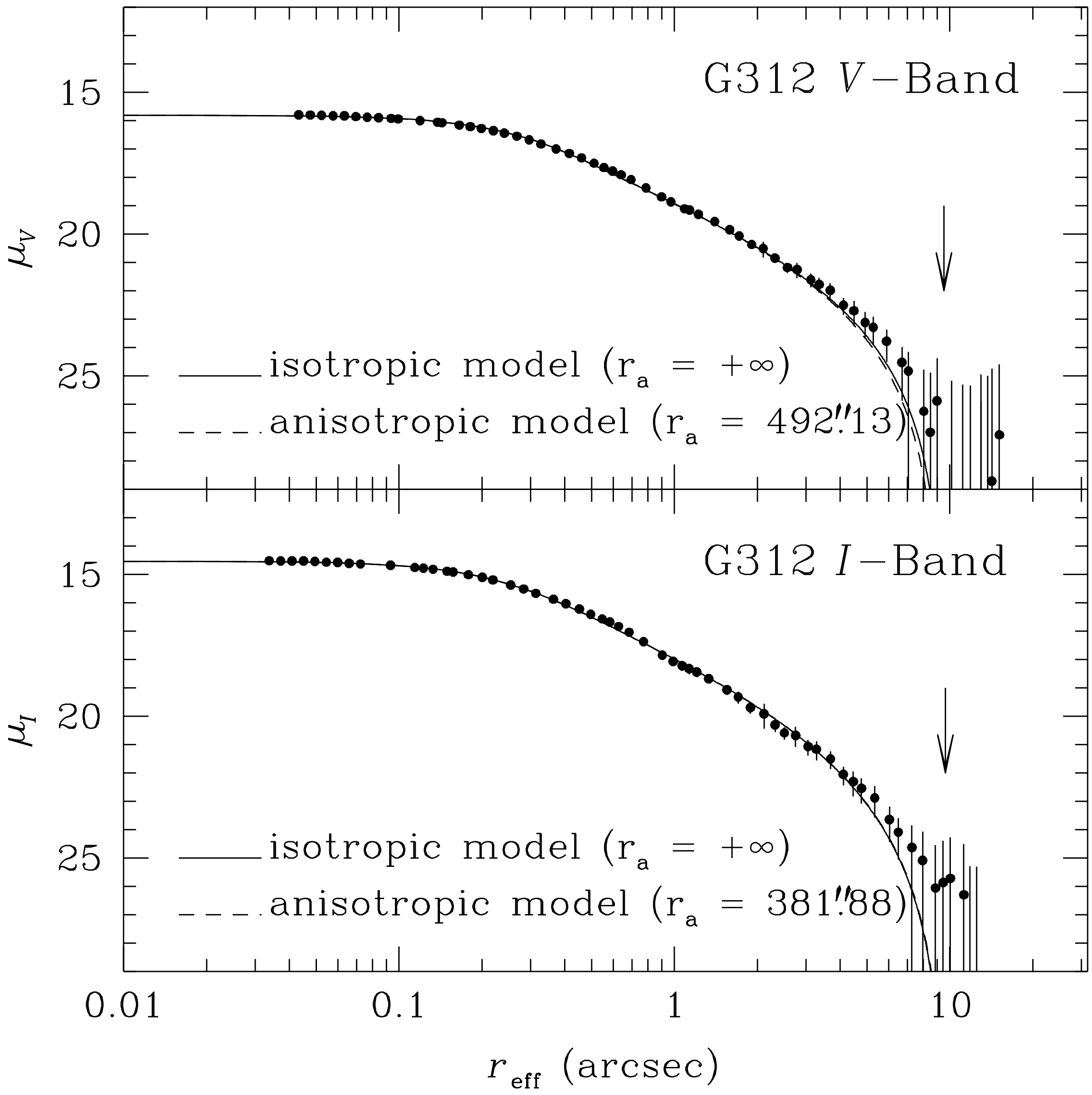

Figure 5.13: The solid points represent the observed surface brightness profiles of G312. The solid lines are the best-fitting isotropic Michie–King models and the dashed lines are the best-fitting anisotropic models. The arrows indicate the tidal radii for the isotropic models.

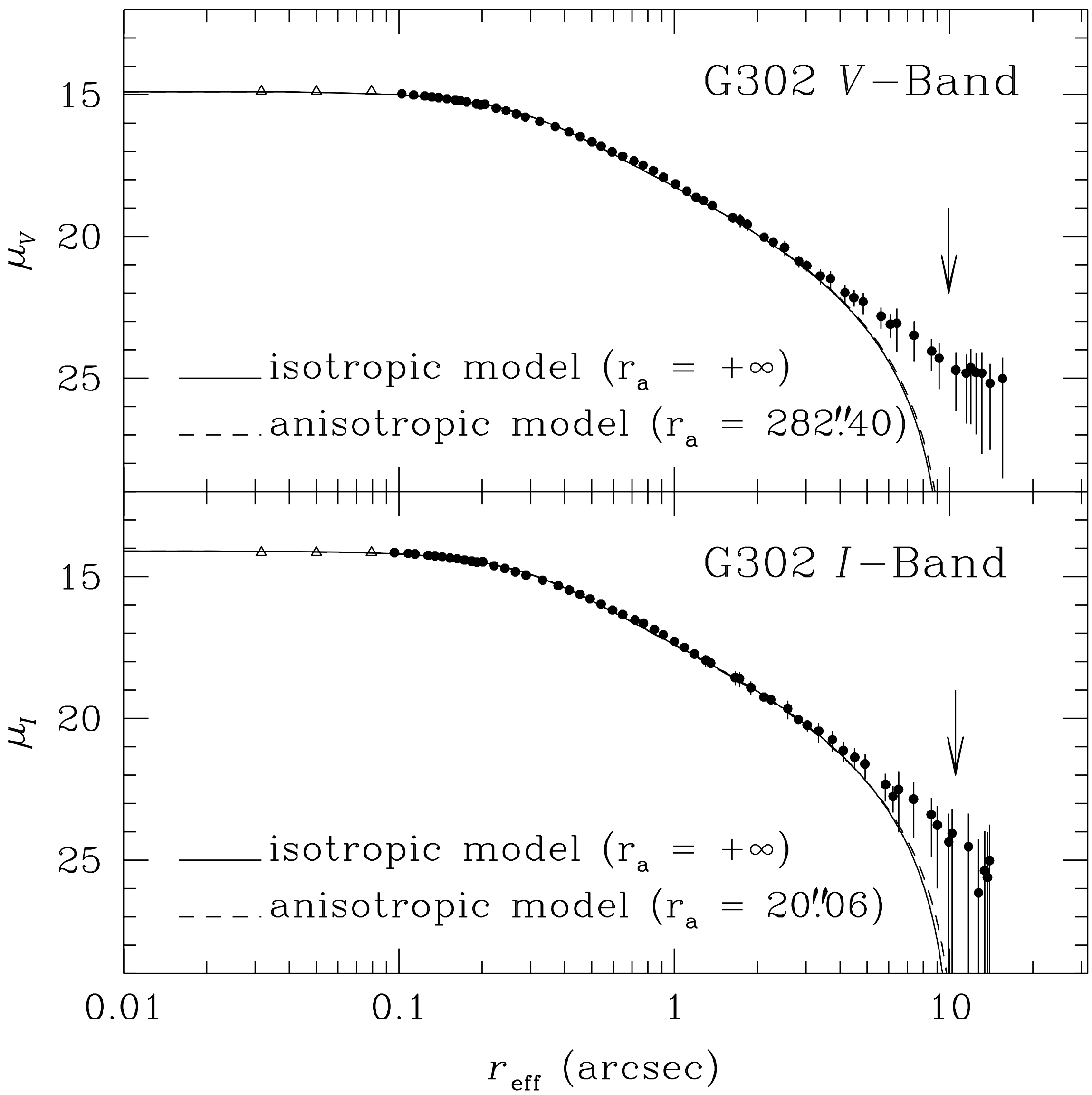

Figure 5.12: The solid points represent the observed surface brightness profiles of G302 while the open triangles in the inner 0.″1 indicate the surface brightnesses corresponding to saturation for the WF3 CCD (these points were not used in the fits). The solid lines are the best-fitting isotropic Michie–King models and the dashed lines are the best-fitting anisotropic models. The arrows indicate the tidal radii of the isotropic models.

globular clusters anisotropic Michie–King models were fit to each globular cluster. The results are listed in Table 5.4. In all cases the anisotropic models yield slightly larger χ^2_ν values than the corresponding isotropic models, which suggests that the isotropic models are formally better fits to the data than the anisotropic models are. Furthermore, the best-fitting anisotropy radii are greater than the fitted tidal radii for each globular cluster, which is physically meaningless. Therefore, I conclude that the overabundance of light at large radii is not due to velocity anisotropy. This supports the hypothesis that these globular clusters are surrounded by extended halos of unbounded stars.

Cluster	Filter	W_0	r_c	r_t	c	r_a	r_h	χ^2_ν	ν
G302	V	7.56	0\.″20	9\.″92	1.70	$+\infty$	0\.″52	1.827	49
		7.61	0\.″20	10\.″12	1.71	282\.″40	0\.″54	1.855	48
	I	7.65	0\.″20	10\.″49	1.73	$+\infty$	0\.″56	0.846	51
		7.47	0\.″21	9\.″80	1.67	20\.″06	0\.″49	0.906	48
G312	V	7.57	0\.″19	9\.″51	1.70	$+\infty$	0\.″53	0.839	53
		7.48	0\.″20	9\.″16	1.67	492\.″13	0\.″49	0.882	52
	I	7.46	0\.″21	9\.″64	1.67	$+\infty$	0\.″49	0.458	53
		7.47	0\.″21	9\.″70	1.67	381\.″88	0\.″49	0.467	52

Table 5.4: Best-fitting Michie–King models for G302 and G312 using the *HST* data.

MINUIT returns formal uncertainties of $\sim$ 5 to 10% on the Michie–King parameters. However, MINUIT was generally unable to compute a fully-accurate covariance matrix for the fitted parameters so MINUIT's uncertainty estimates are not reliable. Therefore, the uncertainties in the fits were estimated by generating a series of artificial globular clusters and fitting seeing-convolved Michie–King models to them in exactly the same way as was done for the real data. It was found that MINUIT tended to underestimate the uncertainties in the fits by a factor of between 1.5 and 2. This suggests the true 1σ uncertainties in the parameters are between $\sim$10 and 15% of the best-fit values of the parameters.

5.3.3 Michie–King Models

The tidal radii were determined by fitting Michie–King models to the observed surface brightness profiles of each globular cluster. The unresolved background light was measured by masking out a circle with a radius of 300 pixels ($\sim 3r_t$) centred on the globular cluster then fitting a plane to the remaining area on the WF3 CCD. Subtracting a plane resulted in residual variations of less than 1% across the WF3 CCD for both the G302 and G312 fields. There is no evidence for intensity or colour gradients in the unresolved background light.

Surface brightness profiles for each globular cluster were obtained in the same way as is described in Chapter 3.2.3. The higher resolution of the *HST* data meant that isophotes could be reliably fit to within $r_{\rm eff} = 0\farcs1$ of the centre of each globular cluster, allowing the core structure to be studied to a much higher degree of precision than is possible with the CFHT data described in Chapter 2. CERN's MINUIT (Version 94.1) was used to fit seeing-convolved one-dimensional Michie–King models to the data in the same manner as described in Chapter 3.2.3.

Each Michie–King model was convolved with the PSF for the WF3 CCD at the location of centre of the globular cluster. The central potential, W_0, King core radius, r_c, tidal radius, r_t, concentration, $c \equiv r_t/r_c$, anisotropy radius, r_a, and half-mass radius, r_h, were determined for G302 and G312 in the V- and I-bands. Table 5.4 gives the parameters of the best-fitting Michie–King models for each globular cluster. The V- and I-band surface brightness profiles, along with the best-fitting Michie–King models, are shown in Figures 5.12 and 5.13. The profiles for both globular clusters are well fit by isotropic Michie–King models out to $\sim 5''$. Beyond this distance from the centre of the globular cluster there is an excess of light over what is predicted by isotropic ($r_a = +\infty$) Michie–King models. In order to test if the excess light is due to velocity anisotropy in the

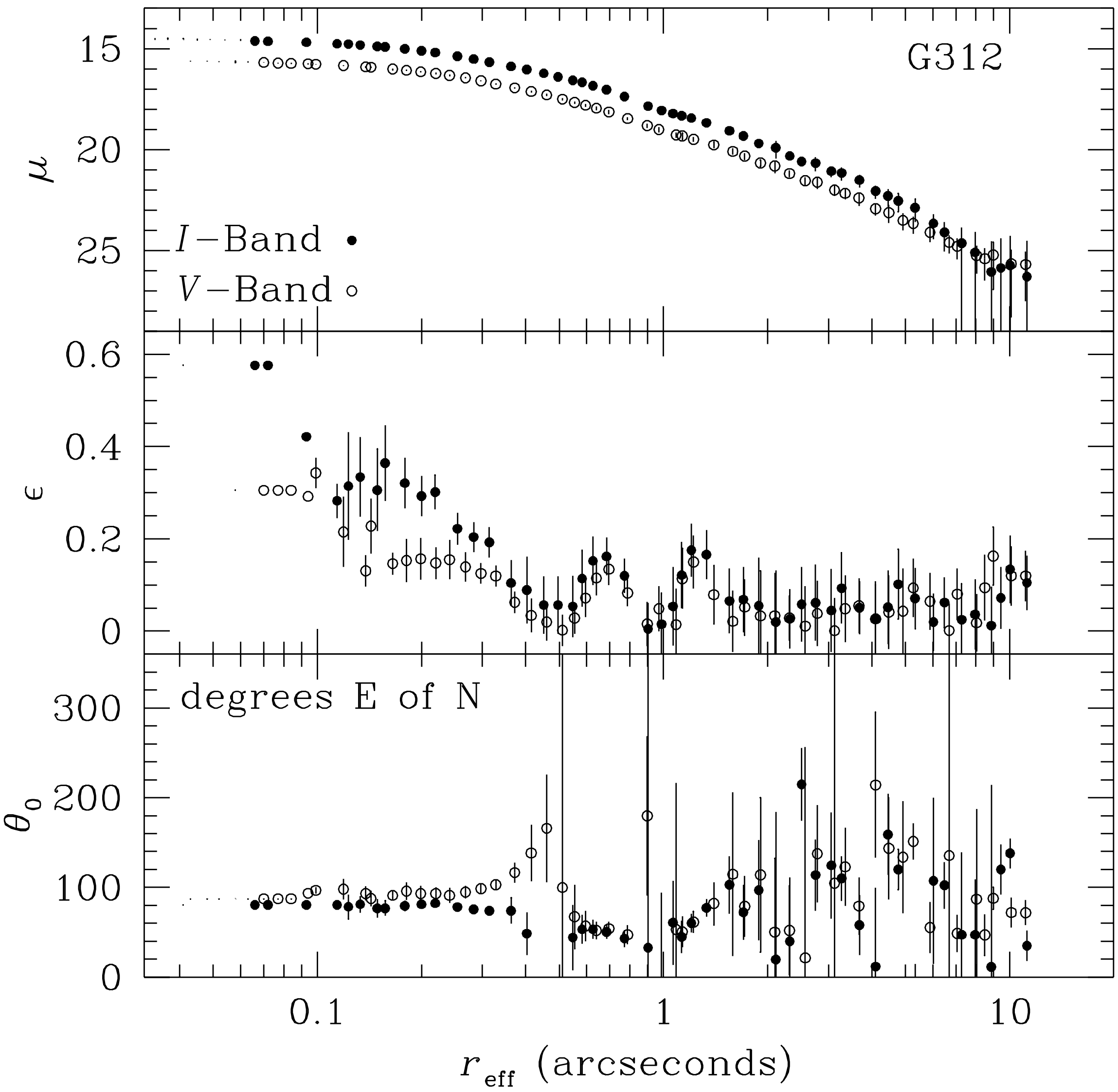

Figure 5.11: This figure shows the calibrated surface brightness profiles, ellipticity profiles, and orientation profiles for G312 in the V- and I-bands.

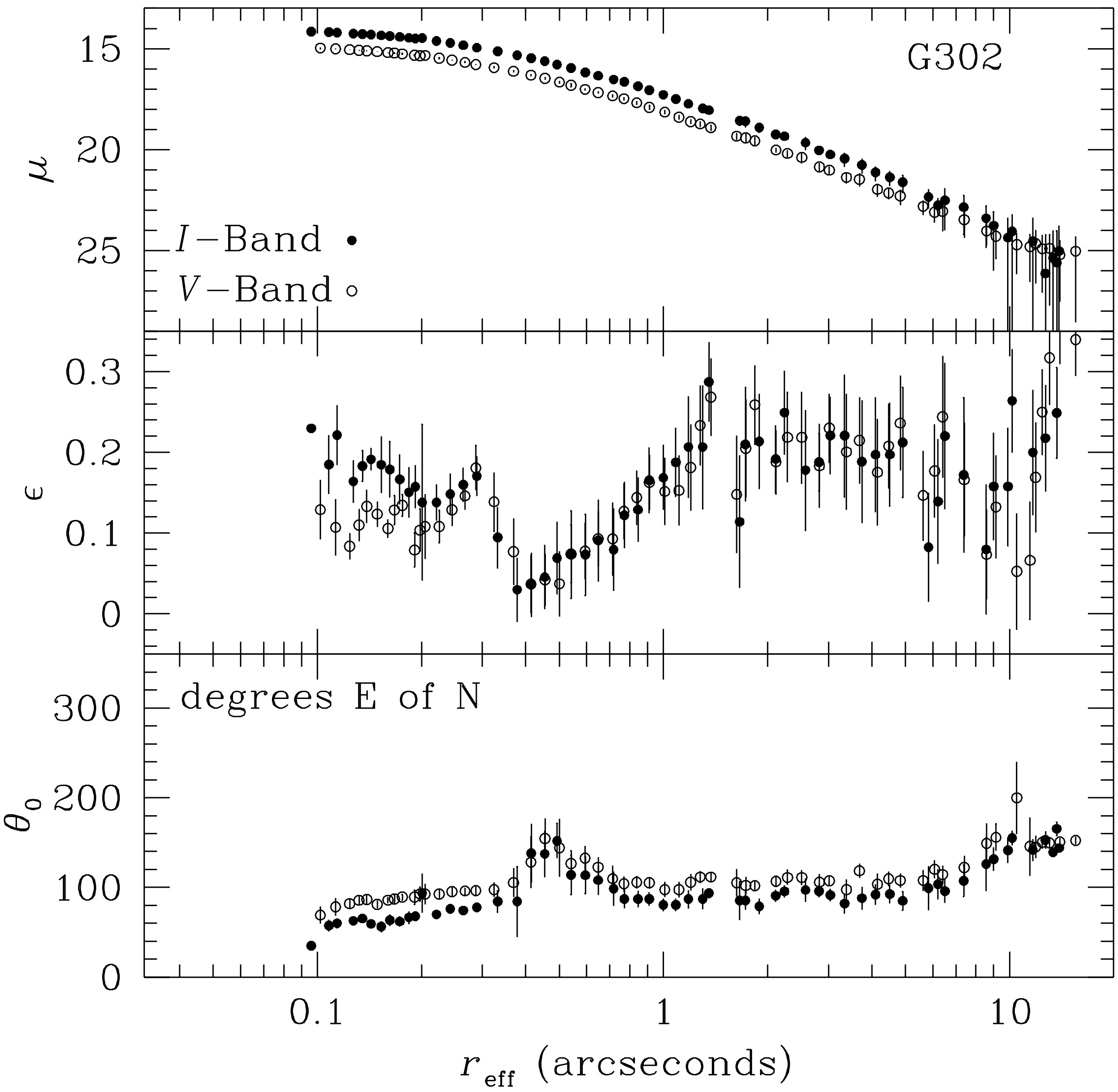

Figure 5.10: This figure shows the calibrated surface brightness profiles, μ, ellipticity profiles, ϵ, and orientation profiles, θ_0, for G302 in the V- and I-bands.

indicate that stochastic star placement can introduce an uncertainty in the ellipticity of between ± 0.01 and ± 0.05. In light of this there is no evidence for G312 being elliptical in the plane of the sky. It is, however, possible that that G312 is elongated along the line-of-sight.

and V-band orientations is due to the different numbers of resolved stars in the different bands and data sets. The ellipticity that I measure ($\epsilon = 0.195 \pm 0.012$) is somewhat higher than that found by Lupton (1989) [90] ($\epsilon = 0.15 \pm 0.02$). Figure 5.10 shows an apparent decrease in the ellipticity of G302 between $r_{\text{eff}} \sim 1''$ and $r_{\text{eff}} \sim 10''$. The slope of $\epsilon(r_{\text{eff}}) = mr_{\text{eff}} + b$ is $m = -0.0381 \pm 0.0383$. In order to determine if this slope represents a real decrease in ellipticity with radius I performed 10,000 bootstrap resamplings of the ellipticity data between $1'' \leq r_{\text{eff}} \leq 10''$ and computed the slope for each set of bootstrapped ellipticities. I found that there was a 22.34% chance of observing a slope at least as great as the slope seen in the actual data simply by chance. Therefore, I conclude that there is no evidence for a change in ellipticity with radius between $r_{\text{eff}} = 1''$ and $r_{\text{eff}} = 10''$ in G302. It is not possible to say if the apparent increase in ellipticity between $r_{\text{eff}} \simeq 0\farcs3$ and $r_{\text{eff}} \simeq 1\farcs0$ is real or due to the presence of a small number of unresolved bright stars located within a few core radii of the centre of G302. Since the stellar FWHM is $\sim 0\farcs2$ the chance location of a single unresolved bright star within $0\farcs3$ of the centre of G302 along the projected minor axis of the globular cluster could reduce the ellipticity of the fitted isophotes.

G312 has a projected ellipticity of $\bar{\epsilon} = 0.065$ but there is considerably more scatter in the fitted position angles (the standard deviation is $\sigma \sim 27°$) than there is in the G302 position angles ($\sigma \sim 10°$). This suggests that the observed projected ellipticity of G312 is primarily due to the stochastic placement of stars within G312, variations in the stellar background of the M31 halo, and the intrinsic precision of the ELLIPSE algorithm. Running the ELLIPSE task on a series of circular artificial Michie–King globular clusters that had been convolved with the WF3 PSF suggests that seeing alone can produce ellipticities of between 0.01 and 0.02 at radii of between approximately $0\farcs5$ and $2''$. This agrees with the fluctuations in ellipticity seen in Figure 5.11 at these radii. While seeing has very little effect on the observed ellipticity beyond $r_{\text{eff}} \sim 2''$, artificial star tests

5.3.2 Ellipticities

Figures 5.10 and 5.11 show the ellipticity and orientation profiles for G302 and G312 respectively. The error bars in Figures 5.10 and 5.11 should be treated as guides to the reliability of the individual measurements and *not* taken as statistically rigorous estimates of the uncertainties in each point. In order to estimate the overall projected ellipticity of each globular cluster the weighted mean ellipticities, $\overline{\epsilon}$ and position angles, $\overline{\theta_0}$ (in degrees east of north on the sky) were determined using the values for the individual isophotes between $r_{\text{eff}} = 1''$ and $r_{\text{eff}} = 10''$. The results are presented in Table 5.3. The uncertainties are standard errors in the mean and N is the number of isophotes used to compute $\overline{\epsilon}$ and $\overline{\theta_0}$.

Cluster	Filter	$\overline{\epsilon}$	$\overline{\theta_0}$	N
G302	V	0.194 ± 0.011	$-71^\circ \pm 2^\circ$	24
	I	0.195 ± 0.012	$-87^\circ \pm 2^\circ$	24
G312	V	0.072 ± 0.015	$77^\circ \pm 5^\circ$	24
	I	0.058 ± 0.014	$77^\circ \pm 6^\circ$	24

Table 5.3: Ellipticities and position angles for G302 and G312 from the *HST* data.

The projected major axis of G302 points approximately towards the centre of M31. The ellipticity of each globular cluster is the same in the I-band as it is in the V-band but the projected major axis of G302 in the V-band is located $16^\circ \pm 3^\circ$ west of the projected major axis in the I-band. This shift in orientation between the two colours is visible at all radii in G302 and is likely due to a small number of giant stars dominating the light from the globular cluster. This data shows that the projected major axis of G302 in the V-band is oriented 20° farther west from the V-band orientation obtained by Lupton (1989) [90] ($\theta_0 = 0\overset{\circ}{.}0 \pm 0\overset{\circ}{.}6$) but that Lupton's orientation is only 4° east of my I-band orientation. This supports the idea that the observed difference between the I-

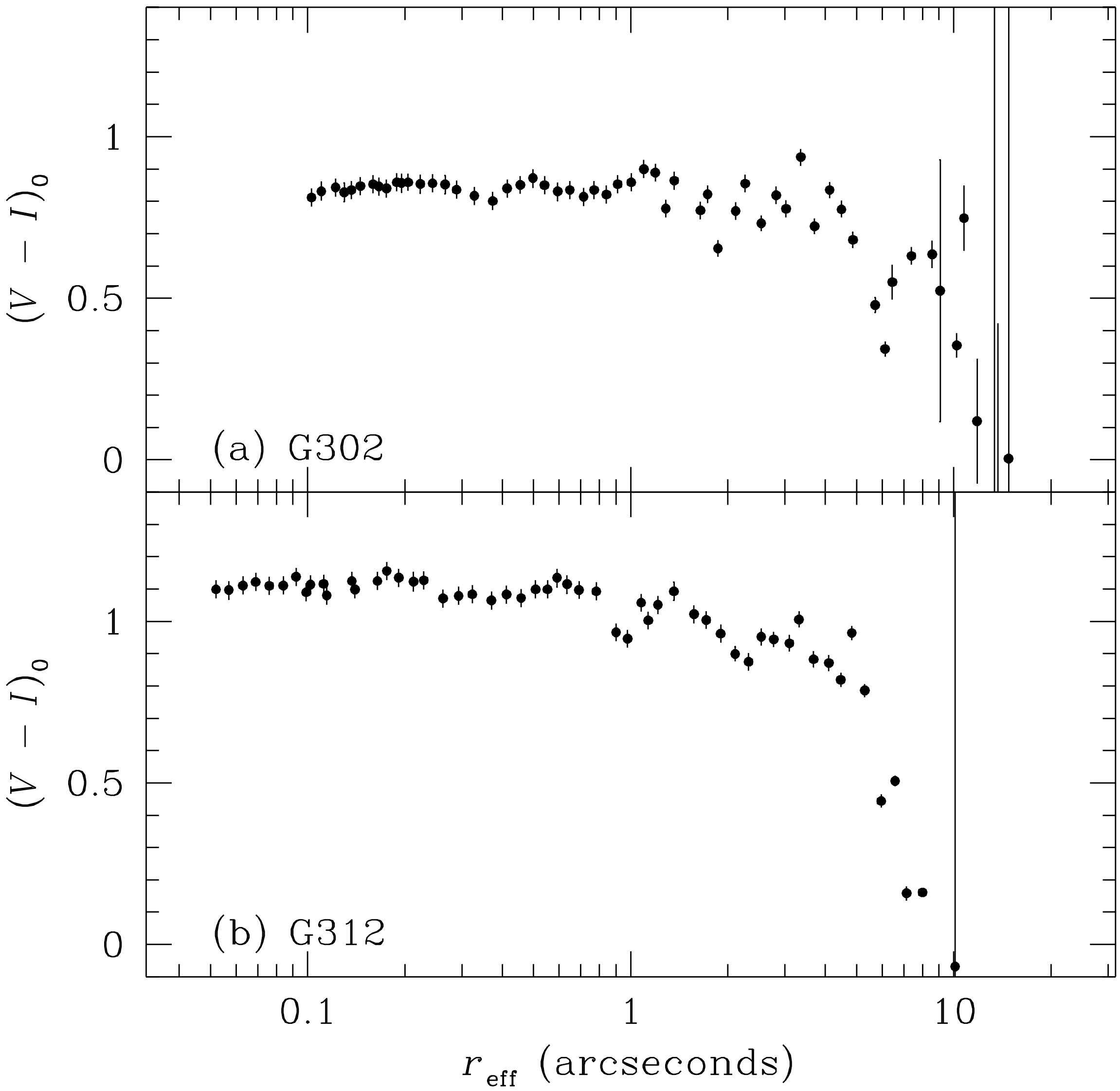

Figure 5.9: This figure shows the integrated colour profiles for G302 and G312.

5.3 Structure

5.3.1 Colour Gradients

The mean colour for $r_{\rm eff} \leq 2\farcs5$ for G312 is $\langle (V-I)_0 \rangle = 1.07$ while for G302 $\langle (V-I)_0 \rangle = 0.83$. These colours are consistent with G302 having a metal-poor stellar population and G312 having a metal-rich stellar population.

Figure 5.9 shows the dereddened $(V-I)_0$ colour profiles of G302 and G312. These profiles were obtained by subtracting the I-band isophotal surface brightness profile from the V-band profile then dereddening the resulting profile. The error bars represent the 1σ standard error in the colour. The inner portion of the G302 profile is truncated at $r_{\rm eff} \sim 0\farcs1$ (= 1 pixel) since the innermost pixels ($r \leq 1$ pixel) of the WFC images of G302 were slightly saturated. Individual stars can be resolved to within $r_{\rm eff} \simeq 2\farcs5$ of the centre of the globular cluster and the isophotes become less certain when the light becomes resolved into individual stars. Artificial star tests suggest that the large scatter in the colour profiles in the outer regions of G302 and G312 represent stochastic star placement within the globular clusters, not intrinsic colour gradients. In the inner $2\farcs5$ the colour gradients are $d(V-I)_0/dr_{\rm eff} = -0.028 \pm 0.007$ for G302 and $d(V-I)_0/dr_{\rm eff} = -0.090 \pm 0.007$ for G312. To determine if these colour gradients are due to chance 10,000 bootstrap resamplings of the colour data for each globular cluster were performed and the colour gradients for each resampled data set were computed. This analysis gave a 2.1255% chance that the observed colour gradient (for $r_{\rm eff} \leq 2\farcs5$) in G302 is due to chance and a 0.0005% chance that the observed colour gradient (for $r_{\rm eff} \leq 2\farcs5$) in G312 is due to chance. Therefore the existence of a radial colour gradient in G312 can not be rejected based on the results of Monte-Carlo simulations. However, these simulations only weakly (at the 2.4σ level) suggest that there is a radial colour gradient in G302.

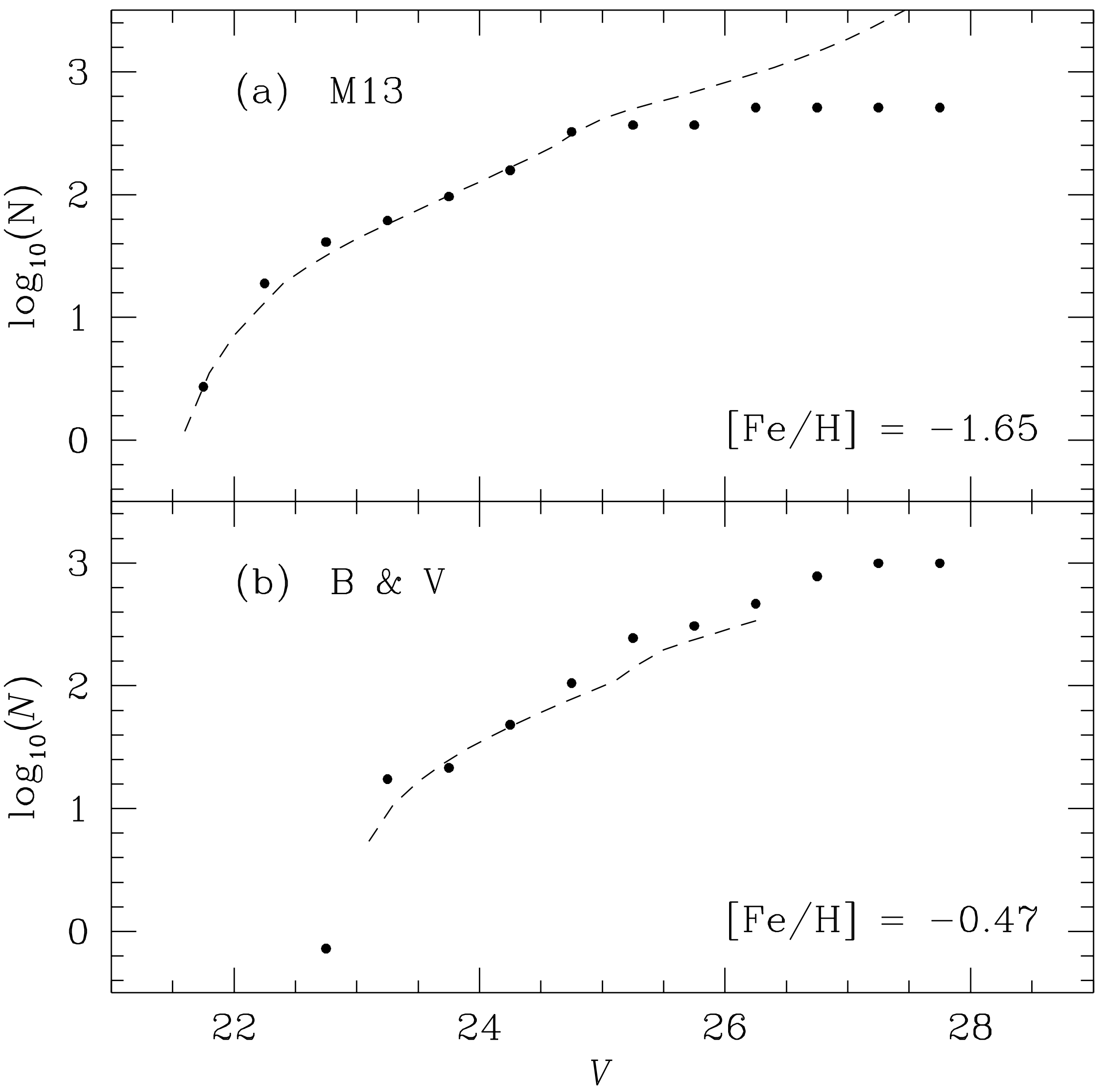

Figure 5.8: The upper panel (a) compares the cumulative luminosity function for G302 (solid circles) to the cumulative luminosity function of the metal-poor Galactic globular cluster M13. Panel (b) compares the cumulative luminosity function for G312 with a theoretical luminosity function for an old metal-rich globular cluster. The comparison luminosity functions have been scaled so that they contains the same number of stars at $V = 24$ as the M31 globular cluster luminosity functions do.

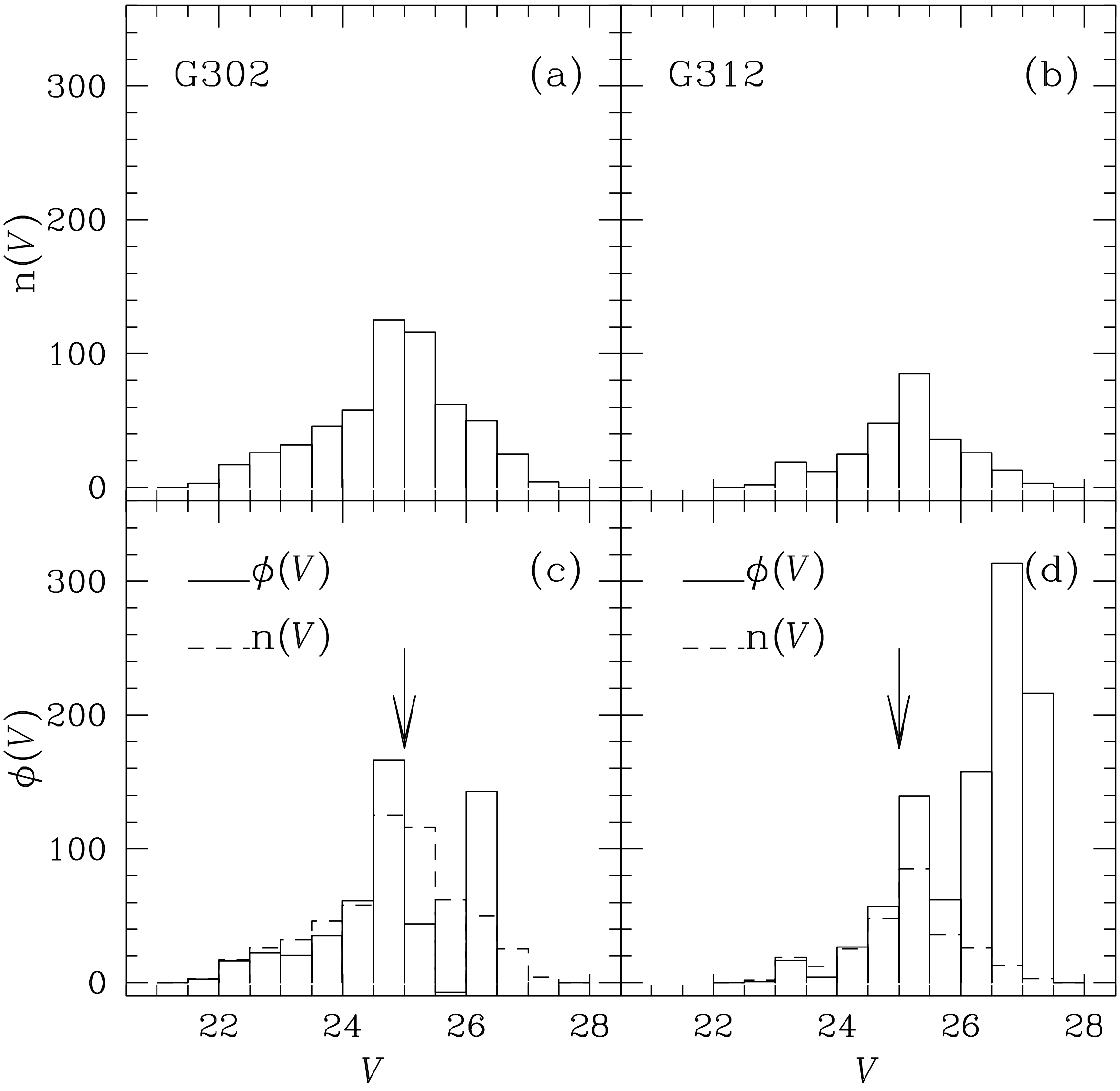

Figure 5.7: The upper panels, (a) and (b), show the observed luminosity functions for G302 and G312 respectively. Only stars between $2''.5 \leq r < 12''.5$ were used to construct these luminosity functions. The lower panels, (c) and (d) show the completeness-corrected luminosity functions with the completeness-corrected background luminosity function subtracted (solid lines) and the observed luminosity functions (dashed lines). The completeness corrected luminosity functions become unreliable below the level of the horizontal branch (indicated with an arrow).

thus allows an estimate of the completeness corrected luminosity function to be made from incomplete information. The drawbacks to the forward approach are that there is no obvious way to compute the uncertainties in the resulting luminosity function, and that some *a priori* information is needed about the form of the true luminosity function.

This forward method will give different results depending on the initial guess at $\phi(V)$ and the scheme used to adjust ϕ' during the iteration. I found that for the *HST* data presented in this thesis the luminosity function is not dependent on the initial guess at the form of the luminosity function when $V \lesssim 25$ (approximately the level of the horizontal branch). I adjusted $\phi'(V)$ using $\phi'_i(V) = \phi'_{i-1}(V) + \Delta n(V)$ and iterated $n'(V) = \mathbf{P}\phi'(V)$ until Δn was minimized.

Figure 5.7 shows the observed and completeness corrected, background subtracted luminosity functions for G302 and G312. These luminosity functions are reliable for $V \lesssim 25$. Figure 5.8a compares the cumulative luminosity function for G302 with that for the metal-poor ([Fe/H] $= -1.65$) Galactic globular cluster M13 (Simoda & Kimura 1968 [132]) while Figure 5.8b compares the cumulative globular cluster for G312 to a theoretical luminosity function for an old ($t_0 = 14$ Gyr) globular cluster with [Fe/H] $= -0.47$ and [O/Fe] $= +0.23$ from Bergbusch & VandenBerg (1992) [11]. Stellar evolution models do not show any relationship between the slope of the luminosity function of the upper red-giant branch and either the iron abundance or the age of the stars (Bergbusch & VandenBerg 1992 [11]) so Figure 5.8 can not be used to determine the ages or the iron abundances of G302 or G312. There is a general agreement between the shape of the G312 luminosity function and the shape of the theoretical metal-rich luminosity function, as well as between the shape of the G302 luminosity function and the metal-poor comparison luminosity function, which suggests that the star counts are not seriously incomplete down to the level of the horizontal branch ($V \simeq 25$).

	G302		G312	
V	$n(V)$	$\phi(V)$	$n(V)$	$\phi(V)$
21.75	3	2.719	0	0.000
22.25	17	16.184	0	0.000
22.75	26	22.139	2	0.725
23.25	32	20.397	19	16.635
23.75	46	34.960	12	4.148
24.25	58	61.228	25	26.724
24.75	125	166.622	48	57.009
25.25	116	43.772	85	139.459
25.75	62	0.000	36	61.921
26.25	50	142.707	26	157.769
26.75	25	0.000	13	313.156
27.25	4	0.000	3	216.386

Table 5.2: V-band luminosity functions for G302 and G312.

Given $\mathbf{P}$ there is no ideal method for reconstructing a stellar luminosity function from incomplete star count data. For a recent review of the problem see Fahlman (1993) [51]. Ideally the true luminosity function, $\phi(V)$, can be obtained from the observed luminosity function, $n(V)$, using $\phi(V) = \mathbf{P}^{-1}n(V)$ as described in Drukier et al. (1988) [46] and Mighell (1990) [98]. Unfortunately many faint artificial stars are lost in the noise and thus not recovered at all. This results in some artificial stars essentially bin-jumping off the faint end of the finding-probability matrix so there is insufficient information to reliably invert $\mathbf{P}$. An alternative to computing $\mathbf{P}^{-1}$ is to use a model luminosity function, $\phi'(V)$, and solve the forward equation $n'(V) = \mathbf{P}\phi'(V)$. The estimated luminosity function can then be adjusted until $\Delta n \equiv n - n'$ is minimized. This approach will not accurately reconstruct the faint end of the luminosity function since $\mathbf{P}$ does not contain sufficient information at faint magnitudes, due to bin-jumping by faint stars, to do this. However, unlike the inversion method, the forward approach will work if $\mathbf{P}$ is nearly singular and

$$\begin{array}{cc}
 & \begin{array}{cccccccccccc} 21.75 & 22.25 & 22.75 & 23.25 & 23.75 & 24.25 & 24.75 & 25.25 & 25.75 & 26.25 & 26.75 & 27.25 \end{array} \\
\begin{array}{c} 21.75 \\ 22.25 \\ 22.75 \\ 23.25 \\ 23.75 \\ 24.25 \\ 24.75 \\ 25.25 \\ 25.75 \\ 26.25 \\ 26.75 \\ 27.25 \end{array} &
\begin{pmatrix}
1.000 & 0.000 & 0.000 & 0.000 & 0.000 & 0.000 & 0.000 & 0.000 & 0.000 & 0.000 & 0.000 & 0.000 \\
0.000 & 1.000 & 0.000 & 0.000 & 0.000 & 0.000 & 0.000 & 0.000 & 0.000 & 0.000 & 0.000 & 0.000 \\
0.000 & 0.000 & 1.000 & 0.000 & 0.000 & 0.000 & 0.000 & 0.000 & 0.000 & 0.000 & 0.000 & 0.000 \\
0.000 & 0.000 & 0.000 & 1.000 & 0.071 & 0.000 & 0.000 & 0.000 & 0.000 & 0.000 & 0.000 & 0.000 \\
0.000 & 0.000 & 0.000 & 0.000 & 0.857 & 0.000 & 0.000 & 0.000 & 0.000 & 0.000 & 0.000 & 0.000 \\
0.000 & 0.000 & 0.000 & 0.000 & 0.000 & 0.615 & 0.032 & 0.000 & 0.000 & 0.000 & 0.000 & 0.000 \\
0.000 & 0.000 & 0.000 & 0.000 & 0.000 & 0.000 & 0.548 & 0.023 & 0.007 & 0.000 & 0.000 & 0.000 \\
0.000 & 0.000 & 0.000 & 0.000 & 0.000 & 0.000 & 0.065 & 0.526 & 0.099 & 0.000 & 0.000 & 0.000 \\
0.000 & 0.000 & 0.000 & 0.000 & 0.000 & 0.000 & 0.000 & 0.053 & 0.447 & 0.094 & 0.013 & 0.000 \\
0.000 & 0.000 & 0.000 & 0.000 & 0.000 & 0.000 & 0.000 & 0.000 & 0.057 & 0.170 & 0.077 & 0.000 \\
0.000 & 0.000 & 0.000 & 0.000 & 0.000 & 0.000 & 0.000 & 0.000 & 0.000 & 0.132 & 0.026 & 0.014 \\
0.000 & 0.000 & 0.000 & 0.000 & 0.000 & 0.000 & 0.000 & 0.000 & 0.000 & 0.000 & 0.013 & 0.027
\end{pmatrix}
\end{array}$$

while for G312 WF3 CCD the finding-probability matrix is:

$$\begin{array}{cc}
 & \begin{array}{cccccccccc} 22.75 & 23.25 & 23.75 & 24.25 & 24.75 & 25.25 & 25.75 & 26.25 & 26.75 & 27.25 \end{array} \\
\begin{array}{c} 22.75 \\ 23.25 \\ 23.75 \\ 24.25 \\ 24.75 \\ 25.25 \\ 25.75 \\ 26.25 \\ 26.75 \\ 27.25 \end{array} &
\begin{pmatrix}
1.000 & 0.000 & 0.000 & 0.000 & 0.000 & 0.000 & 0.000 & 0.000 & 0.000 & 0.000 \\
0.000 & 1.000 & 0.000 & 0.000 & 0.000 & 0.000 & 0.000 & 0.000 & 0.000 & 0.000 \\
0.000 & 0.000 & 0.600 & 0.100 & 0.067 & 0.000 & 0.000 & 0.000 & 0.000 & 0.000 \\
0.000 & 0.000 & 0.000 & 0.800 & 0.000 & 0.000 & 0.000 & 0.000 & 0.000 & 0.000 \\
0.000 & 0.000 & 0.000 & 0.000 & 0.667 & 0.014 & 0.014 & 0.000 & 0.000 & 0.000 \\
0.000 & 0.000 & 0.000 & 0.000 & 0.067 & 0.500 & 0.014 & 0.000 & 0.000 & 0.000 \\
0.000 & 0.000 & 0.000 & 0.000 & 0.000 & 0.081 & 0.301 & 0.000 & 0.000 & 0.000 \\
0.000 & 0.000 & 0.000 & 0.000 & 0.000 & 0.000 & 0.055 & 0.125 & 0.000 & 0.000 \\
0.000 & 0.000 & 0.000 & 0.000 & 0.000 & 0.000 & 0.000 & 0.000 & 0.038 & 0.000 \\
0.000 & 0.000 & 0.000 & 0.000 & 0.000 & 0.000 & 0.000 & 0.000 & 0.000 & 0.010
\end{pmatrix}
\end{array}.$$

The rows of $\mathbf{P}$ are the input V-band magnitudes of the artificial stars and the columns are the recovered V-band magnitudes of the stars.

5.2 Luminosity Functions

The raw, $n(V)$, and completeness corrected, $\phi(V)$, V-band stellar luminosity functions for G302 and G312 are presented in Table 5.2. The raw luminosity functions include all stars within $2\farcs5 \le r < 12\farcs5$ of the centre of each globular cluster. The background luminosity function for each globular cluster was obtained by taking the luminosity functions for the M31 halo near each globular cluster and scaling them to the area covered by each globular cluster. This scaled background luminosity function was subtracted from the raw luminosity function before the effects of incompleteness were considered. Subtracting the raw background luminosity function assumes that the completeness corrections in the WF2 and WF4 fields are the same as in the WF3 field. An examination of Figure 5.7 shows that the completeness corrections are small for stars with $V \lesssim 25$. Therefore, using the raw background luminosity function, instead of the completeness-corrected background luminosity function, will not alter the results. The raw and completeness corrected luminosity functions are related by $n(V) = \mathbf{P}\phi(V)$ where $\mathbf{P}$ is the finding-probability matrix. $\mathbf{P}$ describes the probability of a star with a true magnitude of $V_{\rm in}$ being recovered with a magnitude of $V_{\rm rec}$.

Artificial star tests suggest that completeness corrections need to be applied to the raw globular cluster and background luminosity functions. These corrections are very small for $V \lesssim 25$, but artificial star tests suggest that bin-jumping (the tendency for stars with input magnitudes in one magnitude bin to be recovered in a different magnitude bin) becomes significant at approximately the level of the horizontal branch and needs to be compensated for in order to accurately reconstruct the luminosity function. For G302 the finding-probability matrix is:

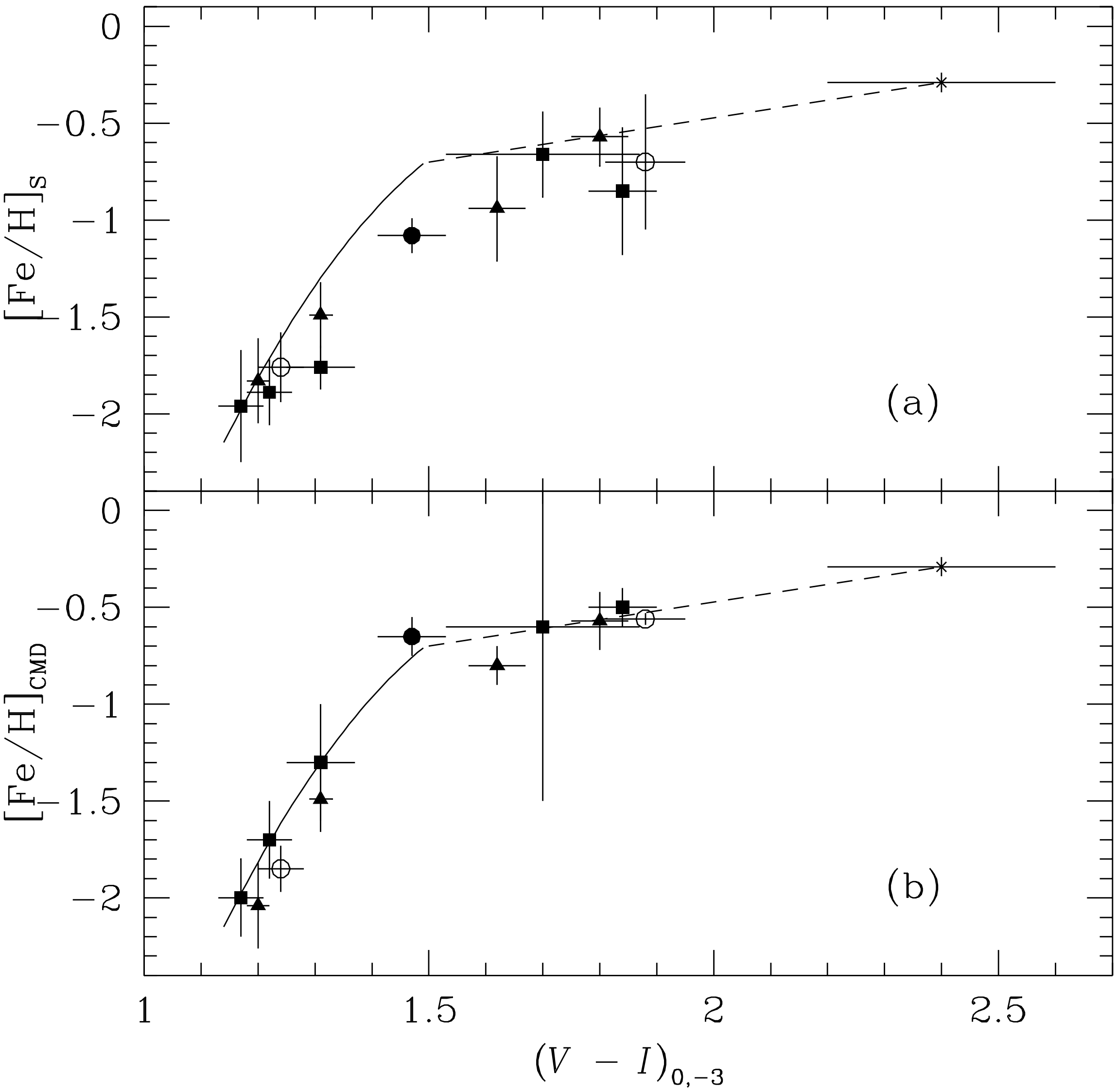

Figure 5.6: The open circles represent the data for G302 and G312 from Chapter 5. The solid circle is data from Rich et al. (1996) [119], the solid squares are data from Couture et al. (1995) [31], and the solid triangles are data from Ajhar et al. (1996) [1]. The horizontal error bars only include the uncertainty due to the width of the red-giant branch, not any uncertainties in the reddening or distance modulus of the individual globular clusters. The solid line shows the DCA relationship between iron abundance and the $(V - I)_{0,-3}$ colour while the dashed line shows my extension of this relationship to include the metal-rich Galactic globular cluster NGC 6553 (indicated with a "*"). Spectroscopic [Fe/H] values from HBK are plotted in panel (a) and [Fe/H] values derived from the CMDs are plotted in panel (b).

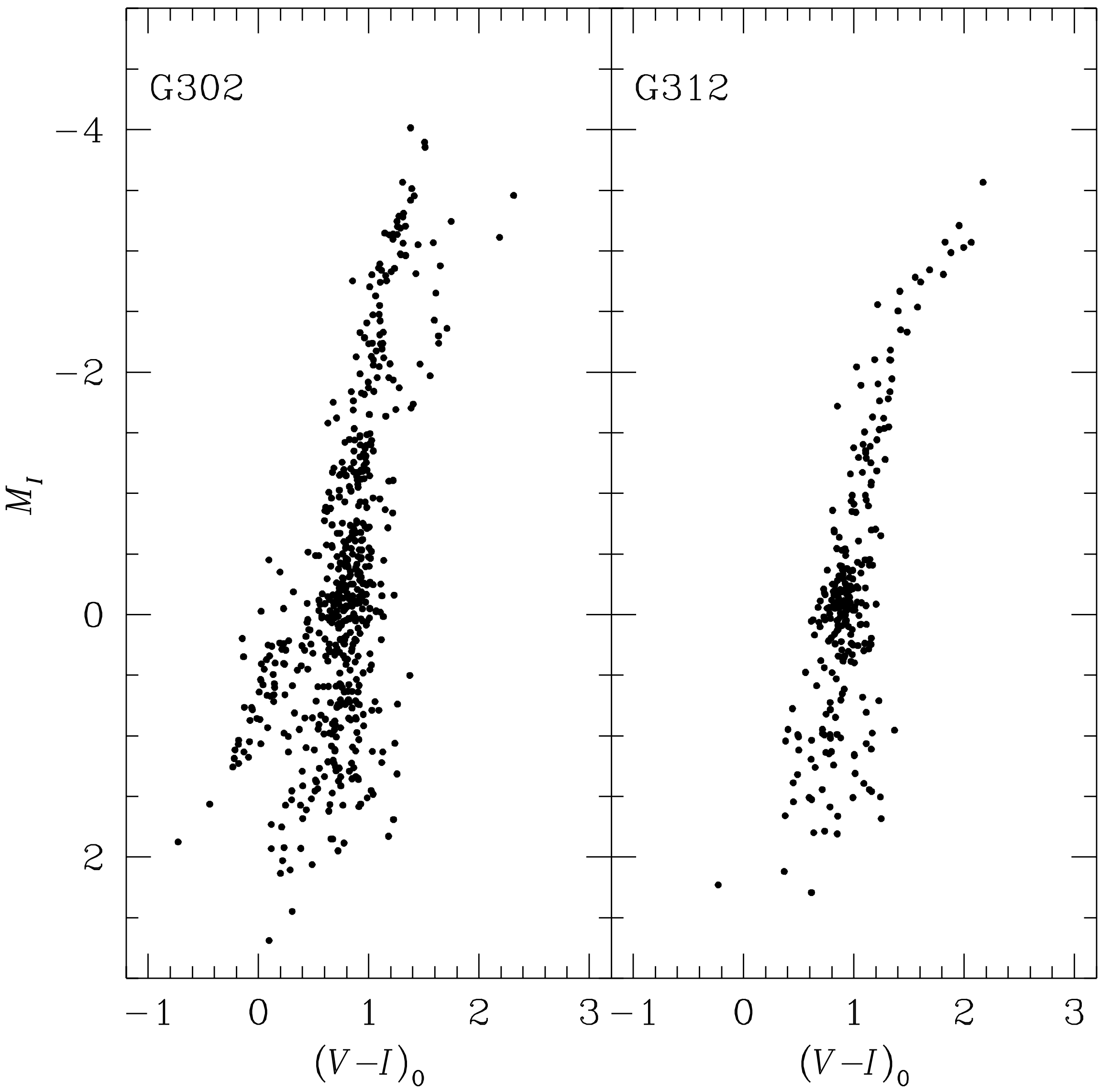

Figure 5.5: This figure shows the $(M_I, (V-I)_0)$ CMDs for G302 and G312. A distance modulus of $\mu_0 = 24.3$, a reddening of $E_{V-I} = 0.1$, and an extinction $A_I = 0.19$ was assumed as discussed in Chapter 4.3.

systematically overestimated. Since iron abundances are more difficult to measure in spectra of metal-rich globular clusters it is more likely that the [Fe/H] values for the metal-rich globular clusters have been underestimated than it is that the [Fe/H] values for the metal-poor globular clusters have been overestimated.

Cuillandre et al. (1997) [35] found dust beyond the optical limit of the M31 disc, and that the distribution of this dust correlates with the distribution of H I beyond the disc. Since G108 is located within the extended disc of H I around M31 it is possible that G108's $(V-I)_{0,-3}$ colour may be due to internal reddening in the extended disc of M31. Using the H I maps of Emerson (1974) [49], and the relationships between H I column density and reddening given in Cuillandre et al. (1997) [35], I find an excess reddening of $E_{V-I} = 0.14 \pm 0.02$. However, an examination of the CMD for G108 (Figure 20 of Ajhar et al. 1996 [1]) suggests that internal reddening from M31 does not exceed $E_{V-I} \sim 0.05$. This discrepancy may be due to the patchy nature of the H I distribution in the outer regions of M31's extended disc. Brinks & Bajaja (1986) [20] found many small regions in the H I distribution in M31 where the H I column densities were significantly less than the H I column densities in the surrounding column densities. These holes were typically a few arcminutes in diameter, smaller than the beam-size used to construct the Emerson (1974) [49] H I maps. It is possible that G108 (which has an angular diameter of $\sim 0\farcm4$) is located in a hole in the H I distribution that is smaller than the resolution of the H I maps. If this is the case then the Emerson (1974) [49] H I maps will lead to an overestimate of the reddening toward G108 and my estimate of the excess reddening towards G108 would not be inconsistent with the published CMD for that globular cluster.

If the *Hipparcos* distance modulus ($\mu_0 = 24.77 \pm 0.11$) of Feast & Catchpole (1997) [53] is adopted then the metal-rich globular clusters in Figure 5.6 would be in better agreement with the extended DCA relation. However, the metal-poor globular clusters would have $(V-I)_{0,-3}$ colours that are bluer than would be expected if the distance modulus of the M31 globular cluster system is $\mu_0 = 24.3 \pm 0.1$. This would result in the metal-poor globular clusters lying on the left of the DCA relation, implying that the spectroscopically determined iron abundances for the metal-poor M31 globular clusters have been

If the spectroscopic iron abundances ($[Fe/H]_S$) are adopted then nine of the twelve M31 globular clusters are redder than predicted by the extended DCA relation. This discrepancy is present at all iron abundances but is most noticeable for the metal-rich globular clusters. The individual uncertainties in $[Fe/H]_S$ for all the globular clusters except G1 and G327 are large enough to account for the difference between their locations in Figure 5.6a and the predictions of the extended DCA relation. A recent paper by de Freitas Pacheco (1997) [39] gives iron abundances for twelve globular clusters in the M31 system. Most of his iron abundances are higher than the HBK values by $\sim$0.2 dex. An examination of the CMDs for each globular cluster shows that several globular clusters have red-giant branches that are significantly redder and flatter than would be expected from their spectroscopic iron abundances. This is particularly noticeable for the more metal-rich globular clusters. To test if errors in the spectroscopically determined iron abundance determinations are sufficient to account for the discrepancies between the globular clusters and the extended DCA relation in Figure 5.6a I replotted the globular clusters using iron abundances determined from the shapes of the red-giant branches. This data is shown in Figure 5.6b. All of the globular clusters now fall within their uncertainties of the extended DCA relationship with the exception of G108, which has a $(V-I)_{0,-3}$ value nearly 3σ redder than its predicted value. Alternately the iron abundance Ajhar et al. (1996) [1] derived from G108's CMD could be in error. However, their Figure 20 shows the upper portion of the red-giant branch of G108 to be not quite as flat than that of 47 Tuc, indicating that G108 has slightly less iron than 47 Tuc does. It would be difficult, using their data, to fit a fiducial to the G108 red-giant branch that is flatter (and thus more iron rich) than the 47 Tuc fiducial. Therefore it is unlikely that the estimated iron abundance of G108 is in error.

One possible explanation for the red colour of G108 is that the H I in M31 extends $\sim$ 15 kpc beyond the outer edge of the optical disc and past the location of G108.

Since several of the M31 globular clusters in Figure 5.6a have iron abundances at least as high as that of 47 Tuc the DCA relationship was extended to higher iron abundances. Extending this relationship to globular clusters more metal-rich than 47 Tuc ([Fe/H] $= -0.71$) is somewhat difficult since the red-giant branch in the $((V-I)_0, M_I)$ plane becomes asymptotically flat as the iron abundance increases. This makes it difficult to define $(V-I)_{0.-3}$ since, as [Fe/H] approaches the Solar value, this point occurs in the horizontal portion of the red-giant branch. In order to extend the relationship to higher iron abundances I determined $(V-I)_{0,-3}$ for the metal-rich Galactic globular cluster NGC 6553 using the $(I,(V-I))$ CMD of Ortolani et al. (1990) [104]. I assumed a distance modulus of $\mu_0 = 13.35$ (Guarnieri et al. 1995 [60]), a reddening of $E_{B-V} = 0.78$ (Bico & Alloin 1986 [16]), and an iron abundance of [Fe/H] $= -0.29$ (Zinn & West 1984 [156]). Using this data I found $(V-I)_{0,-3} = 2.4 \pm 0.2$ for NGC 6553. This point lies just below the region where the red-giant branch becomes horizontal so there is a significant uncertainty in the value of $(V-I)_{0,-3}$ for NGC 6553 solely due to the width of the red-giant branch in $(V-I)_0$ at $M_I = -3$. I extrapolated the DCA relation to [Fe/H] $= -0.29$ simply by connecting the [Fe/H] $= -0.71$ end of the DCA relation to the location of NGC 6552. The resulting relation is:

$$[\mathrm{Fe/H}] = -15.16 + 17.0(V-I)_{0,-3} - 4.9(V-I)_{0,-3}^2 \tag{5.3}$$

for $-2.2 \leq$ [Fe/H] ≤ -0.7 (from DCA) and

$$[\mathrm{Fe/H}] = -1.36 + 0.44(V-I)_{0,-3} \tag{5.4}$$

for $-0.7 \leq$ [Fe/H] ≤ -0.29 (my extension). It should be stressed that *this extension to high iron abundances is an estimate and is intended* only *to provide a reasonable estimate of what happens to the DCA relation at high iron abundances.*

5.1.4 The Colour–Iron Abundance Relation

Figure 5.5 shows the CMDs for G302 and G312 after converting the calibrated magnitudes to absolute I-band magnitudes. This was done to determine the colour of the red-giant branch for each globular cluster at $M_I = -3$, hereafter referred to as $(V-I)_{0,-3}$. DCA found a strong relationship between iron abundance and $(V-I)_{0,-3}$ for Galactic globular clusters with $-2.2 \leq$ [Fe/H] ≤ -0.7. Figure 5.6a shows the relationship between $(V-I)_{0,-3}$ and $[\mathrm{Fe/H}]_S$ for G302 and G312 and several other M31 globular clusters with published CMDs. The published data has been adjusted to a distance modulus of $\mu_0 = 24.3$. The $[\mathrm{Fe/H}]_S$ values were all taken from HBK so the $(V-I)_{0,-3}$ colour and iron abundance are determined completely independently of each other for each globular cluster. Colour, iron abundance, and reddening data for each globular cluster is listed in Table 5.1 along with the source of the CMD, the projected distance of each globular cluster from the centre of M31 (R_{M31}), and Y, the projected distance of each globular cluster from the major axis of M31 with positive Y being on the northwest side of the major axis of M31.

Cluster	$(V-I)_{0,-3}$	$[\mathrm{Fe/H}]_\mathrm{S}$	$[\mathrm{Fe/H}]_\mathrm{CMD}$	E_{V-I}	R_{M31}	Y	Reference
G1	1.47 ± 0.06	-1.08 ± 0.09	-0.65 ± 0.10	0.10 ± 0.03	$152'.3$	$+29'.1$	[119]
G11	1.22 ± 0.04	-1.89 ± 0.17	-1.7 ± 0.20	0.10 ± 0.03	$75'.7$	$+43'.6$	[31]
G58	1.80 ± 0.05	-0.57 ± 0.15	-0.57 ± 0.15	0.14 ± 0.04	$28'.2$	$+27'.3$	[1]
G105	1.31 ± 0.02	-1.49 ± 0.17	-1.49 ± 0.17	0.08 ± 0.02	$64'.8$	$-29'.9$	[1]
G108	1.62 ± 0.05	-0.94 ± 0.27	-0.80 ± 0.10	0.15 ± 0.04	$20'.8$	$+19'.7$	[1]
G219	1.20 ± 0.02	-1.83 ± 0.22	-2.04 ± 0.22	0.08 ± 0.02	$87'.2$	$-58'.8$	[1]
G302	1.24 ± 0.04	-1.76 ± 0.18	-1.85 ± 0.12	0.10 ± 0.03	$32'.1$	$-30'.4$	§5.1.2
G312	1.88 ± 0.07	-0.70 ± 0.35	-0.56 ± 0.03	0.10 ± 0.03	$49'.8$	$-49'.7$	§5.1.3
G319	1.70 ± 0.17	-0.66 ± 0.22	-0.6 ± 0.90	0.10 ± 0.03	$72'.1$	$-69'.0$	[31]
G323	1.17 ± 0.04	-1.96 ± 0.29	-2.0 ± 0.20	0.10 ± 0.03	$53'.8$	$-53'.8$	[31]
G327	1.31 ± 0.06	-1.78 ± 0.11	-1.3 ± 0.30	0.10 ± 0.03	$99'.7$	$+19'.9$	[31]
G352	1.84 ± 0.06	-0.85 ± 0.33	-0.5 ± 0.10	0.10 ± 0.03	$87'.1$	$-49'.6$	[31]

Table 5.1: Properties of selected globular clusters in the M31 system.

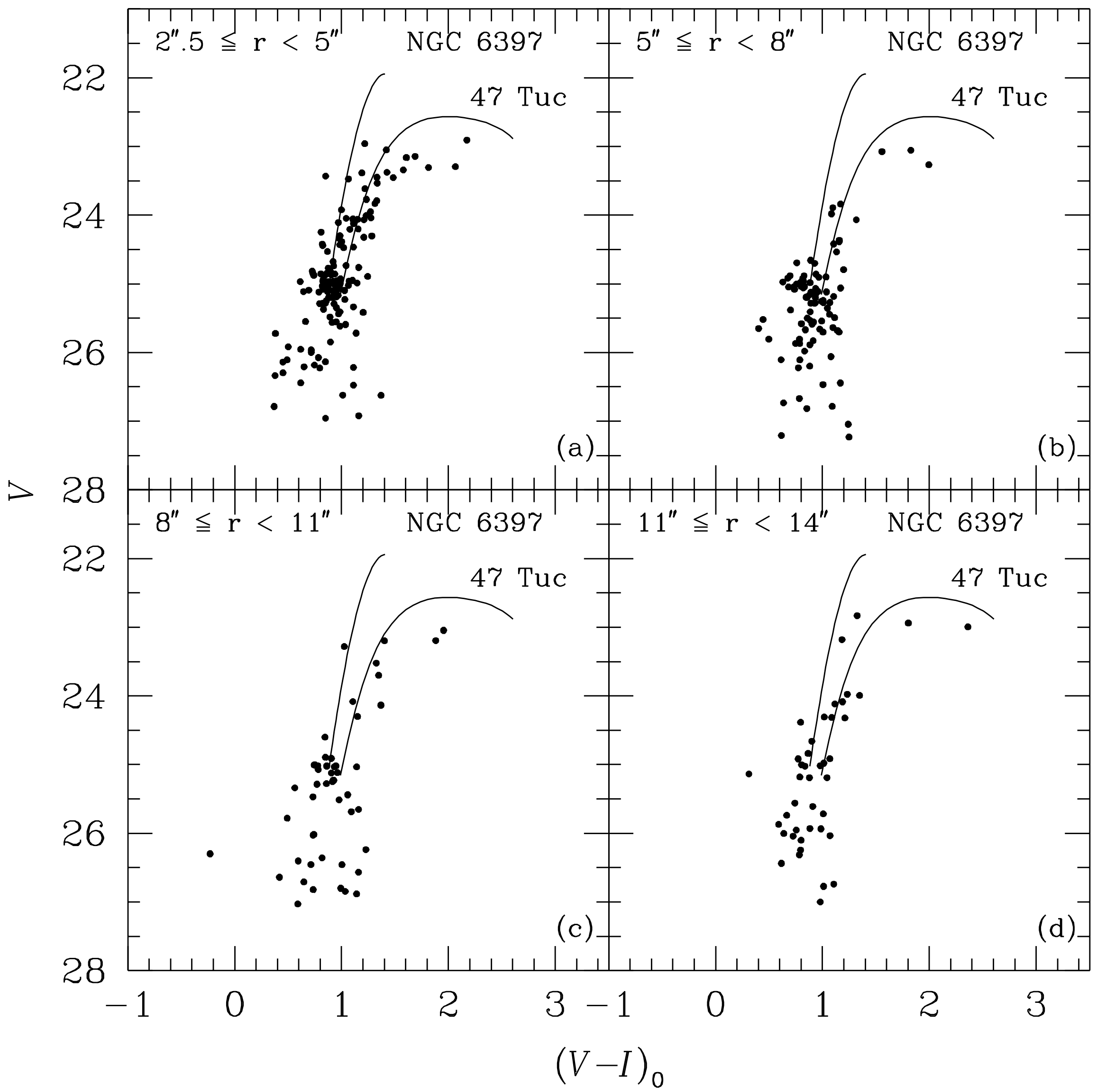

Figure 5.4: This figure shows CMDs for four annuli centred on G312. Since G312 has a metallicity similar to the mean metallicity of the M31 halo stars in the line of sight near G312 it is not possible to determine the limiting radius of G312 in this figure. The fiducial sequences are from DCA.

Since so few halo stars are expected in the upper red-giant branch of G312 the observed width of the red-giant branch provides a good estimate of the true photometric uncertainties in our observations. Photometric and spectroscopic evidence strongly suggests that all stars in a single Galactic globular clusters[1] have the same metallicity and there is no evidence to suggest that this should be different for globular clusters in M31. The mean width of the red-giant branch is $\sigma_{V-I} \sim 0.08$, consistent with what is predicted by the artificial star simulations (see Chapter 4.4). Therefore I believe that the width of the red-giant branch in Figure 5.2 is typical of a single-metallicity population for the WFC observations. This figure can be compared to Figures 6.3 and 6.4 to show that the large range of metallicities seen in the halo of M31 is not merely an artifact of photometric uncertainties along the halo red-giant branch.

Figure 5.4 shows no radial dependence in the morphology of the G312 CMD.

[1]Some of the most massive Galactic globular clusters, such as ω Cen and M22, show evidence for having a range of metallicities. However, these two Galactic globular clusters are ~ 10 times more massive than G312 is.

5.1.3 G312

Figure 5.2 shows the CMD for the globular cluster G312. As for G302 only stars between $2\farcs5 \leq r \leq 10''$ are shown since both star counts and the surface brightness profiles suggest that the Michie–King tidal radius of G312 occurs at $\sim 10''$. Interpolating between the fiducial giant branches suggests that G312 has an iron abundance of $[\mathrm{Fe/H}] = -0.56 \pm 0.03$, comparable to the mean iron abundance of stars in the halo of M31. This is in broad agreement with the spectroscopic iron abundance determined by HBK of $[\mathrm{Fe/H}] = -0.70 \pm 0.35$. The small number of red giants falling under the metal-poor fiducial sequences is consistent with the expected degree of contamination (see Chapter 5.1.1) from disc and metal-poor halo stars in M31 (see Chapter 6.1.2 for details on the metallicity distribution of halo stars in M31). If the *Hipparcos* distance to M31 is adopted then the iron abundance of G312 becomes $[\mathrm{Fe/H}] = -0.7$, consistent with the spectroscopically determined iron abundance.

The horizontal branch of G312 is a red clump located at $V \sim 25$ and slightly to the blue of the red-giant branch. This is consistent with G312 being a metal-rich globular cluster. No horizontal branch stars bluer than $(V-I)_0 = 0.6$ are present on the CMD so it is not possible to directly determine the magnitude of the horizontal branch in the RR Lyrae gap. Therefore, I estimated $\overline{V_{\mathrm{RR}}}$ by taking the weighted mean magnitude of the red clump stars ($\overline{V_{\mathrm{HB}}} = 25.09 \pm 0.09$) and added a correction of $\Delta V_{\mathrm{HB}}^{\mathrm{rich}} = 0.08$ (see Sarajedini et al. 1995 [126], and Ajhar et al. 1996 [1]) to get $\overline{V_{\mathrm{RR}}}$. This gives $\overline{V_{\mathrm{RR}}} = 25.17 \pm 0.09$ for G312. Using the iron abundance derived from the shape of the red-giant branch, and the Chaboyer et al. (1996) [28] relation (Equation 5.1), gives a distance modulus of $\mu_0 = 24.30 \pm 0.09$ for G312. If the Chaboyer et al. (1997) [27] relation (Equation 5.2, which is based on *Hipparcos* parallax data) is used then the distance modulus for G312 becomes $\mu_0 = 24.47 \pm 0.08\,^{+0.13}_{-0.18}$.

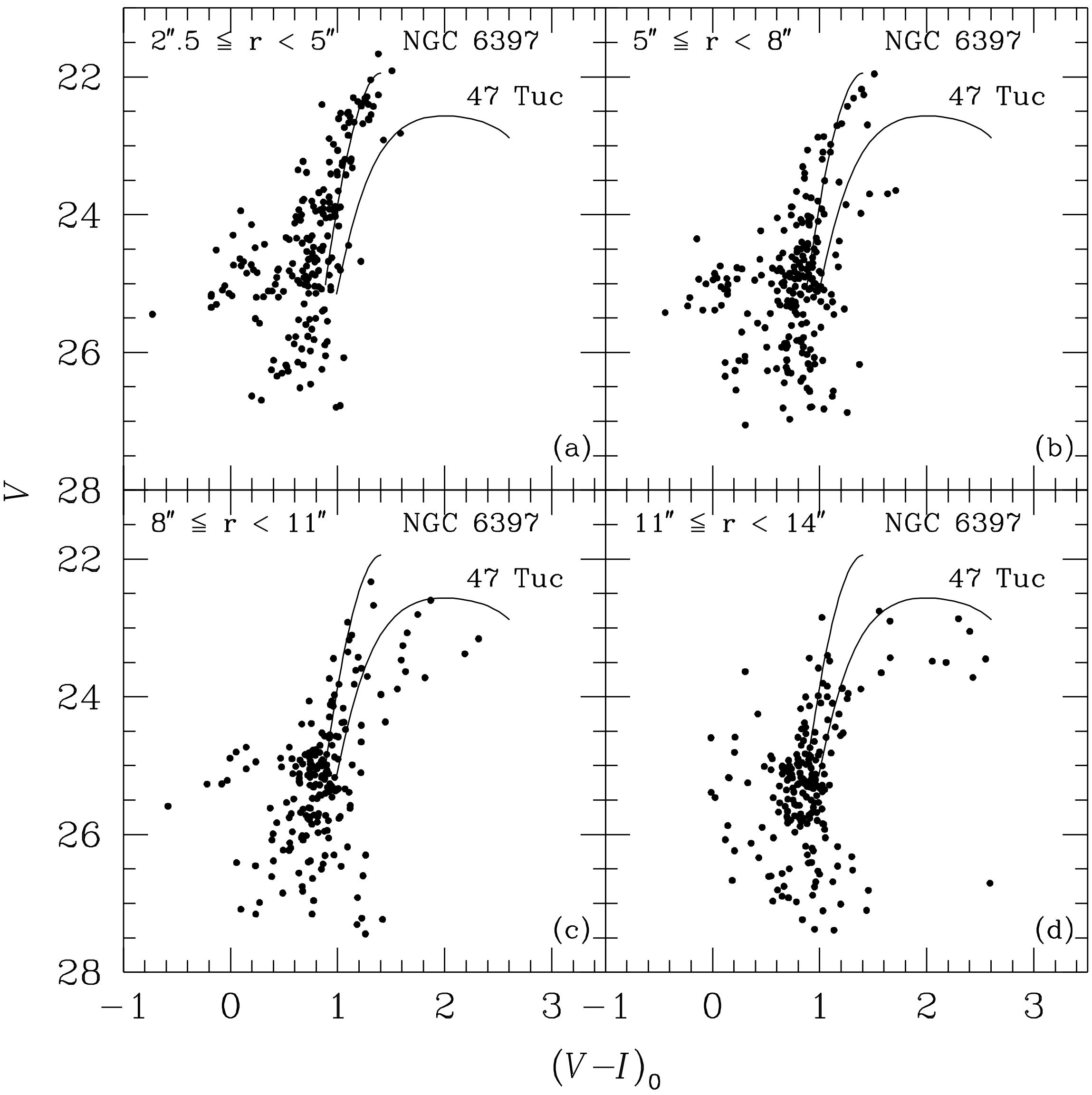

Figure 5.3: This figure shows CMDs for four annuli centred on G302. The fiducial sequences are from DCA.

$$M_V(\mathrm{RR}) = 0.20[\mathrm{Fe/H}] + 0.98 \tag{5.1}$$

(Chaboyer et al. 1996 [28]), gives a distance modulus of $\mu_0 = 24.32 \pm 0.09$ for G302. Chaboyer et al. (1997) [27] have derived a new relation,

$$M_V(\mathrm{RR}) = (0.23 \pm 0.04)\left([\mathrm{Fe/H}] + 1.9\right) + \left(0.39 \pm 0.08\,^{+0.13}_{-0.18}\right), \tag{5.2}$$

between the iron abundance and absolute magnitude of RR Lyrae stars which utilizes the *Hipparcos* parallaxes. Equation 5.2 gives a distance modulus of $\mu_0 = 24.53 \pm 0.08\,^{+0.13}_{-0.18}$ for G302, placing G302 $\sim$ 100 kpc in front of M31 if M31 is 900 kpc from the Earth. This is inconsistent with the HBK radial velocity and the orbital parameters from Chapter 5.5.3.

In order to identify the outer limiting radius of G302, and to search for any radial dependence in the morphology of the various branches of the CMD, I constructed CMDs in four annuli centred on the cluster. These CMDs are shown in Figure 5.3. The fiducial sequences plotted in Figure 5.3 are those of NGC 6397 ([Fe/H] $= -1.91$) and 47 Tuc ([Fe/H] $= -0.71$) taken from DCA. For $r \lesssim 8''$ the NGC 6397 fiducial provides a good fit to the G302 red-giant branch. The globular cluster appears to end at a radius somewhere between $8''$ and $11''$, in agreement with what is found by fitting Michie–King models (see Chapter 5.3). Beyond $11''$ the red-giant branch of the metal-rich halo population is clearly visible. The apparent increase in the number of blue horizontal branch stars in the inner regions of G302 is an illusion. A KS test shows that the radial distribution of blue horizontal branch stars is the same as that of the red-giant branch stars at the 99.91% confidence level. This indicates that the null hypothesis (that there is no difference between the radial distributions of the blue and red horizontal branch stars) can not be rejected. Therefore, there is no evidence in the data that there is a difference in the radial distribution of these two types of stars.

No stars brighter than the tip of the red-giant branch are present in the data. The lack of such super-luminous stars supports the hypothesis that globular clusters in M31 have ages similar to those of the Galactic globular clusters. Spectral line blanketing in cool giants can cause very red giants to appear fainter than bluer, less evolved, red-giant branch stars. This can result in some massive evolved stars appearing to have $V-I$ colours considerably redder than the rest of the globular cluster stars. Artificial star tests suggest that all the stars brighter than the horizontal branch were found so it is unlikely that any super-luminous asymptotic-giant branch stars in the outer regions of G302 have been missed. However, these stars, being more evolved, will have slightly more massive progenitors than the rest of the red- and asymptotic-giant stars. It is, then, possible that mass segregation will have concentrated them in the inner $r = 2\farcs5$ of the globular cluster making them undetectable with our data. To date no super-luminous asymptotic-giant stars have been detected in any M31 globular cluster (e.g. see Rich et al. 1996 [119], Fusi Pecci et al. 1996 [56], Jablonka et al. 1997 [79] for CMDs obtained using *HST* observations). This strongly supports the idea that the M31 globular clusters have comparable ages to those of the Galactic globular clusters. It should be emphasized, however, that although there is no evidence in the data for G302 having an age that is any different from the ages of the Galactic globular clusters, it is possible that super-luminous stars are present in the inner regions of G302.

Further evidence that G302 is an old globular cluster with an age similar to that of the Galactic globular clusters comes from de Freitas Pacheco (1997) [39]. That study used integrated spectra and single-population stellar population models to estimate the ages of twelve M31 globular clusters including G302. The result was a mean age of 15 ± 2.8 Gyr for those globular clusters and an age of 17.0 ± 2.9 Gyr for G302.

The weighted mean magnitude of the stars in the RR Lyrae gap is $\overline{V_{\rm RR}} = 24.93 \pm 0.09$ (standard deviation). Using this, the derived iron abundance of [Fe/H] $= -1.85$, and

5.1.2 G302

Figure 5.1 shows the CMD for the globular cluster G302. Stars located between $2''.5 \leq r \leq 10''$ from the centre of the cluster are shown. The $r = 10''$ cut-off approximately corresponds to the tidal radius of the globular cluster while the $r = 2''.5$ cut-off is the point where extreme crowding conditions make it impossible to obtain reliable stellar photometry. To estimate the metallicity of G302 I took the dereddened fiducial red-giant branch sequences for several Galactic globular clusters (from Da Costa & Armandroff 1990 [36], hereafter referred to as DCA), shifted them to the distance of M31 ($\mu_0 = 24.3$), and overlaid them onto Figure 5.1. The lack of a turn-over at the top of the G302 red-giant branch is consistent with a metal-poor population with an iron abundance of $[\mathrm{Fe/H}] \simeq -1.5$ to -2.2. I interpolated between the DCA fiducial sequences to obtain $[\mathrm{Fe/H}] = -1.85 \pm 0.12$ for G302, where the uncertainty is one-third of the spread in the red-giant branch and corresponds to approximately one standard deviation if I assume the spread in the red-giant branch is due to normally distributed errors in the photometry. This estimate of the iron abundance for G302 agrees with spectroscopic estimates by HBK, $[\mathrm{Fe/H}] = -1.76 \pm 0.18$, and de Freitas Pacheco (1997) [39], $[\mathrm{Fe/H}] = -1.80 \pm 0.2$. If the *Hipparcos* distance modulus for M31 ($\mu_0 = 24.77 \pm 0.11$, Feast & Catchpole 1997 [53]) is adopted the iron abundance for G302 becomes $[\mathrm{Fe/H}] = -2.2$. This is $\sim 2.5\sigma$ less than the spectroscopic values (which are independent of distance).

Asymptotic-giant branch stars in G302 are clearly present to the blue of the low-metallicity fiducial sequences. Unfortunately the asymptotic-giant branch blends with the blue edge of the red-giant branch so it is not possible to unambiguously distinguish asymptotic-giant branch stars from red-giant branch stars. This is primarily due to photometric scatter ($\sigma_{V-I} \simeq 0.06$ at $V = 23$) and, to a lesser degree, contamination from stars in the halo of M31.

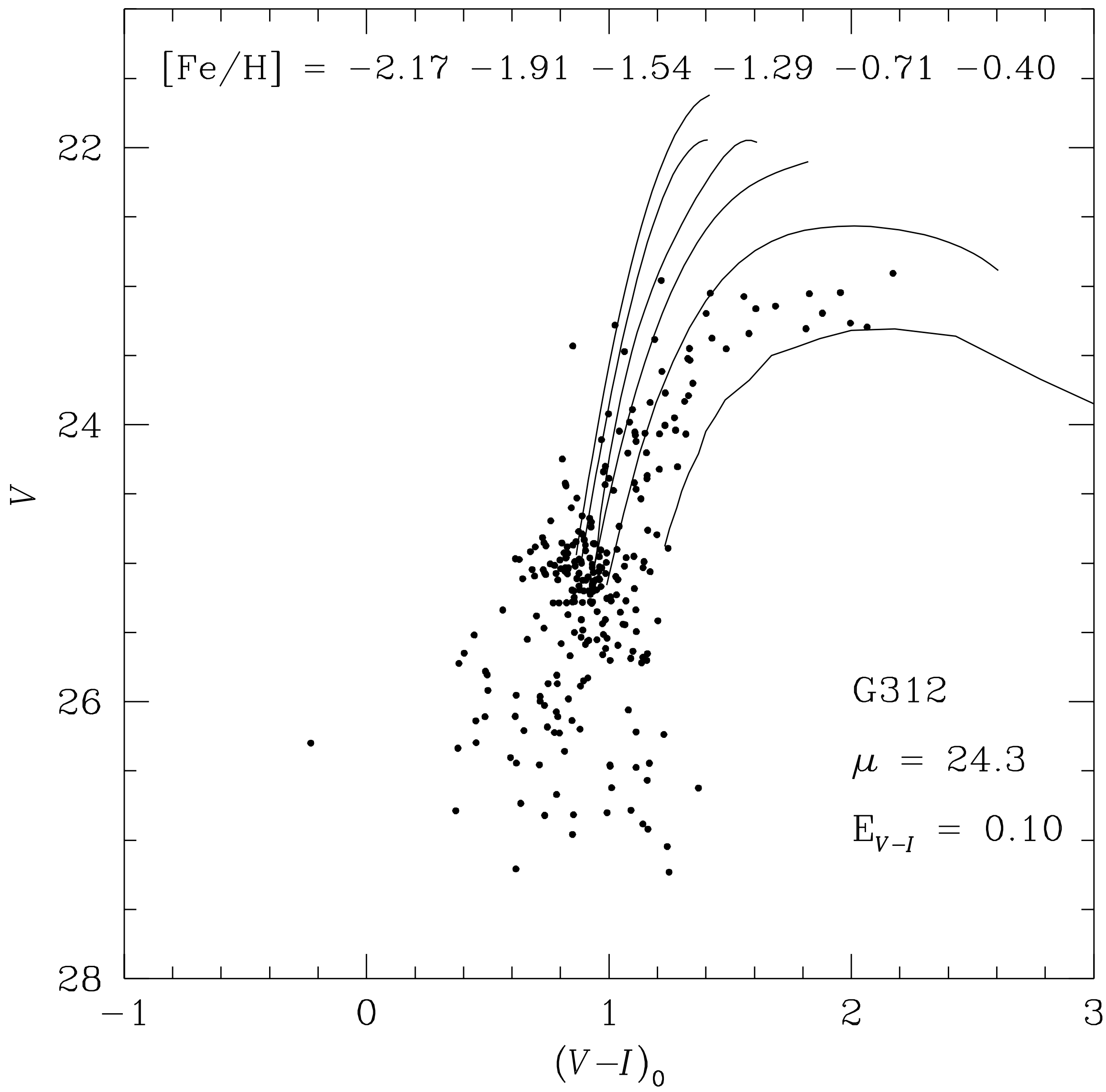

Figure 5.2: This figure shows the CMD for G312. As in Figure 5.1 only stars between $2''.5 \leq r \leq 10''$ are plotted. The fiducial sequences are from DCA with the exception of the [Fe/H] = −0.40 fiducial which is from Bergbusch & VandenBerg (1992) [11]. The lack of a blue horizontal branch is consistent with G312 being metal-rich.

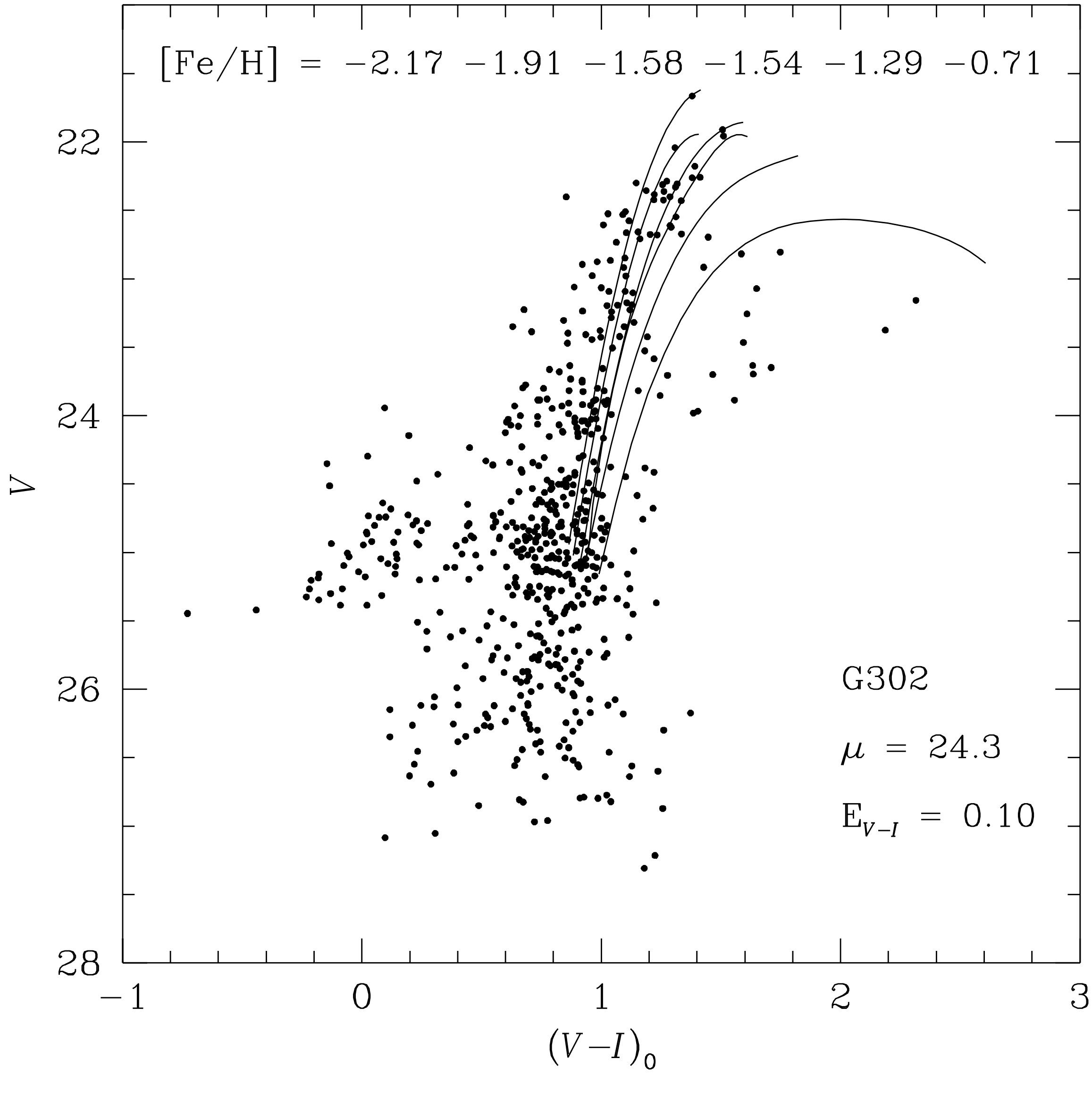

Figure 5.1: This figure shows the CMD for G302. Only stars between $2''.5 \leq r \leq 10''$ are plotted to minimize contamination from stars in the halo of M31 and from unreliable photometry due to the extreme crowding in the central regions of G302. The distinct blue horizontal branch is consistent with a metal-poor stellar population. The fiducial sequences are of Galactic globular clusters and were taken from DCA.

20 ± 5 halo stars in the red-giant branch for G302. Near G312 the background surface density is $\Sigma_{\rm bkgd} = 0.0174 \pm 0.0012$ stars/$\square''$, corresponding to 5 ± 1 stars in the red-giant branch of G312. These estimates are reasonably consistent with the numbers of objects in the upper halves of Figures 5.1 and 5.2 that do not fall on either the red-giant branch or the asymptotic-giant branch of each globular cluster.

On the basis of these calculations I expect that no more than $\sim 7\%$ of the objects in the G302 CMD are not members of that globular cluster and no more than $\sim 16\%$ of the objects in the G312 CMD are not members of that globular cluster. These numbers are consistent with the number of discrepant objects in each CMD so I conclude that the morphologies of the CMDs in Figures 5.1 and 5.2 are real and not due to contamination.

Chapter 5

HST Observations of G302 and G312

5.1 The Colour–Magnitude Diagrams

5.1.1 Contamination

There are four possible sources of contamination in the CMDs of the globular clusters. The first three—Galactic halo stars, background galaxies, and M31 disc stars—are discussed in Chapter 6.1.1. By scaling those results to the area on the sky covered by each globular cluster I estimate that at most 15 ± 4 of the objects with $V \leq 24$ in each of Figures 5.1 (G302) and 5.2 (G312) are due to contamination from these three sources.

The fourth source of contamination is the halo of M31 itself. To estimate the number of halo stars that should be visible in the CMD for each globular cluster I computed the stellar surface densities in the WF2 and WF4 CCDs for each field. These CCDs were centred $\sim 60''$ from the centre of the WF3 CCD (and thus the globular clusters). Since G302 and G312 have tidal radii of $\sim 10''$ the WF2 and WF4 CCDs will not suffer from contamination from globular cluster stars. The mean background surface density for M31 halo stars with $V \leq 24$ near G302 is $\Sigma_{\rm bkgd} = 0.0654 \pm 0.0024$ stars/$\Box''$, corresponding to

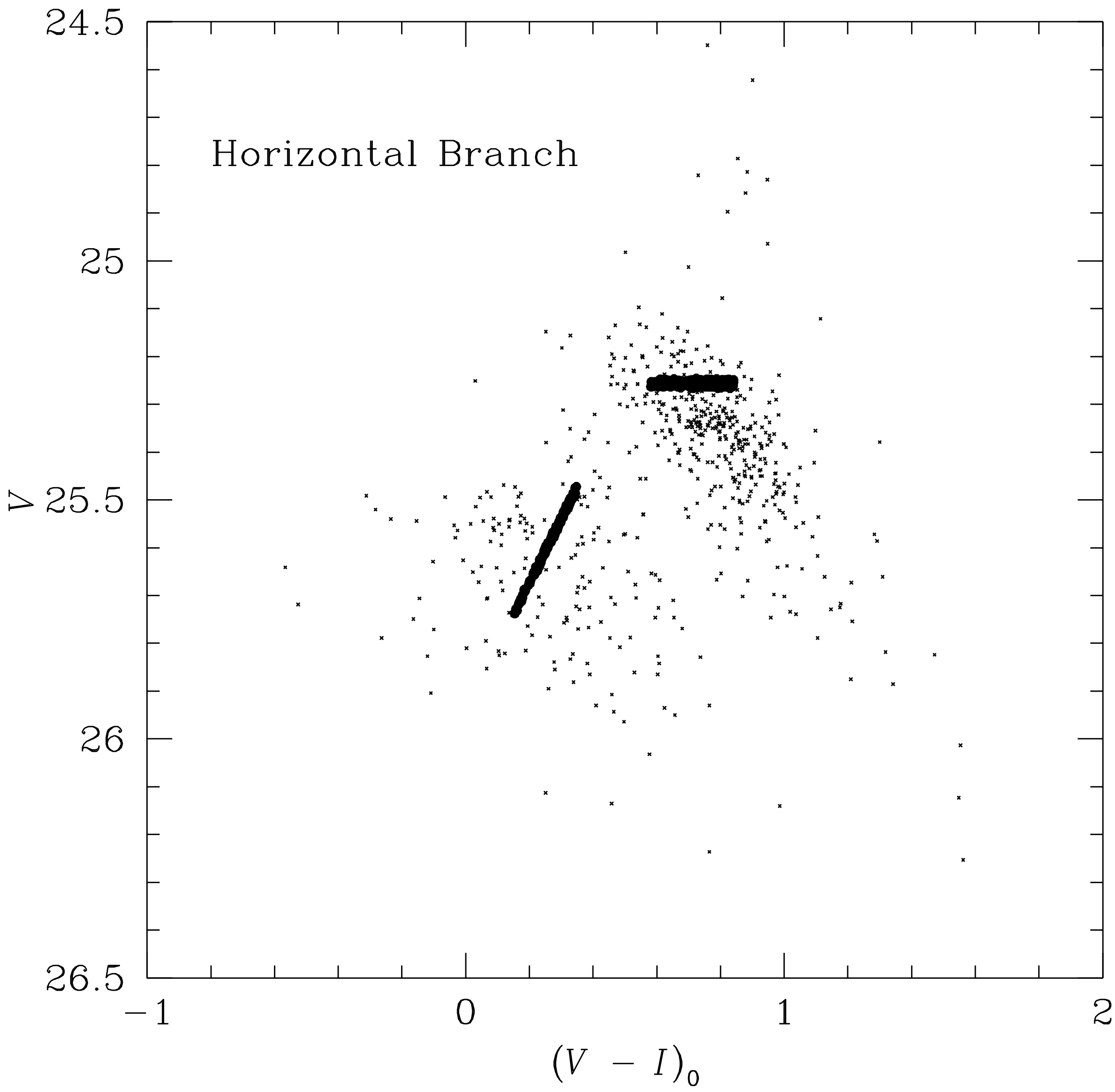

Figure 4.4: The large solid circles show the input artificial horizontal branch. The horizontal branch has been divided into distinct red and blue parts to aid in the identification of scatter from each component. Small solid squares show the recovered colours and magnitudes of the artificial stars.

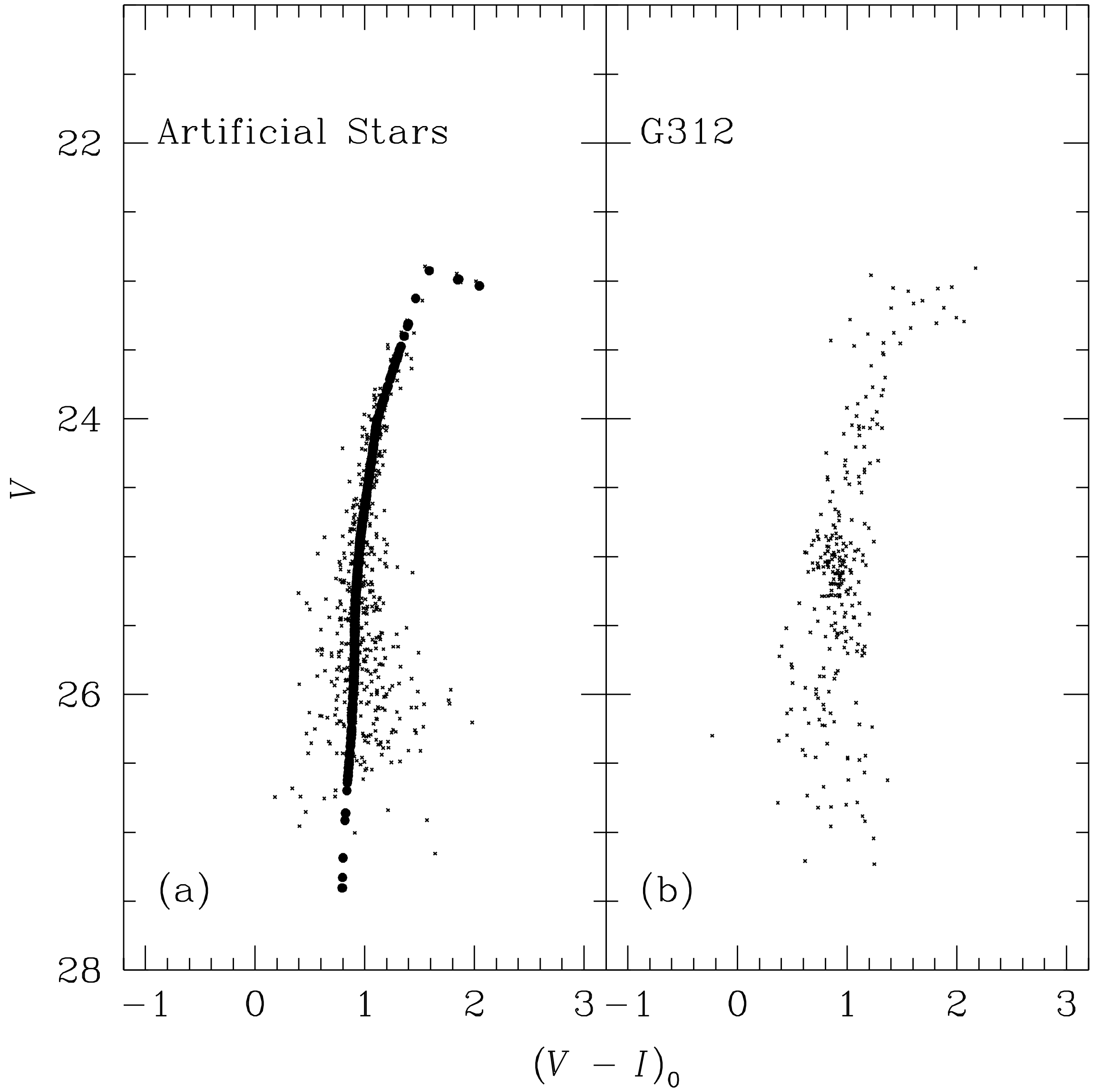

Figure 4.3: The left-hand panel (a) shows a CMD for a set of artificial stars added to the G312 WF3 field. Large solid circles represent the input colours and magnitudes while small solid squares represent the recovered photometry. For clarity, only red-giant branch stars are shown in this figure. The right-hand panel (b) shows the observed CMD for red giants in G312. The spread in the recovered colours in the artificial stars is approximately the same as the spread in colour observed in the G312 CMD suggesting that the observed width of the red-giant branch is due to photometric uncertainties and is not intrinsic to G312.

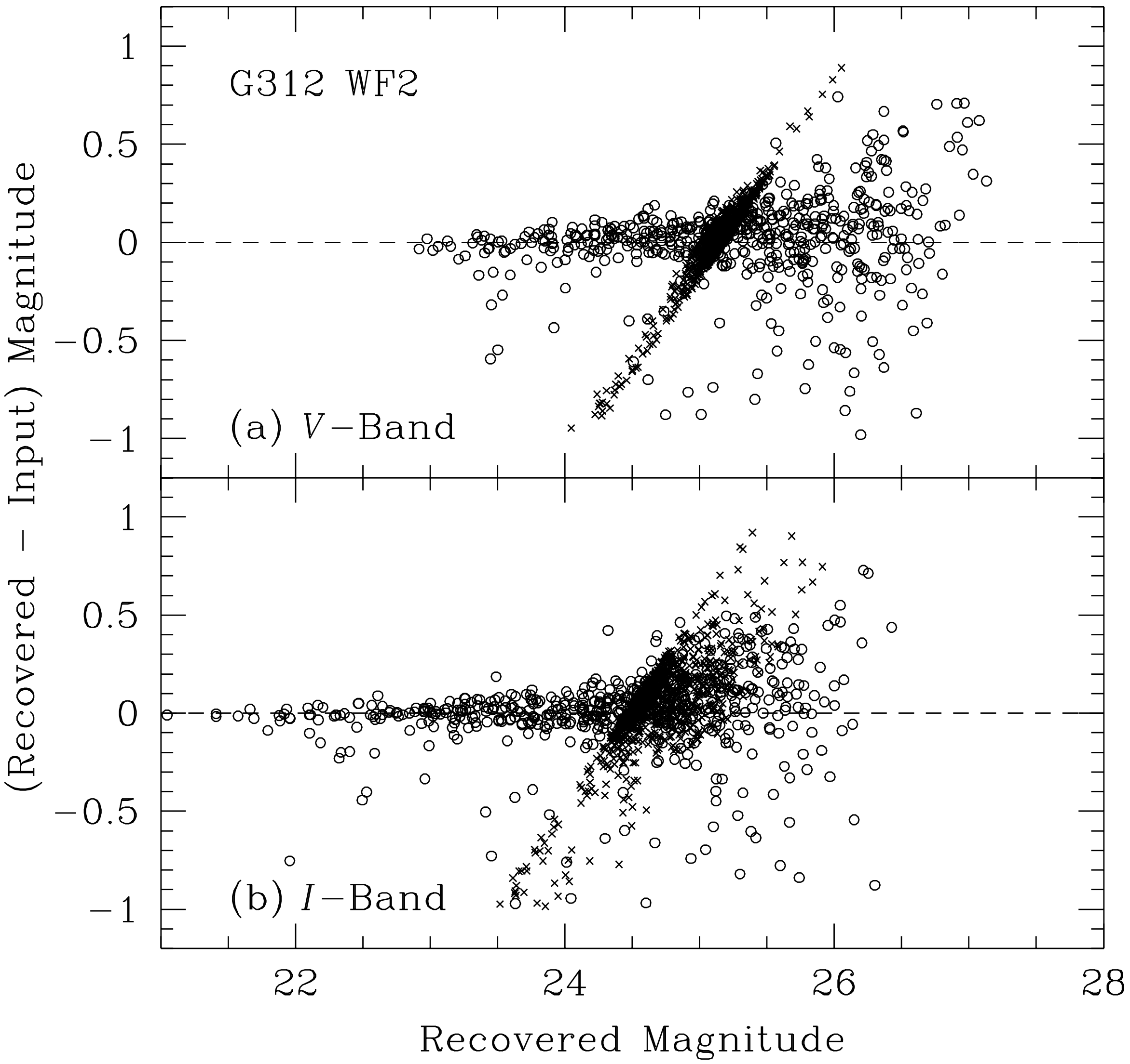

Figure 4.2: This figure shows the scatter in the recovered magnitudes of the artificial stars added to the WF2 background field $\sim 1'$ south of the globular cluster G312. The upper (a) panel shows the observed magnitude shifts for the V-band photometry while the lower (b) panel shows the observed magnitude shifts in the I-band. Open circles denote red-giant branch stars while crosses denote horizontal branch stars. Only stars with Δ mag ≤ 1 mag are shown. Negative magnitude shifts indicate that the star was recovered brighter than it was input while positive shifts indicate the star was recovered fainter than it was input. The apparent excess scatter in the horizontal branch artificial stars is an artifact of the large number of artificial horizontal branch stars (see Chapter 4.4).

branch is primarily due to photometric uncertainties. Figure 4.3 shows that photometric uncertainties are sufficient to explain all the observed width of the red-giant branch of G312.

Table 4.10 and Figure 4.4 show that horizontal branch stars, because of the large colour spread in the horizontal branch, can suffer badly from systematic differences between their input and recovered magnitudes. Blue horizontal branch stars are scattered by as much 0.5 mag in $(V-I)_0$ while red horizontal branch stars have a tendency to be recovered redder and fainter than they really are. This tends to move red horizontal branch stars into the lower half of the red-giant branch resulting in an underestimate of the total number of red horizontal branch stars in the globular cluster. These results show that stars from the red and blue sides of the horizontal branch can be scattered into the RR Lyrae gap making it very difficult to distinguish RR Lyrae candidates from other horizontal branch stars that have simply scattered into the RR Lyrae gap.

RR Lyrae stars are variable stars with periods of ~ 10 to ~ 20 hours. They can, in principle, be identified simply by constructing a light curve for each star and looking for variability. Unfortunately this approach will not work for the *HST* data used in this thesis since the observations occurred over approximately three hours, which is only $\sim 15\%$ to $\sim 30\%$ of the period of the RR Lyraes. Since the photometric uncertainties at the level of the RR Lyraes ($V \sim 25$) are $\sigma_V \sim 0.09$ mag and the variability of an RR Lyrae star is $\Delta V \sim 0.5$ mag it was not possible to determine if any of the stars in the RR Lyrae gap were varying in magnitude over the course of the observations.

V	$[V]$	$[\sigma_V]$	$[\delta_V]$	$\hat{\sigma}_V$	$[(V-I)_0]$	$[\sigma_{(V-I)_0}]$	$[\delta_{(V-I)_0}]$	$\hat{\sigma}_{(V-I)_0}$	N
22.75	22.947	0.058	−0.008	0.039	1.536	0.074	0.002	0.049	2
23.25	23.361	0.065	−0.030	0.061	1.382	0.082	−0.013	0.028	19
23.75	23.800	0.064	−0.006	0.056	1.237	0.089	−0.010	0.062	31
24.25	24.262	0.081	0.024	0.055	1.081	0.102	0.009	0.064	55
24.75	24.781	0.087	0.023	0.085	1.007	0.115	0.028	0.087	78
25.25	25.251	0.104	0.041	0.098	0.918	0.138	−0.006	0.094	110
25.75	25.752	0.128	0.043	0.176	0.890	0.177	−0.009	0.187	116
26.25	26.235	0.179	0.068	0.277	0.881	0.244	0.004	0.192	88
26.75	26.654	0.232	0.138	0.412	0.873	0.319	0.042	0.184	33
27.25	27.076	0.308	0.347	0.052	0.826	0.415	−0.011	0.169	3

Table 4.9: Magnitude shifts in the red-giant branch artificial star data.

V	$[V]$	$[\sigma_V]$	$[\delta_V]$	$\hat{\sigma}_V$	$[(V-I)_0]$	$[\sigma_{(V-I)_0}]$	$[\delta_{(V-I)_0}]$	$\hat{\sigma}_{(V-I)_0}$	N
24.25	24.384	0.073	−0.744	0.100	0.623	0.106	0.099	0.159	12
24.75	24.911	0.086	−0.194	0.123	0.429	0.134	0.010	0.181	94
25.25	25.182	0.102	0.055	0.090	0.537	0.153	−0.020	0.136	823
25.75	25.615	0.214	0.486	0.200	0.945	0.236	0.400	0.293	12
26.25	26.054	0.246	0.890	0.000	1.569	0.274	0.856	0.000	1

Table 4.10: Magnitude shifts in the horizontal branch artificial star data.

the systematic uncertainties in the photometric reductions do not affect the morphology of the CMDs above $V \sim 26$.

Figure 4.3 shows a CMD created from a set of artificial red-giant branch stars added to the G312 WF3 image. The horizontal branch stars have been omitted in order to show the increase in the scatter in the recovered colours at fainter magnitudes. The amount of scatter seen at a particular magnitude is comparable to the amount of scatter seen in the CMD of G312, which is believed to be made up of stars with a single metallicity. If the stellar populations in M31's globular clusters are analogous to the stellar populations in the Galactic globular clusters then the observed spread in G312's red-giant

can be used to directly determine the uncertainty in a star's observed magnitude. An examination of this figure suggests that the distribution of artificial horizontal branch stars is different from the distribution of artificial red-giant branch stars. To test if the two distributions are the same I performed a Kolmogorov–Smirnov (KS) test. The results showed that the distributions of recovered magnitudes for the artificial red-giant branch and horizontal branch stars are the same at the 98.892% confidence level in the V-band and at the 99.999% confidence level in the I-band. This suggests that the null hypothesis (that the distributions of the two types of stars are the same) can not be rejected. Therefore there is no evidence that the apparent excess scatter in the magnitudes of the horizontal branch artificial stars is anything other than an artifact of the large number of artificial horizontal branch stars.

Table 4.9 lists the systematic shifts in V and $(V-I)_0$ as well as the degree of scatter as a function of magnitude for the artificial red-giant branch stars of G312. Table 4.10 lists these quantities for the G312 artificial horizontal branch stars. In these tables the notation $[x]$ indicates the median value of the individual x_i values. The columns are (1) the boundaries of the bin, (2) the median recovered magnitude, $[V]$; (3) the median photometric uncertainty in the recovered magnitudes (from DAOPHOT), $[\sigma_V]$; (4) the median magnitude difference, $[\delta_V] \equiv [V_{\mathrm{recovered}} - V_{\mathrm{input}}]$; (5) the amount of scatter present in the artificial stars in that bin, $\hat{\sigma}_V \equiv \left[\left|\delta_V - [\delta_V]\right|\right]$; columns (6) to (9) are the same quantities for the $(V-I)_0$ colour; and (10) is the number of artificial stars in that bin. These quantities are identical to those described by Stetson & Harris (1988) [142] except for $\hat{\sigma}$, which is defined in non-parametric terms instead of in Gaussian terms.

There is a slight tendency for the reduction process to underestimate the brightnesses of stars near the photometric limit of the data (see column 4 of Table 4.9). However, this systematic shift is less than the internal scatter in the photometry and is smaller than ~ 0.05 mag for red-giant branch stars at the level of the horizontal branch. Therefore,

4.4 Artificial Star Tests

In order to determine the effects of crowding, and the efficiency of the star-finding and photometry techniques, on the photometry a series of artificial star tests were performed. The following procedure was used to generate and recover artificial stars:

1. For each field a series of artificial stars with $(V, (V-I))$ colours based on the observed CMD and luminosity function of the M31 halo stars was generated.

2. The artificial stars were added on to each of the original images. The total number of artificial stars added in each field was $\sim 10\%$ of the total number of stars in that field.

3. The entire data reduction process for the photometry that was described in Chapter 4.3 (FIND/ALLFRAME/culling/matching) was performed on this new set of images. The resulting photometry was then matched against the original list of artificial stars for that field.

4. This process was repeated until the number of recovered artificial stars was approximately the same as the number of real stars found on that CCD.

This process was performed for each CCD field.

Figure 4.2 shows the relationship between the input magnitudes of the artificial stars and their recovered magnitudes for a typical set of stars, in this case using the WF2 field near the globular cluster G312. Artificial stars with magnitude differences of more than $\pm\Delta V = 1$ mag have been omitted. This figure plots the magnitude difference as a function of the recovered magnitude, not the input magnitude, of the artificial stars. This was done because the observed magnitudes of stars in the real data set are recovered magnitudes, not the true (or input) magnitudes of the real stars. Therefore, Figure 4.2

ID	X	Y	r	V	σ_V	χ_V	I	σ_I	χ_I
802	417.826	417.893	$0''.039$	17.983	0.060	1.509	17.020	0.061	1.704
811	419.875	419.020	$0''.198$	18.662	0.078	1.841	17.422	0.053	1.494
770	415.495	417.557	$0''.274$	19.926	0.055	1.014	18.819	0.065	1.407
866	417.573	427.651	$0''.972$	22.019	0.086	1.941	20.250	0.045	1.217
783	429.730	414.665	$1''.191$	22.086	0.056	1.330	20.499	0.050	1.467
803	405.224	418.070	$1''.294$	22.180	0.053	1.224	20.275	0.048	1.413
841	396.894	424.414	$2''.221$	22.310	0.073	1.267	20.965	0.059	1.244
871	412.104	427.591	$1''.141$	22.355	0.072	1.544	21.183	0.066	1.812
915	418.244	434.008	$1''.603$	22.645	0.079	1.777	21.687	0.068	1.789
796	434.824	416.729	$1''.658$	22.676	0.041	0.920	21.468	0.035	0.953
⋮	⋮	⋮	⋮	⋮	⋮	⋮	⋮	⋮	⋮

Table 4.8: A sample of the stellar photometry for the globular cluster G312.

CCD	ID	X	Y	V	σ_V	χ_V	I	σ_I	χ_I
WF3	503	689.043	346.030	17.369	0.050	0.827	16.723	0.025	0.758
WF2	1198	252.106	634.779	17.758	0.057	0.745	16.875	0.055	0.830
WF4	537	650.877	360.807	17.934	0.051	0.982	17.217	0.026	0.801
WF3	802	417.826	417.893	17.983	0.060	1.509	17.020	0.061	1.704
WF4	869	310.743	507.150	18.569	0.028	0.630	17.479	0.026	0.789
WF3	811	419.875	419.020	18.662	0.078	1.841	17.422	0.053	1.494
WF3	1654	229.986	766.329	18.743	0.035	0.907	18.116	0.019	0.601
WF3	412	167.937	301.246	18.896	0.034	0.877	16.521	0.030	0.756
WF3	770	415.495	417.557	19.926	0.055	1.014	18.819	0.065	1.407
WF3	1451	676.379	661.313	20.225	0.038	0.948	18.614	0.025	0.736
⋮	⋮	⋮	⋮	⋮	⋮	⋮	⋮	⋮	⋮

Table 4.6: A sample of the stellar photometry for G312 and the surrounding fields.

ID	X	Y	r	V	σ_V	χ_V	I	σ_I	χ_I
2583	437.139	413.836	0.″230	18.195	0.065	1.341	17.356	0.059	1.551
2606	439.952	415.701	0.″332	18.454	0.063	1.462	17.642	0.064	1.830
2489	438.016	410.038	0.″265	18.854	0.095	1.700	17.995	0.057	1.240
2474	441.016	410.137	0.″308	19.183	0.111	1.823	17.977	0.073	1.819
2554	442.354	412.389	0.″332	19.741	0.101	1.325	18.639	0.076	1.507
2532	429.789	412.006	0.″921	20.376	0.079	1.847	19.356	0.067	1.961
2420	440.762	402.723	0.″989	20.812	0.071	1.629	19.648	0.063	1.828
2553	428.372	414.756	1.″084	20.947	0.058	1.355	19.735	0.043	1.256
2460	418.943	405.789	2.″108	21.148	0.027	0.679	19.992	0.029	0.922
2456	427.305	405.329	1.″368	21.241	0.048	1.071	19.853	0.046	1.304
⋮	⋮	⋮	⋮	⋮	⋮	⋮	⋮	⋮	⋮

Table 4.7: A sample of the stellar photometry for the globular cluster G302.

V	G302 σ_V	G312 σ_V	I	G302 σ_I	G312 σ_I
20.25	...	...	20.25	0.031	...
20.75	...	...	20.75	0.026	0.023
21.25	...	...	21.25	0.031	0.028
21.75	0.038	...	21.75	0.036	0.033
22.25	0.037	...	22.25	0.038	0.039
22.75	0.043	0.046	22.75	0.046	0.043
23.25	0.049	0.049	23.25	0.051	0.049
23.75	0.055	0.051	23.75	0.067	0.063
24.25	0.065	0.062	24.25	0.081	0.077
24.75	0.079	0.077	24.75	0.118	0.099
25.25	0.094	0.090	25.25	0.145	0.153
25.75	0.129	0.121	25.75	0.217	0.222
26.25	0.176	0.182	26.25	0.333	0.314
26.75	0.262	0.271	26.75	0.570	0.457
27.25	0.356	0.310	27.25	...	...
27.75	...	...	27.75	...	...
28.25	...	...	28.25	...	...

Table 4.4: Photometric uncertainties for G302 and G312.

CCD	ID	X	Y	V	σ_V	χ_V	I	σ_I	χ_I
WF3	892	64.328	212.348	17.032	0.082	1.000	16.294	0.071	1.000
WF2	3440	466.457	631.376	17.628	0.084	0.744	16.365	0.077	0.727
WF3	2583	437.139	413.836	18.195	0.065	1.341	17.356	0.059	1.551
WF3	2606	439.952	415.701	18.454	0.063	1.462	17.642	0.064	1.830
WF3	2489	438.016	410.038	18.854	0.095	1.700	17.995	0.057	1.240
WF4	4532	300.305	699.237	19.152	0.031	0.739	17.418	0.030	0.877
WF3	2474	441.016	410.137	19.183	0.111	1.823	17.977	0.073	1.819
WF2	150	321.521	80.650	19.311	0.036	0.657	16.489	0.089	0.941
WF2	2719	310.787	523.757	19.669	0.070	1.499	18.432	0.063	1.959
WF3	2554	442.354	412.389	19.741	0.101	1.325	18.639	0.076	1.507
⋮	⋮	⋮	⋮	⋮	⋮	⋮	⋮	⋮	⋮

Table 4.5: A sample of the stellar photometry for G302 and the surrounding fields.

V	G302F σ_V	G312F σ_V	I	G302F σ_I	G312F σ_I
20.25	0.035	0.033	20.25	0.033	0.028
20.75	0.033	0.038	20.75	0.028	0.029
21.25	...	0.031	21.25	0.030	0.028
21.75	0.050	0.035	21.75	0.031	0.031
22.25	0.043	0.038	22.25	0.034	0.034
22.75	0.039	0.042	22.75	0.041	0.040
23.25	0.045	0.045	23.25	0.049	0.048
23.75	0.053	0.053	23.75	0.061	0.060
24.25	0.062	0.061	24.25	0.075	0.073
24.75	0.076	0.076	24.75	0.100	0.100
25.25	0.091	0.090	25.25	0.142	0.144
25.75	0.121	0.122	25.75	0.208	0.205
26.25	0.165	0.166	26.25	0.299	0.304
26.75	0.235	0.241	26.75	0.463	0.459
27.25	0.344	0.346	27.25	0.752	0.677
27.75	0.547	0.492	27.75	...	...

Table 4.3: Photometric uncertainties in the *HST* photometry of the halo stars.

uncertainties for the entire culled data set are listed in Table 4.3. The mean photometric uncertainties for the globular cluster stars are listed in Table 4.4.

stars with a final χ value greater than two were discarded. In order to eliminate stars with poorly determined magnitudes an interactive approach based on the uncertainty in the calibrated magnitude was used. A plot of uncertainty vs magnitude was made and a locus defined that corresponded to the expected photometric scatter at a given magnitude. Any stars that were judged to have a significantly greater uncertainty than the typical value for that magnitude were discarded. Visual examinations of the CMDs and the WFC images suggested that this culling processes did not remove any legitimate stars. It should be stressed that this culling was done *solely* on the basis of the photometric uncertainty of each star, not on the star's location on the CMD or the CCD. Mean photometric uncertainties for the entire culled data set are listed in Table 4.3. The mean photometric uncertainties, based on the formal photometric uncertainties returned by DAOPHOT II/ALLFRAME, are listed in Table 4.4.

The entire data set of photometry is published on Volume 9 of the AAS CD-Rom series. The first ten lines of the complete set of calibrated stellar photometry for G302 and its surrounding fields is listed in Table 4.5 while a sample of the photometry for G312 and its surrounding fields (with the exception of the PC field) is listed in Table 4.6. Column (1) gives the CCD that the star was observed on. Column (2) gives an identification number for each star. The identification numbers are only unique for stars on a given CCD. Columns (3) and (4) give the location of the star on the CCD in pixel coördinates. Column (5) is the V-band magnitude, column (6) the 1σ uncertainty in the V-band magnitude, and column (7) is the value of the DAOPHOT χ statistic. Columns (8) to (10) are the same as columns (5) to (7) except they give values for the I-band. Tables 4.7 and 4.8 list a sample of the photometry for stars within $10''$ of the centre of G302 and G312. This data is the same as for Tables 4.5 and 4.6 except the CCD is always WF3, so a CCD name is not listed in the tables and an extra column, giving r, the distance of the star from the centre of the globular cluster, has been added. Mean photometric

transfer efficiency correction of 2% (Holtzman et al. 1995a [72]) for all the WFPC2 images. The reddening from the Milky Way galaxy in the direction of G302 and G312 is $E_{B-V} = 0.08 \pm 0.02$ (Burstein & Heiles 1982 [23]). The E_{B-V} reddening was converted to a E_{V-I} reddening using the relationship of Bessell & Brett (1988) [13]: $E_{V-I} = 1.25E_{B-V} = 0.10 \pm 0.03$. The interstellar extinctions were taken from Tables 12A and 12B of Holtzman et al. (1995) [73]. These extinction values are dependent on the stellar spectrum. For a K5 giant the extinctions were $A_V = 0.320$ and $A_I = 0.190$.

The standard distance modulus for M31 is $\mu_0 = (m - M)_0 = 24.3 \pm 0.1$ (van den Bergh 1991 [148]). This value agrees well with other M31 distance moduli obtained using Population II distance indicators. Pritchet & van den Bergh (1987) [114] found $\mu = 24.34 \pm 0.15$ from RR Lyrae variables in the halo of M31 while Christian & Heasley (1991) [29] found $\mu \sim 24.3$ from the brightest red giants in M31 globular clusters. Studies of Population I distance indicators such as Cepheids (e.g. Freedman & Madore 1990 [54]) and carbon stars (e.g. Brewer et al. 1995 [19]) find $\mu \simeq 24.4$, slightly larger than the Population II value. The lower distance modulus was adopted since the halo and globular clusters of M31 appear to consist of Population II stars. As this work was being completed, parallax measurements from the *Hipparcos* satellite were published which have led to a revised estimate of the distance to M31. The new distance modulus of $\mu_0 = 24.77 \pm 0.11$ (Feast & Catchpole 1997 [53]), or 900 ± 45 kpc, is a 25% increase over the distance adopted in this work. However, other researchers (e.g. Madore & Freedman 1997 [93]) have argued that the *Hipparcos* data supports the old distance scale so the question of M31's distance has still not been answered.

ALLFRAME's χ statistic represents the ratio of the observed pixel-to-pixel scatter in the PSF fitting residuals to the expected amount of scatter given the noise properties of the data. Values of χ that are significantly greater than unity indicate that a stellar image is not well fit by the stellar PSF and thus may not be a star. In light of this any

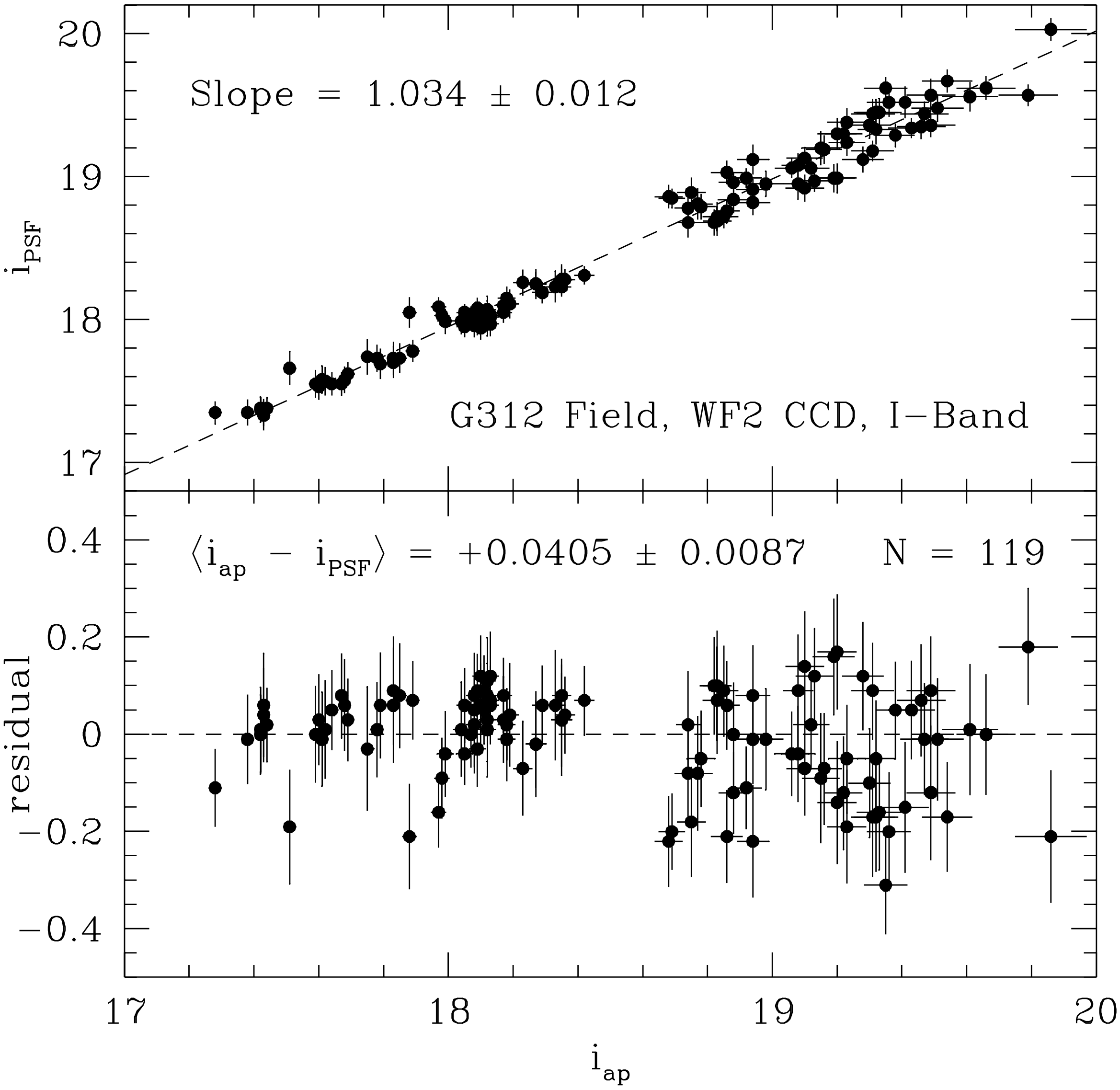

Figure 4.1: The upper panel shows the aperture-magnitude vs PSF-magnitude relation for the *I*-band photometry for the WF2 CCD in the G312 field. Stars were discarded until the slope of this relation approached unity. The lower panel shows the residuals ($(i_{\rm ap} - i_{\rm PSF}) - \Delta i$, where $\Delta i = \langle i_{\rm ap} - i_{\rm PSF} \rangle$). Stars that failed the culling process described in Chapter 4.3 have not been plotted.

interactively discarded until the slope approached unity and discarding additional stars failed to drive the slope closer to unity. The aperture correction was then computed from the sample of stars that survived this culling process. Table 4.2 lists the adopted aperture corrections for the WF2 and WF4 CCDs. Figure 4.1 shows the residuals for the I-band aperture corrections to the WF2 CCD in the G312 field. I was unable to obtain reliable aperture corrections for the PC images of the G312 field due to a lack of bright stars in this field. Photometry in this field exhibited an unusually high degree of scatter despite the stellar images appearing to be normal to the eye. As a result the PC data in the G312 field is not included in any of the analysis presented here.

Field	CCD	Filter	$\langle \mathrm{ap} - \mathrm{PSF} \rangle$	Slope	N
G302	PC	F555W	-0.0226 ± 0.0355	0.992	12
		F814W	-0.0222 ± 0.0218	1.009	29
	WF2	F555W	$+0.0184 \pm 0.0216$	1.065	25
		F814W	$+0.0374 \pm 0.0099$	1.017	80
	WF3	F555W	-0.0124 ± 0.0101	1.003	87
		F814W	$+0.0150 \pm 0.0063$	1.018	217
	WF4	F555W	$+0.0333 \pm 0.0119$	1.011	90
		F814W	$+0.0297 \pm 0.0053$	1.005	252
G312	PC	F555W	...	...	...
		F814W	...	...	...
	WF2	F555W	-0.0344 ± 0.0144	1.008	186
		F814W	$+0.0405 \pm 0.0087$	1.034	119
	WF3	F555W	-0.0198 ± 0.0081	1.018	101
		F814W	-0.0030 ± 0.0013	1.015	125
	WF4	F555W	$+0.0513 \pm 0.0165$	1.001	85
		F814W	$+0.0333 \pm 0.0102$	1.027	89

Table 4.2: Aperture corrections for the *HST* data.

The photometry was calibrated to standard Johnson–Cousins V- and I-band magnitudes using the transformations of Holtzman et al. (1995b) [73]. I adopted a charge

detections closer to the centres of the globular clusters than this were usually spurious.

The resulting list of stellar candidates was used as input to ALLFRAME. ALLFRAME does simultaneous PSF fitting on all the *original* images (*not* the combined median-subtracted image) to preserve the photometric properties of the data. The PSFs used (Stetson 1996 [137]) were two-dimensional Moffatians with $\beta = 1.5$, $\gamma = 2$ and a look-up table of residuals. The PSFs varied quadratically over each CCD to account for variations in the form of the PSF from one part of the CCD to another. Only stars that appeared in at least seven frames in each filter were considered to be real stars. Tests with different minimum numbers of frames showed that requiring stars to be found on at least seven frames provided a clean CMD without significantly affecting the limiting magnitude of the CMD.

Aperture corrections were obtained for each CCD in the following manner. First a set of ~ 50 bright, isolated stars was selected on each CCD and all the remaining stars were subtracted from these images. Next, the total magnitude in an aperture with a radius of $0\farcs5$ (Holtzman et al. 1995b [73]) was measured for each star. Aperture corrections were defined in the sense $\Delta v = v_{\rm ap} - v_{\rm PSF}$ for each of the isolated stars. We discarded any star with a combined photometric uncertainty of $\sqrt{\sigma_{\rm ap}^2 + \sigma_{\rm PSF}^2} > 0.14$, which corresponds to a signal-to-noise ratio of ~ 10 for each of the aperture and PSF magnitudes. The size of the aperture correction should be independent of magnitude so a plot of $v_{\rm ap}$ vs $v_{\rm PSF}$ (see Figure 4.1) should yield a slope of unity with a zero-point offset corresponding to the value of the aperture correction. However, the WF CCDs suffer from considerable cosmic ray contamination that may bias the observed aperture magnitudes towards brighter magnitudes. In addition the presence of background galaxies and undetected faint stars can bias the $v_{\rm ap} - v_{\rm PSF}$ relation away from a slope of unity. To correct for this a plot of the PSF-magnitudes as a function of the aperture-magnitudes for each WF CCD was made. Stars that biased the best-fitting straight line away from a slope of unity were

4.3 Data Reductions

Photometry was performed on stars imaged by the WFPC2's Wide Field CCDs using the DAOPHOT II/ALLFRAME software (Stetson 1987 [141], Stetson 1994 [138]). All nineteen images for each field were re-registered to a common coördinate system and median-combined. This served to eliminate cosmic-ray hits and to increase the signal-to-noise ratio in the data allowing fainter stars to be detected. Cosmic rays strike each CCD at a rate of ~ 20 per second so on a 500 second exposure $\sim 1.7\%$ of the pixels are affected by cosmic rays.

In order to eliminated large-scale gradients in the images due to unresolved light from the globular clusters (the gradient in the light from the halo of M31 was $\lesssim 1\%$ in both the G302 and G312 fields) a square median-filter was run over the combined image to produce a map of the large-scale gradients. This smoothed image was then subtracted from the combined image and a constant sky added back to produce a median-subtracted image. The size of the square median-filter was ~ 5 times the stellar full-width at half-maximum (FWHM) to avoid smoothing out structure in the stellar images (e.g. Stetson & Harris 1988 [142]). Subtracting the median-filtered image resulted in a reasonably clean subtraction of the integrated light from each globular cluster to within ~ 25 pixels ($\simeq 2\farcs5 \simeq 9$ pc) of the centre of each globular cluster. This process is the digital equivalent of unsharp masking.

The DAOPHOT FIND routine, with a FIND threshold of $7.5\sigma_{\rm sky}$, was used to detect peaks on the median-subtracted image. Experiments with different FIND thresholds showed that $7.5\sigma_{\rm sky}$ excluded most of the mis-identifications of noise spikes and cosmic-ray events as stars at faint magnitudes while including almost all of the stars down to near the photometric limit of the data. FIND was able to reliably detect stars to within ~ 25 pixels ($\sim 2\farcs5$) of the centre of each globular cluster. Artificial star tests showed that

globular clusters. Centring the globular clusters on the WF3 CCD ensured that as much as possible of any extended halos would be located on the same CCD as the globular cluster itself. This avoided possible systematic effects that may occur if surface brightness data and stellar number density data is transferred between the PC and WFC CCDs, with their different pixel scales and sensitivities.

3. Locating the globular clusters at the centre of the WF3 CCD allowed the use of the WF2 and WF4 CCDs to probe the stellar populations in the halo of M31. These results are presented in Chapter 6. Having two background fields for each globular cluster field made it possible to differentiate between stellar number-density enhancements that are due to statistical fluctuations in the star counts from M31 halo stars and those that are due to physical structures, such as extended halos, that are related to the globular clusters. If the globular clusters had been centred on the PC CCD then all three WFC CCDs would have been available to image the background. However, if this had been done then any extended stellar halos around the globular clusters might have overfilled the PC's field of view. This would have resulted in cluster stars contaminating the background fields.

Field	Date (1995)	Filter	Exposure (s)
G302	Nov. 5	F555W	8×500
			2×160
		F814W	7×500
			1×400
			1×160
G312	Oct. 31	F555W	8×500
			2×160
		F814W	7×500
			1×400
			1×160

Table 4.1: Log of the *HST* observations.

are bright, isolated clusters located in the halo of M31 so the amount of contamination from stars in the disc of M31 is small.

Each globular cluster was centred on the WF3 CCD. The globular clusters were located on the WF3 CCD instead of taking advantage of the higher spatial resolution offered by the smaller pixels of the PC CCD for three reasons:

1. The tidal radii of G302 and G312, as determined by fitting Michie–King models to the surface brightness profiles of G302 and G312 derived from the HRCam observations taken at the CFHT, are $r_t \simeq 10''$ (see Chapter 3). Therefore each globular cluster would occupy a significant fraction of the total field of view of the PC, leaving insufficient area left to make reliable determinations of the spatial variations in the background stellar density.

2. Grillmair et al. (1995) [59] found evidence for extended stellar halos, extending to ~ 2 to 3 times the tidal radius, in several Galactic globular clusters. Recently, GAF found weak evidence for stellar density enhancements out to $\sim 2r_t$ in some M31

4.2 Observations

I received eight orbits of *HST*[2] time. I obtained deep V- and I-band images of two bright globular clusters, G302 ($\alpha_{2000.0} = 00^{\mathrm{h}}45^{\mathrm{m}}25\overset{\mathrm{s}}{.}2$, $\delta_{2000.0} = +41°05'30''$) and G312 ($\alpha_{2000.0} = 00^{\mathrm{h}}45^{\mathrm{m}}58\overset{\mathrm{s}}{.}8$, $\delta_{2000.0} = +40°42'32''$) in the halo of M31. Deep V- and I-band HRCam images of these two clusters are also available (see Chapter 2). The *HST* data were obtained using the *HST* in cycle 5 program #5609. The WFPC2 operated at a temperature of $-88°$C and with a gain setting of 7 e^-/ADU.

Table 4.1 lists the exposures obtained in each filter. Exposure times were based on the central surface brightnesses of the two globular clusters that were determined from the CFHT observations (see Table 3.1 in Chapter 3) and chosen to avoid saturating the cores of the globular clusters. The total exposure times were 4320 seconds in the F555W (WFPC2 broadband V) filter and 4060 seconds in the F814W (WFPC2 broadband I) filter for each field. The data was preprocessed through the standard STScI pipeline for WFPC2 images. Known bad pixels were masked, and geometric corrections were applied using standard techniques.

G302 is located $32\overset{\prime}{.}1$ from the centre of M31 (at a projected distance of $R_{\mathrm{M31}} = 6.8$ kpc), approximately along the southeast minor axis. G312 is located $49\overset{\prime}{.}8$ from the centre of M31 ($R_{\mathrm{M31}} = 10.5$ kpc), also approximately along the southeast minor axis. G302 and G312 are located in fields 12 and 13 respectively of Figure 2.1. These globular clusters were selected for observation with the *HST* because there were deep CFHT images available for each cluster (see Chapter 2.1). This will allow me to make a direct comparison between the structural parameters obtained using ground-based data and that obtained using the superior resolution of the *HST*. It will then be possible to identify systematic differences between the results obtained from the two data set. G302 and G312

[2]The NASA/ESA *Hubble Space Telescope* and the Space Telescope Science Institute are operated by the Association of Universities for Research in Astronomy, Inc., under NASA contract NAS5-26555.

the WFPC2 means that seeing has a much smaller effect on the cluster images than it does for the ground-based data. Therefore structural parameters can be determined more reliably from *HST* data. By comparing the observed structural parameters between *HST* observations of a globular cluster and the CFHT observations of the same cluster it will be possible to directly determine how reliable the ground-based observations are.

Third, the ratio of cluster size to PSF size (resolution ratio) for the CFHT images of the M31 globular clusters presented in this thesis is $\sim 0\farcs7/10'' = 0.07$. This is similar to the resolution ratio ($\sim 0\farcs05/1'' = 0.05$) for globular clusters in the Virgo cluster of galaxies when observed with the Planetary Camera (or the up-coming Advanced Camera). If a comparison of the structural parameters for the M31 globular clusters determined from the ground-based data with those determined from the space-based data suggests that ground-based observations can give reliable results then it will be possible to use the *HST* to obtain detailed structural information of globular clusters out to approximately the distance of M87 (~ 17 Mpc). This would allow the structures of globular clusters in elliptical and cD galaxies to be studied to determine how the gravitational potential of the parent galaxy influences the structure of a globular cluster.

Four, *HST* images will be deep enough ($V_{\rm lim} \sim 27$) to resolve enough stars beyond the King tidal radius of a cluster to search for extended halos of unbound stars around the globular cluster. The lower resolution of the CFHT images presented in this thesis makes it impossible to observe sufficient stars to identify such a halo from the ground.

Chapter 4

The *HST* Data

4.1 Motivation for the *HST* Observations

While this work was in progress a corrective optics package was successfully installed on the *HST*. Space-based observations of M31's globular clusters have several advantages over ground-based observations[1]. In light of this I applied for time to use the *HST*'s WFPC2 to obtain high-resolution images of two globular clusters in M31. The main motivations for doing this were as follows.

First, individual stars in M31 globular clusters can be resolved on WFPC2 images to within $\sim 2''$ of the centre of the globular cluster. In the CFHT observations individual stars can only be resolved in the deepest exposures and only stars in the outer regions of the globular clusters can be resolved. Therefore, *HST* images can be used to construct CMDs that reach below the level of the horizontal branch. This allows stellar population studies to be done to determine ages and metallicities.

Second, the stellar PSF on WFC images has a FWHM of $\sim 0\farcs15$. This is ~ 5 times smaller than the size of the seeing disc in the CFHT data. The improved resolution of

[1]Recent advances in adaptive optics for astronomical telescopes have made ground-based observations of globular clusters in M31 comparable to *HST* observations. The Adaptive Optics Bonnette at the CFHT (for example) can obtain diffraction-limited near-infrared images of the cores of M31 globular clusters.

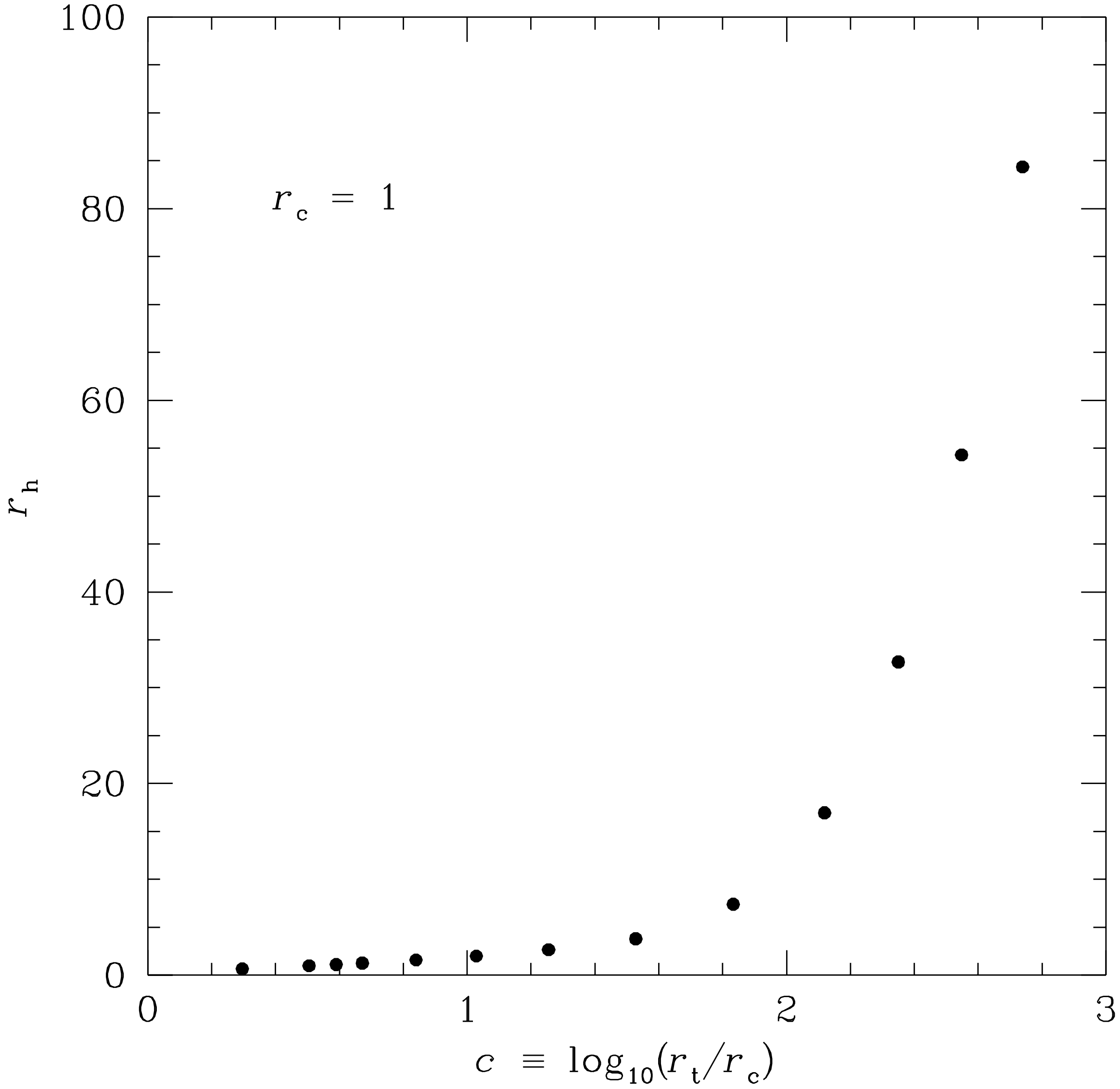

Figure 3.10: This figure shows the one-to-one relationship between the concentration of an isotropic single-mass King model and its three-dimensional half-mass radius.

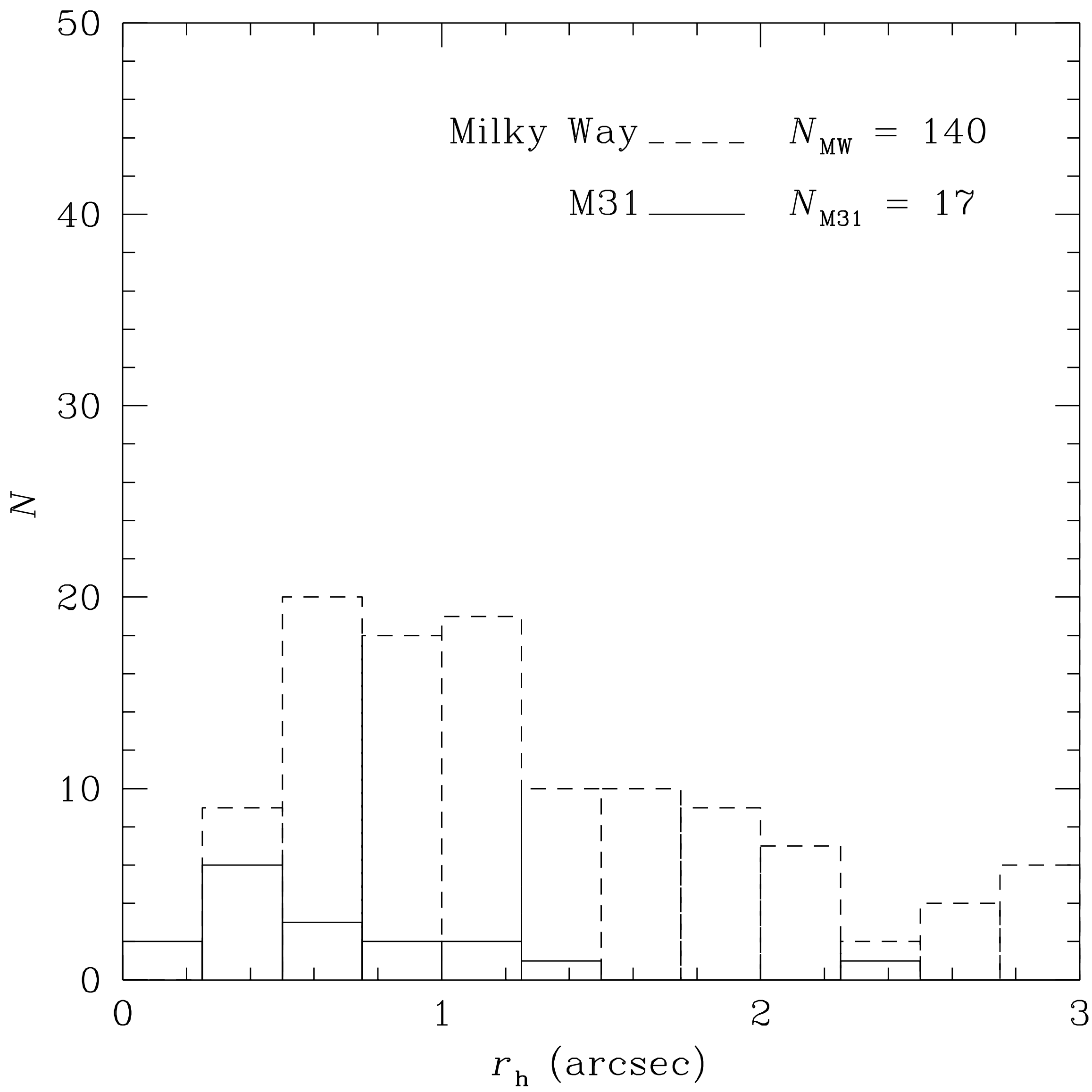

Figure 3.9: This figure shows half-mass radii derived from the CFHT HRCam images. The solid histogram represents the M31 globular clusters while the dashed histogram represents the Galactic globular clusters. The half-mass radii for the Galactic globular clusters have been scaled to a distance of 725 kpc.

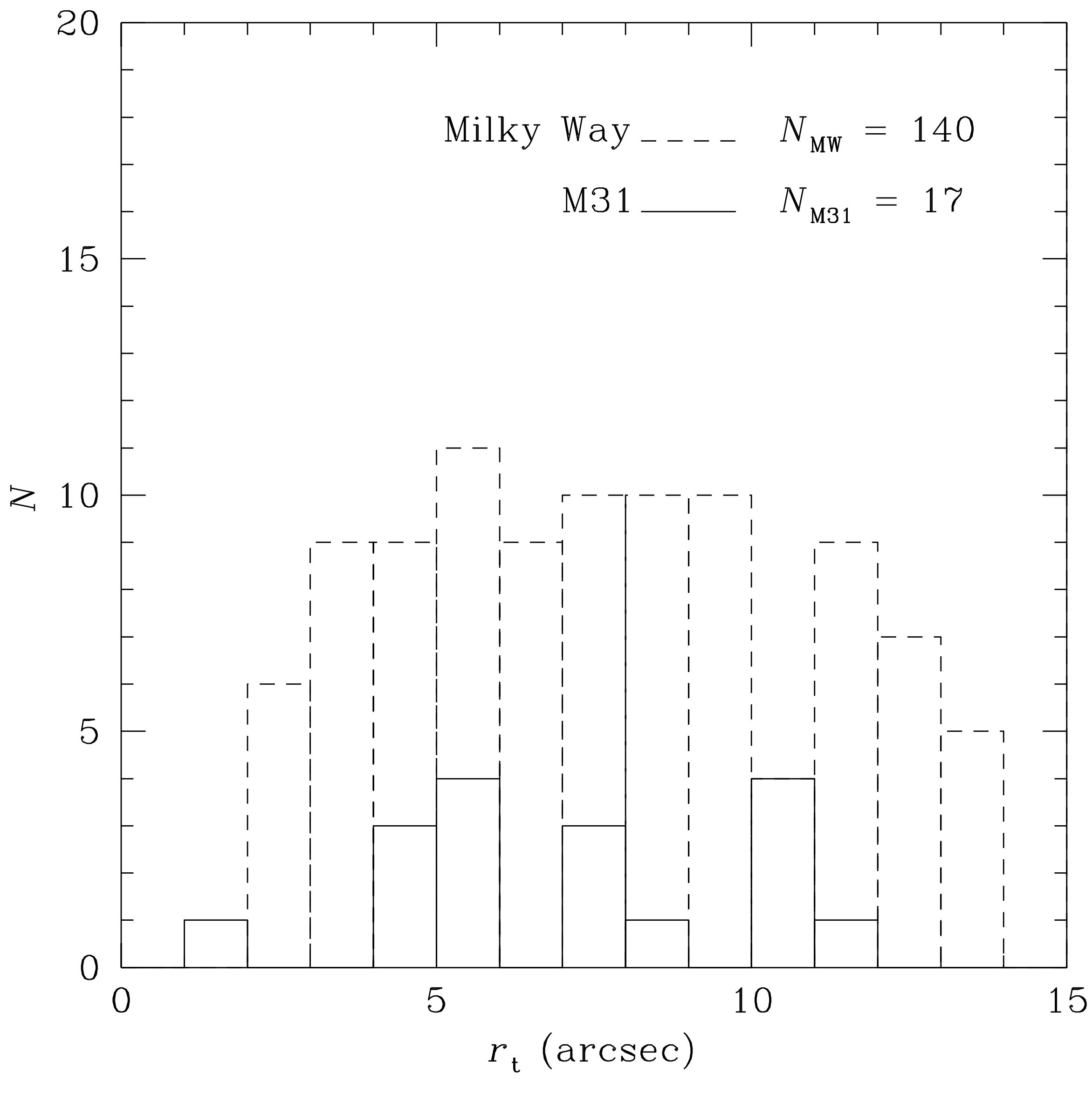

Figure 3.8: This figure shows tidal radii derived from the CFHT HRCam images. The solid histogram represents the M31 globular clusters while the dashed histogram represents the Galactic globular clusters. The tidal radii for the Galactic globular clusters have been scaled to a distance of 725 kpc.

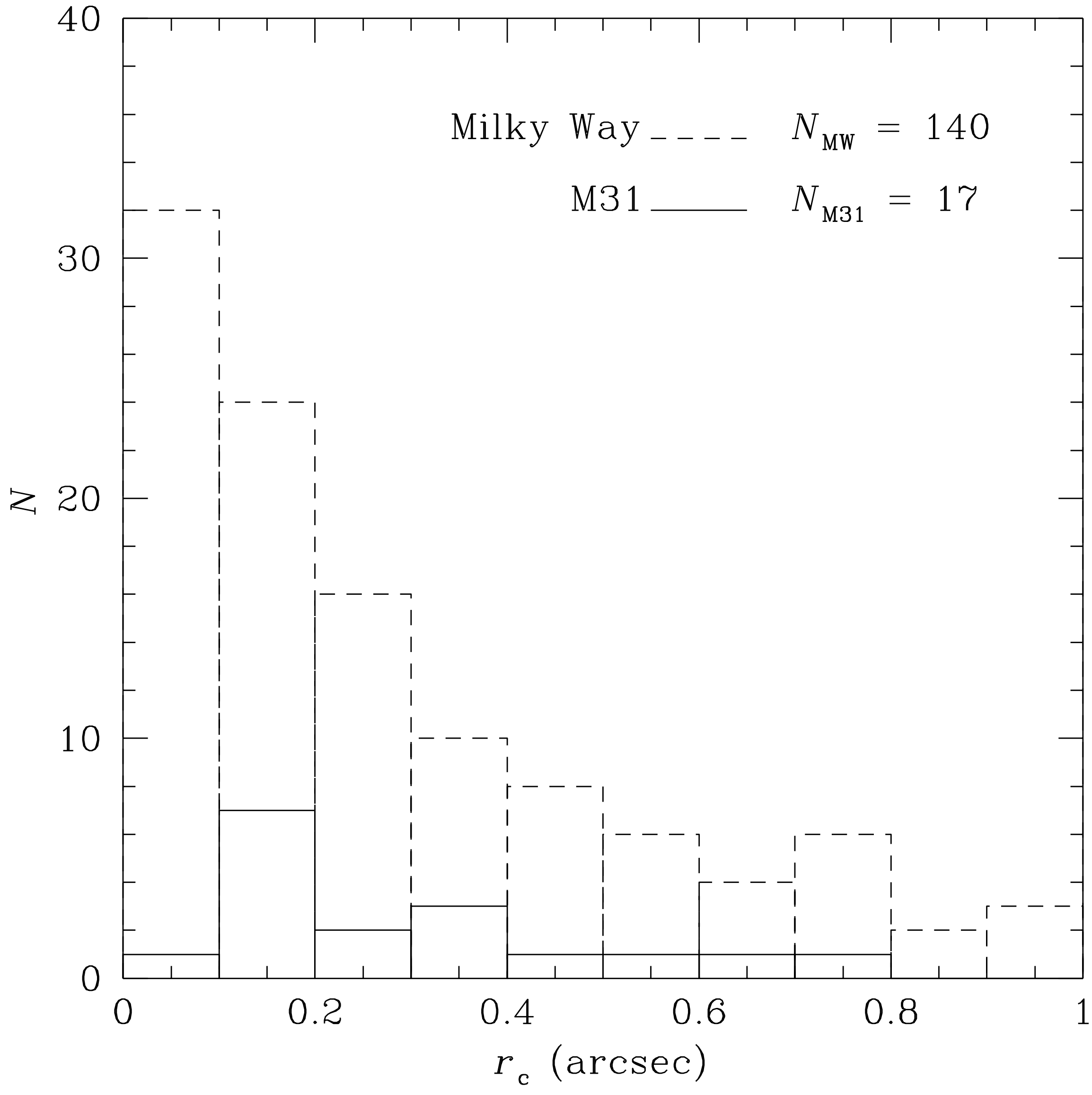

Figure 3.7: This figure shows core radii derived from the CFHT HRCam images. The solid histogram represents the M31 globular clusters while the dashed histogram represents the Galactic globular clusters. The core radii for the Galactic globular clusters have been scaled to a distance of 725 kpc.

corresponds to $M_V = -6.85$. Therefore, both samples of globular clusters have similar limiting magnitudes.

The data in Tables 3.3 and 3.4 gives a mean normalized tidal radius of $\langle r_t/\mathcal{M}_{\rm cl}^{1/3}\rangle_{\rm M31} = 0.35 \pm 0.03$ pc/$\mathcal{M}_{\odot}^{1/3}$ for the M31 globular clusters assuming a distance modulus of $\mu_0 = 24.3$ and a mass-to-light ratio of $\Upsilon_V = 2$ (Dubath & Grillmair 1997 [47] find $\Upsilon = 1.9 \pm 0.4$). The rotation velocities for the two galaxies are $V_{\rm rot} = 220$ km$\cdot$s^{-1} for the Galaxy and $V_{\rm rot} = 265$ km$\cdot$s^{-1} for M31 (Roberts 1966 [123]). The ratio of these is $(V_{\rm rot,M31}/V_{\rm rot,Gal})^{2/3} = 1.132$. Multiplying the mean normalized tidal radius by this ratio gives a scaled, mean normalized tidal radius of $\langle r_t/\mathcal{M}_{\rm cl}^{1/3}\rangle_{\rm M31} = 0.40 \pm 0.03$ pc/$\mathcal{M}_{\odot}^{1/3}$. This is within 1σ of the Galactic value.

This result agrees with Cohen & Freeman's (1991) [30] scaled value of 0.42 for the M31 globular clusters. Comparing the tidal radii in the two globular cluster systems depends on the assumed distance to M31. If the distance modulus of M31 is increased to the *Hipparcos* value of $\mu_0 = 24.77$ (a distance of 900 kpc) (Feast & Catchpole 1997 [53]) then the scaled, mean normalized tidal radius for the M31 globular clusters in this sample becomes $\langle r_t/\mathcal{M}_{\rm cl}^{1/3}\rangle_{\rm M31} = 0.43 \pm 0.04$ pc/$\mathcal{M}_{\odot}^{1/3}$. This is a slightly better agreement with the Galactic value than is obtained with a distance modulus of $\mu_0 = 24.3$.

The mean projected ellipticity of the M31 globular clusters presented here is $\langle\epsilon\rangle_{\rm M31} = 0.12 \pm 0.04$. Lupton (1989) [90] obtained $\langle\epsilon\rangle_{\rm M31} = 0.12 \pm 0.06$ for the outer ($4''$ to $6''$) regions of 18 M31 globular clusters. His paper quotes mean projected ellipticities of 0.08 ± 0.06 for the Galactic globular clusters and 0.11 ± 0.07 for those in the Large Magellanic Cloud.

M31 globular clusters are upper limits on the true core radii while the tidal radii for the M31 globular clusters are reasonable estimates of the true tidal radii. This will result in the concentration ($c \equiv \log_{10}(r_t/r_c)$) being systematically underestimated, which will lead to the half-mass radii of the M31 globular clusters being systematically underestimated.

The tidal radii will be affected by the gravitational potential of the parent galaxy (see e.g. Innanen et al. 1983 [78], Heggie & Ramamani 1995 [66]). In order to compare the tidal radii of the globular clusters in M31 with the tidal radii of the globular clusters in the Milky Way Galaxy it is necessary to correct for the differences in the masses of the two galaxies. For a spherical logarithmic potential the tidal radius of a globular cluster is given by:

$$\frac{r_t}{\mathcal{M}_{\rm cl}^{1/3}} = \left(\frac{R_p}{V_{\rm rot}}\right)^{2/3} \left(\frac{G}{2g(e)}\right)^{1/3}, \tag{3.14}$$

where $\mathcal{M}_{\rm cl}$, is the mass of the globular cluster, R_p is the perigalactic distance of the globular cluster's orbit, $V_{\rm rot}$ is the amplitude of the flat portion of the galactic rotation velocity curve, G is the Newtonian gravitational constant, and $g(e)$ is a slowly varying function of the orbital eccentricity, $e = (R_a - R_p)/(R_a + R_p)$. R_a is the apogalactic distance of the globular cluster's orbit. The function $g(e)$ varies slowly with eccentricity has values of $g(0) = 1$ for circular orbits, and $g(0.6) \simeq 2$ for orbits with eccentricities similar to those of the Galactic globular clusters.

The globular clusters in the Milky Way Galaxy have a mean normalized tidal radius of $\langle r_t/\mathcal{M}_{\rm cl}^{1/3}\rangle_{\rm Gal} = 0.46$ pc$/\mathcal{M}_{\odot}^{1/3}$. This value was taken from Cohen & Freeman (1991) [30] who assumed a mass-to-light ratio of $\Upsilon_V \equiv \mathcal{M}_V/L_V = 2$ for Galactic globular clusters. They limited their sample of Galactic globular clusters to those with $M_V < -7.1$ mag (the bright half of the Galactic globular cluster distribution). The faintest M31 globular cluster in the sample presented in this thesis has $V = 17.45$ (excluding G185B) which

of the globular clusters in the two galaxies.

The mean half-mass radius for the M31 globular clusters is $\langle r_h \rangle_{\mathrm{M31}} = 0\farcs75 \pm 0\farcs14$ while the mean half-mass radius for the Milky Way globular clusters is $\langle r_h \rangle_{\mathrm{MW}} = 1\farcs29 \pm 0\farcs06$. The half-mass radii for the Galactic globular clusters were determined by constructing a series of isotropic King models with central potentials between $W_0 = 1$ and $W_0 = 12$ and computing the concentration and half-mass radius for each model. The one-to-one correspondence between these two quantities in an isotropic King model is shown in Figure 3.10. Half-mass radii for the Galactic globular clusters were found by spline-interpolating the published concentration parameters on this diagram.

An examination of Figure 3.9 shows that the shapes of the distributions of half-mass radii are similar in the two galaxies. However, the mean half-mass radius is $\sim 40\%$ smaller in M31 than it is in the Milky Way Galaxy. This difference between the two mean values is significant at more than the 99.99% confidence level (a $\sim 3.5\sigma$ difference). If a distance of 900 kpc is adopted for M31 the new mean half-mass radius for the Milky Way globular clusters (after being scaled to the distance of M31) is $\langle r_h \rangle_{\mathrm{MW}} = 1\farcs15 \pm 0\farcs06$, corresponding to a difference at the 99% confidence level (a $\sim 2.5\sigma$ difference). This suggests that the difference between the two mean half-mass radii is not due to the uncertainty in the distance to M31.

Since the half-mass radius is computed from the best-fitting Michie–King model, and the fitted core radii for the M31 globular clusters are only upper limits on the true core radii of those clusters, the difference in the mean half-mass radii is probably an artifact of the model-fitting process and the uncertainties in the data, and not a real difference in the structural properties of the globular clusters in the two galaxies. Since the half-mass radius increases when the concentration increases any systematic uncertainty in determining the concentration of a globular cluster will result in a systematic uncertainty in the half-mass radius. As discussed above, and in Chapter 5.6, the core radii for the

3.3 Properties of the M31 Globular Cluster System

Figures 3.7, 3.8, and 3.9 compare the distributions of core, tidal, and half-mass radii of the M31 globular clusters studied in this thesis with the distributions of those same quantities for the Galactic globular cluster system. In all three figures the core, tidal, and half-mass radii for the Galactic globular clusters have been scaled to the apparent sizes they would have at 725 kpc ($\mu_0 = 24.3$ kpc).

The core, half-mass, and tidal radii will, to some degree, be dependent on the strength of the galactic potential. Heggie & Ramamani (1995) [66] investigated the effects of a galactic tidal field on King models and found that, while tidal truncation can lead to triaxial globular clusters that are $\sim 50\%$ larger than the Michie–King models described in Chapter 3.2.1, the cores of globular clusters are almost unaffected by tidal truncation. The fitted half-mass radii in Table 3.3 are small compared to the size of the cluster so it is reasonable to assume that, to the accuracy of the data, the strength of the galactic potential is not affecting the half-mass radii.

The mean core radius of the M31 globular clusters is $\langle r_c \rangle_{\mathrm{M31}} = 0\farcs28 \pm 0\farcs05$ where the mean core radius of the Milky Way globular clusters is $\langle r_c \rangle_{\mathrm{MW}} = 0\farcs28 \pm 0\farcs02$. The quoted uncertainties are the standard errors in the mean. While the means are the same Figure 3.7 shows that the distributions of core radii are quite different. M31 appears to lack clusters with small ($r_c \lesssim 0\farcs1$) core radii. Chapter 5.6 shows that, due to the effects of seeing, the core radii measured for M31 globular clusters and listed in Table 3.3 should be considered to be upper limits on the true core radii of the M31 globular clusters. This would explain the apparent lack of globular clusters with small core radii in M31. In light of this there is no point making a more detailed comparison between the core radii

Cluster	R_{M31} (kpc)	Magnitude V	I	ϵ V	I	θ_0 V	I	Flag V	I
G2	31.6	15.39	14.60	0.000	0.000	...	...	1	1
G185A	0.3	14.23	13.04	0.080	0.183	26°.1	17°.4	1	1
G185B	0.3	17.81	16.69	0.167	0.244	76°.6	77°.8	1	1
G196	1.5	16.93	15.95	0.191	0.286	...	...	1	1
G208	1.3	16.61	15.42	0.000	0.000	...	...	1	1
G212	1.6	17.45	16.69	0.143	0.164	−56°.1	−75°.1	1	1
G213	2.2	...	13.41	...	0.045	...	63°.9	4	4
G215	1.7	16.18	16.39	0.079	0.258	−37°.5	51°.5	2	2
G218	1.9	16.31	15.45	0.052	0.165	−40°.1	60°.4	2	2
G222	1.9	15.14	13.95	0.104	0.149	...	...	3	3
G231	2.7	15.86	14.88	0.043	0.000	−75°.3	...	3	3
G233	2.8	15.14	14.14	0.184	0.000	−55°.3	...	3	3
G302	7.6	15.06	14.09	0.205	0.198	−83°.5	−81°.8	4	4
G312	10.8	15.65	14.53	0.043	0.088	78°.0	53°.4	4	4
Bo153	1.2	16.02	14.74	0.050	0.188	...	...	2	2
vdB2	0.2	14.56	13.37	0.083	0.042	82°.4	45°.4	1	1
V253	1.7	17.68	16.39	0.156	0.258	37°.4	42°.9	1	1

Table 3.4: Ellipticities and position angles for the CFHT data.

unreliable fit; 4 = globular cluster is partially resolved into stars.

Cluster	R_{M31}	W_0		r_c		r_t		r_h		Flag	
	(kpc)	V	I	V	I	V	I	V	I	V	I
G2	31.6	8.47	8.48	0″.11	0″.11	10″.43	10″.19	1″.46	1″.47	1	1
G185A	0.3	6.33	6.10	0″.38	0″.39	8″.31	7″.13	0″.39	0″.36	1	1
G185B	0.3	1.46	0.61	0″.55	0″.89	1″.40	1″.32	0″.11	0″.07	1	1
G196	1.5	7.23	6.28	0″.48	0″.53	6″.07	11″.18	0″.56	0″.38	1	1
G208	1.3	4.98	4.34	0″.59	0″.65	6″.19	5″.17	0″.26	0″.22	1	1
G212	1.6	6.08	4.81	0″.31	0″.41	5″.78	4″.02	0″.36	0″.25	1	1
G213	2.2	3.80	7.09	0″.47	0″.16	3″.00	5″.79	0″.20	0″.52	4	4
G215	1.7	7.98	6.64	0″.09	0″.19	5″.81	5″.03	0″.95	0″.43	2	2
G218	1.9	7.65	6.69	0″.16	0″.25	8″.26	6″.81	0″.73	0″.44	2	2
G222	1.9	7.85	8.02	0″.13	0″.11	7″.77	7″.50	0″.86	0″.99	3	3
G231	2.7	6.53	6.54	0″.55	0″.29	13″.55	7″.34	0″.41	0″.41	3	3
G233	2.8	7.94	8.42	0″.36	0″.11	10″.61	9″.91	0″.92	1″.40	3	3
G302	7.6	8.02	7.83	0″.17	0″.20	11″.96	11″.81	0″.99	0″.84	4	4
G312	10.8	8.32	7.91	0″.12	0″.16	10″.36	10″.25	1″.28	0″.90	4	4
Bo153	1.2	9.73	8.14	0″.03	0″.07	5″.34	4″.90	3″.64	1″.10	2	2
vdB2	0.2	7.86	7.43	0″.09	0″.12	5″.71	5″.41	0″.86	0″.63	1	1
V253	1.7	7.29	6.39	0″.11	0″.19	4″.48	4″.40	0″.58	0″.39	1	1

Table 3.3: Two-dimensional Michie–King model fits to the CFHT data.

The structural parameters obtained by fitting integrated light models to G302 and G312 are in agreement with those obtained by fitting artificial clusters to the data and with the structural parameters derived from the *HST* data. This suggests that the Michie-King parameters, and the ellipticities in Tables 3.3 and 3.4 are reasonable estimates of the true values.

3.2.7 Two-Dimensional Integrated Light Models

Unfortunately, the amount of exposure time required to resolve individual stars in M31 globular clusters is large. Further, clusters that were projected onto the disc, or the nuclear regions, of M31 are seen against a sea of surface brightness fluctuations that look like stars. This makes the identification of stars, even in deep exposures, uncertain. Because of these two effects it was not possible to use the forward approach of comparing artificial globular clusters to the data to determine the Michie–King parameters for most of the globular clusters in the CFHT data set. In order to salvage something useful from the situation I fit two-dimensional Michie–King models of the integrated light from a globular cluster directly to the background-subtracted images of each globular cluster.

Modeling the integrated light of the cluster should work well on images with poorer seeing or shorter exposure times since individual stars will not be resolved. This approach will result in an integrated light model being a good approximation to the CCD image of the globular cluster. For globular clusters such as G302 and G312, where individual stars are well-resolved in the clusters' outer regions, modeling the integrated light will not be as successful as building an artificial cluster from artificial stars.

The two-dimensional isotropic Michie–King models were fit in the same manner as described in Chapter 3.2.3. The following parameters were solved for simultaneously: W_0, r_c, total magnitude, ϵ, and θ_0. Once the best-fit was determined the three-dimensional half-mass radius, r_h, was computed and the model cluster was subtracted from the data image. The subtracted image was examined by eye to obtain an estimate of the quality of the subtraction, which was used to set a flag indicating the overall reliability of the fit. The results of directly fitting the two-dimensional integrated light Michie–King models to each globular cluster are presented in Tables 3.3 and 3.4. The fit quality flags are: 1 = good subtraction, reliable fit; 2 = fair subtraction, uncertain fit; 3 = poor subtraction,

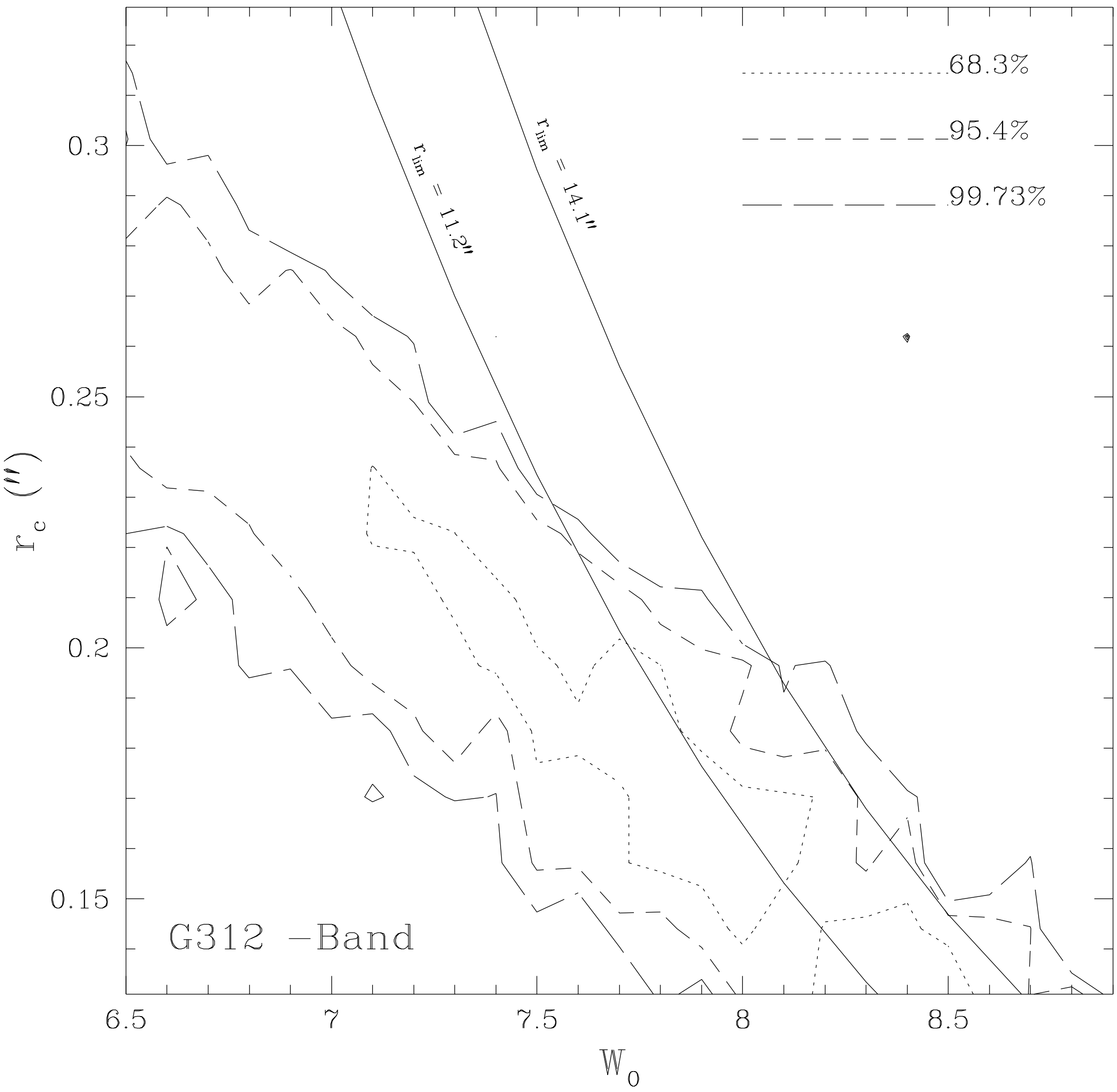

Figure 3.6: Probability contours for the CFHT G312 V-band data.

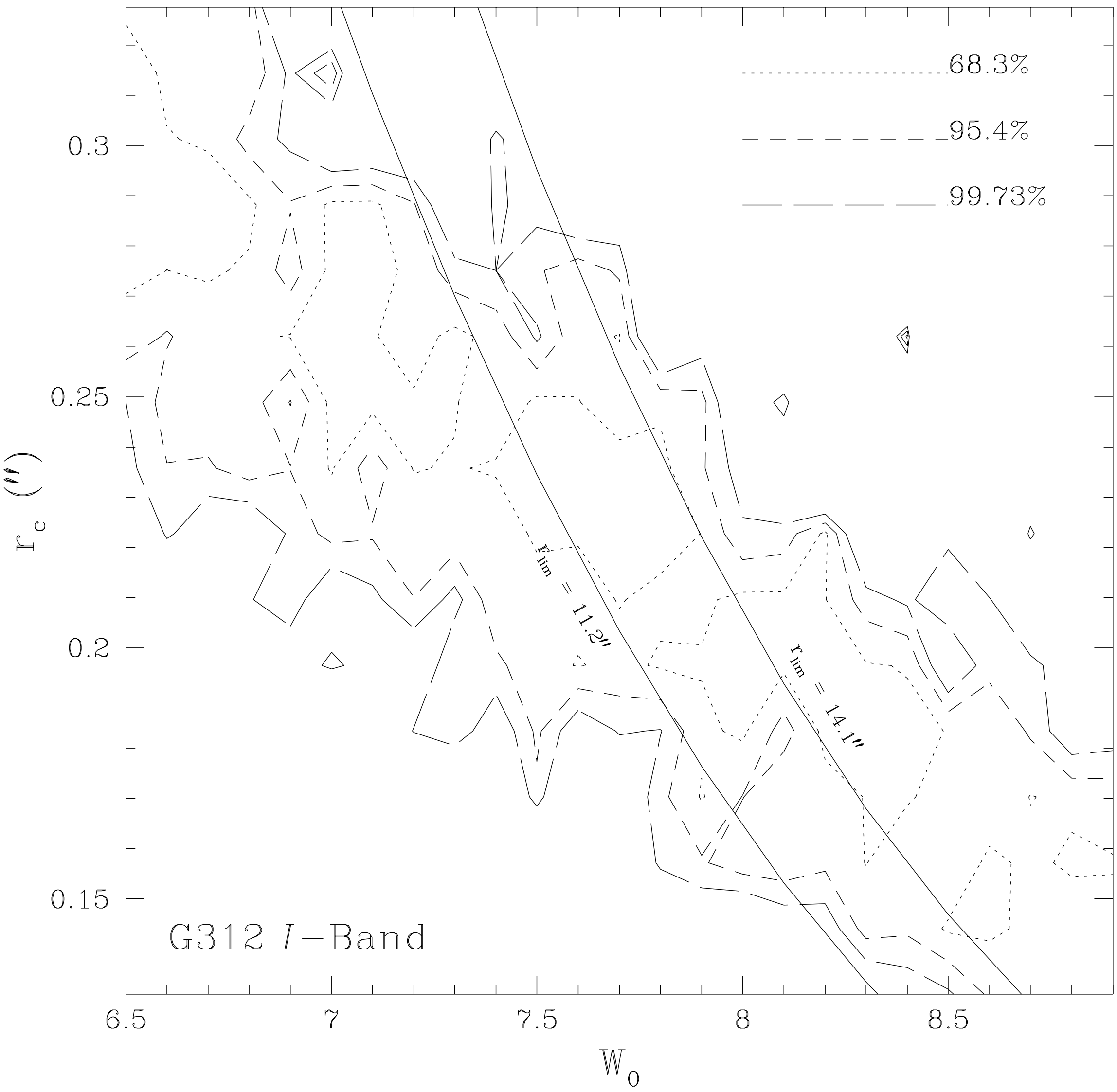

Figure 3.5: Probability contours for the CFHT G312 *I*-band data.

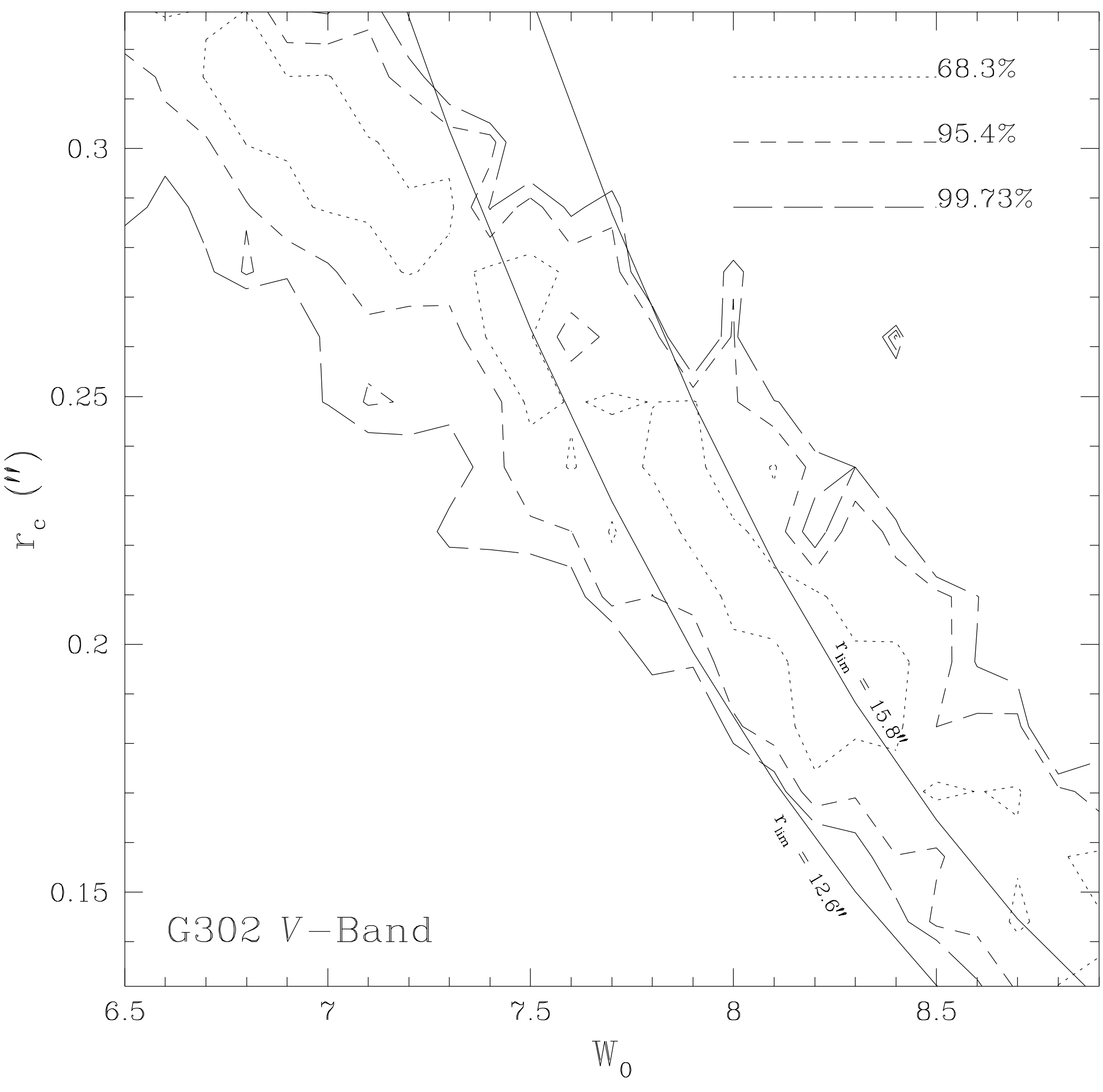

Figure 3.4: Probability contours for the CFHT G302 V-band data.

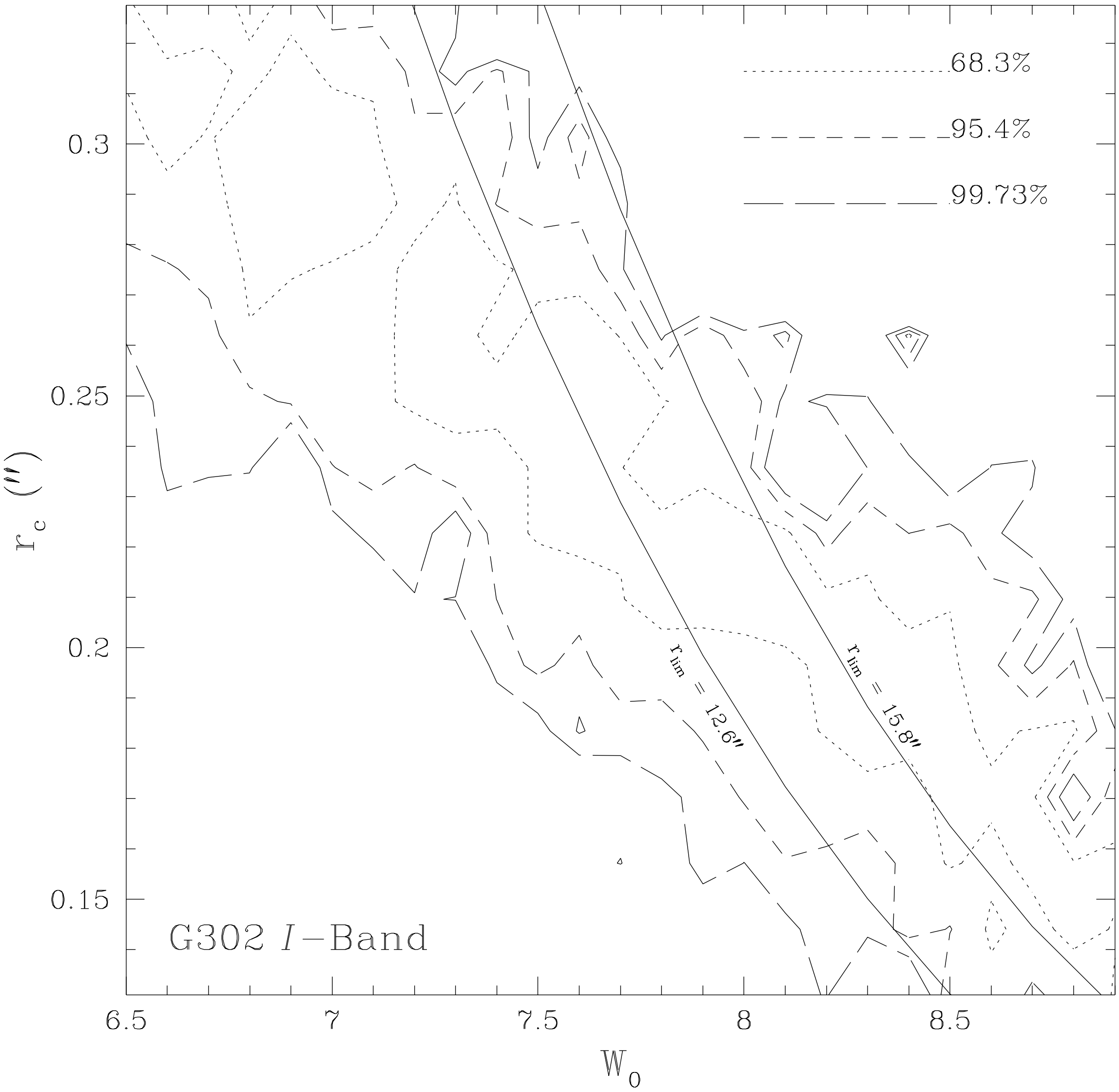

Figure 3.3: Contour plots showing the probability that the observed surface brightness profile can be obtained from an artificial cluster with a given set of Michie–King parameters. The solid lines represent the upper and lower cut-offs determined from the star-count data (see Chapter 3.1). The combination of artificial cluster comparisons and the limiting radii determined from the star-counts provide strong constraints on the range of models that can reproduce the observations.

are in agreement with those obtained from fitting two-dimensional artificial cluster models to the CFHT data (see Table 3.2). This strongly suggests that it is possible to obtain reliable core and tidal radii of globular clusters in M31 from ground-based observations *if* the seeing is good enough that individual stars in the outer regions of the clusters can be resolved. The resolved stars are needed in order to use star counts to constrain the tidal radii of the globular clusters.

branch and may contain significant contributions from field stars that are superimposed on the core. Much of the scatter in r_c may be due to the random placement of these bright stars within the core. Fortunately star count data (see Chapter 3.1) can provide an additional constraint on the tidal radius. By superimposing the upper and lower limits on the tidal radius, as determined from star count data, it is possible to identify the most probable Michie–King parameters and estimate the uncertainties in them. Table 3.2 lists these parameters. The limiting radii in Table 3.2 are those obtained from the star-counts and represent the radii at which the observed projected stellar densities drop sharply towards zero. The ranges given for each parameter in Table 3.2 represent the range of values allowed given the 1σ uncertainties in the best-fit artificial clusters and star-count data.

Cluster	Filter	W_0	r_c	$r_{\rm lim}$	c
G302	V	7.4–8.0	$0''.21$–$0''.24$	$11''.8$–$15''.1$	1.8
	I	7.6–8.0	$0''.21$–$0''.25$	$11''.8$–$15''.1$	1.8
G312	V	7.5–8.5	$0''.13$–$0''.20$	$9''.2$–$13''.1$	1.8
	I	7.1–7.7	$0''.20$–$0''.26$	$9''.2$–$13''.1$	1.7

Table 3.2: Results from two-dimensional Michie–King models and star counts for G302 and G312.

A comparison of the core and tidal radii for G302 and G312 derived using the one-dimensional method (see Table 3.1) and those derived using the two-dimensional methods (see Table 3.2) shows that fitting one-dimensional models leads to systematic errors in the Michie–King parameters. The core radii obtained from one-dimensional fitting are overestimated by $\sim 33\%$. The tidal radii obtained by fitting one-dimensional models are overestimated by $\sim 25\%$. The core and tidal radii for G302 and G312 were also determined using *HST* WFPC2 images in the V- and I-bands (see Chapter 5). The core and tidal radii obtained by fitting Michie–King models to this *HST* data (see Table 5.4)

3.2.6 Two-Dimensional Artificial Cluster Models

In order to estimate the Michie–King parameters of an M31 globular cluster *without* using one-dimensional convolutions a grid of artificial clusters with Michie–King parameters based on those obtained by fitting a one-dimensional Michie–King model to the radial profile of the globular cluster was constructed. This procedure was tested on the V- and I-band images of G302 and G312. The adopted grid for G302 and G312 had W_0 between 6.5 and 8.9, and r_c between $0''.13$ and $0''.33$. The artificial clusters were circularly symmetric and had no velocity anisotropy (i.e. $r_a = +\infty$). For each artificial cluster a surface brightness profile was derived and the χ^2_ν between it and the surface brightness profile of the real globular cluster in question was calculated. To convert the χ^2_ν statistic into a confidence level a set of 100 artificial clusters with $W_0 = 7.4$ and $r_c = 0''.24$ were generated and the χ^2_ν between each of these artificial clusters and the original artificial cluster was computed.

Contour plots showing the probability of fit for G302 and G312 are shown in Figures 3.3, 3.4, 3.5, and 3.6. The jumpiness in the contours is due to modeling the clusters as a set of individual stars rather than a smooth light distribution. Since the stars are placed randomly in the artificial cluster (within the limitations imposed by the model surface brightness profile, ellipticity, and orientation) models with identical input parameters can return significantly different observed surface brightness profiles.

As can be seen in Figures 3.3, 3.4, 3.5, and 3.6, these simulations do not give a unique set of Michie–King parameters for any of the clusters under investigation. Instead the clusters can be modeled with a range of Michie–King models of similar tidal radii. The large uncertainties in the core radius are due to the shape of the core being smeared out by the seeing, and to the large size of the pixels relative to the scale of the PSF. In addition, the light in the core is dominated by a small number of stars near the top of the red-giant

of treating seeing-convolution are not equivalent. In general S_1 and S_2 will have the same shape *only* if $C(r,\theta)$ and $P(r,\theta)$ have the same ellipticities *and* orientations.

For realistic PSFs and cluster profiles it is usually not possible to perform the convolution and extraction of radial slices analytically so numerical methods must be used. To investigate the effects of seeing on realistic globular clusters I constructed a grid of 400 circularly symmetric artificial clusters with identical Michie–King parameters ($W_0 = 7.4$, $r_c = 0\farcs236$ ($= 1.8$ pixels), $r_t = 10\farcs493$ ($= 80$ pixels), and $c = 1.65$) and fit seeing-convolved Michie–King models to their radial surface brightness profiles. This process compares one-dimensional profiles, but the convolutions are applied to the two-dimensional distributions. The parameters returned by these fits were $\overline{W_0} = 7.31 \pm 0.08$, $\overline{r_c} = 0\farcs303 \pm 0\farcs008$ ($= 2.31 \pm 0.06$ pixels), $\overline{r_t} = 12\farcs682 \pm 0\farcs487$ ($= 96.81 \pm 3.72$) pixels, and $\overline{c} = 1.62 \pm 0.02$ (the uncertainties are standard deviations). Fitting one-dimensional Michie–King models results in r_c being overestimated by $\sim 28\%$ while the concentration of the cluster is underestimated by $\sim 2\%$. This suggests that fitting one-dimensional models to surface brightness profiles gives a reasonable estimate of the overall shape of the surface brightness profile but seriously overestimates the radial scale. Because of this the fitted one-dimensional core and tidal radii in Table 3.1 should be treated as upper limits to their true values.

Unfortunately the discrepancies between the fitted and intrinsic core and tidal radii will vary with the seeing quality, the signal-to-noise ratio of the images, and the intrinsic shape of the cluster, so a simple correction factor can not be used to go from the fitted one-dimensional Michie–King parameters to the intrinsic Michie–King parameters. Therefore, seeing must be treated as a two-dimensional phenomenon when modeling surface brightness profiles.

radius axis[2] of the light distribution on the CCD image. However, the analysis described in Chapter 3.2.3 involved first taking one-dimensional profiles of a Michie–King model and the seeing function, convolving them, then comparing the resulting profile to the observed one-dimensional profile.

The difference between these two approaches can be illustrated using a Gaussian model cluster of ellipticity ϵ_c:

$$C(r,\theta) \propto \exp\left(-\frac{1}{2}r^2\left[\frac{\cos^2(\theta)}{\sigma_{c,x}^2}+\frac{\sin^2(\theta)}{\sigma_{c,y}^2}\right]\right), \tag{3.10}$$

and a Gaussian PSF of ellipticity ϵ_p:

$$P(r,\theta) \propto \exp\left(-\frac{1}{2}r^2\left[\frac{\cos^2(\theta)}{\sigma_{p,x}^2}+\frac{\sin^2(\theta)}{\sigma_{p,y}^2}\right]\right), \tag{3.11}$$

where σ_x and σ_y are the standard deviations of the two-dimensional Gaussians, and both ellipses have the same orientation. The surface brightness profiles of each are obtained by extracting the radial profiles along their effective radius axes then convolving these one-dimensional profiles to get

$$S_1(r_{\text{eff}}) \propto \exp\left(-\frac{1}{2}\frac{{r_{\text{eff}}}^2}{\sigma_{c,x}^2(1-\epsilon_c)+\sigma_{p,x}^2(1-\epsilon_p)}\right). \tag{3.12}$$

On the other hand, convolving $C(r,\theta)$ and $P(r,\theta)$ directly then extracting the radial profile gives:

$$S_2(r_{\text{eff}}) \propto \exp\left(-\frac{1}{2}\frac{{r_{\text{eff}}}^2}{\sqrt{\sigma_{c,x}^2+\sigma_{p,x}^2}\sqrt{\sigma_{c,x}^2(1-\epsilon_c)^2+\sigma_{p,x}^2(1-\epsilon_p)^2}}\right), \tag{3.13}$$

which differs in shape from $S_1(r_{\text{eff}})$. Although this example is for a special case (one in which $C(r,\theta)$ has the same orientation as $P(r,\theta)$) it demonstrates that the two methods

[2]The effective radius, r_{eff}, of an ellipse with semi-major and semi-minor axes a and b respectively is defined by $\pi {r_{\text{eff}}}^2 \equiv \pi ab$. The effective radius axis is either of the two axes along which the edge of the ellipse intersects the edge of a circle of radius r_{eff}.

3.2.5 Systematic Biases in Seeing Convolutions

It is not obvious that convolving a one-dimensional seeing profile with a one-dimensional surface brightness model is physically realistic. The effects of seeing on light from an astronomical source with a given intrinsic shape is usually treated as distortions in the wavefront of the light caused by turbulent cells in the Earth's atmosphere. Pressure and temperature differences between adjacent turbulent cells result in the index of refraction varying from one cell to the next which introduces distortions in the wavefront of the light. An alternative way of thinking of the problem, which is useful when thinking about image reconstruction, is to follow the paths of individual photons from the source to the detector. Each photon is perturbed from its original path by atmospheric effects, *and* by the telescope's optics. Further, the exact location of the photon when it strikes the CCD detector is not known due to the finite size of the detector's pixels. All three of these effects need to be taken into account to accurately reconstruct the original light source from the image that is observed at the detector.

The observed distribution of light on the CCD, $O(\mathbf{x})$, is related to the intrinsic distribution from the source, $I(\mathbf{y})$ by

$$O(\mathbf{x}) = \iint I(\mathbf{y})\, P(\mathbf{x} \mid \mathbf{y})\, d\mathbf{y} \tag{3.9}$$

where $P(\mathbf{x} \mid \mathbf{y})$ is the conditional probability that a photon from a location $\mathbf{y}$ on the sky will be observed at location $\mathbf{x}$ on the CCD. In other words, $P(\mathbf{x} \mid \mathbf{y})$ is a function that describes the path of a photon through the atmosphere, and the telescopes optics. If $P(\mathbf{x} \mid \mathbf{y})$ is independent of position on the CCD, and the pixel size is small compared to the spatial scale on which the flux from the source varies, then $P(\mathbf{x} \mid \mathbf{y}) = P(\mathbf{x} - \mathbf{y})$, making Equation 3.9 a two-dimensional convolution integral.

The observed surface brightness profile is obtained by taking a slice along the effective

image over the exposure time of the image.

The IRAF task NOAO.ARTDATA.MKOBJECT and the DAOPHOT II PSF were used to add these artificial stars to a background region on the image containing the M31 globular cluster in question. Stars were added until the total flux in the added stars matched that of the appropriate real cluster, then Poisson and read-out noise was added. An example of an artificial cluster is shown in Figure 3.2. Elliptical isophotes were fit to these artificial clusters in exactly the same manner as they were to the real clusters and the resulting surface brightness profiles were compared with that of the real cluster using a χ^2_ν statistic. Since this modeling procedure is physically similar to what is happening to the light from the real cluster, and since the artificial clusters were placed on background regions of the original images, any systematic effects affecting the real clusters will also affect the artificial ones.

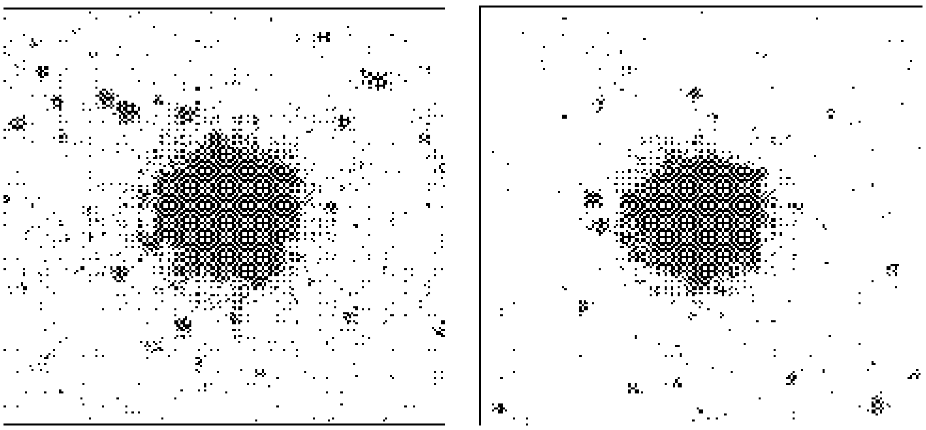

Figure 3.2: The left-hand figure shows the I-band image of G312 while the right-hand image shows an artificial cluster with $W_0 = 7.7$, $r_c = 0\farcs23$ ($= 1.76$ pixels), and $\epsilon = 0.0$. The artificial cluster is made up of 116,790 stars with $20.5 \leq I \leq 29.9$. It has been placed on an M31 halo field located $\sim 35''$ south of G312.

3.2.4 The Artificial Clusters

In order to investigate the accuracy of fitting one-dimensional Michie–King profiles to the data, and to investigate the fitting algorithm's stability against stochastic effects in the locations of stars within the cluster and the field that the cluster sits upon, I created a series of artificial clusters, measured their surface brightness profiles, and fit Michie–King models in the manner described above.

The artificial clusters were constructed by randomly drawing stellar coördinates from a Michie–King profile, and magnitudes from a realistic globular cluster luminosity function. Experiments with a variety of luminosity functions based on those of Galactic globular clusters showed that the observed surface brightness profiles of the artificial clusters did not depend on small changes in the luminosity function such as those caused by metallicity or age spreads similar to those observed in Galactic globular clusters. Therefore, a luminosity function based on that of 47 Tuc (Hesser et al. 1987 [68]) was adopted. The biggest unknown in the adopted luminosity function is the distribution of horizontal branch stars in M31's globular clusters. Galactic globular clusters exhibit a wide range of horizontal branch morphologies that appear to be correlated with metallicity and some as-of-yet unknown second parameter (e.g. Carney et al. 1991 [30]). While there is no direct evidence for a second parameter problem in the M31 globular clusters, spectral studies suggest that the two systems have similar, but not identical, stellar populations (e.g. Burstein et al. 1984 [22], Tripicco 1989 [146], Covino et al. 1994 [32]) so it is not inconceivable that a second parameter may be active in the M31 globular cluster system. For simplicity I have assumed that stars are uniformly distributed along the horizontal part of the horizontal branch and ignored any complications introduced by the instability strip and the extreme blue tail of the horizontal branch. The faint end of the luminosity function was truncated at the magnitude where each star contributed one count to the

Cluster	Filter	$\mu(0)$	W_0	r_c	r_a/r_c	r_t	c
G312	V	16.70 ± 0.02	7.5	$0''.29$	$+\infty$	$13''.92$	1.7
		16.70 ± 0.02	7.5	$0''.29$	1552	$13''.92$	1.7
	I	15.48 ± 0.01	7.4	$0''.29$	$+\infty$	$12''.81$	1.6
		15.49 ± 0.01	7.4	$0''.29$	21	$13''.79$	1.7
G352	V	17.23 ± 0.01	6.4	$0''.41$	$+\infty$	$9''.19$	1.4
	I	15.99 ± 0.01	6.9	$0''.32$	$+\infty$	$9''.79$	1.5
G355	V	17.41 ± 0.01	13.0	$0''.02$	$+\infty$	$16''.38$	2.9
Bo153	V	17.09 ± 0.01	4.5	$0''.42$	$+\infty$	$3''.59$	0.9
	I	15.17 ± 0.01	5.7	$0''.27$	$+\infty$	$4''.16$	1.2
vdB 2	V	15.52 ± 0.01	4.3	$0''.47$	$+\infty$	$3''.64$	0.9
	I	14.07 ± 0.03	5.1	$0''.38$	$+\infty$	$4''.34$	1.1
vdB 5	V	17.42 ± 0.01	5.7	$0''.41$	$+\infty$	$6''.23$	1.2
	I	16.08 ± 0.03	7.0	$0''.29$	$+\infty$	$9''.47$	1.5
V253	V	18.26 ± 0.10	13.0	$0''.02$	$+\infty$	$19''.25$	2.9
	I	16.85 ± 0.25	8.2	$0''.19$	$+\infty$	$14''.42$	1.9

3.1 (continued)

Cluster	Filter	$\mu(0)$	W_0	r_c	r_a/r_c	r_t	c
G2	V	16.50 ± 0.02	8.2	$0\farcs23$	$+\infty$	$17\farcs36$	1.9
		16.50 ± 0.02	8.2	$0\farcs23$	690	$17\farcs39$	1.9
	I	15.85 ± 0.01	7.9	$0\farcs26$	$+\infty$	$16\farcs80$	1.8
		15.85 ± 0.01	7.9	$0\farcs26$	367	$16\farcs81$	1.8
G70	V	16.98 ± 0.01	7.2	$0\farcs32$	$+\infty$	$12\farcs04$	1.6
G177	V	16.99 ± 0.01	5.9	$0\farcs37$	$+\infty$	$6\farcs06$	1.2
	I	17.88 ± 0.03	6.6	$0\farcs28$	$+\infty$	$7\farcs17$	1.4
G185	V	15.08 ± 0.01	5.0	$0\farcs65$	$+\infty$	$6\farcs93$	1.0
	I	14.41 ± 0.03	5.4	$0\farcs58$	$+\infty$	$7\farcs53$	1.1
G185B	V	18.51 ± 0.10	2.1	$0\farcs59$	$+\infty$	$1\farcs98$	0.5
	I	17.20 ± 0.10	1.4	$0\farcs72$	$+\infty$	$1\farcs81$	0.4
G196	V	19.07 ± 0.50	5.9	$0\farcs69$	$+\infty$	$12\farcs05$	1.2
	I	17.80 ± 0.01	6.2	$0\farcs73$	$+\infty$	$14\farcs86$	1.3
G208	V	18.41 ± 0.01	3.6	$0\farcs86$	$+\infty$	$5\farcs01$	0.8
	I	16.82 ± 0.01	4.8	$0\farcs65$	$+\infty$	$6\farcs33$	1.0
G212	V	18.52 ± 0.10	6.1	$0\farcs34$	$+\infty$	$6\farcs72$	1.3
	I	18.14 ± 0.10	5.6	$0\farcs45$	$+\infty$	$6\farcs52$	1.2
G213	V	15.67 ± 0.01	5.5	$0\farcs38$	$+\infty$	$5\farcs15$	1.1
	I	14.17 ± 0.01	6.6	$0\farcs27$	$+\infty$	$6\farcs91$	1.4
G215	V	16.87 ± 0.10	8.7	$0\farcs10$	$+\infty$	$11\farcs25$	2.0
	I	16.48 ± 0.25	7.5	$0\farcs21$	$+\infty$	$10\farcs41$	1.7
G218	V	17.31 ± 0.05	8.9	$0\farcs15$	$+\infty$	$18\farcs47$	2.1
	I	16.27 ± 0.25	7.8	$0\farcs28$	$+\infty$	$16\farcs12$	1.8
G222	V	15.80 ± 0.01	7.2	$0\farcs25$	$+\infty$	$9\farcs90$	1.6
	I	14.74 ± 0.01	7.2	$0\farcs25$	$+\infty$	$9\farcs92$	1.6
G231	V	17.29 ± 0.01	5.3	$0\farcs56$	$+\infty$	$7\farcs06$	1.1
	I	16.20 ± 0.01	5.5	$0\farcs51$	$+\infty$	$7\farcs01$	1.1
G233	V	16.43 ± 0.01	7.2	$0\farcs35$	$+\infty$	$13\farcs44$	1.6
	I	15.18 ± 0.01	7.5	$0\farcs29$	$+\infty$	$13\farcs91$	1.7
G263	V	16.54 ± 0.01	7.3	$0\farcs32$	$+\infty$	$13\farcs60$	1.6
	I	15.68 ± 0.01	6.6	$0\farcs42$	$+\infty$	$10\farcs70$	1.4
G302	V	16.48 ± 0.01	7.6	$0\farcs31$	$+\infty$	$15\farcs42$	1.7
		16.48 ± 0.01	7.6	$0\farcs31$	487	$15\farcs43$	1.7
	I	15.33 ± 0.03	7.5	$0\farcs32$	$+\infty$	$15\farcs48$	1.7
		15.33 ± 0.03	7.5	$0\farcs32$	649	$15\farcs48$	1.7

Table 3.1: Best-fitting one-dimensional Michie–King models.

be well fit with combined Michie-King–power-law models, Central power-law cusps could not be reliably identified for profiles where the seeing FWHM is similar to r_c. Therefore I chose not to attempt to fit central power-laws to the M31 globular cluster data.

outer regions of a globular cluster. Unfortunately the CFHT data is highly uncertain at large radii. I attempted to fit anisotropic Michie–King models to the profiles of several of the globular clusters in Table 3.1 but found that the resulting fits were no better than, and often worse than, the best fits with isotropic Michie–King models. The existence of anisotropy in any of the M31 globular clusters in the CFHT data set can not be ruled out, but there is no convincing evidence for it from fitting one-dimensional Michie–King models.

Reduced chi-square-fitting is an objective way to identify a single best-fitting model for each data set. However, since the surface brightness data points were not independent, the χ^2_ν value for a fit could not be used to rigorously estimate the reliability or uniqueness of that fit. The fits to most of the globular clusters looked reasonable to the eye, although some clusters were not well fit. In general the clusters that were well fit by Michie–King models were those with similar Michie–King parameters in both the V- and I-bands. Globular clusters with parameters that differ by more than $\sim 20\%$ between the V- and I-bands were usually poorly fit by Michie–King models.

Approximately 20% of Galactic globular clusters have collapsed cores (e.g. Djorgovski & King 1986 [44]) characterized by central power-law cusps in their surface brightness distributions. To investigate the possibility that some of the M31 globular clusters have central power-law cusps I modified the fitting software to allow the simultaneous fitting of a Michie–King model with a central power-law to a surface brightness profile. This involved the introduction of three additional free parameters: the power-law slope, the radius at which the power-law profile switches to a Michie–King profile, and, to avoid infinite projected density at $r = 0$, an inner cut-off radius interior to which the surface brightness profile is assumed to be constant. These three power-law parameters, and the core radius, are determined by the shape of the inner few pixels of the surface brightness profile, which are dominated by the seeing. I found that, although the outer regions could

CERN's MINUIT (Version 94.1) function minimisation package was used to fit one-dimensional seeing-convolved Michie–King models to the V- and I-band surface brightness profiles of each cluster. The fitting was done by simultaneously solving for the two Michie–King parameters: central potential, W_0, and the anisotropy radius, r_a; as well as the two scaling parameters: core radius, r_c, and central surface brightness, μ_0. Once the best-fitting model was found the tidal radius, r_t, and the concentration, $c \equiv \log_{10}(r_t/r_c)$, were computed. After some experimentation a weighting scheme of $w_i = (1/\sigma_i)^2$, where σ_i is the root-mean-square (RMS) scatter in the isophotal intensity about the i'th fitted isophote, was adopted. This weighting scheme was tested by fitting Michie–King models to a series of profiles created by drawing points from an unconvolved Michie–King distribution. Good agreement was found between the input and the fitted models. The exact form of the weighting did not significantly affect the values of the best-fit parameters provided that the weighting assigned to each data point was reasonably indicative of the reliability of that point relative to the other points in the profile.

Each Michie–King model was convolved with the appropriate one-dimensional seeing function. For the purposes of the convolution the seeing profile was calculated out to a radius where $M(r)/M(0) = 10^{-8}$. For Moffatian profiles with $\beta = 2.5$ this corresponds to $r \simeq 35 \times$ FWHM. For profiles with $\beta = 1.5$ the limiting radius of the calculated seeing is $r \simeq 303 \times$ FWHM. The uncertainty in the shape of the seeing profile has a significant effect on the results of the fitting. A series of convolutions of Michie–King models with Moffatian seeing profiles in which the Moffatian seeing parameters were allowed to vary by up to $\pm 3\sigma$ from their observed values were performed. This resulted in variations of up to $\pm 20\%$ in the fitted values of r_c and $\pm 5\%$ in r_t.

Table 3.1 gives the best-fit parameters for isotropic Michie–King models. Typically anisotropic Galactic globular clusters have anisotropy radii of between approximately 5 and 10 times their core radii, indicating that anisotropy becomes important only in the

3.2.3 One-Dimensional Models

Tidal radii were determined by fitting one-dimensional Michie–King models to the observed V- and I-band surface brightness profiles of each globular cluster. Surface brightness profiles for each globular cluster were obtained using the IRAF (Version 2.10.1) implementation of the STSDAS task ISOPHOTE.ELLIPSE. This task uses Jedrzejewski's (1987) [80] isophote-fitting algorithm to fit elliptical isophotes to the observed isophotes. This algorithm determines the centres, ellipticities, orientations, and intensities of a series of ellipses logarithmically spaced between $\sim 0\farcs131$ ($\sim$ 1 pixel) and $\sim 20\farcs0$ ($\sim$ 150 pixels). The spacing between successive ellipses varies from significantly less than the size of the seeing disc (FWHM $\sim 0\farcs7$) near the centre of each globular cluster to several times the size of the seeing disc beyond the tidal radius of the globular cluster. The properties of the ellipses are not independent of each other for radii of less than approximately eight times the size of the seeing disc (e.g. Schweizer 1979 [129]). Since the spacing between ellipses is logarithmic the degree of correlation will vary with the distance from the centre of the globular cluster. There is an additional correlation caused by the overlap in the subsets of pixels being used to compute successive best-fitting ellipses. In light of these effects the uncertainties in the surface brightnesses, ellipticities, and orientations of the isophotal ellipses returned by ELLIPSE were taken to be guides to the reliability of the individual values relative to the values for the other fitted ellipses for that globular cluster. They were *not* treated as statistically rigorous uncertainty estimates. In the inner regions of each globular cluster ($r_{\mathrm{eff}} \lesssim 2\farcs0$) the large gradient in surface brightness, and the small number of pixels, make the fitted ellipses less reliable than those fit further out. Finally, the one-dimensional surface brightness profiles for each globular cluster along the effective radius axis of the globular cluster were extracted.

convolved with the seeing and compared in some way to the original data. These techniques avoid the enhancement of noise that can occur in image restoration but requires a *priori* knowledge of the underlying model that describes the data. Michie–King models (Michie 1963 [97], King 1966 [82]) and their extensions (e.g. Gunn & Griffin 1979 [61], Lupton & Gunn 1987 [91]) have been found to give reasonable fits to the surface brightness profiles and stellar density profiles of roughly three-quarters of the Galactic globular clusters. Since the Michie–King parameterisation has been successfully used for so many Galactic globular clusters (see Trager et al. 1993 [145] for a recent compilation) it is a natural choice for use with the M31 globular clusters. Michie–King models have been used purely to facilitate the comparison of the shapes of the surface brightness profiles of the M31 globular clusters with those of the Galactic globular clusters. The fits presented in this thesis should *not* be interpreted as being representative of the dynamical states of the clusters in question. For simplicity I have chosen to use single-mass Michie–King models instead of the more physically realistic multi-mass models of Gunn & Griffin (1979) [61].

A variety of different methods were used to determine the best-fitting Michie–King parameters for the globular clusters that were observed with the CFHT. These methods are described in the following sections.

disc or bulge of M31 (e.g. G185) unresolved background light can be a significant source of noise.

3. Globular clusters are not inherently smooth sources of light. The azimuthal placement of stars in a sphericaly symmetric globular cluster is stochastic. Since the number of stars on the upper red-giant branch and the asymptotic-giant branch is small it is possible for these bright stars not to be uniformly distributed at a given radius. The brightest stars in M31 globular clusters can be resolved in the CFHT images. While Michie–King models describe the radial dependence of the surface number density of stars they say nothing about the positions of individual stars within a globular cluster. So, the stochastic placement of the resolved red giants adds an additional component of noise to the CCD image of the globular cluster.

Observed surface brightness profiles are dependent on both the underlying surface brightness profile of the object and on the seeing, regardless of whether the seeing is dominated by the atmosphere, as in ground-based observations, or the optical system of the telescope, as is the case for *HST* observations. For ground-based imaging, seeing effects can significantly alter the observed profiles of extended objects that only subtend a few arcsecond on the sky (e.g. Schweizer 1979 [129]). If the PSF is well defined then it can be used to restore the image. Unfortunately image restoration can be very sensitive to small errors in the PSF and can be biased by noise in the images. The Lucy–Richardson (Richardson 1972 [121], Lucy 1974 [89]) algorithm, for example, will only preserve flux if there is no read-noise present in the image.

A second approach involves modeling the data in some way and finding the model that gives the best fit to the observations. This approach requires that the form of the PSF, and underlying model that describes the source, be well known. The model is

3.2.2 Fitting Methods

The problem of fitting a model globular cluster to CCD observations is a difficult one. Ideally a physically-realistic model would be used to generate a model cluster and this model would be compared directly with the observed data. A quantitative goodness-of-fit would be defined and the model parameters would be varied until the best-fitting model was found. This approach has several problems associated with it.

1. The light from stars in a globular cluster is smeared out by the PSF, which effectively makes the problem one of fitting a model to data that has been degraded by an instrumental response function (in this case the PSF). To make matters worse the observed PSF (which is measured from a CCD image) is an approximation of the true PSF (which is the actual blurring experianced by the stellar image due to seeing) and must be determined observationally. The observed PSF contains noise, which makes a direct deconvolution of the observed images undesirable.

2. All sources of noise must be identified and correctly parameterized in order for a goodness-of-fit statistic to be meaningful. The noise on a CCD image comes primarily from four sources. First, there is read-out noise and quantisation noise inherent in the CCD electronics. The amount of read-out noise is far greater than the amount of quantisation noise for the data used in this thesis. Second, there is Poisson noise from the source itself. For all but the shortest exposures in this thesis the Poisson noise dominates the total noise. Third, there is sky-noise, i.e. Poisson noise arising from scattered light in the sky. For CFHT the sky brightnesses are typically $\mu_V = 21.1$ mag per $\square''$ and $\mu_I = 19.2$ mag per $\square''$. Finally, there is Poisson noise from the background that the globular cluster is sitting upon. The contribution from the background varies greatly from field to field. For fields in the halo of M31 (e.g. G302) the background is negligible. However, for fields in the

density profile of the cluster. The models also contains two scaling parameters: the King core radius, and the central density. Such models have been found to be very effective at reproducing the surface brightness and surface stellar number-density profiles of most Galactic globular clusters (e.g. Peterson & King 1975 [110], Alcaino 1977 [2], Harris & Racine 1979 [63], Madore 1980 [94], Djorgovski & King 1984 [45], Webink 1985 [154], Peterson & Reed 1987 [109], and Trager et al. 1993 [145]).

In real life, however, globular clusters are not quite this simple. There are several physical effects which need to be considered in order to construct physically realistic dynamical models of globular clusters. Encounters between stars (which are most important in the core of a cluster) can be taken into account by setting the right-hand side of Equation 3.2 equal to a collision term, $\Gamma(f)$. This term denotes the rate of change of f due to stellar encounters. Since this thesis does not consider the detailed stellar interactions within a globular cluster I will assume that $\Gamma(f) = 0$, i.e. globular clusters are collisionless systems. For details on solving Equation 3.2 using the Fokker–Planck approximation see §8.3 of Binney & Tremaine (1987) [17]. Gunn & Griffin (1979) [61] have extended the single-mass Michie–King model described above to incorporate realistic stellar mass functions. Lupton & Gunn (1987) constructed rotating Michie–King models. For simplicity the single-mass, non-rotating Michie–King models are used in this thesis. Figures 3 and 9 of Gunn & Griffin (1979) [61] suggest that the tidal radii obtained by fitting single-mass Michie–King models are similar to the tidal radii obtained using multi-mass Michie–King models, but the detailed shape of the cluster profile (parameterized by the central potential W_0) can be significantly different. Similarly, rotation is mainly important when fitting models to the velocity structure of a cluster, something which is not done in this thesis.

an *isotropic* Michie–King model, or simply a King (1966) [82] model. A model with $r_a \neq +\infty$ (some of the velocity dispersion is perpendicular to the radial direction in the cluster) is called an *anisotropic* Michie–King model.

Since the spatial density is a function of the dimensionless central potential, W_0, and not directly of the radius, r, Equation 3.5 has to be solved using Poisson's Equation:

$$\nabla^2 W(R) = 4\pi G\sigma^{-2} r_c^2 \rho\Big(W(R), r_a\Big), \tag{3.7}$$

where $R = r/r_c$ is the dimensionless radius and r_c is the King core radius. The King core radius is defined to be the radius that satisfies $-4\pi G\sigma^{-2} r_c^2 \rho(0) = 9$ and approximately corresponds to the half-power radius of the projected mass density of the cluster. Once the spatial density as a function of radius has been found it is then projected into the plane of the sky using:

$$\Sigma(r) = 2\int_{s=r}^{r_t} \frac{\rho(s)\, s}{\sqrt{s^2 - r^2}}\, ds, \tag{3.8}$$

where r_t is the King tidal radius of the globular cluster. This is the radius where the spatial density of the cluster drops to zero, i.e. $\rho(r_t) \equiv 0$. Unfortunately the term "tidal radius" is somewhat confusing since, in Michie–King theory, r_t is *not* determined by the tidal field of the gravitational potential well that the globular cluster sits in. The King tidal radius is simply the radius at which the cluster escape velocity is $v_e = 0$[1].

These models are based on the work of Michie (1963) [97] and King (1966) [82]. This simple approach results in model globular clusters that are similar to isothermal spheres out to near the tidal radius. In the outer regions of the cluster the spatial density rapidly drops to zero. Michie–King models are parameterized by their central potential and their anisotropy radius. These two parameters determine the shape of the surface

[1]Through-out this thesis the term tidal radius will be used since this term is in standard use in the astronomical literature.

$$\rho(\mathbf{x}) = \iiint\limits_{|\mathbf{v}|\geq 0} f(\mathbf{x},\mathbf{v})\, 4\pi v^2\, d\mathbf{v}. \tag{3.3}$$

A globular cluster does not extend to infinity but has a physical cut-off radius. Any stars whose velocities carry them beyond this radius will no longer be gravitationally bound to the cluster. Modifying the King (1966) [82] distribution function to include velocity anisotropy gives:

$$f(r,\mathbf{v}) = k \exp\left(\frac{-r^2 v_\perp^2}{2r_a^2\sigma^2}\right) \exp\left(\frac{(V(r)-V(0))}{-\sigma^2}\right) \left[\exp\left(\frac{-v^2}{2\sigma^2}\right) - \exp\left(\frac{-v_e^2}{2\sigma^2}\right)\right]. \tag{3.4}$$

Here, $V(r)$ is related to the total energy of a star by $E = 1/2v^2 + V(r)$, the escape velocity for a star at a distance r from the centre of the cluster is $v_e = \sqrt{-2V}$, and σ is the one-dimensional velocity dispersion of the stars. The radial component of the velocity within the cluster is v, and the component of the velocity that is perpendicular to the radial direction in the cluster is $v_\perp$. The anisotropy radius of the cluster is r_a.

Integrating over the velocities (up to the escape velocity) gives:

$$\rho(W(r), r_a) = 4\sqrt{2}\pi k \sigma^3\, e^{W(r)-W_0} \int_{\eta=0}^{W(r)} A(\eta, r_a) \left(e^{-\eta} - e^{-W(r)}\right) \eta^{1/2}\, d\eta, \tag{3.5}$$

where $W(r) = -V(r)/\sigma^2$ and $\eta = v^2/2\sigma^2$. The dimensionless central potential is $W_0 = W(0)$. The anisotropy term, $A(\eta, r_a)$, is given by:

$$A(\eta, r_a) = \frac{\exp(-r^2/r_a^2\,\eta)}{r/r_a\sqrt{\eta}} \int_{y=0}^{(r/r_a)\sqrt{\eta}} \exp\left(y^2\right)\, dy. \tag{3.6}$$

where $A(\eta, r_a)$ goes to one as r_a goes to infinity, i.e. the amount of anisotropy in the cluster's velocity dispersion tensor goes to zero as the anisotropy radius goes to infinity. A model with $r_a = +\infty$ (all of the velocity dispersion is in the radial direction) is called

3.2 Fitting Michie–King Models

3.2.1 The Theory Behind Michie–King Models

It is possible to use straight-forward dynamical models of globular clusters to predict the surface brightness profile that a cluster will have on the sky. In this thesis I am primarily interested in the overall structures of the globular clusters of M31, not in their detailed spatial and dynamical structures. Therefore I will use the models of Michie (1962) [97] and King (1966) [82] to describe their observed surface brightness profiles.

To first-order accuracy globular clusters can be approximated as collisionless spherical systems of stars moving under the influence of a smooth, self-generated, gravitational potential $\Phi(\mathbf{x}, t)$. At a given time, t, the phase-space density of the stars is given by $f(\mathbf{x}, \mathbf{v}; t)$. The phase-space density is simply the number of stars at position $\mathbf{x}$ with velocity $\dot{\mathbf{x}} = \mathbf{v}$ so it is physically meaningless to have $f(\mathbf{x}, \mathbf{v}; t) < 0$. Each star is accelerated by the smooth underlying gravitational potential generated by the other stars so a star's acceleration is given by $\mathbf{a} = \dot{\mathbf{v}} = \ddot{\mathbf{x}} = -\nabla\Phi(\mathbf{x}, t)$. If close encounters between stars are ignored then stars flow smoothly from one part of phase-space to another and the continuity equation holds:

$$\frac{df}{dt} = \frac{\partial f}{\partial t} + \sum_{i=1}^{3} v_i \frac{\partial f}{\partial x_i} + \sum_{i=1}^{3} \dot{v}_i \frac{\partial f}{\partial v_i} = 0 \tag{3.1}$$

which is equivalent to

$$\frac{\partial f}{\partial t} + \mathbf{v} \cdot \nabla f - \nabla\Phi \cdot \frac{\partial f}{\partial \mathbf{v}} = 0. \tag{3.2}$$

Equation 3.2 is called the collisionless Boltzmann equation and is the fundamental equation of stellar dynamics in the absence of star-to-star interactions. The three-dimensional space density at location $\mathbf{x}$ can be found by integrating $f(\mathbf{x}, \mathbf{v}; t)$ with respect to velocity:

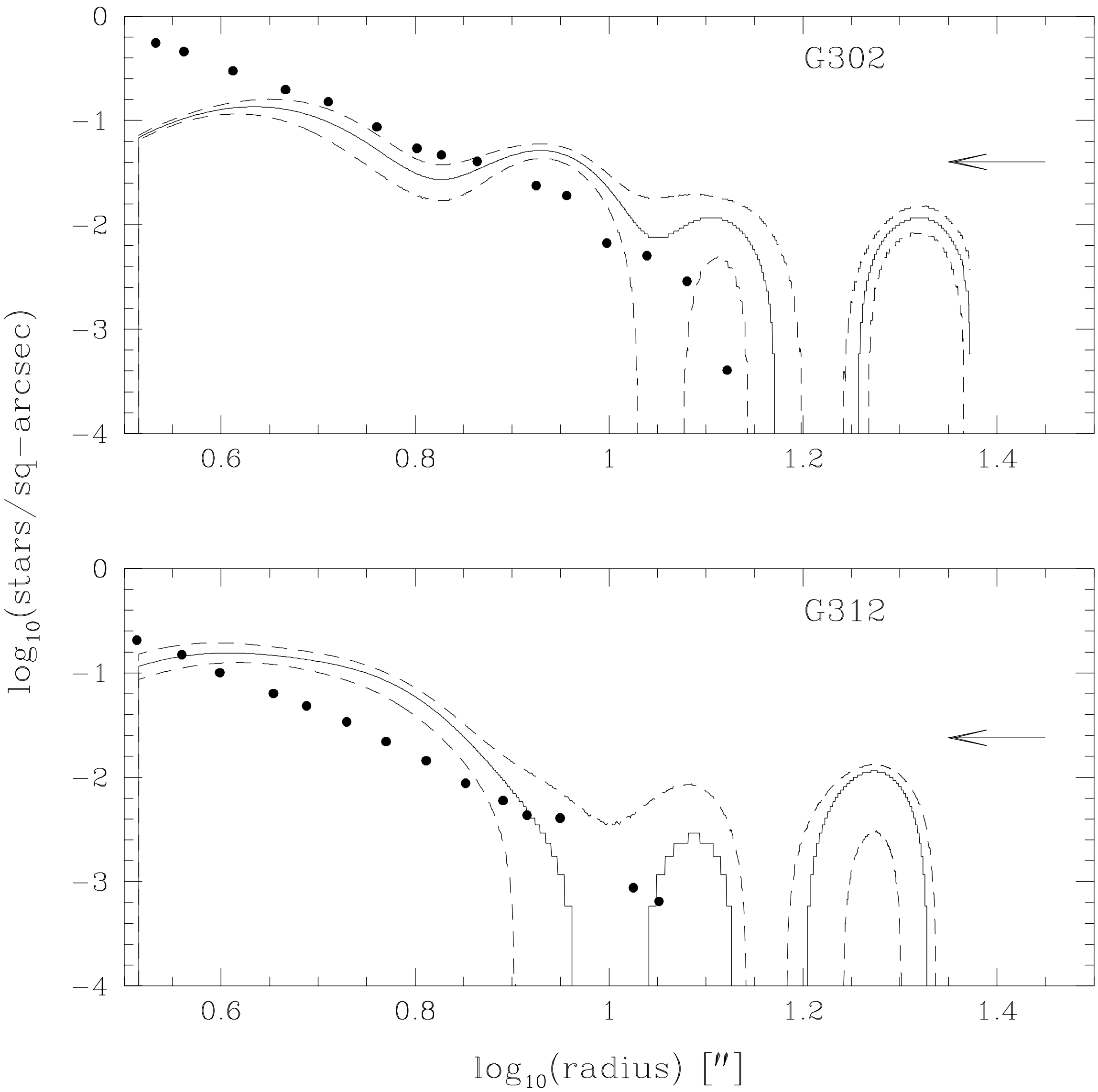

Figure 3.1: Adaptive kernel smoothing of the star count data for the outer regions ($r \geq 25''$) of G302 and G312 (solid lines). The error curves (dashed lines) were obtained from bootstrapping and represent the combined 1σ uncertainties in the smoothing and in the background determinations. The stellar background densities are indicated by the arrows and filled circles represent the I-band integrated light profiles. The agreement between the limiting radii determined from star counts and the integrated light profiles can be seen. The turn-down at $\log_{10}(r_{\rm eff}) \sim 0.5$ ($r_{\rm eff} \sim 3''$) on each profile is an artifact caused by truncating the star-count data at $r_{\rm eff} = 25$ pixels.

locating the outer edges of globular clusters in M31.

The dashed lines in Figure 3.1 show the 1σ uncertainties in the smoothed star count profiles for each globular clusters. These uncertainties were estimated by generating 10,000 star fields using bootstrap resampling of the original stellar positions for each globular cluster. These data sets were smoothed in the same manner as the original data. The upper and lower dashed lines indicate the approximate uncertainty in the shapes of the smoothed star count profiles. The uncertainties are small when the stellar density of the cluster stars is greater than the stellar density of the background.

For G302 the stellar density profiles give a 1σ range for the limiting radius of $11''\!.8 \leq r_{\rm lim} \leq 15''\!.1$. For G312 the limiting radius from Figure 3.1 is $9''\!.2 \leq r_{\rm lim} \leq 13''\!.1$ (also see Table 3.2). The structures seen at radii less than $\log_{10}(r_{\rm eff}) \sim 1.2$ in each cluster are probably artifacts caused by small number statistics. The density enhancement at $\log_{10}(r_{\rm eff}) \sim 1.1$ is only significant at the 1σ level and has a width approximately equal to the smoothing scale, h, at that radius. This suggests that this density enhancement is not real. Also, the integrated light profiles of each cluster are still dropping at $\log_{10}(r_{\rm eff}) \sim 1$ suggesting that the stars in this density enhancement are still a part of the cluster.

The density enhancements at $\log_{10}(r_{\rm eff}) \sim 1.3$ lie beyond the fitted Michie–King tidal radii of the globular clusters (see Tables 3.1, 3.2, and 5.4). It is not clear that these enhancements are anything other than a statistical effect caused by the small numbers of stars located at radii between $\sim 10''$ and $\sim 25''$. G312, for example, has only 45 stars between these radii, giving it a projected stellar density of $\Sigma = 0.027 \pm 0.004$ stars/$\Box''$, well within the 1σ uncertainty of the background density, $\Sigma_{\rm bkgd} = 0.026 \pm 0.004$ stars/$\Box''$. Further, the widths of these density enhancements are approximately the same as the smoothing parameters used to generate the projected surface density profiles. However, these density enhancements are reminiscent of the halo of escaped stars predicted by Oh & Lin (1992) [103]. This possibility will be explored in more detail in Chapter 5.4.

standard deviation h at the location of each star then summing the contributions from all the Gaussians. The choice of the smoothing parameter, h, is somewhat arbitrary. Silverman (1982) [131] suggests using $h = 1.06\sigma n^{-1/5}$ where n is the local number of data points and σ is the standard deviation of the data, for Gaussian-like distributions since this approximately corresponds to minimizing the integrated mean square error between the derived smoothed profile and the intrinsic profile that the data are drawn from. However, star counts in the outer regions of a globular cluster do not follow a Gaussian surface number density distribution so this prescription will underestimate h. Vio et al. (1994) [151] suggest using $h = 0.9 \min(\sigma, x/1.34) n^{-1/5}$, where x is the interquartile range of the distribution, since this is valid for a wider range of distributions than the Gaussian approximation is. Both of these schemes tend to provide too little smoothing resulting in significant noise in the smoothed profile. After some experimentation I adopted values of h roughly two to three times larger than those obtained using these data-based schemes.

Figure 3.1 shows the smoothed projected surface density profiles for G302 and G312 with the mean stellar backgrounds subtracted. These profiles were obtained using the adaptive kernel smoothing procedure described above and were used to estimate the limiting radius of the globular clusters. Since the projected stellar densities in the outer regions of the globular clusters are similar to those in the halo of M31 the detailed shape of the smoothed star count profile will be strongly influenced by statistical fluctuations in the actual number of stars and by the details of the smoothing procedure. Therefore Figure 3.1 has only been used to estimate the location of the outer edge of each globular cluster. A comparison between the outer edge of the smoothed stellar density profiles and the outer edge of the integrated light profiles shows that both methods find the outer edges of the globular clusters to be at approximately the same locations. This suggests that both integrated light profiles and stellar density profiles provide consistent ways of

Chapter 3

CFHT Results

3.1 Star Counts

Star counts were obtained in the outer regions of G302 and G312 using standard DAOPHOT/ALLSTAR techniques. To aid in finding stars the integrated light from each cluster was modeled using the ARTDATA package in IRAF and subtracted from each image. Only stars located at least 25 pixels ($\sim 3\farcs3$) from the cluster centre were used since stars nearer to the centre suffer from severe incompleteness problems. Subtracting the model cluster significantly altered the photometric properties of the stars located where the model was subtracted. However, since this study is primarily interested in the number density of stars in the outer regions of the clusters, not precise magnitudes of the individual stars, photometric accuracy is not required. To minimize contamination from cosmic rays, noise spikes, pixel defects, residuals from the subtraction of the unresolved light and other false detections, the V- and I-band star lists were matched and only objects that appeared in both bandpasses were considered to be stars. Due to the short exposure times for many of the HRCam images, stars could not be resolved in most of the clusters.

The adaptive kernel smoothing techniques described by Merritt & Tremblay (1994) [96] were used to create smoothed one-dimensional surface density profiles from the G302 and G312 star count data. Adaptive kernel smoothing is done by placing a Gaussian of

Field	Filter	α	β	γ	FWHM	ϵ	θ_0
Bo153	V	$0\farcs83$	2.21	2	$1\farcs01$	0.03	$\cdots$
	I	$0\farcs42$	1.75	2	$0\farcs59$	0.07	$\cdots$
vdB2	V	$\cdots$	$\cdots$	$\cdots$	$0\farcs69$	0.03	$-8°$
	I	$\cdots$	$\cdots$	$\cdots$	$0\farcs72$	0.20	$-64°$
vdB5	V	$0\farcs77$	2.30	2	$0\farcs92$	0.04	$-49°$
	I	$0\farcs56$	2,00	2	$0\farcs72$	0.08	$-64°$
V253	V	$1\farcs07$	4.13	2	$0\farcs86$	0.14	$-80°$
	I	$0\farcs66$	3.47	2	$0\farcs62$	0.13	$-77°$

2.3 (continued)

Field	Filter	α	β	γ	FWHM	ϵ	θ_0
G2	V	$0''.66$	2.65	2	$0''.73$	0.06	$40°$
	I	$0''.65$	2.30	2	$0''.78$	0.12	$-20°$
G70	V	...	...	...	$0''.68$	0.05	$39°$
G177	V	$0''.77$	2.30	2	$0''.92$	0.04	$-49°$
	I	$0''.56$	2.00	2	$0''.72$	0.08	$-64°$
G185	V	...	...	...	$0''.69$	0.03	$-8°$
	I	...	...	...	$0''.72$	0.20	$-64°$
G185B	V	...	...	...	$0''.69$	0.03	$-8°$
	I	...	...	...	$0''.72$	0.20	$-64°$
G196	V	$0''.64$	2.47	2	$0''.73$	0.04	...
	I	$0''.47$	1.93	2	$0''.62$	0.06	...
G208	V	$0''.83$	2.21	2	$1''.01$	0.03	...
	I	$0''.42$	1.75	2	$0''.59$	0.07	...
G212	V	$1''.07$	4.13	2	$0''.86$	0.14	$-80°$
	I	$0''.66$	3.47	2	$0''.62$	0.13	$-77°$
G213	V	...	...	...	$0''.83$	0.06	$-89°$
	I	...	...	...	$0''.56$	0.06	$-63°$
G215	V	$1''.07$	4.13	2	$0''.86$	0.14	$-80°$
	I	$0''.66$	3.47	2	$0''.62$	0.13	$-77°$
G218	V	$1''.07$	4.13	2	$0''.86$	0.14	$-80°$
	I	$0''.66$	3.47	2	$0''.62$	0.13	$-77°$
G222	V	$0''.41$	2.06	2	$0''.51$	0.04	...
	I	$0''.40$	1.75	2	$0''.56$	0.08	...
G231	V	$0''.58$	1.85	2	$0''.78$	0.01	$55°$
	I	$0''.56$	2.02	2	$0''.72$	0.09	$-9°$
G233	V	$0''.58$	1.85	2	$0''.78$	0.01	$55°$
	I	$0''.56$	2.02	2	$0''.72$	0.09	$-9°$
G263	V	...	...	...	$0''.71$	0.07	$32°$
	I	...	...	...	$0''.71$	0.10	$5°$
G302	V	$0''.58$	1.90	2	$0''.77$	0.04	$65°$
	I	$0''.51$	2.15	2	$0''.63$	0.08	$60°$
G312	V	$0''.56$	2.51	2	$0''.64$	0.03	$90°$
	I	$0''.50$	2.40	2	$0''.58$	0.04	$-35°$
G352	V	...	...	...	$0''.73$	0.07	$53°$
	I	...	...	...	$0''.70$	0.10	$30°$
G355	V	...	...	...	$0''.78$	0.04	$-72°$

Table 2.3: Seeing characteristics for the CFHT HRCam images.

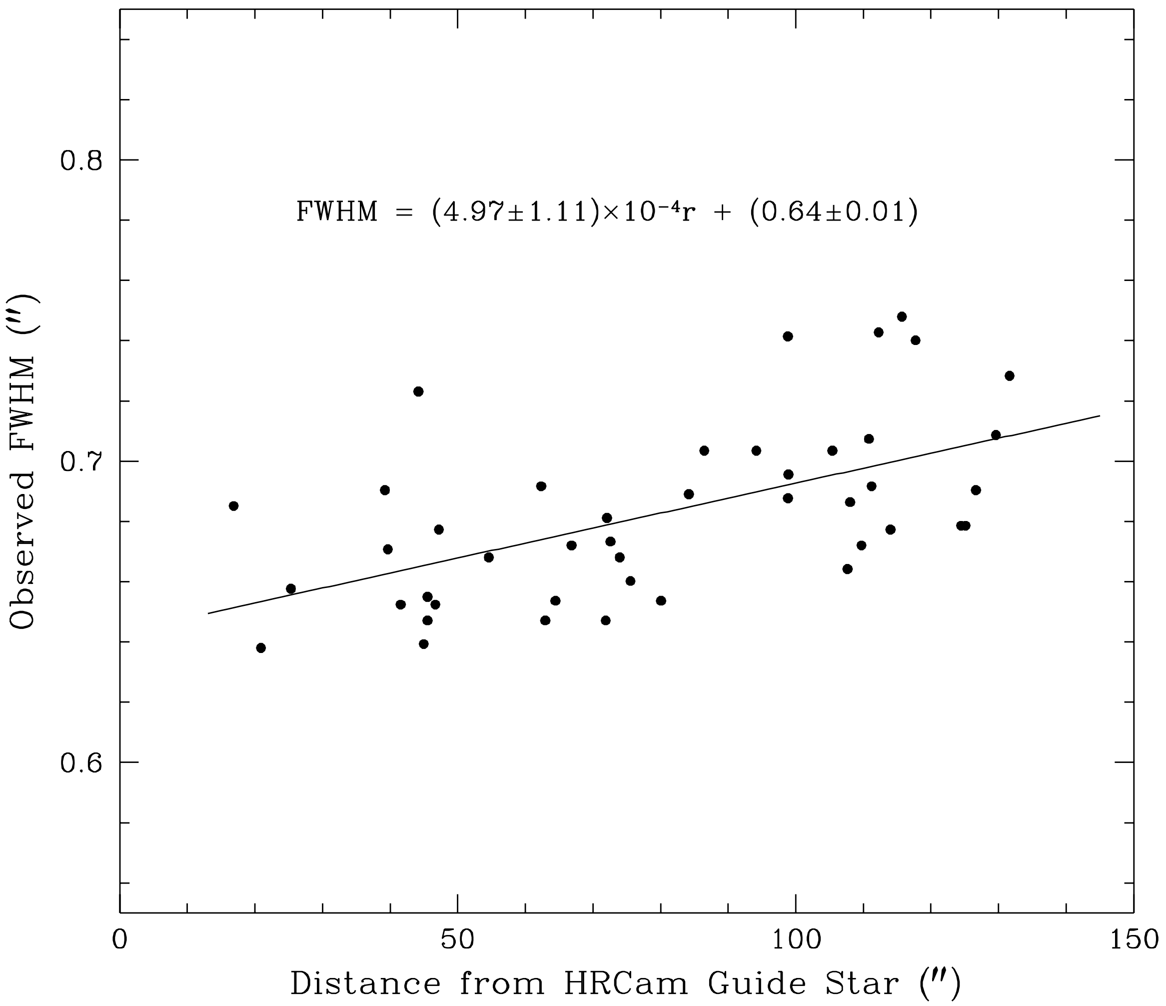

Figure 2.2: The Gaussian FWHMs of the stellar profiles vary with the distance from the HRCam guide star. This figure shows the variation in FWHM for the I-band image of G302. The variations in this figure are typical of the variations seen during the entire CFHT observing run. G302 is located $\sim 40''$ from the HRCam guide star and has a tidal radius of $\sim 10''$. Since the systematic changes in the stellar FWHM over the region of the sky covered by the globular cluster is less than the scatter in the FWHM at a given distance from the guide star the PSF was assumed to be constant over the region of the CCD covered by the globular cluster. The solid line is the best-fitting straight line to the data.

$\epsilon \equiv 1 - b/a$, for the PSFs were $0.03 \lesssim \epsilon \lesssim 0.08$. In principle the ellipticity can be treated by fitting a two-dimensional Moffatian to the stellar profiles. However the PSF derived using the DAOPHOT II PSF routine includes a table of residuals which will compensate for deviations in the PSFs away from the assumed functional form. This combination of analytical and empirical components enables DAOPHOT II to more accurately model the shape of the PSF than the purely analytical Moffatian description can. Therefore, this thesis uses the DAOPHOT II PSFs for seeing-convolutions.

Since the seeing varies as a function of time and colour a separate PSF was determined for each cluster and each filter. Seeing parameters for each PSF are given in Table 2.3. If Moffatian parameters (α, β, and γ) are given then the FWHM was computed from the one-dimensional Moffatian using $\mathrm{FWHM} = 2\alpha(2^{1/\beta} - 1)^{1/\gamma}$. The ellipticities, ϵ, and position angles, θ_0, were measured from the DAOPHOT II PSF. Through-out this thesis position angles are assumed to be measured in degrees east of north on the sky unless otherwise indicated. For some fields it was not possible to obtain a good fit using Moffatians. In these cases the FWHM was estimated directly from the surface brightness profiles of several stars in that field. The globular cluster V253 is object number 253 in Vetešník's (1962) [150] catalogue. Similarly the globular cluster Bo153 is object 153 in the Battistini et al. (1982) [7] catalogue, while the globular clusters vdB2 and vdB5 are from van den Bergh (1969) [149].

2.3 Seeing

A typical Galactic globular cluster has a King (1966) [82] core radius of ~ 1 pc and and tidal radius of ~ 125 pc (although there is a large spread in these values from cluster to cluster). At the distance of M31 these sizes correspond to angles on the sky of $\sim 0\farcs25$ and $\sim 35''$ respectively. Since the seeing discs for this data typically had FWHMs of $\sim 0\farcs7$, the observed shapes and light distributions of the clusters were significantly affected by the seeing. In order to correct for this it is necessary to accurately determine the shape of the PSF and its dependence on position on the CCD image.

Figure 2.2 shows that the star-to-star scatter in the stellar FWHM at the location of the cluster exceeds the systematic change in FWHM across the cluster by a factor of ~ 4. This suggests that the positional variations in the PSF can be ignored if only those stars located near the cluster are used to define the PSF.

I found that a modified Moffatian (Moffat 1969 [100], Kormendy & McClure 1993 [84]):

$$M(r) = M_0\left[1 + \left(\frac{r}{\alpha}\right)^{\gamma}\right]^{-\beta}, \tag{2.2}$$

provided a good fit to the isolated bright stars on most of the frames. The central intensity is given by $M_0 = M(0)$. The parameter α is an estimate of the width of the intensity profile and is approximately given by $10^5 \cdot \lambda/r_0$ (Walker 1987 [153]) where λ is the wavelength of the light and r_0 is the coherence length of the atmospheric turbulence. The parameter β controls the sharpness of the intensity profile and is a measure of the spectrum of the sizes of the atmospheric turbulence cells that cause the seeing. γ controls the size and shape of the core of the seeing profile.

Moffatians were fitted to several stars in each image in order to find the mean seeing profile for each image. This functional form, however, assumes a circularly symmetric PSF—which was not the case for the CFHT data presented here. Typical ellipticities,

2.2.3 Background Subtraction

The unresolved background light from the M31 halo and disc was removed by fitting and subtracting a surface on each frame. To prevent high-frequency contamination in the fitted background a single pass with DAOPHOT II (Stetson 1987 [141], 1991 [140], 1992 [139], Stetson et al. 1990 [143]) was made to identify and remove field stars from each image. In addition, galaxies and globular clusters were modeled and subtracted using the IRAF STSDAS.ISOPHOTE.ELLIPSE and STSDAS.ISOPHOTE.BMODEL tasks. The resulting images were visually inspected and regions with poor subtractions, and other cosmetic defects, were masked. Two-dimensional third-order splines were fit to most of the images to allow for large-scale variations in the background. For some fields subtracting a constant background was sufficient.

Residual large-scale variations across each field after subtracting the fitted backgrounds were usually less than $\sim 1\%$ of the original background value. The fields located near the centre of M31 showed larger residuals than those located away from the galaxy. This is due to the large amount of small-scale galactic structure near the centre of M31. A visual examination of fields such as the G185 field or G177 reveals the presence of dust lanes and small-scale surface brightness fluctuations arising from unresolved stars along the line-of-sight in M31. Figures 7.1 and 7.2 in Chapter 7 show an example of the detailed structure that becomes visible in many of the fields once the large-scale structure in the unresolved light has been removed.

Night	Date	$K_{0,V}$	$K_{0,I}$
1	Aug. 16/17	24.023 ± 0.005	23.827 ± 0.027
2	Aug. 17/18	24.053 ± 0.019	23.910 ± 0.009
3	Aug. 18/19	24.040 ± 0.009	23.873 ± 0.034
4	Aug. 19/20	23.767 ± 0.019	23.668 ± 0.011

Table 2.2: Photometric zero-points for the HRCam images.

2.2.2 Calibrating the Data

During the observing run several standard stars from the lists of Landolt (1983) [85], and the M92 Consortium fields of Stetson & Harris (1988) [142], were observed. The standard star data was processed by Hodder (1995) [70] to obtain magnitude zero-points for the first three nights of the observing run. Unfortunately no standard stars were observed on the night of August 19/20 so these data were calibrated by calculating the zero-point offset between M31 halo stars observed in the G312 field on the night of August 18/19 (for which standard star observations were made) and the night of August 19/20 (for which no standard stars were observed). This was the only field observed on the night of August 19/20 that was also observed on one of the three photometric nights. The photometric zero-points for the night of August 19/20 are $\sim 2\sigma$ brighter than the zero-points for the other three nights. This is probably due to the night of August 19/20 not being photometric and suggests that magnitudes determined on night 4 be treated with some caution.

The relationship between the observed count rate, C, in ADU per second, and the calibrated surface brightness, μ, in magnitudes per square arcsecond, is:

$$\mu = K_0 - 2.5\log_{10}(C) - 2.5\log_{10}(1/S^2) \tag{2.1}$$

where K_0 is the zero-point, and S is the pixel scale ($0\farcs131$/pixel for the data presented here). The zero-points, and their standard errors, for each night are listed in Table 2.2.

on the exposure time of the images. On a typical 1000 second exposure the procedure described above found a few dozen cosmic rays.

Multiple exposures were made of most of the fields. The deep exposures in each field were combined to improve their signal-to-noise properties in the following way. First, the individual frames were examined and those that were of significantly lower quality than the others (e.g. worse seeing, evidence of telescope motion, etc.) were discarded. The remaining images of each field were re-registered to a common coördinate system and then averaged using the appropriate IRAF routines. Table 2.1 lists the exposure times, noise characteristics, and number of CCD images combined for each field imaged in this study. The read-out noise and gain values have been adjusted for the number of frames that were combined to get a final image in each filter.

selecting regions of the sky that are devoid of bright objects and taking a large number of short exposures instead of a small number of long ones. The location on the sky of each exposure can be shifted by a few pixels to prevent underlying structure in the sky from illuminating the same pixel and thus appearing to be a flat-fielding artifact. Since the pixel sensitivity is wavelength dependent this process must be performed for each filter used.

Several sky flats were obtained during either the morning or evening twilight periods on each night and these images were median-combined to produce a master flat-field frame for each filter. Each flat-field frame is normalized to a mean pixel value of one and then the data images were divided by the appropriate master flat-field frames.

The next step is to remove cosmic rays from the images. A cosmic ray striking a pixel will create a high signal that will stand out above the pixel-to-pixel noise in the image. These pixels were identified as follows. First, each pixel is compared with its neighbours in a 5×5 or 7×7 comparison box. If the flux in that pixel exceeded the mean flux in the box of surrounding pixels by $\sim 5\sigma$, where σ is the standard deviation in the sky in the comparison box, that pixel is flagged as a potential cosmic ray. Next, a plane is fit to the border pixels of the box around each cosmic ray candidate and subtracted. The mean flux in the background-subtracted box is then compared with the flux in the candidate pixel. If the ratio of these fluxes is less than ~ 0.05 then the pixel is flagged as a cosmic ray and replaced by the mean of its neighbours. The IRAF[3] implementation of this algorithm NOAO.IMRED.CCDRED.COSMICRAYS was used to remove cosmic rays from the data images. The box sizes and other parameters of the algorithm depend on the noise characteristics, seeing, background structure, and cosmic ray characteristics so they were interactively adjusted for each image. The number of cosmic ray hits depended

[3]Image Reduction and Analysis Facility (IRAF), a software system distributed by the National Optical Astronomy Observatories (NOAO).

2.2 Data Reduction

2.2.1 Preprocessing

Bias subtraction and flat fielding was done for all images using standard CCD preprocessing methods (e.g. Walker 1990 [152]). First, an electronic pedestal voltage was subtracted from each image. Next, bias frames were created by taking several (~ 60) zero-second exposures with the shutter closed. A master bias was created by median-combining these images. The master bias frame was then subtracted from each image.

The dark current for the SAIC 1 CCD chip is 0.2 e^- per minute per pixel (CFHT Observers' Manual 1990 [26]). The longest exposure (1000 seconds) has a total dark count of 3.3 e^- per pixel, which corresponds to 2.08 ADU per pixel. Assuming a sky brightness of $\mu_V = 21.1$ mag per $\square''$ (CFHT Observers' Manual 1990 [26]) the contribution to the noise from the dark current will be only $\sim 1.5\%$ of the contribution from a uniform sky. The presence of unresolved stars in the disc and halo of M31 cause considerable surface brightness fluctuations in the sky which contribute to the noise in the images. These surface brightness fluctuations are large compared to the level of dark current in these exposures. Therefore the dark current can be ignored since its contribution to the total noise is small compared to the contribution from surface brightness fluctuations.

An ideal CCD would have uniformly sensitive pixels. However, in real life variations in pixel-to-pixel sensitivity can be quite large. To compensate for this several images of blank regions of sky were taken during the morning and evening twilight periods. The twilight sky provides a near-uniform illumination of the CCD at similar wavelengths to those of images of the night sky. Unfortunately the twilight sky is not a truly uniform source of light. Stars, galaxies, and other objects are still present in the sky and they can rise above the noise during long exposures. This contamination can be reduced by

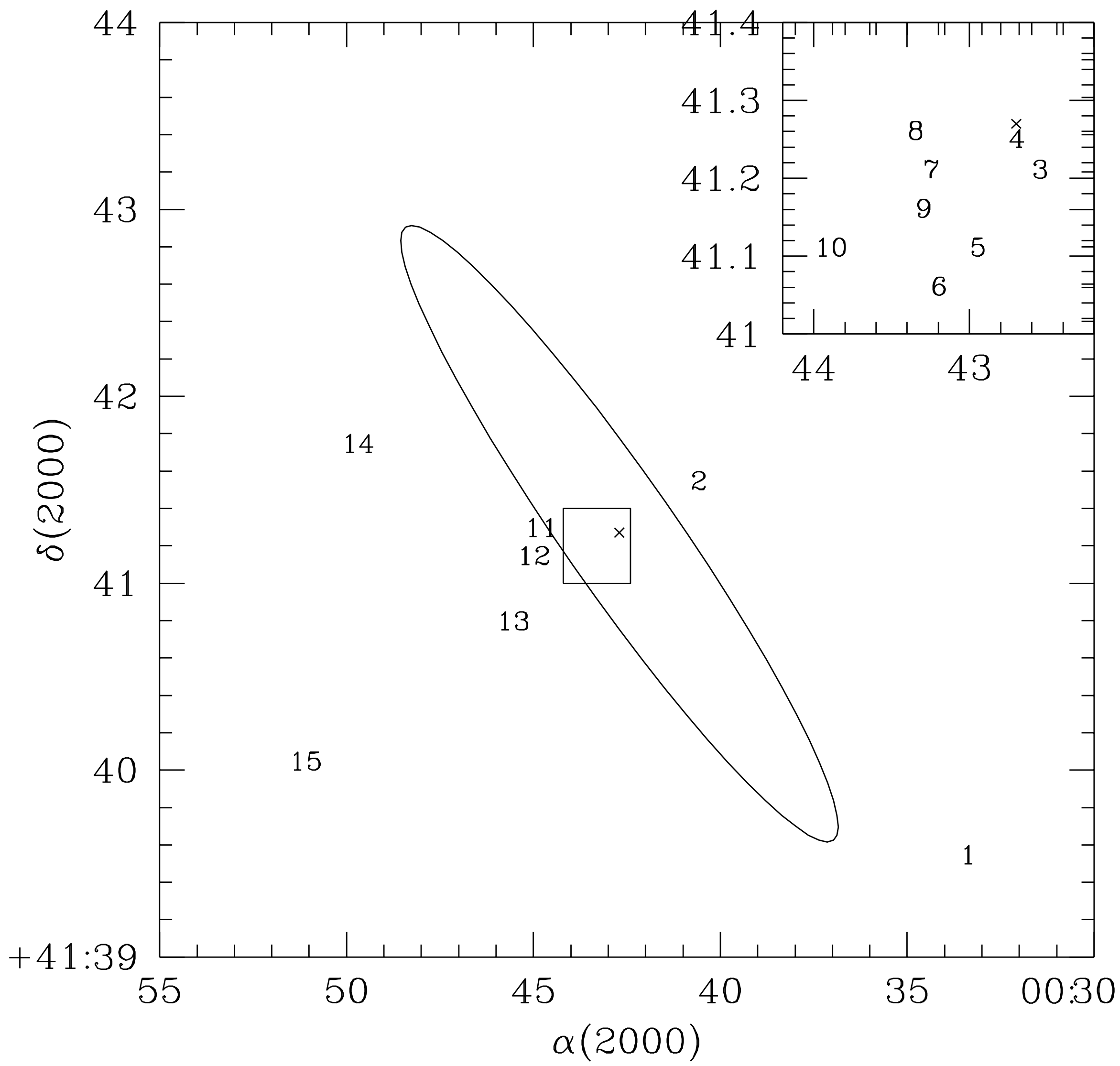

Figure 2.1: This figure shows the approximate locations of the fields listed in Table 2.1. The ellipse shows the approximate size and orientation of the optical edge of the disc of M31 and the cross shows the approximate location of the centre of M31.

Field	α (2000.0)	δ (2000.0)	Date (1990)	Filter	Time (s)	RN (ADU)	Gain	N
1	$00^h33^m33\overset{s}{.}6$	$+39°31'20''$	Aug. 19/20	V	100.0	4.08	1.6	1
				I	100.0	4.08	1.6	1
2	$00^h40^m48\overset{s}{.}9$	$+41°11'31''$	Aug. 18/19	V	30.0	4.08	1.6	1
3	$00^h42^m34\overset{s}{.}4$	$+41°13'30''$	Aug. 16/17	V	450.0	4.08	1.6	1
				I	100.0	4.08	1.6	1
4	$00^h42^m44\overset{s}{.}2$	$+41°14'56''$	Aug. 16/17	V	300.0	4.08	1.6	1
				I	100.0	1.67	9.6	6
5	$00^h42^m58\overset{s}{.}7$	$+41°08'52''$	Aug. 17/18	V	600.0	4.08	1.6	1
				I	240.0	2.88	3.2	2
6	$00^h43^m15\overset{s}{.}5$	$+41°06'32''$	Aug. 18/19	V	300.0	2.88	3.2	2
				I	120.0	1.82	8.0	5
7	$00^h43^m18\overset{s}{.}3$	$+41°10'55''$	Aug. 17/18	V	450.0	4.08	1.6	1
				I	360.0	4.08	1.6	1
8	$00^h43^m25\overset{s}{.}7$	$+41°15'27''$	Aug. 17/18	V	300.0	2.88	3.2	2
				I	120.0	1.82	8.0	5
9	$00^h43^m36\overset{s}{.}8$	$+41°07'30''$	Aug. 17/18	V	300.0	4.08	1.6	1
				I	240.0	2.88	3.2	2
10	$00^h44^m03\overset{s}{.}3$	$+41°04'28''$	Aug. 18/19	V	450.0	4.08	1.6	1
				I	450.0	4.08	1.6	1
11	$00^h45^m13\overset{s}{.}0$	$+41°16'03''$	Aug. 16/17	V	450.0	4.08	1.6	1
				I	450.0	4.08	1.6	1
12	$00^h45^m25\overset{s}{.}2$	$+41°05'30''$	Aug. 16/17	V	1000.0	2.88	3.2	2
				I	400.0	2.88	3.2	2
13	$00^h45^m58\overset{s}{.}8$	$+40°42'32''$	Aug. 17–20	V	600.0	1.32	15.3	15
				I	321.4	1.09	22.4	14
14	$00^h50^m10\overset{s}{.}0$	$+41°41'01''$	Aug. 18/19	V	600.0	2.36	4.8	3
				I	300.0	2.36	4.8	3
15	$00^h51^m33\overset{s}{.}9$	$+39°57'34''$	Aug. 18/19	V	450.0	4.08	1.6	1

Table 2.1: The CFHT fields.

for looking at low surface brightness objects such as the outer regions of partially resolved globular clusters. The image scale with this set-up is $0\farcs131$ per pixel and the CCD covers an area of $\sim 2\ \square'$ on the sky. Each of the four nights were photometric with the typical seeing being $\theta \sim 0\farcs7$. Table 2.1 lists the fields that were imaged. Some of these fields contain more than one globular cluster. The right ascensions and declinations are for the approximate centres of each field and were taken from Crampton et al. (1985) [33] and Huchra et al. (1991, hereafter referred to as HBK) [76]. N is the number of exposures taken in each filter. Figure 2.1 shows the locations of the fields relative to the disc of M31.

Chapter 2

The CFHT Data

2.1 Observations

The ground-based image data used in this thesis were obtained at the Canada–France–Hawai‘i Telescope[1] (CFHT) between August 16 and 20, 1990 by Greg Fahlman and Carol Christian. Deep V- and I-band photometry[2] was obtained for fifteen fields in M31 that contained twenty-two globular clusters. Most of these fields were located roughly along the projected minor axis of M31 and extend from near the centre of that galaxy out to a projected distance of $\sim$ 40 kpc. The minor axis fields were chosen such that they were spaced at approximately equal logarithmic intervals along the minor axis. In addition some of the fields are located off the minor axis in order to image bright globular clusters that did not lie on the minor axis.

The DAO/CFHT HRCam (McClure et al. 1989 [95]) with the SAIC 1 CCD detector was used to obtain the images. The HRCam is an adaptive-optics system that performs tip-tilt corrections to reduce the effects of seeing on the images. The SAIC 1 CCD chip has a low read-out noise, RN = 6.5 e$^-$, and a gain of 1.6 e$^-$/ADU, making it well suited

[1]The Canada–France–Hawai‘i Telescope is operated by the National Research Council of Canada, le Centre National de la Recherche Scientifique de France, and the University of Hawai‘i.

[2]The V-band filter used here had a central wavelength of $\lambda_0 = 5485$ Å and a bandwidth of $\Delta\lambda = 908$ Å. The I-band filter used here had a central wavelength of $\lambda_0 = 8325$ Å and a bandwidth of $\Delta\lambda = 1975$ Å.

reliable structural parameters.

Another goal for the *HST* data is to search for extended halos of escaped stars around G302 and G312. Such halos have been predicted by dynamical models of globular clusters, and have been observed around some Galactic globular clusters. The small apparent size of the M31 globular clusters make them ideal targets for searching for extended stellar halos.

Finally, the *HST* data includes background fields in the halo of M31. This data will used to construct deep CMDs that could be used to study the stellar populations in the halo of M31. I will estimate the metallicity distribution of stars in the halo of M31 and compare this with the metallicity distribution in the Galactic halo and the M31 globular cluster system.

1.4 The Goals of this Thesis

The original goals of this work were to study the internal structures of the globular clusters in M31 and to compare them to the internal structures of the globular clusters in the Milky Way Galaxy. Globular clusters are believed to have formed at the same time as the Galactic and M31 halos, making them some of the oldest objects in the Universe. Therefore globular clusters can provide a tracer for the formation and dynamic evolution of their parent galaxies.

In this work I will determine the core, tidal, and half-mass radii of approximately two dozen globular clusters in M31 and compare the distributions of these quantities with the distributions of these radii for the Galactic globular clusters. In addition, I will measure the projected ellipticities and the orientations of the apparent major axes of the M31 globular clusters and compare these to those of the Galactic globular clusters. The internal structures of globular clusters are determined by the stellar dynamics within the clusters, and by the tidal field that the clusters are located in. If the globular clusters' structural parameters turn out to be similar then this would suggest that the two galaxies have had similar dynamical histories. If they turn out to be significantly different then this would suggest that M31 and the Milky Way Galaxy, despite being morphologically similar, have lived very different lives. These differences would then have to be taken into account in any theory of galaxy formation.

While this work was in progress I was able to obtain time on the *HST* to image two globular clusters in M31. This data was used to determine structural parameters of the globular clusters to a much higher degree of precision than could be done using the ground-based data presented in this thesis. The structural parameters determined using the space-based observations will be compared with those obtained using the ground-based observations in order to see if ground-based observations can return

The mean ellipticity of the Galactic globular clusters is $\bar{\epsilon} = 0.08 \pm 0.07$ while the mean ellipticity of the globular clusters in the Large Magellanic Cloud $\bar{\epsilon} = 0.11 \pm 0.07$. The quoted uncertainties are the standard deviations of the distributions of ellipticities in each galaxy. Unfortunately Lupton does not provide information on the standard errors in the means for these quantities. However, he quotes results from two-tailed Wilcoxian tests that suggest that the ellipticity distributions of the M31 and Galactic globular clusters are the same at the 99.6% confidence level. A similar test suggests that the distributions for M31 and the Large Magellanic Cloud are the same at the 66% confidence level. Baev et al. (1997) [5] found systematic differences between the shapes of M31's disc and halo globular clusters. They found that the disc globular clusters are triaxial ellipsoids while the halo globular clusters are oblate or prolate spheroids, but cautioned that this is a preliminary result since the sample of halo globular clusters in their study is small compared to the sample of disc globular clusters.

The first CMDs for globular clusters in M31 were for G1 by Heasley et al. (1988) [65] and G219 (= Mayall IV) by Christian & Heasley (1991) [29]. Couture et al. (1995) [31] undertook a systematic study of five M31 globular clusters (G11, G319, G323, G327 = Mayall VI, and G352 = Mayall V) with a range of iron abundances. Unfortunately none of these ground-based studies was able to reach the level of the horizontal branch at $V \simeq 25$. The first CMDs constructed from *HST* data were for G1 (Rich et al. 1996 [119]); G58, G105, G108, and G219 (Ajhar et al. 1996 [1]); and G280, G351, and Bo468 (Fusi Pecci et al. 1996 [56]). These CMDs were able to resolve stars one to two magnitudes below the red portion of the horizontal branch.

tidal radii of these clusters as the pre-refurbishment FOC's point-spread function (PSF) overfilled the FOC's field of view.

Cohen & Freeman (1991) [30] derived tidal radii for thirty M31 globular clusters by fitting seeing-convolved King (1962) [83] models. Although their fits to individual clusters were quite uncertain they did find a mean tidal radius for the M31 clusters—after adjustment for differences in galactic masses and rotation velocities—that was very similar to that of the Milky Way clusters.

Globular clusters do not exist in isolation but sit in the tidal field of a galaxy. Any stars that move beyond the tidal radius of a globular cluster will have velocity vectors similar to the velocity vector of the globular cluster. This can result in a globular cluster being surrounded by an extended halo of unbound stars which move in approximately the same direction as the globular cluster and have approximately the same velocity. This idea has been explored numerically by Oh & Lin (1992) [103] who predicted that globular clusters could be surrounded by extended halos of escaped stars which can persist for up to a Hubble time. Evidence for extended halos has been observed in some Galactic globular clusters by Grillmair et al. (1995) [59]. In addition, Grillmair et al. (1996, hereafter referred to as GAF) [58] have observed an excess of resolved and unresolved stars beyond the formal Michie–King tidal radii of several globular clusters in M31, as would be expected if extended halos were present.

There has been some interest in determining the ellipticities of M31 globular clusters. Pritchet & van den Bergh (1984) [115] measured an ellipticity of $\epsilon = 0.22$ for the region of G1 with $12'' \lesssim r \lesssim 35''$. Spassova et al. (1988) [135] measured ellipticities for approximately two dozen globular clusters while a study by Lupton (1989) [90] suggested that the mean ellipticity measured in the inner 7 to 14 pc of an M31 globular cluster ($\bar{\epsilon} = 0.08$) is indistinguishable from the mean ellipticity of Galactic globular clusters. In the outer 14 to 21 pc, however, the mean ellipticity of an M31 cluster is 0.11 ± 0.08.

The first study of the internal structures of globular clusters in M31 was undertaken by Battistini et al. (1982) [7], who estimated core radii for $\sim$ 120 clusters. Pritchet & van den Bergh (1984) [115] found that the surface brightness profile for G1 (= Mayall II)[4] had an excess of light at large radii compared to the best-fitting seeing-convolved analytical King (1966) [82] model (King models, and their cousins Michie–King models, are discussed in detail in Section 3.2.1). They did find that G1 was well fit by empirical King (1962) [83] models with core radii of $r_c \lesssim 0.5$ pc. Crampton et al. (1985) [33] used seeing-convolved King (1962) [83] models to derive a relation between the observed full-width at one-quarter maximum of the surface brightness profiles and true core radius. They used this relation to estimate the core radii for nearly 500 M31 globular clusters. Their values, however, are systematically $\sim$ 50% larger than those of Battistini et al. (1982) [7], despite the better seeing conditions of the Crampton et al. (1985) [33] data set. Bendinelli et al. (1990) [9] used ground-based data to produce seeing-deconvolved radial profiles for six bright globular clusters in M31. However, seeing and pixel scale limitations restricted them to resolutions of $\sim 0\farcs3$, insufficient to resolve the cores of the clusters. Still, their data suggested that M31 globular clusters have King-like profiles similar to those of Galactic globular clusters.

The core structures of some of M31's globular clusters have been studied using the pre-refurbished *HST*. Bendinelli et al. (1993) [8] detected a power-law density cusp in G105 using *HST*'s Faint Object Camera (FOC) images and a variety of image restoration and seeing deconvolution techniques. In addition, Fusi Pecci et al. (1994) [57] used similar methods to obtained half-width at half-maxima (HWHM) and half-light radii (r_{hl}) for thirteen M31 globular clusters from FOC images. They found HWHMs similar to the core radii of Galactic globular clusters. Their data, however could not be used to find the

[4] The G-numbers used in this thesis are from Sargent et al. 1977 [127]. The prefix "K" is used in some of the astronomical literature but this thesis always uses the prefix "G".

globular clusters can be easily resolved with the *Hubble Space Telescope* (*HST*) and large ground-based telescopes at sites with sub-arcsecond seeing. M31's low inclination ($i = 12\overset{\circ}{.}5$, Hodge 1992 [71]) means that many of its globular clusters are not superimposed against the disc of M31 making identification of globular clusters, and photometry of their stars, relatively straight-forward. M31 offers a unique laboratory to study the outer regions of globular clusters. Star counts are not reliable in the outer regions of Galactic globular clusters since the projected stellar densities of the clusters beyond distances of approximately half the tidal radius, are overwhelmed by random fluctuations in the background stellar number density (Innanen et al. 1983 [78]). However, M31's globular clusters have sufficiently small angular sizes ($\theta \sim 10''$ to $30''$) that both the cluster and the background can be imaged on a single large format CCD image. This eliminates the need to match photometric zero-points between the cluster and the background, which makes possible a more precise subtraction of the background light from the cluster light. Therefore, isophotal analysis is easier to perform on an M31 cluster than it is on a Galactic cluster.

M31 is the nearest "grand design" spiral galaxy to our own and is often considered a twin of the Milky Way galaxy. M31 is the most massive member of the Local Group of galaxies and is approaching us at $v_h = -297$ km$\cdot$s^{-1}. The galaxy has ~ 300 globular clusters, approximately twice the number that our Galaxy has, but has a comparable globular cluster specific frequency[3]. For M31 $S_{\mathrm{M31}} = 0.7 \pm 0.2$ while for the Galaxy $S_{\mathrm{Gal}} = 0.5 \pm 0.1$ (Harris 1991 [62]). The globular cluster luminosity function is the same as for the Galaxy suggesting that both globular cluster systems have undergone similar overall dynamical evolutions.

argued that the *Hipparcos* parallaxes are consistent with the accepted distance to M31 of ~ 725 kpc. In this thesis results are presented for both distance scales.

[3]Specific frequency, S, is essentially the number of globular clusters per unit luminosity of the parent galaxy.

1.3 Globular Clusters in M31

Globular star clusters are self-gravitating collections of between 10^4 and 10^6 stars that are usually associated with galaxies, although there is evidence that some clusters of galaxies contain a population of "free" globular clusters that are associated with the potentials of clusters of galaxies as a whole, and not any individual galaxy (West et al. 1995 [155]). Almost all of the Galactic globular clusters are made up of stars with a single overall chemical abundance suggesting that they formed in a single star-formation event[1]. Globular clusters typically have integrated magnitudes of $-10 \leq M_V \leq -4$, making globular cluster systems visible out to redshifts of $z \sim 0.04$, the approximate distance to the Great Wall galaxies. The shape of the globular cluster luminosity function has been assumed to be universal so it has been used as a distance indicator (see Harris 1991 [62] for a review). However, recent work has suggested that the shape of the globular cluster luminosity function may depend on the metallicity of the globular cluster system (Ashman et al. 1995 [3]) and the details of the dynamical evolution of individual globular clusters (e.g. Okazaki & Tosa et al. 1995 [105], Murali & Weinberg 1996 [102]). Because of the wide-spread use of globular clusters to determine distances to external galaxies it is important to determine if globular clusters truly are the same from one galaxy to the next. This is best determined by studying the physical structures and stellar populations of globular clusters in nearby external galaxies.

The nearest large globular cluster system outside the Milky Way Galaxy is that of the Andromeda Galaxy (= M31 = NGC 224 = UGC 00454). M31 is located at a distance of 725 kpc ($\mu_0 = 24.3$, van den Bergh 1991 [148])[2] so individual stars in M31's

[1] The most massive Galactic globular clusters, such as ω Cen, do exhibit spreads in metallicity. This is probably due to the globular cluster being massive enough to retain debris from supernovae explosions for use in a second generation of star formation.

[2] Recent parallax measurements from the *Hipparcos* satellite suggest that M31 may be at a distance of $\sim$ 900 kpc (Feast & Catchpole 1997 [53]) while others (e.g. Madore & Freedman (1997) [93]) have

in the M31 system based on the positions and radial velocities of the clusters. These groups may be associated with sub-structure in the stellar halo of M31. This is similar to the situation in the Galactic halo where several globular clusters are believed to have originated in external galaxies that are orbiting, or have been accreted by, the Galaxy. Lin & Richer 1992 [86] show that four young globular clusters are located in the Magellanic Stream and thus may have been stripped from the Large Magellanic Cloud. Ibata et al. 1994 [77] found a dwarf galaxy crashing into the far side of the Milky Way. If accretion has played a significant rôle in adding material to the halo of M31 then stars from different accretion events could have different ages and metallicities resulting in the halo of M31 resembling a patchwork of different stellar populations. Any such clumps in the M31 halo will be seen in projection against the rest of the halo so a CMD will show features from both the underlying halo population and the population of the clump. If the halo of M31 is made up of accreted clumps then CMDs of the halo will show evidence of multiple populations. The exact mix of stellar populations will vary from one accreted clump to the next.

The formation of galactic halos is a central problem in astronomy and has implications for our understanding of galactic formation and evolution. Until recently it has been assumed that the spiral galaxies in the Local Group (M33, M31, and the Milky Way galaxy) formed at similar times out of the same proto-galactic material. However, evidence that the halo of M31 may have very different chemical abundances from those of the Galactic halo has opened up the possibility that M31 and the Galaxy have had very different formation histories, or chemical enrichment histories, or both. If this is the case then the assumption that all galaxies of a particular Hubble type have comparable stellar populations will have to be rethought. It should, however, be noted that the current estimates of the metallicity of the halo of M31 are dependent on the distance to M31. If the distance to M31 is increased then the halo metallicity will decrease.

They found that the halo luminosity function for red-giants was steeper than G1's red-giant luminosity function, and had a less pronounced horizontal branch. They compared their M31 halo luminosity functions to those of several Galactic globular clusters covering a range of metallicities and found that no single-metallicity luminosity function could reproduce the M31 halo's luminosity function.

Deep CMD studies have the potential to provide direct information on the chemical composition and age of the halo of M31. This is important as there is some debate as to the ages of the globular clusters in the M31 system. There is considerable evidence that the halo of M31 is an old stellar system. First, integrated colours (Frogel et al. 1980 [55], Bohlin et al. 1993 [18]) and the morphologies of CMDs of individual clusters suggest that the M31 globular cluster system has an age comparable to that of the Galactic globular cluster system. Second, no extended asymptotic-giant branch stars have been detected in the halo or the bulge of M31 (Rich & Mighell 1995 [120]) as would be expected if an intermediate-age population was present. Third, the presence of RR Lyrae variables implies that at least part of the stellar population is old.

On the other hand, measurements of Hβ enhancements (Burstein et al. 1984 [21], Tripicco 1989 [146]) in the spectra of M31 globular clusters, relative to spectra of Galactic globular clusters, have led to speculation that the M31 globular clusters could contain a higher fraction of main-sequence stars than the Galactic globular clusters do. This would imply that the M31 globular clusters are younger than their Galactic counterparts. It has recently been suggested (e.g. Faber 1995 [50]) that Hβ enhancements in red elliptical galaxies are due to the presence of a population of young main-sequence turn-off stars. It is, therefore, of great interest to obtain CMD-based determinations of the mix of ages and metallicities in the nearest population of stars resembling a "red elliptical" galaxy—the halo of M31.

Ashman & Bird (1993) [4] have identified several distinct groups of globular clusters

1.2 The Halo of M31

The stellar populations in the halo of M31 provide a direct tracer of the star formation history, and the early evolution, of that galaxy. The earliest published colour–magnitude diagrams (CMDs) of the M31 halo were obtained by Crotts (1986) [34] and Mould & Kristian (1986) [101]. Mould & Kristian (1986) [101] studied a field ~ 7 kpc from the centre of M31 along the southeast minor axis and found a mean iron abundance of $\overline{[\mathrm{Fe/H}]} \sim -0.6$, comparable to that of the metal-rich Galactic globular cluster 47 Tuc. Subsequent ground-based studies by Pritchet & van den Bergh (1988) [113], Christian & Heasley (1991) [29], Davidge (1993) [37], Durrell et al. (1994) [48], and Couture et al. (1995) [31] produced CMDs reaching down to near the level of the horizontal branch stars. These studies confirmed that the M31 halo has a mean metallicity of $[\mathrm{m/H}] \sim -0.6$, similar to that of 47 Tuc. This makes the M31 halo approximately eight times more metal-rich than the Galactic halo, which has $[\mathrm{m/H}] \sim -1.5$.

Several of these studies have found that the observed spread in colour across the red-giant branch is larger than what would be expected from photometric uncertainties, and could be due to an intrinsic spread in the metallicity of the halo of M31 ($0.3 \lesssim \sigma_{[\mathrm{m/H}]} \lesssim 0.5$). Couture et al. (1995) [31] undertook a deep V- and I-band study of the halo of M31 in the vicinity of five of M31's globular clusters. They found that the halo was dominated by a stellar population with a mean iron abundance comparable to that of 47 Tuc but that a small component of the red giants had iron abundances of between -1 and -1.5. This is consistent with Pritchet & van den Bergh's (1987) [114] detection of RR Lyrae variables in the halo of M31.

Recently Rich et al. (1996) [119] used the *HST* to obtain CMDs and luminosity functions of the metal-rich M31 globular cluster G1 (= Mayall II) and the field near it.

was located within the Milky Way galaxy.

The debate over M31's distance was finally put to rest in 1923 when Edwin Hubble identified Cepheid variables in M31 and was able to use the Cepheid period–luminosity relation to derive a distance of 285 kpc (Hubble 1925 [75]). This demonstrated that M31 was not a part of the Milky Way galaxy but a separate stellar system located a considerable distance from our own.

Detailed discussions of these early references to, and observations of, M31 can be found in Hodge (1992) [71], and de Vaucouleurs (1987) [40].

In the nineteen-forties Walter Baade took advantage of the wartime black-outs of Los Angeles to obtain deep photographic images of M31 to study a discrepancy between the periods of the brightest Cepheids in Galactic globular clusters and the periods of Cepheids with comparable brightnesses in M31. This discrepancy eventually led to Baade's discovery that the Cepheids in the disc of M31 were Population I stars while those in the Galactic globular clusters were Population II stars and thus followed different period–luminosity relations. Applying the Population I period–luminosity relation to the Cepheids in M31 led to a revised distance of $\sim$ 550 kpc for that galaxy, a discovery that doubled the estimated size of the Universe.

Recently parallax measurements from the *Hipparcos* satellite have been published which have led to a further revision of the distance to M31, and thus the size of the Universe. If the preliminary *Hipparcos* results are confirmed by further studies then the new distance to M31 would be $\sim$ 900 kpc: an increase of $\sim$ 25% in the estimated size of the Universe (Feast & Catchpole 1997 [53]). Despite M31 being very near-by on the cosmological map there is still considerable uncertainty as to such fundamental parameters as its distance. The careful study of this galaxy can still teach us much about the fundamental nature of the Universe.

times the distance of Sirius" (de Vaucouleurs 1987 [40]). This would have placed M31 at a distance of only 5.3 kpc from Earth, but it is important to realize that Herschel's description is essentially that of what we would today consider a galaxy. The idea that external galaxies might exist was first proposed by Thomas White in 1750 and by Immanuel Kant in 1755. However, these philosophers based their ideas on religious and philosophical considerations, not on observational evidence or physical laws (Hoskin 1970 [74], Jones 1971 [81]).

In 1847 George Bond observed dark "canals" in the Andromeda nebula. These were the first recorded observations of spiral arms in external galaxies, although the "Bond canals" were not recognized as the lanes between spiral arms until some forty years later. Bond also resolved approximately 1500 stars with a limiting magnitude of $V \sim 15$ in front of the nebula. The brightest super-giants in M31 are bright enough to have been detected in Bond's photographic plates.

During the nineteenth, and early twentieth, centuries there was considerable debate as to whether M31 was a diffuse object within the Milky Way galaxy or a separate external galaxy. Support for the external galaxy hypothesis came from radial velocity measurements which showed that M31 was approaching us with a heliocentric radial velocity of $v_h \sim -300$ km$\cdot$s^{-1}, and was rotating (e.g. Slipher 1913 [133], Pease 1918 [107]). These observations were difficult to explain if M31 was a small, near-by, nebula. In addition, spectroscopy of M31 (Scheinel 1898 [130]) revealed a Solar-type spectrum indicating that M31 was made up of a large number of stars similar to those found in the Solar neighbourhood, and not a diffuse gas as would be expected if the nebula were a star-forming region. On the other hand, in 1885 a "new star" was observed near the nucleus of M31. This star, which was named S Andromedae, reached a maximum visual magnitude of 6.7 then faded over several hundred days (see de Vaucouleurs & Corwin 1985 [41] for a complete light curve). S Andromedae's nova-like appearance was used to argue that M31

Chapter 1

Introduction

1.1 Historical Background for the Andromeda Galaxy

The Andromeda Galaxy is one of the few external galaxies that is visible to the naked eye and has been a part of humanity's store of myths and legends since antiquity. The earliest written reference to the galaxy was by the 4$^{\text{th}}$-century Roman poet Rufus Festus Avienus, who alluded to the nebula in Andromeda in his translation of the *Phaenonena* of Aratus, a Greek poem describing the constellations, which is apparently based on a lost work of Eudoxus of Cnidos. Several hundred years later the Persian astronomer Abu I-Husain al-Sufi (903–986 A.D.) depicted the constellation of Andromeda with a *lathka sahibiya* or "nebulous spot" at the location of the Andromeda Galaxy. The earliest known telescopic observations of the Andromeda Nebula were by Simon Marius in 1612, Ismael Bullialdus in 1667, and Edmond Halley in 1715. Charles Messier catalogued the object as "M31" in his *Catalogue of Nebulæ and Stellar Clusters*, originally published in 1774.

After its recognition as a non-stellar object there was considerable debate over the nature of the Great Nebula in Andromeda. William Herschel described the nebula as a collection of millions of stars that was at a distance of no more than "two thousand

Acknowledgement

Regardless of what UBC's graduation requirements say a work like this can never be the product of just one person. Many people have contributed to this thesis in various ways and it would be impossible to list them all. I would, however, like to thank Greg Fahlman and Harvey Richer for their endless instruction, suggestions, and patience through-out my incarceration at UBC. I would also like to thank the entire crew of astronomers at UBC for sharing their knowledge of astronomy, and generally being a good group of people to work and play with.

Thank go out to Peter Stetson for kindly making available his ALLFRAME software, which proved so valuable in reducing the *HST* data presented here. I would like to thank Dave Bohlender and Christian Vanderriest for obtaining the SIS spectra of G185 and G185B. I would also like to thank Kent Ashman, Pat Côté, Pat Durrell, Rodrigo Ibata, and Sydney van den Bergh for many useful discussions and suggestions.

A dissertation is not completely written in a vacuum so I would like to thank those people in the real world whom I saw far too little of over the past few years: Barry, the CHL managers, the CHL Widows' Club, Doug, Kelly & Gail, Kerry, Marc, Martha & Alan, Owen & Fiona, Phil & Jill, Tara, the von Schulmann clan, and the rest of the people who have kept life interesting over the past half-decade. And to my parents, for so many years of support and encouragement—thanks!

Most importantly, I owe a very great deal to Kyla. Not only has she kept me somewhat sane, she has been been an inspiration and a star that outshines any mere globular cluster.

Finally, I would like to thank Lewis Vending for the many balanced meals.

- Couture, J., Racine, R., Harris, W. E., & Holland, S. (1995), *Astronomical Journal*, **109**, 2050
- Holland, S., & Harris, W. E. (1991), *Astronomical Journal*, **103**, 131

A list of conference presentations that I gave where preliminary results from this thesis were presented is given below.

- HST *WFPC2 Observations of Tidal Tails in Globular Clusters in M31*
  ◦ 189$^{\mathrm{th}}$ Meeting of the AAS at Toronto, Ontario, January 12–16, 1997.
- *The Double Cluster G185 in M31*
  ◦ 185$^{\mathrm{th}}$ Meeting of the AAS at Tucson, Arizona, January 8–12, 1995.
- *The Internal Structure of the M31 Globular Cluster G302*
  ◦ 182$^{\mathrm{nd}}$ Meeting of the AAS at UC Berkeley, California, June 6–10, 1993.
  ◦ 24$^{\mathrm{th}}$ Meeting of the CASCA at the University of Victoria, B.C., June 1–4, 1993.

Publications

Some of the material in this thesis has been previously published in the astronomical literature. Most of Chapter 5 appeared in Holland et al. (1997) [*Astronomical Journal*, **114**, 1488]. Chapter 6 appeared in Holland et al. (1996) [*Astronomical Journal*, **112**, 1035] and most of Chapter 7 appeared in Holland et al. (1995) [*Astronomical Journal*, **109**, 2061]. A full list of my publications prior to the completion of this thesis is given below.

- Holland, S., Fahlman, G. G., & Richer, H. B. (1997), *Astronomical Journal*, **114**, 1488
- Richer, H. B., Fahlman, G. G., Ibata, R. A., Pryor, C., Bell, R. A., Bolte, M., Mandushev, G. Harris, W. E., Hesser, J. E., Holland, S., Ivanans, N., Stetson, P. B., VandenBerg, D. A., & Wood, M. (1996), *Astrophysical Journal*, **484**, 741
- Holland, S., Fahlman, G. G., & Richer, H. B. (1996), *Astronomical Journal*, **112**, 1035
- Richer, H. B., Harris, W. E., Fahlman, G. G., Bell, R. A., Bond, H. E., Hesser, J. E., Holland, S., Pryor, C., Stetson, P. B., & van den Bergh, S. (1996) *Astrophysical Journal*, **463**, 602
- Holland, S., Fahlman, G. G., & Richer, H. B. (1995), *Astronomical Journal*, **109**, 2161

List of Figures

List of Tables

Table of Contents

This thesis also presents the deepest colour–magnitude diagram for M31's halo. There is no evidence for young stars, or of a second parameter problem in M31's halo. The halo stars have [m/H] ~ -0.6 with a spread of $-2.0 \lesssim$ [m/H] $\lesssim -0.2$. The M31 halo is ~ 8 times more metal-rich than the Galactic halo and ~ 4 times more metal-rich than the M31 globular cluster system.

Abstract

The results of two studies of M31's globular cluster system are presented. One study used deep V- and I-band images of 24 M31 globular clusters taken with CFHT's HRCam. This data is the best available ground-based data for determining structural parameters (such as core and tidal radii, ellipticities, and orientations) for M31's globular clusters. Two-dimensional Michie–King models were fit to each cluster and the results compared to the structural parameters of the Galactic clusters. There is no evidence for any difference between the mean tidal radii and ellipticities of globular clusters in the two galaxies. Core radii and half-mass radii are too strongly affected by seeing to allow a comparison between the two galaxies.

The second study used deep *HST* WFC V- and I-band images of G302 and G312, two globular clusters in M31's halo, to obtain the deepest colour–magnitude diagrams of any M31 globular cluster. Structural parameters were determined for the two clusters and compared to those from the CFHT data. Tidal radii and ellipticities from the CFHT data agree with the more reliable results obtained from *HST* data. The core radii agree for seeings of $\lesssim 4$ times the cluster's core radius. It is not possible to obtain reliable core parameters for the M31 clusters using ground-based telescopes unless adaptive optics are used to reduce the seeing to $\lesssim 0\farcs1$. However, the overall sizes and shapes of the clusters can easily be measured if FWHM $\lesssim 1''$. Images of M31 clusters obtained from the ground have similar resolutions to those of Virgo globular clusters obtained with the *HST*'s PC. Therefore detailed structural parameters can be obtained for globular clusters in the elliptical galaxies of the Virgo cluster.

THE GLOBULAR CLUSTERS AND HALO OF M31

By

Stephen Holland

B. Sc. (Physics & Astronomy) University of Victoria (1989)

M. Sc. (Astronomy) McMaster University (1991)

A THESIS SUBMITTED IN PARTIAL FULFILLMENT OF

THE REQUIREMENTS FOR THE DEGREE OF

DOCTOR OF PHILOSOPHY

in

THE FACULTY OF GRADUATE STUDIES

PHYSICS & ASTRONOMY

We accept this thesis as conforming

to the required standard

. . . .

. . . .

. . . .

THE UNIVERSITY OF BRITISH COLUMBIA

November 1997